DOCTORAL DISSERTATION

Displacement Forecasting in Mining Areas using Satellite SAR Interferometry and Machine Learning

Dariusz Głąbicki, MSc, Eng.

Supervisors:
Wojciech Milczarek, DSc, PhD, Eng.
Milan Lazecky, PhD

A thesis presented for the degree of
Doctor of Philosophy

Faculty of Geoengineering, Mining and Geology
Department of Geodesy and Geoinformatics

Wrocław University
of Science and Technology

Wrocław, 2023

ABSTRACT

Displacement Forecasting in Mining Areas using Satellite SAR Interferometry and Machine Learning

Dariusz Głąbicki, MSc Eng.

Underground mining activity has a significant impact on the ground surface, which is manifested as ground surface displacement that poses a threat to civil infrastructure. Monitoring and forecasting of ground deformation caused by mining activities is crucial for effective planning of mining operations and reducing their impact on the surface. In recent years, the method of satellite-based SAR interferometry (InSAR) has been applied to the measurement of displacements in mining areas due to its high spatial and temporal resolution. This method can provide a considerable amount of data on ground surface movements. Machine learning methods are being applied in a growing number of fields due to their effectiveness in processing large data sets, finding patterns in the data and exploring hidden relationships in the data.

The dissertation investigated the application of vertical ground surface displacement measurements by InSAR methods in an underground mining area to create data-driven machine learning models. These models were adapted to forecast future displacement values by using historical displacement data in time series forecasting. The research was carried out in the Legnica-Głogów Copper Belt area, where underground mining of copper ores is carried out, affecting the ground surface.

InSAR time series processing methods: the Persistent Scatterer InSAR (PSInSAR) method and the Small Baseline Subset (SBAS) method, were used in the analysis of satellite radar imagery to measure the time course of displacements in the study area for the period from 20 May 2016 to 26 October 2020. In addition, a transformation of displacements from acquisition geometry of satellite data to vertical and horizontal displacement geometry was performed using satellite data acquired from two orbits. The vertical displacement values measured by remote sensing method were verified with the obtained levelling data.

The study further investigates the application of selected statistical methods, machine learning algorithms and neural networks, used in time series forecasting, to create predictive models based on InSAR measurement data. The research focused on the potential of using machine learning models as global data-driven models, trained on datasets of time series with similar characteristics. The study showed that global machine learning models outperformed baseline methods by up to 45%. The model with the highest forecast accuracy was the Ensemble model using a set of regression models.

The results of the research carried out in the dissertation are contributing to the understanding of the processes occurring on the surface as a result of underground mining operations. The developed models can be used to predict surface displacements, providing a tool to support decision-making processes in planning mining operations.

Keywords: ground surface displacement, subsidence, mining area, satellite SAR interferometry, machine learning, neural networks, time series forecasting

---

European Funds
Knowledge Education Development

Wrocław University of Science and Technology

European Union
European Social Fund

Doctoral thesis co-financed by the European Union under the European Social Fund,
project no POWR.03.02.00-00-I003/16

STRESZCZENIE

Prognozowanie Przemieszczeń na Terenach Górniczych z wykorzystaniem Satelitarnej Interferometrii SAR i Uczenia Maszynowego

mgr inż. Dariusz Głąbicki

Podziemna działalność górnicza ma istotny wpływ na powierzchnię terenu, objawiający się w postaci przemieszczeń powierzchni gruntu zagrażających infrastrukturze budowlanej i technicznej. Monitorowanie i prognozowanie deformacji terenu wywołanych działalnością górniczą jest kluczowe dla efektywnego planowania eksploatacji i zmniejszania jej wpływu na powierzchnię. W ciągu ostatnich lat metoda satelitarnej interferometrii radarowej SAR (InSAR) znalazła zastosowanie w pomiarze przemieszczeń na terenach górniczych dzięki wysokiej rozdzielczości przestrzennej i czasowej. Metoda ta może dostarczyć dużą ilość danych na temat zmian powierzchni terenu na badanym obszarze. Metody uczenia maszynowego są stosowane w rosnącej liczbie dziedzin ze względu na ich skuteczność w przetwarzaniu dużych zbiorów danych, odnajdywaniu wzorców w danych i badania ukrytych relacji.

W ramach rozprawy doktorskiej zbadano zastosowanie pomiarów przemieszczeń pionowych powierzchni terenu metodami InSAR na obszarze górnictwa podziemnego do utworzenia modeli uczenia maszynowego opartych na danych. Modele te zostały przystosowane do prognozowania wartości przemieszczeń w przyszłości poprzez wykorzystanie danych historycznych o przemieszczeniach w prognozowaniu szeregów czasowych. Badania przeprowadzono na obszarze Legnicko-Głogowskiego Okręgu Miedziowego, w którym prowadzone jest wydobycie rud miedzi metodą górnictwa podziemnego, mające wpływ na powierzchnię terenu.

Metody przetwarzania szeregów czasowych InSAR: metoda Persistent Scatterer InSAR (PSInSAR) oraz metoda Small Baseline Subset (SBAS), zostały wykorzystane w analizie satelitarnych zobrazowań radarowych w celu pomiaru czasowego przebiegu przemieszczeń na obszarze badań w okresie od 20 maja 2016 do 26 października 2020. Dodatkowo przeprowadzono transformację przemieszczeń z geometrii akwizycji danych satelity do geometrii przemieszczeń pionowych i poziomych, z wykorzystaniem danych satelitarnych pozyskanych z dwóch orbit. Wartości przemieszczeń pionowych zmierzone metodą teledetekcyjną zweryfikowano z pozyskanymi danymi niwelacyjnymi.

W dalszej części pracy zbadano zastosowanie wybranych metod statystycznych, algorytmów uczenia maszynowego i sieci neuronowych, stosowanych w prognozowaniu szeregów czasowych, do utworzenia modeli predykcyjnych opartych na danych pochodzących z pomiaru InSAR. W badaniach skupiono się na potencjale wykorzystania modeli uczenia maszynowego jako modeli globalnych, uczonych na zbiorach szeregów czasowych o podobnych charakterystykach. W pracy wykazano, że globalne modele uczenia maszynowego osiągają skuteczność przewyższającą bazowe metody o nawet 45%. Modelem o najwyższej dokładności był model Ensemble wykorzystujący zbiór modeli regresji.

Wyniki interdyscyplinarnych badań przeprowadzonych w pracy doktorskiej stanowią wkład w zrozumienie procesów zachodzących na powierzchni na skutek prowadzenia podziemnej eksploatacji górniczej. Opracowane modele mogą zostać wykorzystane do prognozowania przemieszczeń powierzchni terenu, stanowiąc narzędzie wspomagające procesy decyzyjne w planowaniu eksploatacji górniczej.

Słowa kluczowe: przemieszczenia powierzchni terenu, osiadania, teren górniczy, satelitarna interferometria SAR, uczenie maszynowe, sieci neuronowe, prognozowanie szeregów czasowych

---

Fundusze Europejskie Wiedza Edukacja Rozwój

Politechnika Wrocławska

Unia Europejska Europejski Fundusz Społeczny

Praca doktorska współfinansowana ze środków Unii Europejskiej w ramach Europejskiego Funduszu Społecznego, nr projektu POWR.03.02.00-00-I003/16

Acknowledgements

Although a PhD thesis is written by one person, a significant group of people indirectly contribute to its creation. This is where I would like to include my thanks to all those who have contributed to the creation of this dissertation. It would be impossible to mention everyone, therefore I will acknowledge the most important people below.

I would like to thank my supervisors, Wojciech Milczarek and Milan Lazecky, for the knowledge and experience they provided, the support and commitment they showed, the patient answers to the questions asked and for introducing me to the world of academia.

I would like to thank the staff of the Department of Geodesy and Geoinformatics, with Jan Blachowski in the lead. In particular, I would like to thank my colleagues from room 2.11: Ania Kopeć, Natalia Bugajska-Jędraszek, Ola Kozłowska-Woszczycka, Marek Sompolski, Michał Tympalski, Paweł Trybała and Karolina Owczarz. Conversations with you on a variety of topics, and the atmosphere you created, provided a much needed distraction from writing this thesis and helped me in keeping a sober mind.

The research internship completed during my PhD was an extremely valuable and rewarding experience. I would like to thank the staff at the University of Leeds, my biggest thanks go to Professor Tim Wright and Professor Andy Hooper for their hospitality and support during the internship. I would also like to thank the InterDok programme for enabling the internship financially.

Special thanks go to my parents, without whose support I would not have been in this place of my life. I am forever grateful to my family for their support and motivation.

Someone once told me that I would meet a lot of fantastic people on my PhD, and it's true. In addition to that, I found love. I would like to thank my girlfriend Ania for her steadfast belief in me and for making my life brighter.

Dariusz Głąbicki
Wrocław, April 5, 2023

Podziękowania

Doktorat jest dziełem jednego człowieka, ale do jego powstania w sposób pośredni przyczynia się spora grupa ludzi. W tym miejscu chciałbym zawrzeć podziękowania dla wszystkich, którzy przyczynili się do stworzenia tej rozprawy. Nie sposób wymienić wszystkich, dlatego najważniejsze osoby postaram się wspomnieć poniżej.

Dziękuję promotorom, Wojciechowi Milczarkowi i Milanowi Lazecky'emu, za przekazaną wiedzę i doświadczenie, okazane wsparcie i zaangażowanie, cierpliwe odpowiadanie na stawiane pytania i wprowadzenie mnie w świat nauki.

Dziękuję pracownikom i doktorantom z Katedry Geodezji i Geoinformatyki, z kierownikiem Janem Blachowskim na czele. W szczególności dziękuję koleżankom i kolegom z pokoju 2.11: Ani Kopeć, Natalii Bugajskiej-Jędraszek, Oli Kozłowskiej-Woszczyckiej, Markowi Sompolskiemu, Michałowi Tympalskiemu, Pawłowi Trybale i Karolinie Owczarz. Rozmowy z Wami na przeróżne tematy i stworzona przez Was atmosfera stanowiły przyjemną odskocznię od pisania rozprawy i pomogły zachować trzeźwy umysł.

Staż naukowy zrealizowany podczas doktoratu był niezwykle cennym i rozwijającym doświadczeniem. Dziękuję pracownikom Uniwersytetu w Leeds, największe podziękowania kieruję w stronę profesora Tima Wrighta oraz profesora Andy'ego Hoopera za okazaną gościnność i wsparcie w trakcie stażu. Dziękuję także programowi InterDok za finansowe umożliwienie wyjazdu.

Szczególne podziękowania kieruję do moich rodziców, bez pomocy których nie znalazłbym się w tym miejscu mojego życia. Jestem dozgonnie wdzięczny swojej rodzinie za jej wsparcie i motywację.

Ktoś powiedział mi, że na doktoracie poznam wielu fantastycznych ludzi, i to prawda. Ja oprócz tego znalazłem miłość. Dziękuję mojej dziewczynie Ani za nieustającą wiarę we mnie i czynienie mojego życia lepszym.

Dariusz Głąbicki
Wrocław, 5 kwietnia 2023

Data sources and funding

Doctoral thesis was realised with the support of co-financing by the European Union under the European Social Fund, project InterDok - Programmes of Interdisciplinary Doctoral Studies at Wrocław University of Science and Technology, project no. POWR.03.02.00-00-I003/16.

The mining and surveying data used in this thesis for the three selected mining areas of the Legnica-Głogów Copper Belt were made available under agreement no. KGHM-BZ-U-0299-2022 signed on 24.05.2022 between KGHM Polska Miedź S.A. and Wrocław University of Science and Technology.

The thesis uses satellite SAR imagery of the Sentinel-1 mission, provided by the European Space Agency as part of the Copernicus programme.

Źródła danych i finansowanie

Praca doktorska została zrealizowana dzięki współfinansowaniu ze środków Unii Europejskiej w ramach Europejskiego Funduszu Społecznego, projekt *InterDok – Programy Interdyscyplinarnych Studiów Doktoranckich na Politechnice Wrocławskiej*, nr projektu POWR.03.02.00-00-I003/16.

Wykorzystane w pracy dane górnicze i geodezyjne dla trzech wybranych obszarów górniczych Legnicko-Głogowskiego Okręgu Miedziowego zostały udostępnione na podstawie umowy nr KGHM-BZ-U-0299-2022 z dnia 24.05. 2022 r. zawartej pomiędzy KGHM Polska Miedź S.A. a Politechnika Wrocławską.

W pracy wykorzystano satelitarne zobrazowania misji Sentinel-1 udostępniane przez Europejską Agencję Kosmiczną w ramach programu Copernicus.

Contents

List of Figures

List of Tables

List of Acronyms

3-D	Three-Dimensional
ACF	Autocorrelation Function
ADALINE	ADAptive LInear NEuron
AI	Artificial Intelligence
AIC	Akaike Information Criterion
ALD	Azimuth Look Direction
ALOS	Advanced Land Observing Satellite
ALS	Aerial Laser Scanning
ANN	Artificial Neural Network
AOI	Area of Interest
API	Application Programming Interface
APS	Atmospheric Phase Screen
AR	Autoregression
ARIMA	Autoregressive Integrated Moving Average
ARMA	Autoregressive Moving Average
ASF	Alaska Satellite Facility
CNN	Convolutional Neural Network
CPT	Coherent Pixel Technique
DEM	Digital Elevation Model
DEM	Discrete Element Modeling
DePSI	Delft Persistent Scatterer Interferometry
DInSAR	Differential SAR Interferometry
DL	Deep Learning
DS	Distributed Scatterer
E-W	East-West (direction)
EGMS	European Ground Motion Service
EM	Electromagnetic
ERS	European Remote Sensing satellite
ES	Exponential Smoothing
ESD	Enhanced Spectral Diversity
FEM	Finite Element Modeling
FFT	Fast Fourier Transform
GBM	Gradient Boosting Machine
GNSS	Global Navigation Satellite System
GPS	Global Positioning System
GPU	Graphics Processing Unit
GRD	Ground Range Detected
GRU	Gated Recurrent Unit
IDW	Inverse Distance Weighting
InSAR	Synthetic Aperture Radar Interferometry

IPTA	Interferometric Point Target Analysis
IS-EPOS	Induced Seismicity - European Plate Observing System
IT	Information Technologies
IW	Interferometric Wide swath
KGHM	Kombinat Górniczo-Hutniczy Miedzi
LGCB	Legnica-Głogów Copper Belt
LiCSAR	Looking into Continents from space with SAR
LOS	Line of Sight
LS	Laser Scanning
LSTM	Long Short-Term Memory
MA	Moving Average
MAE	Mean Absolute Error
MAI	Multiple Aperture InSAR
MAPE	Mean Absolute Percentage Error
ML	Machine Learning
MLP	Multilayer Perceptron
MSE	Mean Squared Error
MTInSAR	Multi-Temporal InSAR
N-BEATS	Neural Basis Expansion Analysis for Interpretable Time Series forecasting
N-S	North-South (direction)
NCB	National Coal Board
NLP	Natural Language Processing
OT	Offset Tracking
PIM	Probability Integral Method
PS	Persistent Scatterer
PSI	Persistent Scatterer Interferometry
PSInSAR	Persistent Scatterer InSAR
RMSE	Root Mean Squared Error
RNN	Recurrent Neural Network
SAR	Synthetic Aperture Radar
SARIMA	Seasonal Autoregressive Integrated Moving Average
SBAS	Small Baseline Subset
SBInSAR	Small Baseline InSAR
SDPS	Surface Deformation Prediction Software
SGD	Stochastic Gradient Descent
SLC	Single Look Complex
SNAPHU	Statistical-cost, Network-flow Algorithm for PHase Unwrapping
SNR	Signal-to-Noise Ratio
SRTM	Shuttle Radar Topography Mission
StaMPS-MTI	Stanford Method for PS - Multi-Temporal InSAR
SVD	Singular Value Decomposition
TCN	Temporal Convolutional Network
TEC	Total Electron Content
TFT	Temporal Fusion Transformer

TLS	Terrestrial Laser Scanning
TOPS	Terrain Observation with Progressive Scans
TS	Time Series
U-D	Up-Down (direction)
UAV	Unmanned Aerial Vehicle
VV	Vertical sent - Vertical received
WGS	World Geodetic System
WLS	Weighted Least Squares

Chapter 1

Introduction

Argumentation

The demand for natural raw materials remains very high and is growing year by year, primarily due to the growth of the economy and the development of new technologies. Economic sectors such as IT (Information Technologies), renewables and the electric car industry are driving steady demand for metals, including copper, silver, lithium, and rare earth metals. The extraction of minerals by mining methods implies changes on the surface of the Earth, accompanying both open-pit and underground mining. The impact of underground mining on the earth's surface manifests itself in the form of continuous and discontinuous deformations, which result in damage to building and technical infrastructure if the deformations occur in urban areas. Therefore, protection of mining areas by monitoring and forecasting ground surface displacement is an important subject, coupled both with active mining areas, as well as post-mining areas where displacements can still occur.

The remote sensing method of satellite SAR interferometry (InSAR) has found application in monitoring ground surface displacement in mining areas, as a complementary method to traditional measurement methods such as leveling and Global Navigation Satellite System (GNSS). InSAR provides displacement measurements with high spatial and temporal resolution over large areas, compared to scattered measurements by traditional methods. The remote sensing method of satellite SAR interferometry (InSAR) has found application in monitoring ground surface displacement in mining areas, as a complementary method to traditional measurement methods such as leveling and Global Navigation Satellite System (GNSS). InSAR provides displacement measurements with high spatial and temporal resolution over wide areas, compared to scattered measurements by traditional methods. The InSAR method has been successfully used in displacement measurements in areas of mining activity around the world. Particularly significant are the multi-temporal InSAR methods, which allow the determination of the course of vertical displacements over short time intervals (6-12 days in the case of Sentinel-1 satellites).

Over the years, a number of methods have been developed to predict displacement in mining areas. These include empirical methods, functional methods and numerical methods. With the developments in the field of artificial intelligence and work on machine learning algorithms, the possibility of creating forecasting models based on artificial intelligence has emerged. The performance of artificial intelligence algorithms in working with remote sensing data, as well as their predictive capabilities, have been confirmed in numerous studies conducted in recent years. Moreover, machine learning can provide insight into the relationships between different variables constituting the model.

Machine learning algorithms require large amounts of training data to create an effective model. The InSAR method is often identified as a potential data source due to its extensive surface coverage and high temporal resolution. However, not many studies have been conducted on the use of InSAR measurements to work with machine learning algorithms, especially in mining displacement investigations.

Aim

This dissertation addresses the previously mentioned gap by combining the InSAR remote sensing method of displacement measurement and artificial intelligence techniques. The research hypothesis of the study is that *models based on machine learning algorithms and measurement data from the InSAR method can be applied to effectively predict vertical ground surface displacement in areas affected by underground mining.*

The objective of this thesis is to investigate the potential of combining InSAR technology with machine learning in forecasting mining displacements. Development of a machine learning-based approach to predicting mining displacements, with InSAR data used as input will be the focus of research conducted in this thesis.

Scope

The research will be carried out in the area of underground copper ore mining in south-western Poland, in the Legnica-Głogów Copper Belt (LGCB) area. In order to prove the stated research hypothesis, studies will be conducted within the specified scope:

- An InSAR measurement of vertical displacements in the study area will be carried out, using measurements from different satellite data acquisition paths and considering the occurrence of horizontal displacements.
- Remote sensing InSAR measurements will be validated with leveling measurements provided by the mining authority.
- The InSAR-based displacement time series will be used as input to train selected machine learning algorithms to develop models predicting vertical displacements.
- The forecasts produced by the developed predictive models will be verified against actual vertical displacement values.

Outline

This chapter introduces the scope and aims of the thesis. Throughout the following chapters, a comprehensive understanding of the theoretical aspects of the problem at hand will be provided. Technical and methodological issues related to the thesis statement will also be explained, and the results of analyses conducted in a selected study area will be presented and discussed.

Chapters 2, 3 and 4 will provide a theoretical background to the studies conducted within the thesis, drawing on examples from world literature on topics of mining subsidence, SAR interferometry and machine learning. Chapter 5 will briefly introduce the study area for which research was conducted as part of the doctoral thesis.

In Chapter 6, the methodological and technical aspects of the first part of doctoral research, focused on InSAR studies, will be explained. In Chapter 7, a methodology for solving the problem of displacement forecasting with the use of machine learning will be presented. Chapter 8 will be dedicated to the analysis and interpretation of results obtained for the study area. Finally, Chapter 9 will provide a summary and final conclusions, along with outlooks for further research on the topic tackled within the thesis.

Chapter 2

Surface displacements induced by mining - determination, modeling and forecasting

2.1 Theoretical description of the ground subsidence phenomenon

Underground exploitation of natural resources leads to the formation of a void in the rock mass, which is successively filled by the rock layers overlying the deposit. As a result of load and gravity, successive layers above the mined seam are sagging. The state of equilibrium in the rock mass is disturbed, causing stresses in the rock layers due to yielding of the overlying strata. As a result of the displacement of rock layers above the mined deposit, *subsidence troughs* are forming at successive layers in the rock mass. This phenomenon propagates to the surface (subsidence trough at the surface layer), and the ground above the mining field begins to subside. The objects within the subsidence trough on the surface are prone to deformations resulting from vertical and horizontal motions of ground within the subsidence trough [109]. It should be emphasised that subsidence troughs belong to a group of continuous deformations, occurring when mining is carried out at considerable depths and when specific mining systems are used. **Due to the characteristics of the chosen study area, the phenomenon of subsidence will be described with the focus on the effects of mining at high depths in the form of continuous deformations.**

Depending on the size of the exploited raw material deposit and the deposit depth, three types of subsidence trough are distinguished [106]: incomplete - when the subsidence w at the bottom of the trough is less than maximum possible subsidence w_{max}; complete - when the bottom of the trough reaches maximum subsidence w_{max}; and overcomplete - when a flat bottom of the subsidence trough reached the w_{max} value [106]. The size of the troughs is not the same as the size of the mined seams. It has been adopted that, at a certain distance from the boundary of the exploitation, defined by a *limit angle* (or *influence angle*) γ, the displacements at the surface are not present. The shape and size of a subsidence trough depend on a number of factors, among which should be distinguished:

- size of the exploited raw material deposit,
- depth of exploitation,

- deposit thickness,
- slope of the deposit,
- physical and mechanical properties of the rock layers overlying the exploited seam,
- duration of the mining operation underground.

Assuming that the exploited seam is horizontal and has a rectangular shape, the subsidence basin occurring at the surface has a shape resembling an ellipse and occurs directly above the seam [109]. Due to the possibility of subsidence at the surface, underground mining involves the transformation of the surface. The ground inside subsidence basins is displaced in vertical and horizontal planes, leading to damage to structures present on the surface, including buildings, roads, rivers, rail networks, as well as altering the environment.

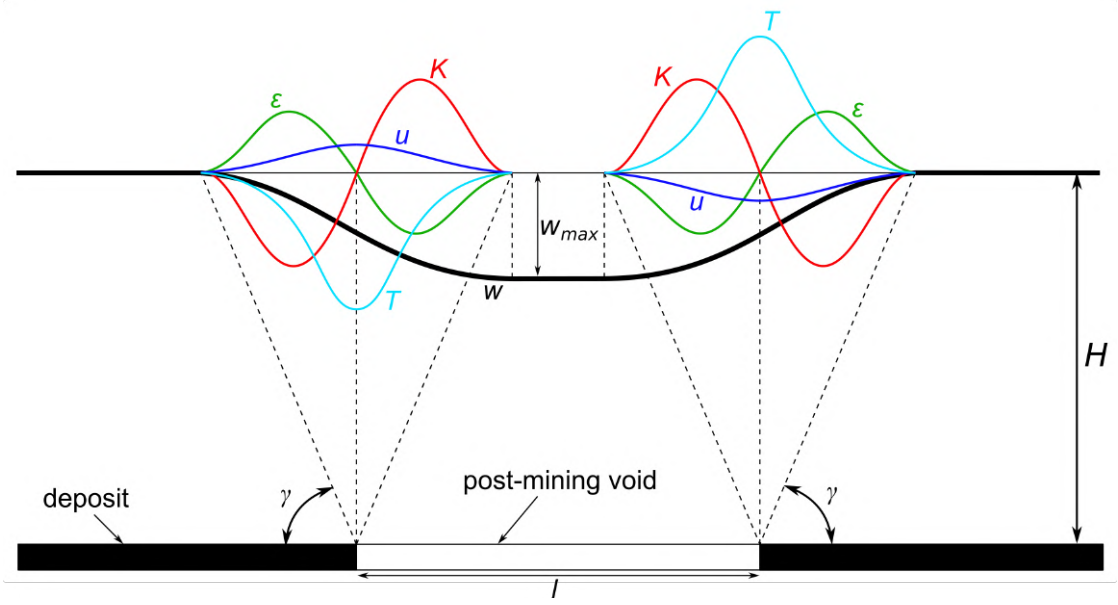

Figure 2.1: A schematic of an overcomplete subsidence trough resulting from an extraction of a flat-lying deposit, after [106].

A schematic of an *overcomplete* subsidence trough is presented on Fig. 2.1. After a sufficiently wide deposit fragment of width l is exploited, bottom part of the subsidence trough achieves the maximum subsidence w_{max}. The value of subsidence decreases with distance from the centre, achieving zero near the point indicated by the influence angle γ [106]. The characterisation of a subsidence trough is performed using a number of indicators. These include [106, 109, 170]:

- Vertical displacement w - the vertical component of the displacement vector of a point on the ground surface, indicating the change in height of the point, measured as a scalar unit, e.g. in millimetres (mm) or metres (m), often referred to as vertical subsidence or just subsidence.
- Horizontal displacement u - the horizontal component of the displacement vector of a point on the ground surface, representing the displacement of a point in the horizontal plane. Often expressed by two orthogonal components (u_x and u_y), as a scalar values in millimetres (mm) or metres (m). The components u_x

and u_y are most commonly measured along east-west and north-south directions. Combining the orthogonal components gives the horizontal displacement in any direction in the horizontal plane. The highest horizontal displacement occurs at the boundary of the exploited field, as indicated on Fig. 2.1.

- Slope/tilt T - represents the gradient (i.e. the first derivative) of the vertical profile of the subsidence basin. Usually expressed by magnitude in millimetres per metre (mm/m), and by angle in degrees (measured from the north direction). Similar to horizontal displacement, the highest slope is achieved at the boundary of the extracted field.

- Curvature K - a quantity indicating the degree of deflection of the natural surface due to the occurrence of a subsidence trough, expressed in units of 1/km (km^{-1}) or millimetres per metre (mm/m).

- Strain ϵ - a measure of the tension or compression of the soil due to deformation within a basin. The parameter is usually expressed as a value with no unit, but stress values expressed in millimetres per metre (mm/m) can often be found in the literature.

It needs to be stressed out that a real profile of a subsidence trough deviates from the theoretical shape. The varying profile of real subsidence trough depends on local factors. The displacements resulting as a *direct* result of the exploitation (*direct influence*) can be also accompanied by *indirect* displacements induced by *indirect* factors (*indirect influence*), e.g. water withdrawal or breaches of slope stability.

2.2 Mining deformation measurement methods

The measurement of ground deformation caused by underground mining activities is an essential part of operation for a mining company, due to the need to control the impact of underground mining on the surface and mitigate any potential mining damages. Deformation measurements provide valuable information for empirical methods of deformation prediction (e.g. Kochmański method, Budryk-Knothe method), and hence they are an integral element in the protection of mining areas. Data on the impact of mining on the surface in the form of displacement values allows better planning of mining works in new mining fields. These reasons, among others, caused the mining companies to create whole departments responsible for surveying in the areas of mining influence.

Historically, the development of mining techniques has been accompanied by the development of traditional surveying methods, which have been used to study the impact of mining on changes in the ground surface. At the same time, it should be emphasised that new measurement methods have also been and are being successively implemented in the mining surveying industry, as evidenced by the large number of scientific articles in international journals in the fields of geodesy, mining, remote sensing and related fields.

Traditional geodesic methods (leveling, tachymetry, and GNSS - Global Navigation Satellite System) are still the most commonly applied techniques for assessing ground deformations in mining areas [36]. Despite the discrete character of the measurement (displacement values are known only at the measurement points), these methods proved to be most accurate, with the possibility of method selection depending on the required accuracy of the deformation measurement. However, often these methods are labeled as expensive (they require costly surveying equipment) and labour-intensive (*in situ* measurements are necessary, often requiring several workers). New methods of measurement are thus seeked, that would provide a similar degree of accuracy at a lower cost and with less work required.

The leveling methods (e.g. geometric, trygonometric, precise) are predominant in the field of mining surveying, providing data on ground surface displacements to the mining companies and researchers alike, and allowing for a better understanding of the behaviour of rock mass under the influence of underground extraction. Models of surface displacements always need a confirmation in ground truth, and leveling is the most frequently used method to acquire in situ measurements [106, 109]. Leveling measurements are carried out in points along leveling lines, providing a discrete information of deformation in leveling points. The deformation value outside of those points is unknown, therefore it is crucial to properly plan the measurement over the area influenced by mining works. Interpolation techniques have been used in past research to estimate the displacement values outside of the leveling lines [15, 17].

Leveling surveys are carried out often annually or quarterly, in some cases (high risk of performed exploitation, e.g. in vicinity of protective pillars) with shorter temporal span (e.g. monthly). A much higher temporal resolution can be achieved by GNSS measurements, with the possibility of e.g. daily or hourly temporal resolution. One has to stress out that GNSS surveys do, like leveling, provide information on ground displacements only in the locations of GPS (Global Positioning System) receivers. Contrary to the leveling method, GNSS measures not only vertical displacement (subsidence or uplift), but also horizontal, giving a full 3-dimensional view on the behaviour of ground surface after mining operations are carried out

underground [202, 209].

At the beginning of the twenty-first century, a remote sensing method of Synthetic Aperture Radar Interferometry (InSAR) has gained in popularity due to the remote character of measurement and relatively low cost (SAR images were provided by space agencies operating the satellites, e.g. European Space Agency - ESA). Shortly thereafter, a number of papers have been published on the use of this technique to measure ground surface displacements over mining areas [22, 171, 181, 214, 223]. With high temporal resolution of measurement (e.g. 6 days in the case of Sentinel-1A and 1B satellites) and reliable ground coverage (contrary to the discrete character of traditional geodesic surveys), InSAR is perceived as a complementary method to geodesic in situ measurements, and is often applied jointly with other methods to study ground surface displacements in mining areas [48, 66, 181, 222, 239]. For a more detailed review on the application of InSAR methods to mining deformation studies, readers are referred to Section 3.4.

Other methods of measuring ground displacements induced by underground mining include Laser Scanning (LS) and photogrammetry. The Terrestrial Laser Scanning (TLS) and Aerial Laser Scanning (ALS) methods provide a very high spatial resolution of ground measurements with point clouds containing millions of measurement points [34, 121, 242]. However, compared to classic surveying methods, these techniques have high data acquisition costs. Photogrammetric approaches employ the use of Unmanned Aerial Vehicles (UAVs) as camera carriers, providing spatial measurements with high-resolution images at a relatively low cost [41, 126].

In terms of the use of deformation measurements as input data for machine learning algorithms requiring extensive datasets, of the methods presented above, the InSAR method can be considered the most feasible due to its high temporal resolution and spatial coverage.

2.3 Modeling and prediction of mining subsidence

The subsidence phenomenon has been studied from the beginning of the twentieth century, as more and more mining districts were increasingly populated, and buildings and transportation infrastructure were prone to mining damages. In order to estimate potential damages to the surface caused by underground extraction, the task was to develop a method of predicting surface subsidence. This method needed to have a number of assumptions about the subsidence phenomenon, since only the mining plans were known. This instituted the need to create a mathematical model that would transfer the known properties of the rock mass, e.g. deposit area, seam thickness and depth [109]. The other problem was the diversity of mining conditions in different areas - a model that would work for one mine, would not be accurate for a different mine without a proper change in model parameters. This resulted in a number of different methods for mining subsidence prediction created around the world, often effective only under specific conditions similar to those observed in the area, for which the model was developed. Nevertheless, there are cases, where different mining subsidence prediction methods from different mining regions are based on the same principle, though have slightly different parameter values.

Methods of predicting mining subsidence can be classified into several groups, based on their main principles. A number of classification methods have been proposed. Following Kowalski [108], the subsidence prediction methods can be divided into:

- analytical (empirical) methods, including geometrical-integral methods;
- stochastic (functional) methods;
- methods that treat the rock mass as a continuous medium;
- numerical methods.

A similar approach to classification was proposed by Kratzsch (empirical, functional and theoretical-model methods) [109], excluding the numerical methods (which were not yet applied at the time of publication, in 1983). The classification listed above is presently used e.g. in Poland, and will be applied in the remainder of this work. Around the world, various different classifications are applied, e.g. Peng [170] proposed to divide subsidence prediction methods into:

- typical curve methods;
- profile function methods;
- influence function methods;
- numerical simulation methods.

Other examples of classification of subsidence modeling methods can be found e.g. in [109, 182].

Table 2.1 lists selected mining subsidence modeling methods applied over the years in various countries around the world, with the emphasis put on the methods developed in Poland. A domination of empirical and stochastic models can be distinguished in the early years, with a rise in application of numerical modeling beginning in the late 80s.

Within the group of empirical methods are models that have been developed

using observations of surface subsidence over mining areas, established mainly using subsidence measurements from coal mining. Empirical methods were at the beginning based on an observation that the amount of vertical displacement is dependent on the thickness of the mining seam, the depth of extraction and the stowing method used to fill the mining void. Basing these methods on measurements over a specific mining area caused many of them to be applicable only in these specific conditions. A number of mining regions were using an empirical method derived for their specific conditions, despite there being an alternative, more universal approach. The first empirical methods of mining subsidence prediction were devised in Germany by Keinhorst in 1928 [101] and Bals in 1931 [10]. In Poland, an empirical method was proposed for the coal mining regions by Budryk and Knothe in 1953, called the *Budryk-Knothe theory* [106]. This method, established for the conditions present in Polish mines, is used to this day for predictions of mining subsidence by mining authorities. Several years later, in 1961, Ehrhardt and Sauer proposed a similar method, called the *Ruhrkohle method*, for mining fields in Germany [50]. Another example of an empirical method is the *Probability Integral Method (PIM)* developed by Liu and Liao in 1965 in China [130]. The PIM approach is still regarded as the main method of mining subsidence prediction in Chinese mines. In the United Kingdom in 1975, the National Coal Board (NCB) developed an empirical method based on measurements in British coal mining regions [1].

Table 2.1: Mining subsidence prediction methods (selected)

Method	**Classification**	**Author(s)**	**Year**	**Source**
Keinhorst method	empirical	Keinhorst	1928	[101]
Bals method	empirical	Bals	1931	[10]
Sałustowicz's model	continuous media mechanics	Sałustowicz	1953	[190]
Budryk-Knothe theory	empirical	Knothe and Budryk	1953	[106]
Litwiniszyn's stochastic rock mass model	stochastic	Litwiniszyn	1954	[128, 129]
Kochmański's model	empirical	Kochmański	1955	[107]
Ruhrkohle method	empirical	Ehrhardt and Sauer	1961	[50]
Probability Integral Method (PIM)	empirical	Liu and Liao	1965	[130]
Batkiewicz's model	stochastic	Batkiewicz	1971	[11]
The UK National Coal Board (NCB) model	empirical	UK NCB	1975	[1]
Application of Finite Element Method (FEM)	numerical	Szostak-Chrzanowski	1988	[200]

Continued on next page

Table 2.1 – continued from previous page

Method	Classification	Author(s)	Year	Source
Application of FEM	numerical	Filcek, Tajduś, Walaszczyk	1994	[63]
Drzęźla's elastic-stick model	continuous media mechanics	Drzęźla	1995	[49]
Two-element Kelvin series model	continuous media mechanics	Kwiatek	2000	[112]
Surface Deformation Prediction Software (SDPS)	numerical	Newman, Agioutantis and Karmis	2001	[160]
Monte Carlo simulation approach	stochastic	Niemiec and Niemiec	2008	[163]
Cellular Automata Model	stochastic	Sikora	2019	[196]

The stochastic methods consider the rock mass as a cohesion-less medium, that is possible to model using the probability theory. The first to propose such approach was Litwiniszyn in 1954 [128, 129]. An alternative solutions were established e.g. by Batkiewicz [11], Niemiec and Niemiec [163], and Sikora [196].

Another group of mining subsidence prediction methods assumes that the rock mass should be treated as a continuous medium, and therefore models of continuous media mechanics should be applied. Examples of models from this group include Sałustowicz's model [190], Drzęźla's elastic-stick model [49], and two-element Kelvin series model [112].

The last group in the classification of prediction methods are the numerical methods, which emerged with the developments in numerical modeling, computer technology and modern mechanics theory. These methods are based on numerical modeling of the rock mass, by applying various 2- or 3-dimensional numerical simulation methods, e.g. Finite Element Modeling (FEM), Discrete Element Modeling (DEM). These methods can model complicated and varying conditions in the rock mass, therefore there is a high interest of applying them to model mining subsidence, at the cost of high computing power required to solve the model. Examples of applying numerical modeling to subsidence studies can be found in [63, 160, 200, 213].

All of the above-mentioned methods have their advantages and disadvantages in certain conditions. While theoretically universal, the numerical methods require an extensive knowledge of the rock mass to be modeled in order to provide a proper solution, although the increase in computation power makes these methods to be used more frequently. Continuous rock mechanics model are more complicated than empirical methods, but provide a broader range of displacement features to be derived. Still, the empirical methods based on subsidence measurements are the most successful and the most frequently applied in a great deal of mining regions, mainly owing to simplicity of calculations and reliability confirmed by in situ measurements.

With the development of machine learning techniques and computer technology required to execute machine learning models, this technique also gained interest in the field of mining subsidence prediction. The first proposition was established by Ambrožič and Turk in 2003 [4]. Since then, numerous approaches have been proposed to employ machine learning and its sub-domain - deep learning algorithms for mining subsidence prediction, e.g. [83, 111, 233, 240]. This field of research is

still active, since neural networks are identified as a tool that can explore hidden relationships in data, and thus potentially model complex behaviours and systems, mining subsidence included. A detailed review of different approaches and solutions proposed in the field of machine learning research on mining subsidence will be provided in Section 4.4.

Chapter summary

This chapter presented literature studies on subsidence of ground surface caused by underground mining activities. The theoretical basis for the formation of subsidence troughs was discussed, methods of measuring ground surface displacement were presented, and methods used to predict subsidence in mining areas were reviewed.

In the light of the study area chosen in this study, emphasis was placed on continuous deformations in the form of subsidence troughs created by the exploitation of deep seams. Among the methods of displacement prediction, a research gap was noted in the application of artificial intelligence methods, including machine learning. As these methods rely on large measurement datasets, the possibility of using SAR Interferometry as a method to provide measurement data to machine learning algorithms was identified.

The principles of functionality and an overview of the applications of InSAR methods will be presented in the next chapter.

Chapter 3

Satellite SAR Interferometry

3.1 Principles of InSAR

Synthetic Aperture Radar (SAR) has made a tremendous step since its discovery, and nowadays it is regarded as one of the most important sources of data in the Earth Observation sector, with more and more satellites carrying SAR sensors are being launched into the orbit. Since SAR interferometry is the main displacement measurement technique exploited in this thesis, this section is aimed at describing the theoretical principles underlying SAR and InSAR. Limitations of SAR and SAR interferometry will be mentioned, with emphasis on the application in the mining industry, as a tool for monitoring ground surface displacements induced by underground mining activity.

3.1.1 Information acquired by satellite SAR systems

SAR is a sensor system based on radar aperture, often exploited for imaging of the Earth's surface from satellites using electromagnetic waves from the microwave spectrum (with wavelengths between approximately 2.5 cm and 30 cm). As opposed to optical Earth imaging systems, e.g. in form of Sentinel-2 or Landsat constellations, a SAR system is an *active* remote sensing system. It is therefore independent of solar radiation, which allows SAR to image the Earth's surface both day and night regardless of light conditions. Use of the microwave spectrum allows SAR to penetrate cloud cover, as microwaves are not reflected by water vapour (however, it causes a signal delay that often affects InSAR measurements; this phenomenon will be further explained later). By measuring the signal delay between two consecutive SAR acquisitions, the change in distance between the satellite and the ground surface can be estimated, corresponding to the eventual displacement occurring in the area. While being a system that opened a lot of opportunities and provided an enormous amount of data for scientific and practical applications, SAR has a number of limitations resulting from its operating principles. In order to fully exploit the possibilities that SAR brings, these limitations and constraints need to be considered and accounted for.

The term *Synthetic* in Synthetic Aperture Radar comes from the concept of simulating a very long antenna, introduced by Wiley in 1965 [220]. Its main principle is that the spatial resolution of an image acquired by a SAR sensor can be artificially improved by moving the sensor in a direction perpendicular to the imaging direction. This causes the imaged object to be recorded by several radar pulses, which can then be combined to simulate a very large antenna. This concept is also

implemented in the case of a SAR sensor mounted on a satellite orbiting the Earth, as will be further discussed in a later subsection.

As the signal is transmitted by the sensor, reflected by the illuminated surface and recorded back by the antenna, it can be regarded as a *two-way trip*. SAR signal recorded by the antenna and saved as an image carries two types of information, stored in form of a complex number z, according to the equation [58, 81]:

$$z = Ae^{-j\phi} \tag{3.1}$$

In the equation above, the complex number z carries two values recorder by the SAR sensor. First, the **amplitude** A, represents the strength of a backscatter of the signal - the higher the amplitude, the stronger the backscatter. The value of amplitude is related to the shape, orientation and electrical properties of the objects reflecting the signal within single resolution cell [58]. Second value, the **phase** ϕ of the signal is related to the distance travelled by the electromagnetic (EM) wave from satellite to the ground and back.

While the amplitude has a multitude of applications and can provide information about objects on the surface, the phase value is of the most interest from the standpoint of interferometric analysis. It is thus crucial to understand how phase is measured by the SAR system.

EM wave transmitted by a SAR sensor is characterised by sinusoidal nature (signal is modulated around a certain frequency). This causes the SAR phase to be known *modulo-2π* - only a fraction of the entire phase is known, equal to the fraction of wavelength between 0 and 2π[1]. The rest of the phase - a number of k full phase cycles of 2π - is unknown. In order to know the entire phase value, and thus the distance travelled by the signal, the $k * 2\pi$ cycles have to be added to the phase measured by SAR.

3.1.2 Geometry of SAR acquisition

Since the data used in this thesis to derive ground surface displacements were acquired by the Sentinel-1 satellites, the description of acquisition geometry will be referring directly to the Sentinel-1. However, it should be noted that majority of modern SAR sensors operate on the same principle, with slight differences in the acquisition geometry or the image acquisition method.

SAR satellites orbit the Earth using a near-polar sun-synchronous orbit, exploiting the Earth's rotation to cover most of the globe with a revisit time of 12 days for a single satellite. In the case of Sentinel-1 satellites, the Sentinel-1A and Sentinel-1B satellites fly in **tandem**, which allows to image a single area with a revisit time of 6 days (each satellite is on the opposite part of the globe). Due to the near-polar orbit and Earth's rotation, the satellite can pass over the same area in two directions. If the satellite passes in the direction from South (S) to North (N), it is referred to as an **ascending** direction. Respectively, if the satellites flight direction is from North to South, it is on a **descending** pass. As mentioned, a single fragment of terrain can be imaged by a SAR satellite from both ascending and descending directions, a fact crucial for the eventual estimation of vertical and horizontal displacements. A graphical representation of orbit directions is presented on Fig. 3.1.

SAR imaging geometry is different from the geometry of acquisition in optical systems in that the radiation beam is not directed straight down, but at an angle. Understanding these differences is crucial in realizing the potential and limitations

[1] In literature, $-\pi$ and $+\pi$ is also used as phase interval.

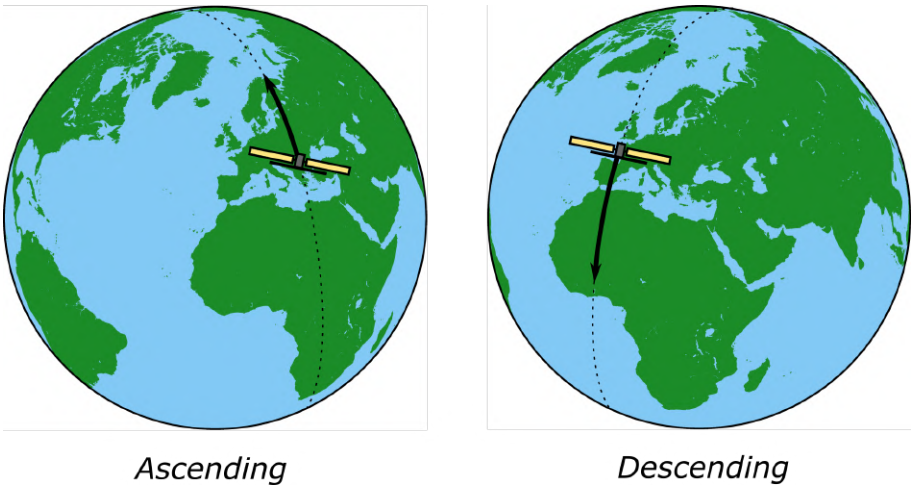

Figure 3.1: Schematic of SAR data acquisition paths, ascending (left) and descending (right)

of methods based on SAR data. A schematic of imaging geometry for a generic satellite SAR sensor is shown on Fig. 3.2.

Since most SAR satellites operating in the past and presently, including Sentinel-1, are equipped with right-looking SAR sensors, the right-looking acquisition geometry will be explained in this section. An image is acquired in a local coordinate system of a SAR sensor. The direction along the satellite orbit is called *azimuth direction*. When looking at a SAR image in local coordinate system of a satellite, azimuth direction is the *height* of the image. SAR sensor illuminates the Earth in a side-looking manner, which means that the radar beam is not transmitted perpendicular to the ground surface, but at an angle. The direction perpendicular to the azimuth direction in the ground plane is called *ground range direction*, or simply *range direction*. On the SAR image, ground range direction would be the *width* of the image.

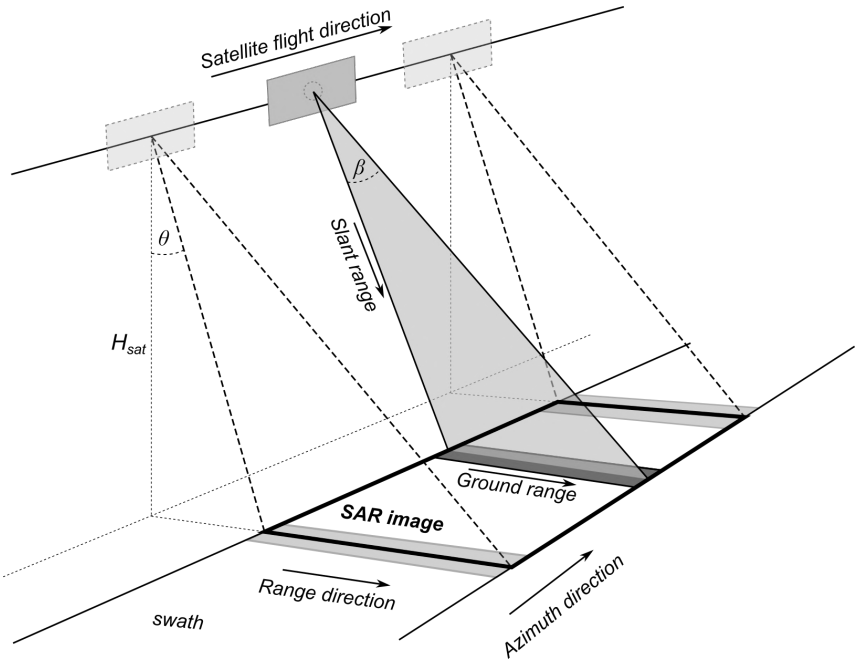

Figure 3.2: Imaging geometry of a satellite SAR sensor in a StripMap mode

Radar beam of width β illuminates a strip of land surface, called a *swath*. A

swath is often tens or hundreds of kilometers wide in the ground direction, depending on the SAR satellite. The direction, in which the satellite "looks" at the surface, is called a *slant range*, or *Line of Sight*. This direction is tilted from the nadir by *off-nadir*, or *look* angle θ. Since a wide area on the surface is covered by a single swath (up to 100 kilometers), the look angle varies depending if the illuminated resolution cell is closer (*near range*) or further (*far range*) from the satellite. For Sentinel-1, the look angle can vary from 23 to 46 degrees [230]. A radar beam is reflected from the Earth's surface under an *incidence angle*. Its value is slightly higher that the look angle, due to the curvature of the Earth [60].

TOPS acquisition mode of Sentinel-1 satellites

A *StripMap* image acquisition geometry was presented previously for a clearer explanation of terms used in SAR interferometry. However, Sentinel-1 operates in an Interferometric Wide Swath (IW) mode using a *TOPS* (Terrain Observation with Progressive Scans) approach. Similarly to another acquisition mode, *ScanSAR*, it produces a wider SAR image in the ground range by scanning individual *subswaths* forming a single swath. This effect is achieved by rotating the antenna around the azimuth direction (changing the look angle). Each subswath consists of a series of *bursts*, which are simply ground footprints produced by the signal recorded by synthetic aperture. What makes TOPS different from ScanSAR is the fact that the sensor is electronically steered back and forth along the azimuth direction, allowing all ground targets to be observed by the entire antenna pattern, reducing the differences in Doppler centroid [43, 204, 230]. A schematic of IW TOPS acquisition is demonstrated graphically on Fig. 3.3.

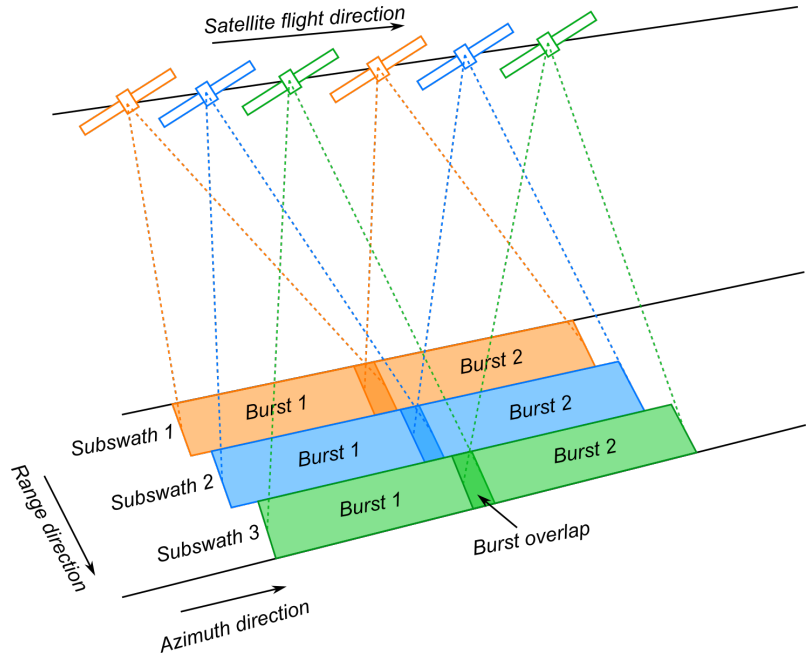

Figure 3.3: Imaging geometry of a satellite SAR sensor in a TOPS mode

Sentinel-1 IW mode produces 3 subswaths, achieving approximately 250 kilometers of coverage in ground range. Each image slice produced over a satellite pass is approximately 170 kilometers long in azimuth direction (corresponding to about 25 seconds of flight). Consecutive bursts within subswaths are overlapped by about 7-8%. Overlap is also present between adjacent subswaths. This ensures that no

gaps are present in the SAR data produced by Sentinel-1 [230].

3.1.3 Interferogram calculation and phase components

A SAR image is recorded as a matrix of complex numbers, containing information about ampitude A and phase ϕ of the recorded signal. Phase is critical from the standpoint of interferometric analysis, since it is related to the distance d between the SAR sensor and the ground resolution cell illuminated by SAR. This relation is given by the equation [60, 81]:

$$\phi = -\frac{2\pi}{\lambda} * 2r = -\frac{4\pi}{\lambda} r, \tag{3.2}$$

where λ is the wavelength of the EM wave ($\lambda = 5.55$ cm for Sentinel-1), and $2r$ is used to include the 2-way travel of the signal.

Interferometric SAR (InSAR) is based on a simple idea that 2 consecutive SAR images, each providing a phase value corresponding to a distance measured between satellite and the ground surface, can be subtracted to calculate phase difference $\Delta\phi$, which can be used to derive the range difference Δr. By modifying Equation 3.2, we get:

$$\Delta\phi = -\frac{4\pi}{\lambda} \Delta r \tag{3.3}$$

Since SAR phase is recorded as an image, the phase difference is calculated on an image basis. An image containing the phase difference between 2 consecutive SAR acquisitions is called an **interferogram**. More precisely, the interferogram is created by multiplying complex image from the first SAR acquisition (called *reference* image) by a complex conjugate of the second SAR acquisition (referred to as *secondary* image), according to an equation [58]:

$$I = z_r z_s^* = A_r A_s e^{-j\Delta\phi}, \tag{3.4}$$

where z_r and z_s are complex reference and complex secondary images, respectively, A_r and A_s are amplitude values of reference and secondary images, respectively, $*$ is the complex conjugate operator.

A single acquisition SAR image rarely exhibits any patterns on the ground and constists mostly of pixels with seemingly random values (due to phase value being only modulo-2π, and a variety of objects contributing to this modulo-2π value within a resolution cell). By combining 2 SAR images and calculating their phase difference, a clear patterns can be distinguished, as well as some erroneous areas. In order to understand the origin of each of a number of possible patterns present on the interferogram, the various components that make up the phase difference have to be explained.

Phase value of the SAR signal can be influenced by many factors, e.g. topography of the terrain, eventual deformation of the ground surface, propagation of the EM wave in the atmosphere, spatial separation between satellites during image acquisition, as well as physical properties of the objects reflecting the signal within the resolution cell. Equation 3.5 (considered one of the most important equations of InSAR) is used to describe factors influencing the interferogram phase:

$$\Delta\phi = \Delta\phi_{flat} + \Delta\phi_{topo} + \Delta\phi_{defo} + \underbrace{\Delta\phi_{tropo} + \Delta\phi_{iono}}_{\Delta\phi_{atm}} + \Delta\phi_{orbit} + \Delta\phi_{noise} \tag{3.5}$$

- $\Delta\phi_{flat}$ - is the ***flat Earth*** contribution, one of the two most dominant contributions to the interferometric phase. This component is induced by the Earth's curvature, and is removed by assuming that all pixels of the interferogram lie on an ellipsoid, e.g. the WGS-84 ellipsoid. Flat Earth phase manifests itself on the interferogram as regular phase ramps, direction of which depends on the current acquisition geometry. In order to estimate and remove this phase contribution, information about the perpendicular baseline between reference and secondary images is required [58].

- $\Delta\phi_{topo}$ - ***topographic phase***, the second main component of the InSAR phase. This contribution is caused by local changes in topography, and can be recognised on an interferogram by regular phase fringes that resemble the topographic situation. As can be easily deduced, the value of the topographic phase is directly related to the terrain elevation, and therefore can be estimated by exploiting elevation data in form of a Digital Elevation Model (DEM). On the other hand, if the topographic information is of interest in the interferometric analysis (InSAR applied to estimate the DEM of an area), all of the components from Equation 3.5 can be estimated and subtracted, and the phase contibution due to topography can be used to calculate the terrain elevation, obtaining the DEM.

- $\Delta\phi_{defo}$ - is the phase component caused by an elevation change that occurred between the consecutive SAR image acquisitions, generally attributed to the ground surface displacement taking place in the studied area. ***The displacement phase***, as it is often called, is the most important phase component from the perspective of applying InSAR in deformation studies. In order to estimate this component, all other phase contributions from Equation 3.5 have to be estimated and subtracted. The remaining phase contribution due to displacement can then be exploited to estimate ground surface displacements.

- $\Delta\phi_{atm}$ - is the total ***atmospheric phase*** change (also called Atmospheric Phase Screen - APS) caused by disturbances in consecutive layers of the atmosphere, with ionosphere and troposphere being the two significant ones. As the radar signal propagates through the atmosphere, it is prone to perturbances caused by a variety of factors, e.g. water vapour and stratification. This phase delay is significant enough to manifest on the interferogram phase image, taking a form similar to deformation signals, making it important to estimate eventual atmospheric phase signals, as they may prevent correct interpretation of the displacement phase.
  Atmospheric phase component is caused by 2 layers of the atmosphere, the **ionosphere** and the **troposphere**. Each of these layers can generate different artifacts in the interferometric phase.

  - $\Delta\phi_{iono}$ - the ionospheric layer of the atmosphere can influence the InSAR phase in form of a ***ionospheric phase delay***. This signal delay is caused by variations in the density of free electrons in the ionosphere (measured using the Total Electron Content - TEC - value). The phase advance caused by these variations can manifest on the interferogram as a continuous trend surface easily modelled using low-order polynomials [58]. Ionospheric effect becomes more significant for lower wavelength (e.g. P-band or L-band) SAR instruments. In the case of Sentinel-1 (which is a

C-band SAR device), this phase contribution is often neglected, especially over mid-latitude areas.

- $\Delta\phi_{tropo}$ - compared to the ionospheric phase delay, tropospheric effects are far more challenging to mitigate. ***The tropospheric phase delay*** can be divided into two distinct components arising from the different contributions of the troposphere to delaying the electromagnetic wave.
  First component, the **turbulent component**, is the result of turbulent mixing processes in the lowest, near-ground (2-3 kilometers above ground) layer of the troposphere. An important characteristic of the turbulent signal is its high spatial correlation, that can be well described using geostatistics, but is very difficult to estimate with high accuracy due to high degree of uncertainty. Temporally, this signal is highly uncorrelated, since the atmospheric conditions can differ with each consecutive acquisition.
  The second component is connected to the stratification of the troposphere. Troposphere is vertically divided into layers with different refraction index values, due to changes of temperature, pressure and water vapour with height. This feature causes a **stratified phase component** to occur. As it is caused by changes in terrain height, the value of this component is highly correlated with elevation, and can be estimated using information about terrain elevation in form of a Digital Elevation Model (DEM).

- $\Delta\phi_{noise}$ - is the ***phase noise*** component, induced by various factors. Each resolution cell (pixel) of a SAR image contains a number of elementary scatterers, each contributing to the characteristic of signal reflectance within a resolution cell. Between two SAR acquisitions, these scatterers can change their positions, or their electric properties can be different during each acquisition. These changes are one of the sources of phase noise. A number of factors can be distinguished, contributing to the presence of decorrelation in interferograms:

  - temporal decorrelation - resulting from temporal changes of scatterers, either because of their movement (e.g. leaves on a tree are moving constantly) or a change of their reflectance properties. This effect is especially visible over vegetation-covered areas (high degree of phase noise over forest areas often results in an inability to detect deformation there), significantly weakening the applicability of InSAR in such areas.
  - geometric decorrelation - induced by a differing positions of a satellite (or satellites) in space (in relation to the ground) during image acquisition, resulting in slightly different look angles. This effect, of course, is reduced with smaller perpendicular baselines (b_{perp}). The higher the baseline, the more evident the geometric decorrelation becomes. If the perpendicular baseline reaches a critical threshold, called *critical baseline* b_c, the decorrelation is strong enough to completely hinder the phase information interpretability (the interferogram is complete noise). The critical baseline depends on the dimension of a resolution cell on the ground, radar frequency and the distance from sensor to the ground [60] (for Sentinel-1, the critical baseline is about 5 kilometers, but it is almost of no concern thanks to high precision of orbital data).
  - volume decorrelation - in many cases the scatterers are distributed in a

volume (e.g. leaves in a tree), which causes the signal to be dispersed and reflected with different phase and amplitude than it would from a flat surface.

Phase noise mitigation techniques involve selecting optimal images with short spatial and temporal baselines in order to reduce the temporal and geometric decorrelation. The noise can also be reduced to some degree by using various filtering techniques. It is a common practice to filter interferograms, since it enhances the phase information, reduces noise significantly, as well as further helps with the unwrapping process [60, 81].

Coherence

During interferometric processing, a measure of **coherence** γ can be calculated to estimate the amount of phase noise present in the interferogram. Coherence of an InSAR pair is the magnitude of complex correlation between two SAR images, calculated on a pixel-by-pixel basis using a moving window. The absolute value of coherence ranges from 0 to 1, and gives a rough estimate of the amount of noise present within a resolution cell, ranging from a lack of noise and pure phase without decorrelation ($\gamma = 1$), to a pure noise ($\gamma = 0$).

3.1.4 Phase unwrapping and displacement estimation

As was already mentioned in previous subsections, phase values measured with an InSAR system are known modulo-2π - only a small fraction of phase corresponding to an incomplete phase cycle is measured. Identifying the remaining number of k full 2π cycles is essential in recovering the entire phase information, allowing for successful estimation of deformation or elevation values, depending on the application. Modulo-2π phase values measured by InSAR are commonly known as **wrapped phase**, whereas the process of adding the remaining $k \times 2\pi$ phase cycles is referred to as **phase unwrapping**. It is considered to be the most difficult step in InSAR processing, due to the ambiguity of the results and possibility of errors caused by phase decorrelation and discontinuities [60].

Assuming that ϕ is the wrapped phase, the process of phase unwrapping consists of obtaining, for each interferogram cell, an integer number of k cycles of 2π, so that the total phase value Ψ is known unambiguously [60]:

$$\Psi = \phi + k * 2\pi \tag{3.6}$$

If one assumes that the phase image corresponds to a smooth, continuous surface, the phase value of a pixel would be a continuation of a value of an adjacent pixel. Therefore, the simplest solution in this case would be, starting with a reference point, to integrate the phase differences. In practice, however, this situation is almost non-existent, since phase values in an interferogram are often interspersed with discontinuities, causing inaccuracies in the solution. These discontinuities may appear due to two factors, 1) phase decorrelation (either geometrical or temporal), and 2) presence of real discontinuities in the area of interest.

The basic idea behind phase unwrapping algorithms is to identify these discontinuities successfully, and to minimise errors induced by them through various optimisation techniques [60]. Over the years, a number of methods for phase unwrapping have been proposed, including a branch-cut method [75], an implementation of a network model [39], a least-squares solution [72] or a network-flow technique [32].

Among all of the methods, the network-flow approach is the most often used in InSAR processing software, in form of a software package called SNAPHU, which stands for Statistical-cost, Network-flow Algorithm for PHase Unwrapping [31]. The main idea behind it is to compute the most likely solution of unwrapped phase, based on the observable input data, through network-flow optimization and division of interferogram into smaller chunks unwrapped individually and merged to obtain the whole unwrapped phase image.

After the interferogram has been (successfully) unwrapped, phase has to be converted from radians to a displacement value (in meters) if it is to be of practical use for measurement purposes. Since this thesis addresses the topic of displacement estimation using InSAR, let us assume that the InSAR processing is used for that purpose. First of all, equation 3.5 is to be used in order to estimate each phase component separately, so it is possible to subtract them from the interferogram image and leave only the displacement component $\Delta\phi_{disp}$.

The flat Earth component $\Delta\phi_{flat}$ and the topographic contribution $\Delta\phi_{topo}$ are estimated in a process called *interferogram flattening* using precise orbit data and an external DEM. Calculation of the atmospheric phase delay $\Delta\phi_{atm}$ can involve a number of methods employing different types of data and approaches. Typically, the tropospheric and ionospheric (if it is not negligible) components are estimated separately and subtracted from interferogram. The orbital phase errors $\Delta\phi_{orbit}$ are reduced by applying precise orbit data of the SAR satellite. Finally, the phase noise $\Delta\phi_{noise}$ is mitigated through various filtering algorithms. After all the components are estimated and removed (or reduced) from the interferogram, theoretically only the displacement phase component $\Delta\phi_{disp}$ should remain on the phase image. However, this is seldom the case since it is impossible to fully estimate each phase component without errors (which is often the case for the tropospheric delay due to its turbulent nature). Nevertheless, a flattened interferogram with possible error sources mitigated should provide information about eventual ground surface displacements occurring over the study area. It should be noted, however, that at this step the displacement phase is measured in radians.

In order to obtain a displacement value from the unwrapped phase, a simple relation can be used [81]:

$$\Delta\phi_{disp} = \frac{4\pi}{\lambda} d \tag{3.7}$$

where λ is the signal wavelength ($\lambda = 5.55$ cm in case of Sentinel-1) and d is the displacement that occurred between two SAR acquisitions forming the interferogram.

Using one or more interferograms, it is possible to determine ground surface displacements occurring in the time period between image acquisition. The different methods based on the use of a pair or a set of multiple SAR images will be presented in the next section.

3.2 InSAR methods description

3.2.1 InSAR methods based on a pair of SAR images

Differential InSAR

A classical approach to processing interferometric SAR data, that has been widely used for detecting various types of ground surface deformation, is the **Differential SAR Interferometry (DInSAR)** technique. Its main principle has been already mentioned in the previous section, where equation 3.5 was introduced. Assuming a repeat-pass approach (where SAR images of an area are acquired at a different time during separate satellite passes), after SAR images are coregistered and the complex conjugation is calculated, an interferogram image containing phase difference values $\Delta\phi$ is acquired. After all phase components except $\Delta\phi_{defo}$ are removed and/or reduced, the remaining phase image should contain only the displacement signal due to a deformation-inducing event. After phase unwrapping, the displacement value can be estimated. The *differential* term in DInSAR was taken from calculating the difference between a raw interferogram and the topographic phase together with the remaining phase components in order to obtain the displacement signal. The topographic phase is simulated by exploiting an external DEM (often the SRTM - Shuttle Radar Topography Mission - 1-arc second [55] DEM is exploited). The DInSAR method is the principle approach of studying ground surface deformation phenomena, as it can provide a spatially comprehensive result, with a relatively high accuracy.

Despite being an essential method in providing data about deformations resulting from earthquakes, landslides, volcanic activity, etc., the DInSAR method has a number of limitations that reduce its applicability on certain conditions [235]:

1. **Acquisition geometry** DInSAR detects displacement in 1 dimension across the Line-of-Sight direction. This often limits the interpretability of results, especially if horizontal displacements are significant [225].

2. **Atmospheric delays** The Atmospheric Phase Screen is challenging to remove completely from the interferogram, and can in some cases obstruct the deformation signal completely or alter the estimated value of displacement [236].

3. **Decorrelation** Phase noise caused by temporal and geometric decorrelation can reduce the accuracy of deformation retrieval or even make it impossible in areas of very low coherence.

4. **Unwrapping errors** High deformation gradients and phase discontinuities may hinder the phase unwrapping process and result in unwrapping errors, introducing ambiguities and complicating the displacement estimation process. If the interferogram is dominated by phase noise, unwrapping can fail, or some unwrapping errors may occur, that lead to underestimation of displacement [60].

Multiple-Aperture Interferometry

A different InSAR method utilizing a single SAR pair is the **Multiple Aperture InSAR (MAI)** method. Contrary to providing displacement rates along Line-of-Sight, the MAI technique can be used to derive along-track displacements, thus being useful in capturing horizontal deformations, with emphasis on N-S direction

(difficult to detect using conventional DInSAR due to orbital alignment of SAR satellites) [12].

The main idea behind MAI is to split the recorded signal in terms of looking backward or forward with respect to the look direction, with 'forward' meaning in the direction of satellites flight, and respectively, backward - opposite to flight direction. In the *split-aperture* process, two interferograms, forward- and backward-looking, are created. Assuming a *squint* angle θ_{SQ} (angle from a nominal LOS direction to the sub-aperture LOS) and antenna angular beam-width α, the along-track displacement x can be estimated from both interferograms using:

$$\Phi_{forward} = -\frac{4\pi x}{\lambda} sin(\theta_{SQ} + \frac{\alpha}{4}) \tag{3.8}$$

$$\Phi_{backward} = -\frac{4\pi x}{\lambda} sin(\theta_{SQ} - \frac{\alpha}{4}) \tag{3.9}$$

Then, by subtracting these interferograms, the along-track displacement x can be estimated:

$$\Phi_{MAI} = \Phi_{forward} - \Phi_{backward} = -\frac{4\pi x}{\lambda} 2sin\frac{\alpha}{4} cos\theta_{SQ} \tag{3.10}$$

assuming $\alpha \approx \frac{\lambda}{l}$, l being the antenna length:

$$x = \frac{l}{2\pi}\Phi_{MAI} \tag{3.11}$$

MAI technique has been widely used in a number of applications as a method complementary to conventional DInSAR and improving the accuracy of 3-dimensional displacement field estimation [8, 12, 212]. Hovewer, due to lower spatial resolution of the result it is commonly used for estimating large-scale displacements (e.g. glacier movements or earthquake displacements).

Pixel-Offset Tracking

Contrary to the phase-based DInSAR and MAI methods, the Offset Tracking (OT) method can use both amplitude and phase information to estimate ground surface displacements in both azimuth and ground range directions. It can therefore be utilised as another method for estimating horizontal displacement values. The Offset Tracking method obtains pixel offset values in range (LOS) and azimuth directions through a cross-correlation algorithm performed on a pair of SAR amplitude or complex images [144]. After allowing for orbital errors, stereoscopic effects and presence of noise, the surface deformation in range and azimuth directions can be estimated.

Despite being able to capture a horizontal field of motion, enhancing the capabilities of InSAR to capture a full 3-D displacement field, attention must be paid to the accuracy of the Offset Tracking method. Since it depends mainly on the spatial resolution of SAR images utilised for the analysis (about 1/10th to 1/30th of a pixel size), the accuracy of the OT method is significantly lower than that of the DInSAR method [144].
The main application of the Offset Tracking method is the observation of crustal movements due to earthquakes, as well as tracking of glacier movements.

3.2.2 InSAR time series methods based on a stack of SAR images

Since the methods described in the previous section are based on only 2 consecutive SAR images acquired before and after a studied phenomenon, these methods can provide only single-value information about surface deformation, i.e. a deformation value between 2 consecutive satellite acquisitions, without further knowledge about the progress of deformation in time. In order to fill this gap, and allow for a time series analysis of deformation based on satellite SAR data, a group of methods were developed, called the time series InSAR methods, or Persistent Scatterer Interferometry (PSI) methods. These methods, while being constantly improved and modified, enable scientists to study long-term deformation phenomena based on a group of multiple SAR acquisitions, later referred to as a **stack** of SAR images.

Persistent Scatterer Interferometry - PSI

The first multi-temporal approach to processing InSAR data was developed by Ferretti et al. in 2000 [57, 61], resulting in patenting of the Permanent Scatterer InSAR PSInSAR^{TM} method and founding of a spin-off company Tele-Rilevamento Europa (TRE) by the Politecnico di Milano. The main idea of the PSInSAR^{TM} method, as the name suggests, is to find characteristic objects on the surface, called Persistent Scatterers (PS). Their main feature is that they reflect the radar signal in a coherent way (that is, with stable phase characteristics), with a high enough amplitude over the course of acquisition of subsequent SAR images. By identifying a set of PS points from the stack of SAR images, differential phase estimation process in these points can be realised in a highly accurate manner, providing a precise information on the displacement values that these points are subject to. In order to find such points, an analysis needs to be carried out on a stack of interferograms. These interferograms are created using a single reference approach - all SAR images are first coregistered to a single reference image. The reference image is chosen from the stack based on the baseline criteria - an image minimising the spatial and temporal baselines is selected. After coregistration, interferograms are calculated for selected pairs. Since the PS candidate points require high phase stability, high spatial and temporal baseline values, that can occur in the case of single-reference interferogram formation, can cause decorrelation and PS points are often likely to be found in urban areas, while the algorithm fails to derive deformation in non-urban areas.

If a deformation time series is to be estimated over rural areas, the Persistent Scatterer InSAR (PSInSAR) approach will often result in a very low density of stable scatterers. If this constraint is to be avoided, a different time series InSAR method would have to be applied. A method that often excels at the task of deriving time series of ground surface deformations over rural areas is the Small BAseline Subset approach.

Small BAseline Subset - SBAS

An approach alternative to the PSI technique was proposed by Berardino et al. in 2002 [13], based on an assumption that by employing a spatio-temporal baseline constraint, the high phase stability condition can be satisfied for a much higher number of pixels. The method was named Small BAseline Subset (SBAS) approach, after the small baseline values required for the interferogram formation and displacement estimation.

Since the phase stability condition can be satisfied more easily than in the case of the PSInSAR method (spatio-temporal decorrelation is minimised by using small baseline interferograms), more stable scatterer points can be found outside of urban areas. These can be referred to as Distributed Scatterers (DSs), since the scattering objects are in this case distributed over the image pixel, contrary to the Persistent Scatterer (PS), where a single dominant scatterer is always present within a resolution pixel. PS targets usually correspond to singular dominant scatterers within a resolution pixel, demonstrating a stable value of reflectibility in all acquisitions within a stack. These are often man-made objects or large groups of exposed rocks and boulders. Opposite to that, DS targets show a fairly good coherence only in some of the interferograms, and can be identified as natural targets: homogeneous ground, non-cultivated lands, desert areas, scattered outcrops, etc. Despite lack of one dominant scatterer, objects reflecting the signal, distributed within a single resolution pixel, can exhibit high coherence over time, thus representing a potential candidate for a stable scatterer [58].

A key principle in the SBAS approach is the way that the interferograms are formed for the time series estimation process. Contrary to the PSInSAR technique, where all interferograms are formed with regards to a single reference image selected as the most appropriate based on the spatio-temporal baseline conditions, interferograms in the SBAS method must fulfill the maximum baseline constraint assumed during processing. The threshold is often set to approximately 25% of critical baseline (approx. 400 meters) in the case of spatial baseline, the temporal threshold is selected more flexibly and can be set a 50 days or even a year. As an example, if the baseline constraint is maximum 50 days (temporal baseline) and 100 meters (spatial baseline), all possible interferometric pairs exceeding this baseline constraint will be excluded from processing (interferograms will not be created). This process leads to the creation of a small baseline network, different than the network created by the PS algorithm, as seen on Figure 3.4, where interferogram networks have been created for the same dataset, using both PS and SBAS approaches. Stable scatterer pixels in the original variant of this method are selected using a coherence-based approach, contrary to the amplitude dispersion technique adapted in the PSInSAR method.

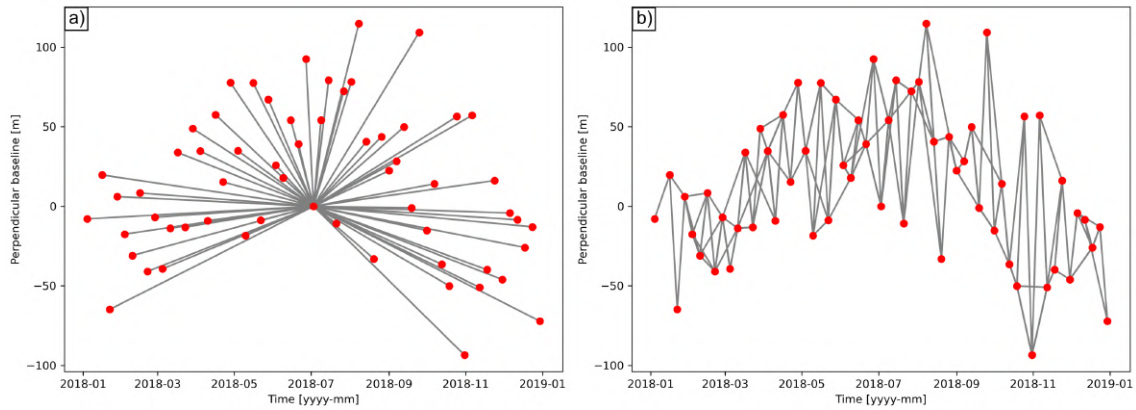

Figure 3.4: Example networks of interferograms formed between a set of SAR images for (a) PSInSAR approach and (b) SBInSAR approach

Stanford Method for Persistent Scatterers - StaMPS

One of the most popular algorithms at the time of writing this thesis is the StaMPS algorithm, developed by Hooper et al. in 2004 [88], because of its availability in the form of an open-source StaMPS-MTI (Stanford Method for Persistent Scatterers - Multi-Temporal InSAR) software [87]. In this approach, PS candidates are selected using the amplitude dispersion criterion, similar to the PSI approach. However, the PS definition in StaMPS is slightly different from the one assumed in PSI, since in StaMPS PS points are points with stable phase characteristics, regardless of the amplitude. This can be noticed in the processing chain of the StaMPS approach, where the initial PS candidates are selected using the amplitude dispersion method, but are then weeded out in an iterative process of calculating their phase characteristics. Also, the amplitude dispersion threshold for StaMPS is higher (0.4 - 0.42) than in PSI (approx. 0.25 [61]). This way, more natural (nonurban) targets can be identified as PSs, giving this approach an opportunity to excel in terrains lacking man-made structures. Another important feature of this approach is that it does not require an *a priori* deformation model to be assumed before the processing (as is the case e.g. in the PSInSAR method), making it an appropriate technique for studying areas subject to non-steady deformation (e.g. volcanic areas, mining areas).

Since this method was selected for processing SAR data for the purpose of this thesis, the technical subjects of this approach, as well as detailed methodology and workflow process will be discussed thoroughly in Chapter 6.

SqueeSAR algorithm

Another significant step in the evolution of MTInSAR algorithms was the development of a SqueeSAR method by Ferretti et al. in 2011 [59]. This method is an extension of the PSInSAR algorithm developed by [61], taking into account processing of both Persistent Scatterers and Distributed Scatterers in a joint manner. This technique can be regarded as a combination of the PS and SBAS approaches, having its principle in the creation of all possible interferometric pairs from the SAR image dataset (e.g. if there are 20 SAR images, $\binom{20}{2} = 190$ interferograms can be created). Then, a coherence matrix is built for each of the DS candidates, employing every interferogram created. Coherence matrices are used to obtain optimal phase values for each DS using a maximum likelihood estimation. This process is referred by the authors of this method as *squeezing*, hence the name of the method, *SqueeSAR*. Phase information is then used in the interferometric processing, a 3D phase unwrapping is applied, APS estimated and removed, and finally displacements are estimated and evaluated [59].

Which method to choose?

A number of publications concerning the comparison of different Multi-Temporal InSAR techniques are available, see for example [3, 100, 165, 228, 231]. A number of MTInSAR methods have been developed over the years, among which are the already mentioned PSInSAR [61], SBAS [13] and StaMPS [88], as well as modifications of PSI and SBAS approaches: NSBAS [47], CPT (Coherent Pixels Technique) [18], DePSI (Delft Persistent Scatterer Interferometry) [99], IPTA (Interferometric Point Target Analysis) [218]. The choice of the most appropriate technique depends mainly on the application and the characteristics of the study area. Use of one method does

not have to reject the use of another, and multiple MTInSAR approaches can be utilised for a single research problem. In general, if analysis is to be conducted in heavily urbanised area, e.g. analysis of the impact of tunneling on the building stability, Persistent Scatterer approaches will yield more accurate results. For non-urban areas, as is often the case for mining deformation analysis, the SBAS approach (or its variants), as well as the StaMPS method can be preferred, for their improved performance in areas lacking man-made structures.

3.2.3 Methods of resolving 3-D displacements from InSAR

As mentioned earlier, InSAR methods suffer from a number of limitations that have to be taken into account if the measurement is to be treated as a reliable information in a decision making process. One of these limitations is the geometry of SAR acquisition, resulting in the calculated displacements to be in the Line-of-Sight (LOS) - slightly tilted from the vertical. This causes the deformation measurement to be relative to the LOS, which can cause some ambiguities in the interpretation process, especially if a significant displacement in the horizontal plane occurs. This problem is visualised in Figure 3.5.

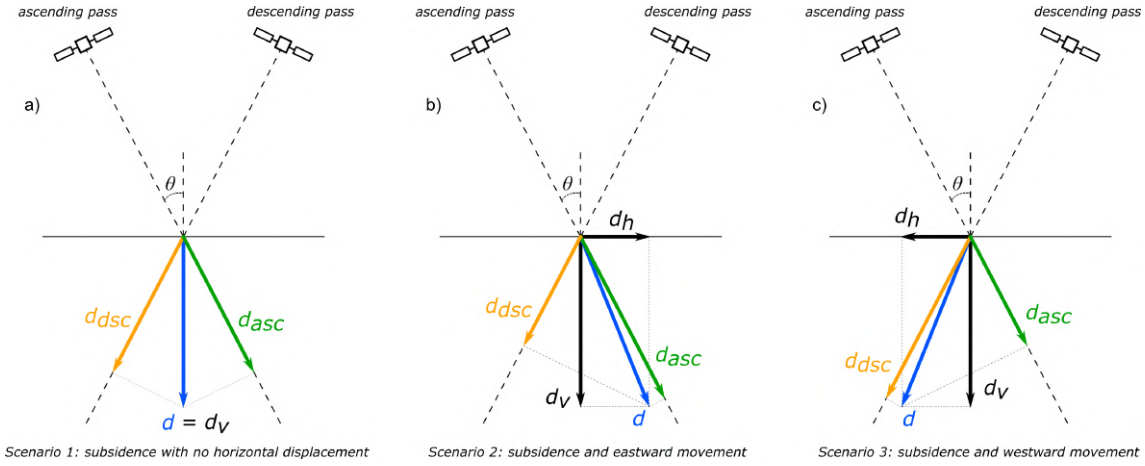

Figure 3.5: InSAR LOS geometry in 3 different scenarios: (a) vertical displacement only; vertical displacement and horizontal displacement to the East (b), and to the West (c)

The simplest solution of this problem would be to simply take into account the incidence angle θ and project the LOS deformation d_{LOS} to vertical d_V, as in Figure 3.5a, using the following formula:

$$d_V = \frac{d_{LOS}}{cos\theta} \tag{3.12}$$

This approach, however, is only correct under the assumption that there are no horizontal displacements present in the studied area, which is a very rare occurrence in practice. Therefore, alternative methods need to be used if one is interested in estimating the vertical and horizontal displacement components without misinterpretation. There are a number of approaches that can be used, depending on data available and the character of deformation present in the studied area. Over the next subsections, these methods will be briefly presented, together with some examples of application in the literature.

Combination of acquisitions from multiple geometries and azimuth measurements

One approach to derive 3-D displacement fields from InSAR data is to exploit observations from both LOS and azimuth measurements in independent acquisition geometries. Since the LOS direction of imaging in SAR is the least sensitive to the North-South component of displacement, measurements in the azimuth flight direction of the satellite seem to be the most suitable for complementing the multi-geometry observations. Azimuth direction is the direction that best represents the N-S direction (it is the closest one), it is also perpendicular to the LOS, which means that it is possible to measure displacements that the LOS direction cannot detect.

Using a weighted least squares (WLS) approach, it is possible to combine m LOS (d_{LOS_m}) and n azimuth measurements (d_{azi_n}) from at least 2 independent geometries of acquisition (preferably ascending and descending to improve the independence of observations), and solve a system of equations to obtain vertical d_U and horizontal d_E, d_N displacement components [62, 225]:

$$\begin{bmatrix} d_U \\ d_E \\ d_N \end{bmatrix} = (B^T \Sigma^{-1} B)^{-1} B^T \Sigma^{-1} L, \tag{3.13}$$

where:

$$B = \begin{bmatrix} a_1 & b_1 & c_1 \\ \vdots & \vdots & \vdots \\ a_m & b_m & c_m \\ 0 & u_1 & v_1 \\ \vdots & \vdots & \vdots \\ 0 & u_n & v_n \end{bmatrix}, \; L = \begin{bmatrix} d_{LOS_1} \\ \vdots \\ d_{LOS_n} \\ d_{azi_1} \\ \vdots \\ d_{azi_n} \end{bmatrix}, \; \Sigma = diag(\sigma^2_{d_1}, \ldots, \sigma^2_{d_m}, \sigma^2_{a_1}, \ldots, \sigma^2_{a_n}),$$

$u_i = -cos(\alpha_{az_i} - \frac{3\pi}{2})$, $v_i = -sin(\alpha_{az_i} - \frac{3\pi}{2})$,

$a_i = cos\theta_i$, i=1,...,m,
$b_i = -sin\theta_i sin(\alpha_{azi_i} - \frac{3\pi}{2})$, i=1,...,m,
$c_i = -sin\theta_i cos(\alpha_{azi_i} - \frac{3\pi}{2})$, i=1,...,m.

Both Offset Tracking (OT) and Multi-Aperture InSAR (MAI) azimuth measurement methods can be adopted and combined with LOS observations to derive 3-D displacements.

First application of this approach was by Fialko et al. in 2001 using DInSAR measurements together with OT from both ascending and descending acquisition of the ERS satellite [62]. After comparing InSAR decomposition results to the GPS data, RMSE (Root Mean Square Error) values of 4.9, 5.9 and 20.5 cm were obtained for the U-D, E-W and N-S displacement directions, respectively. Lower accuracy in the N-S direction is expected because of significantly lower accuracy of the OT technique compared to the accuracy of DInSAR. A number of other examples of merging InSAR LOS and OT observations can be found in the literature, see [89].

In terms of combining MAI observations with LOS InSAR measurements, Jung et al. used this approach with ALOS PALSAR data to map 3-D displacements caused by the 2007 eruption of Kilauea Volcano, Hawaii [98]. The RMSE values after comparison with GPS data were in this case 2.1, 1.6 and 3.6 cm for the U-D, E-W and N-S displacements, respectively. Higher accuracy compared to the LOS-OT merge technique is likely a result of higher accuracy of the MAI method.

However, some drawbacks were also indicated, since MAI is more sensitive to the interferometric coherence, contrary to the OT technique, which is independent of coherence. For more examples of deriving 3-D displacements from the combination of MAI and LOS InSAR, readers are referred to [96].

Integration of InSAR and GPS data

Another approach to estimating 3-D displacements from InSAR is to utilise GPS measurements together with InSAR. This approach allows to use single-geometry InSAR observations, as opposed to previously described methods requiring multiple independent geometries.

GPS can be used to measure positions of discrete locations and thus obtain displacements in 3 dimensions (vertical, horizontal E-W, horizontal N-S). The accuracy of GPS measurements can reach up to one millimeter in horizontal direction and several millimeters in vertical direction. High accuracy of GPS can be joined with the spatial coverage of InSAR to derive 3-D displacement velocities, provided that an area is covered by SAR acquisitions (very likely with modern SAR satellites covering majority of Earth's surface) and there are enough GPS stations in the area (less likely given the sparsity of GPS stations).

First application of this approach was proposed by Gudmundsson et al. in 2002 to derive 3-D displacements in the Reykjanes Peninsula, Iceland. After interpolating the GPS measurements to the spatial resolution of InSAR data, Markov random field-based regularisation was used together with simulated annealing algorithm to solve the displacement components in 3 directions [78]. A modified version of this approach, more computationally efficient and more successful in estimation of 3-D displacements was proposed in [192]. Other works tackling the problem of merging GPS with InSAR observations can be found in [79, 175, 192].

Approaches that implement prior information about deformation patterns

As was mentioned before, there are at least three independent InSAR LOS measurements necessary in order to derive 3-D displacements using the multi-geometry LOS decomposition approach. There are, however, some situations where this restriction can be loosened. These situations include a surface-parallel displacement assumption, or ignoring the N-S component as it is poorly constrained by the LOS measurement. Some mining subsidence related studies also mention the possibility to assume a proportional relationship between the displacement components or between the displacement and the subsidence trough characteristics. Using prior assumptions about the character of deformation, the number of required InSAR observations can be reduced, and only 2 independent LOS geometry measurements (ascending and descending) or a single-geometry LOS measurement can be sufficient to fully derive the 3-D deformation field.

One example of a prior information assisted approach is the assumption of deformation parallel to the ground surface, as is often the case with glacier movement or landslides. The vertical displacement is related to the gradient of elevation, which are calculable using a Digital Elevation Model. This technique allows calculation of 3-D displacements based on 2 independent InSAR LOS measurements, as demonstrated in [77, 97].

Another approach utilizing prior assumptions about displacements is the neglection of the N-S component of deformation. Since SAR satellites are placed on the

near-polar orbit, the displacement in the N-S direction is difficult to be constrained by the LOS geometry of SAR satellites. If the ground movement consists mainly of vertical deformation, or the N-S displacement can be neglected, e.g. in the case of a strike-slip fault oriented in the E-W direction, the N-S direction can be theoretically excluded from further calculations [225].

Samieie-Esfahany et al. proposed another method based on prior information and assumptions to calculate vertical and horizontal deformation components [191]. In this approach, a hypothesis proposed in [109] is implemented, claiming that horizontal displacement is proportional to the tilt of the subsidence trough (which is also a spatial first derivative of vertical deformation). 3-D deformation field is estimated using this assumption, converting LOS measurements to vertical and horizontal components iteratively, using only 2 independent InSAR geometries.

An approach widely used to derive vertical displacements using multi-geometry InSAR measurements, adapted from [81], is to assume decomposition into 2 displacement components: vertical and horizontal in the Azimuth Look Direction (ALD). Given the LOS observations from ascending (d_{LOS}^{asc}) and descending (d_{LOS}^{dsc}) acquisitions acquired using different incidence angles (θ_{asc} and θ_{dsc}), vertical d_V and horizontal $d_{H_{ALD}}$ displacements can be estimated by solving a system of equations [191]:

$$\begin{bmatrix} d_{LOS}^{asc} \\ d_{LOS}^{dsc} \end{bmatrix} = \begin{bmatrix} cos\theta_{asc} & \frac{sin\theta_{asc}}{cos\Delta\alpha} \\ cos\theta_{dsc} & sin\theta_{dsc} \end{bmatrix} \begin{bmatrix} d_V \\ d_{H_{ALD}} \end{bmatrix}, \tag{3.14}$$

where $\Delta\alpha$ is the difference in the heading angles of the respective InSAR acquisitions. This approach is widely used in studying displacement phenomena using InSAR. Due to its calculation simplicity, this approach was chosen as the method used to derive 3-D displacements from InSAR in this thesis. Since the deformation in the vertical directions is of the most importance in this study, and the horizontal displacements are of less interest, this method was considered the most appropriate since it minimizes the error induced in the value of vertical displacement by considering horizontal displacements.

3.3 Practical applications of InSAR

Development of techniques branching from InSAR and using interferometric data to obtain ground surface displacements in spatial and temporal domains has led to a range of applications in various scientific fields. The most notable change can be identified in the geoscientific field, that often relies on spatio-temporal data as a means to explain different phenomena occurring on the Earth's surface and inside the Earth. After the popularisation of InSAR at the beginning of the 21st century as an alternate measurement tool based on remote observations from satellites orbiting the Earth, scientists often incorporate InSAR techniques to better describe natural and anthropogenic events and phenomena changing the Earth's surface. This section provides an overview of the most popular applications of InSAR in various scientific fields.

Since the thesis focuses on applying InSAR to estimate ground surface movements over mining areas, a more detailed review of applications of InSAR for mining deformation monitoring will be tackled separately in Section 3.4.

Earthquakes and plate tectonics

With global coverage and short revisit time of modern SAR satellites, both rapid and long-term deformation monitoring is possible for studying plate tectonics and earthquakes. Contrary to GNSS and geodetic leveling methods, which provide discrete data in the form of points located over the study area, InSAR produces results covering vast areas (depending on satellite's coverage) in the form of grid (raster) data or a collection of (X, Y) points with displacement (Z) variable.

The first example of practical use of InSAR technique was demonstraded on an earthquake event in 1992, captured by the ERS-1 satellite. The acquired imagery was processed by Massonnet et al. [139], and revealed a deformation pattern caused by the Landers, California earthquake. This confirmed the potential of InSAR methods for deformation monitoring and convinced scientists to use this technique regularly.

Earthquakes of high magnitude can be classified as rapid events, and thus a measurement method is required that can capture rapid deformations of the ground surface associated with a seismic event. Since the Differential InSAR method relies on capturing a pair of SAR images to retrieve interferometric phase caused by the deformation signal, it is suited for studying ground displacements resulting from rapid earthquake phenomena. However, due to decorrelation and atmospheric noise present in InSAR data, only high-magnitude or very shallow earthquakes can be observed using DInSAR. Despite that, InSAR is an established technique providing measurements of ground deformation occurring after earthquakes, and determination of earthquake source is possible through inversion and modelling. A number of studies on the matter are available, e.g. [56, 197, 224, 229].

In addition to monitoring rapid, high-magnitude seismic phenomena using DInSAR, Multi-Temporal InSAR approaches can be applied to earthquake studies, allowing measurements of small amplitude movements occurring over long duration, associated with interseismic strain and post-seismic deformation [125, 131, 215].

Volcanism

Volcanic activity, apart from obvious lava flows and eruptions of active volcanoes, often manifests itself on the Earth's surface in form of ground deformations. As the magma chamber present beneath the surface can alternate between inflation and

deflation, so the ground above it can be subject to uplift (when the magma chamber inflates) or subsidence (in the case of deflation). Precise and extensive deformation measurements can thus help in the understanding of volcanic processes and aid in forecasting of potential future activity for risk mitigation.

InSAR is an essential measurement method for the volcanic studies, allowing remote measurements of deformations associated with volcanic activity, independent of ground-based monitoring. Since the first application of InSAR to monitor volcanic deformation of Etna Volcano, Italy [138], interest in the technique grew rapidly and resulted in a significant development of volcanic studies [88, 132, 173, 174, 176]. As was pointed out in a number of publications, processing of InSAR data for volcano studies requires researchers to take into account several factor influencing the interferometric phase, as there is a possibility for topographically-correlated atmospheric signals to show up as false deformation signals [14].

Landslides

Sudden movements of large volumes of rock mass, often occurring on steep slopes as a result of tectonic movements, rapid rainfall or other phenomena, generally called landslides, are also among events often measured with the use of InSAR methods. Global coverage, high spatial resolution and all-weather operation capabilities of SAR data cause InSAR to be the widely applied measurement method for landslide phenomena. Obviously, due to the limited temporal resolution, InSAR cannot be used as a tool for direct response to a landslide event (obtaining a measurement depends on the availability of imagery on a given day). Nevertheless, InSAR methods are being used to study slow movements of the ground surface that are precursors to a more serious landslide incident [42, 95, 199], as well as monitor and detect new landslide areas overlooked by ground survey data [184].

Applications for polar and subpolar regions

Climate changes are influencing regions near the Earth's South and North Poles, causing the glaciers and permafrost to melt, resulting in changes in ground elevation, for example due to soil relaxation after glacier retreat. These small changes can be efficiently monitored using time series InSAR data [103]. Other examples of application of InSAR in studying polar regions involve ice motion monitoring [77, 156] and delineation of glacier grounding lines [152].

Engineering applications

High accuracy and wide spatial coverage of InSAR methods, specifically time series techniques incorporating sets of SAR images to identify pixels of high spatio-temporal coherence to estimate displacements with a millimeter accuracy. Wide area monitoring capabilities of InSAR allow examination of ground displacements for entire cities, making it possible to control the processes of change on the ground surface caused, for example, by water extraction [38] or tunnelling [73].

Application of InSAR in monitoring engineering structures, such as bridges [113], airports [68], dams [150], can also be indicated.

Mapping deformations on a large scale

Global coverage and the resulting volume of data acquired by SAR satellites initiated the idea of developing methods for processing SAR data at regional scales, covering more than one image, often encompassing entire tectonically active regions or areas of entire countries. Another idea, often coupled with regional-scale processing, is to process InSAR data in an automatic manner, providing analysis-ready results for the interested parties. The aim of this approach was to popularise InSAR in a wider circle of researchers, who are not specialised in SAR data processing, and to create algorithms to automate work with large datasets.

An example of an operational system for processing InSAR data at a large scale is **LiCSAR** (Looking into Continents from Space with Synthetic Aperture Radar) system. This system was designed to automatically process Sentinel-1 SAR data to produce geocoded interferograms and coherence estimates for large regions, mainly tectonically and volcanically active [115]. To fully exploit the amount of data processed by LiCSAR, a LiCSBAS processing software was developed for time series analysis [155]. Both LiCSAR and LiCSBAS allow users to generate interferometric products and conduct time series analyses of displacements, free of charge.

Another example of a service providing analysis-ready InSAR products is the **HyP3** service developed by Alaska Satellite Facility (ASF). This service processes SAR data using an on-demand approach, where users can indicate the processing parameters, e.g. area of interest and processing period. Product selection and acquisition is available using both web portal or an API (Application Programming Interface) [93].

InSAR data processing on a regional scale is crucial for crisis prevention and monitoring land surface deformation phenomena over wide areas. A nation-wide InSAR monitoring systems have been developed in a number of countries, including Norway [45], Japan [154], Czech Republic [114] and Germany [80]. A wide-area monitoring system covering the area of the entire European Union was established in 2021, called European Ground Motion Service (**EGMS**). The EGMS provides users with the results of Sentinel-1 processing products, offering both ascending and descending Line-of-Sight time series displacements, as well as estimates of vertical and horizontal (in the East-West direction) displacements [40].

3.4 InSAR for mining displacement monitoring

The idea of using InSAR as a ground surface displacement monitoring tool for mining subsidence was initiated in 1996, when Carnec et al. used ERS-1 SAR data to study subsidence caused by underground coal mining [22]. Since then, many approaches have been taken to study mining-induced ground subsidence phenomena using InSAR in different countries, for example in [51, 171, 181, 214, 223]. Various InSAR techniques have been used over the years since 1996 to investigate subsidence induced by underground exploitation, using satellite SAR imagery available at the time. For approaches and application of InSAR in studying underground mining displacements, several main approaches can be distinguished:

- Short-term displacement monitoring using pair-based Differential InSAR.
- Long-term monitoring of active and abandoned mining areas using Time Series (TS) techniques.
- Applying InSAR-derived displacements for modeling of subsidence and 2D/3D displacement estimation.
- Combining InSAR with other geodetic measurement techniques (e.g. leveling, GNSS) for mining-induced damage assessment.
- Using InSAR results with machine learning algorithms, e.g. for subsidence detection or displacement prediction.

The **DInSAR** approach has a wide range of applications in studying mining-induced subsidence. The general approach is to utilize a pair of satellite SAR images in the repeat-pass interferometric process in order to detect and study short-term displacements occurring in mining areas . This approach can already give a new insight into the subsidence process, which coupled with other measurement methods and *a priori* modeling can help in understanding the source and progress of displacements caused by underground mining [203, 235].

If the temporal evolution of displacements is to be studied, the Time Series methods like **PSInSAR** or **SBInSAR** can be utilized in underground mining areas. The possibility of estimating displacements even in rural areas using Distributed Scatterer techniques like SBInSAR creates a great opportunity for time series monitoring of displacements [70, 169, 193] If the impact of mining in built-up areas is to be studied, the more accurate (but with lower density of measurement points) PS method is also considered [7, 16]. Research on using the SqueeSAR^{TM} has also been conducted [177].

An example of the application of the TS methods is the study of displacements occurring over abandoned underground mines. Since the TS methods are capable of detecting long-term displacements of low values (several millimeters per year) by finding pixels exhibiting stable scattering of radar signal, they are often used in research to study long-term deformation phenomena in post-mining areas. Both slow subsidence and more frequent uplift (often induced by water inflow) can be studied [16, 23, 70, 146, 193, 208].

Application of TS methods in mining deformation monitoring can be constrained if large spatial gradients of deformation are present in the studied area, causing unwrapping errors and ambiguities, and leading to misinterpretations of results. Ground surface can subside rapidly over actively exploited areas, reaching vertical displacement values exceeding the limit per resolution cell of time series approaches

($\frac{\lambda}{4} * cos\theta$) [81]. For large gradients of displacements, an alternative approaches have been proposed, e.g. replacement of TS analysis with DInSAR stacking, allowing the capture of rapid displacements at the cost of accuracy [53, 161]. Another approaches involve merging interferometric analysis with intensity tracking [29], integrating TS methods with DInSAR [169], and merging InSAR with geodetic measurements [28].

Regarding the large gradient of displacement, studies have been also conducted on the comparison of different radar frequencies and their performance in mining areas. All of the available SAR frequencies, i.e. the X-band (e.g. TerraSAR-X) [26, 52, 177, 234], C-band (e.g. ERS, Envisat, Sentinel-1, Radarsat) [22, 70, 137, 147, 193, 223] and L-band (e.g. ALOS Palsar) [2, 48, 161] are considered in studying mining deformation phenomena. Several studies have been conducted to compare performance of different radar frequencies in mining settings [25, 44, 113, 214, 216]. The overall conclusions that can be drawn from these studies are as follows:

- L-band SAR is considered to be the most suitable for rapid mining displacement monitoring, since longer wavelengths are able to capture displacements of larger spatial gradients. On the other hand, the L-band is not as sensitive to slow displacements as the C-band radar, thus the decision whether to use L-band or C-band (if data from both are available) depends on the use case.

- C-band data (ERS, Envisat, Sentinel-1) are often selected by researchers because of their availability thanks to an open data policy of the European Space Agency. With Sentinel-1A and 1B operating, data can be acquired all over the globe with 6-day intervals, providing an extensive source of free-of-charge SAR data for further analysis of subsidence.

- With higher spatial resolution, the X-band data from the TerraSAR-X satellite are often considered for analysis of 3-D deformation fields, since the spatial resolution allows for analysis of along-track measurements on a smaller scale (as is often the case with mining displacements), contrary to coarser C- and L-band data.

Since the subsidence trough emerging as a result of mining activities underground is subject to both vertical and horizontal deformations, the 1-D LOS geometry of measurement of InSAR can be viewed as a disadvantage in this application. This problem is particularly important when there is a need to know displacements in all 3 directions (Vertical, North-South, East-West). Many studies have been conducted on this matter, including using multi-track satellite SAR data to combine different LOS geometries and solve 2-D or 3-D displacement fields [24, 162], or utilizing DInSAR together with along-track measurements to make up for lack of sensitivity to N-S component [52, 90, 211, 234]. Another approach often used for mining displacement monitoring in 3 dimensions includes applying InSAR together with a prior mining deformation model [30, 46, 54, 124, 211].

Chapter summary

In this chapter, the theoretical basis for the satellite SAR interferometry (InSAR) were introduced. As a remote sensing method, InSAR is an effective tool for studying the ground displacement phenomena. However, a number of important limitations need to be considered in order to fully utilize the potential of InSAR and to reduce the possible errors.

A number of approaches for processing InSAR data were introduced, utilizing a pair of SAR images (DInSAR) or a stack of multiple SAR images (PSInSAR, SBInSAR) for resolving time series of displacements.

Geometrical constraints of using InSAR system for measuring ground surface displacements were explained, focusing on the problem of measuring vertical displacements. Numerous approaches of resolving vertical displacements from InSAR measurements were discussed.

Lastly, a review of applications of InSAR methods was provided, with examples in various fields. An emphasis was put on applying InSAR to studying ground surface displacements induced by underground mining. Different constraints were also discussed, which may hinder the result in case of studying displacements in areas of active mining.

The next chapter will provide an overview of machine learning and deep learning algorithms, with emphasis on the issue of time series forecasting, which will be the method applied to time series data obtained from InSAR measurements, in order to predict the ground surface displacements in a mining area.

Chapter 4

Machine Learning as a data processing tool

Over the past decade, the exponential increase in the amount of available data from various types of sources has made it increasingly difficult for humans to process these data and analyse their patterns to provide valuable information. It became necessary to find tools that would allow large datasets to be processed automatically by computer machines. The development of Machine Learning (ML) as a branch of Artificial Intelligence (AI) has made it possible to develop efficient and effective tools capable of processing large datasets in order to gain knowledge about the phenomena to which these data relate. Their capabilities are being used in many branches of science, including the study of stars, finding distant planets, discovering new substances, analysing DNA sequences or investigating new cancer treatment options [158]. Machine learning has also recently become more prevalent in our daily lives, finding applications in areas such as e-mail spam filtering, text and speech recognition, improving search engines, or analysing games of chess to create an AI-driven chess player capable of defeating even grandmaster chess players [206].

4.1 Machine Learning basics

The wide range of applications of machine learning is made possible by the large number of developed algorithms and models, which are be divided into 3 main groups based on the type of input data provided and the problem at hand: **supervised learning**, **unsupervised learning** and **reinforcement learning**. A breakdown of the machine learning groups with example applications is shown in Fig. 4.1. In the following subsections, the basic principles of the first 2 groups, namely supervised learning and unsupervised learning, will be presented. Reinforcement learning is a type of machine learning that creates a system (agent), which improves its accuracy in a given task by interacting with a defined environment, maximising a specified reward and minimising a penalty at the same time. A common example of a reinforcement learning model is a chess engine, analysing next moves on a chess board in order to win a chess game (maximising its reward).

4.1.1 Supervised learning

Supervised learning is a branch of ML that is based on learning a model on input data labelled with output signals. The term *supervised* refers to supervising what the model learns by giving it the correct answers in form of output signals. The

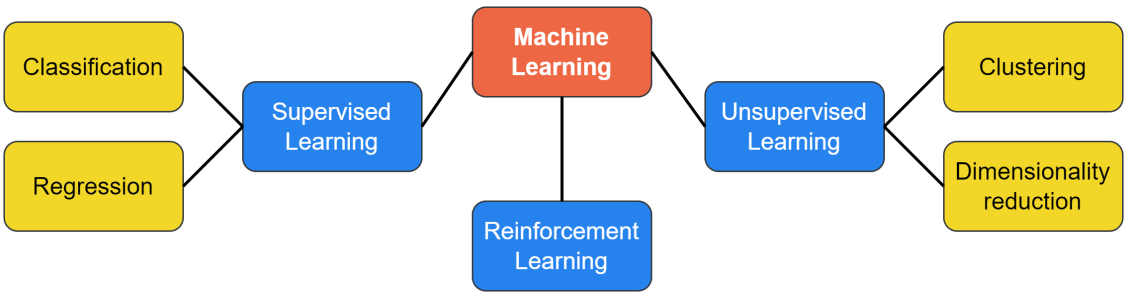

Figure 4.1: Types of machine learning algorithms.

model learns the relationships between input and output signals (**input samples** and **labels**), and then predicts the unknown output for previously unseen input. The data used to train the model is contained in the **training set**, while the data on which the prediction is made is called the **test set**. The training dataset is often split further into training and **validation** sets, to control the model's accuracy during training [158]. A diagram of how the supervised learning algorithm works is shown in Fig. 4.2.

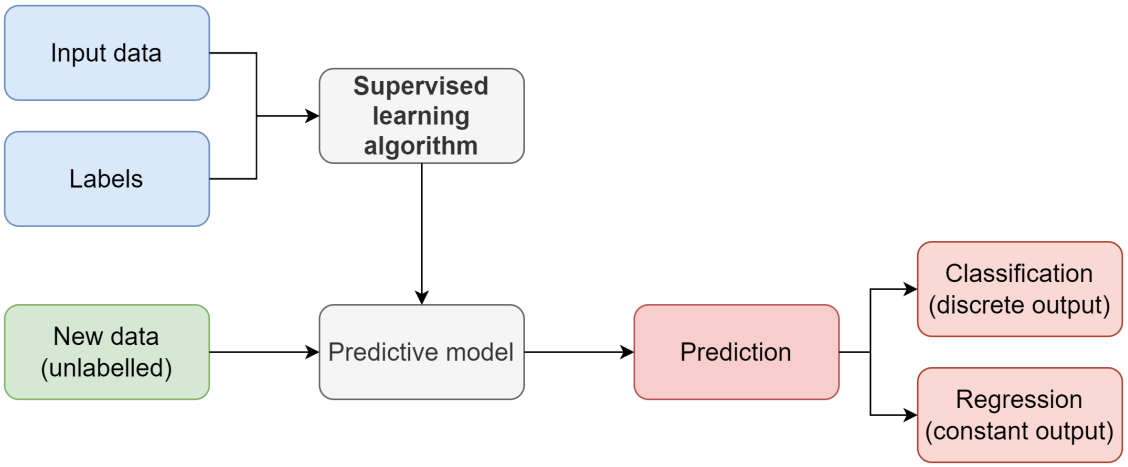

Figure 4.2: Supervised learning flowchart

The training process of the supervised learning algorithm is based on an iterative optimisation of a defined **cost function**, which determines the mismatch between the model-predicted result and the actual value of the label. Finding the local or global minimum of the cost function leads to the selection of appropriate model weights that best model the relationships in the training data. During subsequent iterations (epochs), the algorithm analyses the training data and minimises the cost function using the **gradient descent** method. In the gradient descent method, the weights of the model are decreased or increased based on the gradient of the cost function (the weights are changed in the direction opposite to the gradient, to minimise the cost function). Training lasts until the pre-defined number of epochs is reached, or if the accuracy of the model does not increase with subsequent iterations (a process also called early stopping).

The domain of supervised learning can be further divided into **classification** and **regression**.

Classification

A supervised learning problem becomes a classification task when the output variable is a categorical, unordered variable representing groups that each data instance belongs to. The basic type of classification is *binary classification*, in which the output variable can only take two states, e.g. yes/no, or 0 and 1 in computer language. A machine learning algorithm, based on a set of learning data, finds rules (called *decision boundaries*) to separate individual observations into appropriate classes. The classification task can also take the form of *multiclass classification*, if the predicted variable can assume more than 2 states. Examples of classification include spam filtering (binary classification) or hand-written letter recognition (multiclass classification).

Regression

If the output variable is a continuous value, the supervised learning process takes the form of a regression task. The purpose of regression is to find a model that, based on one or more input variables (also called explanatory or independent variables), will predict the values of the output variable (also called dependent variable). Examples of regression can include: predicting sale volumes, weather forecasting or predicting energy prices.

4.1.2 Unsupervised learning

Unsupervised learning is based on working with unlabelled or unstructured data (in contrast to supervised learning, where the labels of subsequent learning examples are known and used in the training process). Supervised learning models are used to discover the structure of the data being processed and obtain information without the use of labels or rewards [206].

The two main groups of unsupervised learning algorithms are **clustering** algorithms and **dimensionality reduction** methods.

Data clustering

Clustering is an unsupervised learning technique that consists of organising an unstructured dataset into subgroups (known as clusters) that share certain common characteristics, without prior information on where each sample belongs. Using clustering algorithms, it is possible, for example, to find sets of points in space that are close to each other, or to create groups of clients according to their shopping preferences in order to target advertisements [76].

Dimensionality reduction

Dimensionality reduction algorithms are used for working with multi-dimensional data and are often applied at the data preprocessing stage. When the input dataset has numerous variables (features), the use of machine learning algorithms can be time-consuming. The process of dimensionality reduction involves transformation to a feature space with fewer dimensions than the input dataset, while maintaining the variance in the data. The reduced dataset should thus produce similar results in learning with a machine learning algorithm as the dataset before the reduction.

Dimensionality reduction is also useful in data visualisation, when data in a multi-dimensional space (e.g. 5 dimensions) can be transformed to a one-, two- or three-dimensional space [206].

4.2 Deep Neural Networks

The machine learning branch that uses algorithmic structures called deep neural networks to train a model working with on a dataset is called **Deep Learning (DL)**. Deep learning is a subset of machine learning, just as machine learning is a subset of the very broad field of artificial intelligence. The relationship of the different branches is shown in Figure 4.3.

A neural network consists of a unit cell called a neuron. The first research into the concept of an artificial neuron was conducted in the 1940s by McMulloch and Pitts [141].

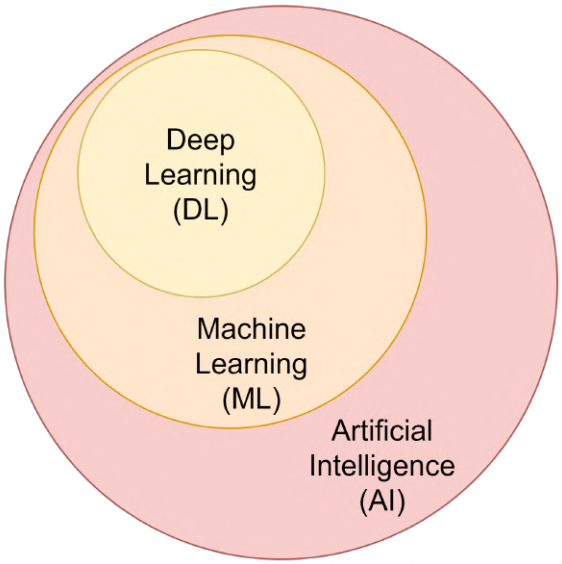

Figure 4.3: Relationship between Artificial Intelligence, Machine Learning and Deep Learning

4.2.1 Principles of neural networks

The *feed-forward neural networks* used in deep learning, also known as deep feed-forward networks or **multilayer perceptrons (MLPs)**, get their name from their layer-based network structure. A basic neural network consists of an *input layer*, into which data is ingested (e.g. in the form of numbers, images, text), followed by one or more than one *hidden layers*, capable of detecting representations and relationships in the data. The network ends with an *output layer*, which, after processing the information through the hidden layers, returns the desired result. Subsequent layers of the feed-forward network contain interconnected units (nodes), called neurons, which, based on the input received, using a specific activation function, pass the output (called *activation*) to subsequent units. A diagram of a neural network is shown in Figure 4.4. The information at the input (the input data) and the output (the result the network should produce based on the input) is known, while the information in the hidden layers is unknown, hence the name of these layers. The task of the model is to process the information in the hidden layers and adjust their

parameters by learning in such a way as to find a translation (representation) of the input data into the output data [76].

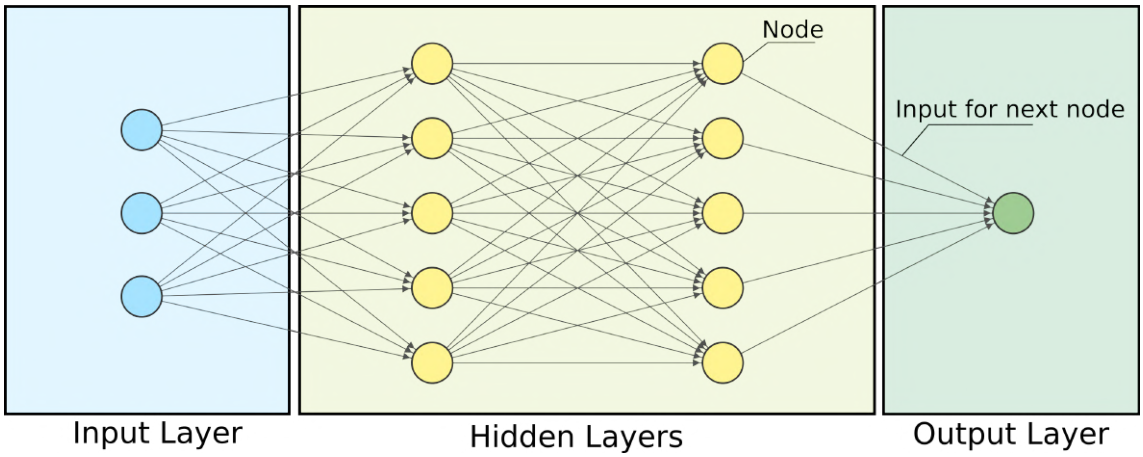

Figure 4.4: A basic example of an artificial feed-forward neural network

4.2.2 Multi-Layer Perceptron - a basic neural network

Basic concepts. Perceptron

First works on neural networks research date back to the 1940s, when scientists attempted to understand the information processing mechanisms of a human brain in order to develop artificial intelligence. In 1943, Warren McMulloch and Walter Pitts proposed the concept of an *artificial neuron*, replicating the nerve cell (neuron) that is the building block of the human brain. In this concept, the artificial neuron is a logic gate, accepting information in the form of input signals. If the input signal has a sufficiently high value, the neuron is activated and returns an output signal [141].

In 1957, Frank Rosenblatt developed the concept of a *perceptron*, based on the artificial neuron model developed by McMulloch and Pitts. This perceptron learned by selecting appropriate values for the weighting coefficients w, by which the input values x are multiplied (bias b is also taken into account) and the output value z is returned.

$$w = \begin{bmatrix} w_1 \\ \vdots \\ w_m \end{bmatrix}, x = \begin{bmatrix} x_1 \\ \vdots \\ x_m \end{bmatrix} \tag{4.1}$$

$$z = w_1 x_1 + \cdots + w_m x_m + b = \mathbf{w}^T \mathbf{x} + b \tag{4.2}$$

The signal is forwarded (or not) by the perceptron based on the value of the decision function $\Phi(z)$, which converts the output values z into binary values:

$$\Phi(z) = \begin{cases} 1, & \text{if } z \geq 0 \\ -1, & \text{if } z < 0 \end{cases} \tag{4.3}$$

The values of the weights in a perceptron are initially set as small random values, which are then updated on the basis of the obtained output values *haty* and the actual values y:

$$w_j := w_j + \Delta w_j \tag{4.4}$$

$$\Delta w_j = \eta(y - \hat{y})x_j, \tag{4.5}$$

where η is a learning rate, and w_j represents a single weight corresponding to *j-th* feature. The process of adjusting and updating weights is called *learning*, and after that process the perceptron is able to make predictions based on given set of input features [180].

Training a neuron

An extension of the perceptron model was the *ADAptive LInear NEuron (ADALINE)* model proposed in 1960. In this model, the decision function $\Phi(z)$ of a unit jump is preceded by a linear activation function [219]. The ADALINE model is otherwise known as the single-layer neural network model (it has an input and an output layer, and no hidden layers between).

The idea behind training a neuron and a neural network is to minimise a loss function L. In case of ADALINE, L takes the form of a mean squared error (MSE) between the predicted output and the real value. The loss function is differentiable, which means that its local or global minimum can be approximated (leading to a minimisation of loss function). The process of reducing the loss function is performed using the gradient descent algorithm. In this algorithm, the gradient of the loss function is calculated with respect to the model parameters. Based on the direction of the gradient, the weights and biases of the model are updated by a small amount in the direction opposite to the gradient of the loss function, according to:

$$\mathbf{w} := \mathbf{w} + \Delta\mathbf{w} \tag{4.6}$$

$$\mathbf{b} := \mathbf{b} + \Delta\mathbf{b} \tag{4.7}$$

After a number of iterations, the weights and biases of the model are updated in a way that minimizes the loss function. The weight update is based on the entire training dataset. An alternative approach is to update weights after each training example. This approach is also called **stochastic gradient descent (SGD)** [180].

Interest in neural networks research declined after 1960 due to the lack of an effective method for learning networks composed of more than one layer. A resurgence of interest appeared in 1986, when a *back-propagation algorithm* was proposed for efficiently learning multilayer neural networks [187].

Multilayer network and backpropagation algorithm

A multilayer neural network is a combination of at least two layers (input and hidden) composed of a certain number of neurons, capable of approximating complex functions and relationships from training data. A fully connected neural network with multiple layers is called a **multilayer perceptron (MLP)**. In this network, units in the input layer are fully connected to the units in the first hidden layer, which are consequently fully connected to the units in the next hidden layer. Units in the last hidden layer are then connected to the units in the output layer.

Considering a network with one hidden layer, training features are supplied to the input layer. Data is propagated forward through the network, and the net input (a sum of weighted signals coming from other units) of the hidden layer is calculated:

$$\mathbf{z}^{(h)} = \mathbf{x}^{(in)}\mathbf{W}^{(h)T} + \mathbf{b}^{(h)}, \tag{4.8}$$

where $\mathbf{z}^{(h)}$ is the net input vector of size $1 \times d$ (d is the number of units in the hidden layer), $\mathbf{x}^{(in)}$ is the vector of features from the input layer of size $1 \times m$ (m is the number of features), $\mathbf{W}^{(h)T}$ is a transposed weight matrix of size $d \times m$, and $\mathbf{b}^{(h)}$ represents a vector of bias units of size $1 \times d$.

Net input vector of the hidden layer is used to compute the activation vector $\mathbf{a}^h$, using the activation function $\sigma()$:

$$\mathbf{a}^{(h)} = \sigma(\mathbf{z}^{(h)}) \tag{4.9}$$

If all training examples are considered, above equations can be presented as:

$$\mathbf{Z}^{(h)} = \mathbf{X}^{(in)}\mathbf{W}^{(h)T} + \mathbf{b}^{(h)}, \tag{4.10}$$

$$\mathbf{A}^{(h)} = \sigma(\mathbf{Z}^{(h)}). \tag{4.11}$$

Data is propagated forward (in form of activations in the hidden layer) to the output layer in a similar way:

$$\mathbf{Z}^{(out)} = \mathbf{A}^{(h)}\mathbf{W}^{(out)T} + \mathbf{b}^{(out)}, \tag{4.12}$$

$$\mathbf{A}^{(out)} = \sigma(\mathbf{Z}^{(out)}), \tag{4.13}$$

where $\mathbf{Z}^{(out)}$ is the net input of the output layer, $\mathbf{A}^{(out)}$ is the activation of the output layer, $\mathbf{W}^{(out)}$ is the weight matrix connecting the hidden layer to the output layer, and $\mathbf{b}^{(out)}$ is the bias vector.

Using the outputs of the network, a loss function $L(W, b)$ is calculated. As the loss function needs to be minimized in order for the model to learn representations present in the data and predict output values, the gradient descent algorithm is used to iteratively minimize the loss function and update parameters of the model (weights and biases). Partial derivatives of loss function are calculated with respect to the weight and bias parameters, to determine the parameter update values. As an example, a weight gradient for the first unit in the output layer is computed as follows:

$$\frac{\partial L}{\partial w_{1,1}^{(out)}} = \frac{\partial L}{\partial a_1^{(out)}} * \frac{\partial a_1^{(out)}}{\partial w_{1,1}^{(out)}} \tag{4.14}$$

The weight is then updated using stochastic gradient descent approach, in the direction opposite $(-)$ to the direction of the gradient, applying a defined learning rate η:

$$w_{1,1}^{(out)} := w_{1,1}^{(out)} - \eta \frac{\partial L}{\partial w_{1,1}^{(out)}} \tag{4.15}$$

This way, the loss is propagated backwards in the network, and the parameter values are updated. Using an iterative approach, where with each iteration the training dataset propagates through the network, the model is trained as the weights and biases are updated using the backpropagation algorithm. As the minimum of the loss function is reached, the model learns the relationships between the input and output training samples by optimising its parameters, and can predict the output for a set of previously unseen input features [180].

4.2.3 Convolutional Neural Networks for image processing

Convolutional Neural Networks (CNNs) are neural network models that are based on how objects are recognised by the human brain using the visual cortex. The first concept of a CNN architecture was proposed in 1989 by Yann LeCun

and his team. It was applied to the task of handwritten digits classification, outperforming current state-of-the-art models [116]. The discovery of CNNs led to a breakthrough in the field of computer vision in machine learning.

As mentioned earlier, the working idea of a CNN is based on the human visual cortex, which focuses on different salient features in a layer-based manner. CNN is built using layers of convolutional kernels, which purpose is to extract relevant features from raw data. The extracted features differ for each layer, starting with low-level features extracted from raw data by the first convolutional layer, and continuing with features of higher level extracted by the subsequent layers. With this approach, CNNs construct a feature hierarchy: first layers extract low-level features (e.g. edges on an image), which are then subsequently merged to extract high-level features by next layers (e.g. shapes of objects). Subsequent layers in a CNN are often subsampled using a pooling operator, controlling the size of the output feature maps and helping with finding the most relevant features in raw data by introducing local invariance to small changes in data. High-level features in form of activation maps are then flattened (in case of an image, a 2D structure is flattened to 1D structure) and passed to a fully connected network (MLP), which predicts an output (continuous target or class label) [180].

Weights in a CNN are constructed as feature maps (2D images) computed from raw data by convolutional layers. An important characteristic of a CNN is that a single element on the feature map is not connected to all elements in the input, but to a small subset of data (nearby samples are more relevant to each other e.g. neighbouring pixels in an image). Another essential feature is that weights are shared across the feature map (different patches of data can have the same relevance in producing the output). These two characteristics make CNN an alternative to MLPs with significantly smaller amount of parameters (weights) required to train the neural network [116].

While the most significant achievements of CNNs in machine learning have occurred in the field of computer vision using 2D convolutional networks, a CNN can also be implemented on data in different number of dimensions, i.e. *sequential data* (1D convolutions) [105] and three-dimensional data (3D convolutions) [205].

4.2.4 Recurrent Neural Networks for sequential data analysis

Sequential data are a special type of data that are organised in a sequence, in which the order of elements is important for the correct interpretation of the data. Compared to other types of data, elements in a sequence are not independent of each other, a feature that is crucial when considering with these types of data using machine learning algorithms. Non-sequential data (e.g. tabular data, images) can be processed by a machine learning model regardless of their order, which is not the case for sequential data.

Examples of sequential data are text data, stock market prices and time series data. As the time series data processing is considered as part of this thesis, this concept will be developed further in this chapter.

When considering sequential data, standard *fully connected* neural network models, such as MLP or CNN, do not consider ordering of the data in a sequence and treat every training sample independently. It should be stressed that such models do not have a memory capable of learning the order of information in a sequence. In a time series context, a standard model will treat recent data samples equally to data samples acquired much earlier. In order to incorporate sequential modeling

into neural networks, a concept of **Recurrent Neural Network (RNN)** has been proposed [187].

The difference between RNN and a standard neural network is the method of the data flow through the network. In a standard feedforward network, data is transferred from the input layer to the hidden layers, which then forward the information to the output layer. In case of a recurrent network, the hidden layer receives input both from the previous layer (input or hidden), as well as from the previous time step in the current hidden layer. This approach to the flow of information is possible by incorporating recurrent layers with backpropagation through time as hidden layers, and allows the RNN to memorize past inputs in a sequence and generate a context, which is then used for generating an output [217]. A schematic of a data flow through the RNN is shown on Fig. 4.5.

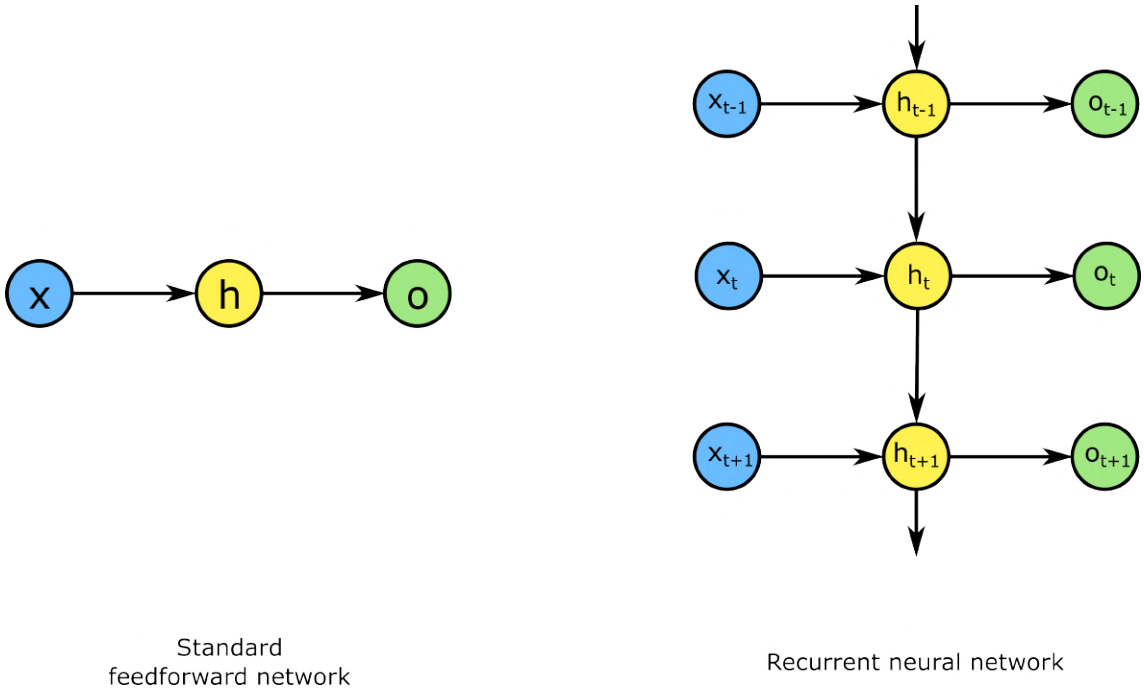

Figure 4.5: Schematic flow of data through a standard feedforward network (left) and a recurrent neural network (right). x - input data, h - hidden units, o - output

The Recurrent Neural Network can work with sequential data of any length, and produce an output in form of a single value or a sequence of values (also known as a *sequence-to-sequence* model, or a *seq2seq* model). However, a problem of vanishing or exploding gradients is present when training RNNs using backpropagation through time on long sequences. This means that while errors are propagated backwards through a long sequence, gradients can accumulate to very high or very low values, resulting in the loss of stability in the model and extremely large or extremely low weight values [168]. One of the solutions to the problem of vanishing and exploding gradients in training recurrent neural networks on long sequences of data was the introduction of a memory unit, the **LSTM cell**.

Long Short-Term Memory (LSTM) cell was first introduced by Hochreiter in Schmidhuber in 1997 [86]. A diagram of the LSTM cell is shown in Figure 4.6. The flow of information through the LSTM cell is controlled by three types of gates:

- the forget gate f_t decides which information is allowed to go through the cell, allowing the cell to control the flow of data in the network. The output of the

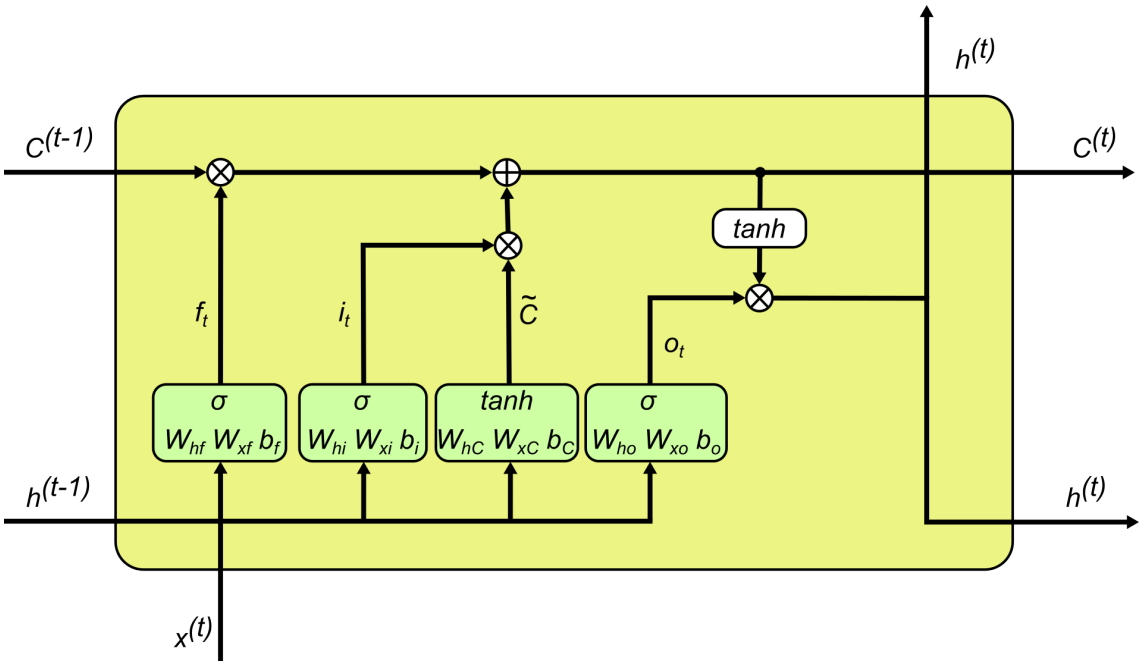

Figure 4.6: Long Short-Term Memory cell structure

forget gate can be presented as:

$$f_t = \sigma(W_{xf}x^{(t)} + W_{hf}h^{(t-1)} + b_f), \tag{4.16}$$

where:

σ is the *sigmoid* activation function
W_{xf} is the input weight matrix,
$x^{(t)}$ is the input vector at the current time t,
W_{hf} is the recurrent weight matrix,
$h^{(t-1)}$ is the hidden layer output vector at previous time step *t-1*,
b_f is the bias vector.

- The input gate i_t and candidate value $\tilde{C}$ update the cell state $C^{(t)}$ of the LSTM cell with new information (candidate value vector defines new values to add to the cell state, and the input gate decides which of these new values will be added). The cell state is responsible for reducing the problem of exploding or vanishing gradients, as various gates in LSTM control its value. The output of the input gate and the candidate value are calculated using:

$$i_t = \sigma(W_{xi}x^{(t)} + W_{hi}h^{(t-1)} + b_i), \tag{4.17}$$

$$\tilde{C} = tanh(W_{xC}x^{(t)} + W_{hC}h^{(t-1)} + b_C). \tag{4.18}$$

  The *tanh* is the hyperbolic tangent function.

- The output gate o_t updates the values of units in the hidden layer by selected values. Its output is computed using:

$$o_t = \sigma(W_{xo}x^{(t)} + W_{ho}h^{(t-1)} + b_o). \tag{4.19}$$

The output is multiplied by the cell state (updated earlier using forget and input gates) to compute the value of the hidden unit h at current time t:

$$h^{(t)} = o_t * tanh(C^{(t)}). \tag{4.20}$$

The LSTM cell has been used in a variety of sequence modeling tasks. Examples of time series forecasting applications of LSTM will be provided later in this Chapter. An alternative approach to LSTM is the **Gated Recurrent Unit (GRU)**, developed more recently in 2014 [37].

4.3 Machine learning with time series data

Time series are present in many areas of modern life. By collating information at different points in time, it is possible to detect changes in time, expose trends and critical points, and make an attempt to forecast the value of a given piece of information in future time. An elementary example would be a simple extrapolation of the trend of the previous week's air temperature values to predict the temperature in the following days (of course, weather forecasting is a very complex process requiring huge amounts of different variables, here a significant simplification was assumed). Another example could be the prediction of demand for goods and services based on historical sales data, taking into account days of the week and holidays. Historical energy consumption data can be used by energy producers to estimate future energy demand. Observing traffic flows on previous days can identify the most congestion-prone hours of the day. In short, wherever we have historical data structured over time, we can forecast it into the future using one of the available time series forecasting methods.

4.3.1 Traditional approaches to time series forecasting

For further considerations, let us assume that we have a time series of past n ordered values with equal temporal spacing: $x_{t-n}, ..., x_{t-2}, x_{t-1}, x_t$. Based on information present in this time series, we want to predict the value of this time series at the next time step *t+1*, or if the forecast horizon is longer, at the next several time steps $t+1, t+2, t+3, ...$ For simplicity, the forecast horizon will be denoted by l. Therefore, the forecast of a value x at a given horizon l in the future will be given by $\hat{x}_t(l)$. The actual value, x_{t+l} will then be compared to the forecast value in order to determine the forecast accuracy [71].
Because of how important the prediction of data such as stock market prices or the temperature in the following days is, and what costs are associated with incorrect prediction, the issue of time series prediction has been the subject research since the second half of the 20th century. The methods used for time series prediction can be divided into several basic groups:

- naive methods;
- time series decomposition methods;
- linear regression models;
- autoregression models;

- moving average models;
- exponential smoothing models;
- machine learning methods.

Naive methods do not use any complex mathematical models. They are often based on the assumption that the projected value is the same as in the previous epoch, or that the projected value is invariant and equal to the average of past values. In the context of the 'simplest' approach to prediction, naive methods are often used as a proxy for the effectiveness for other models using more complex rules.

Time series decomposition methods are based on performing a decomposition of the time series into its basic components and forecasting each of them separately, then combining the forecasts for each component into a final predicted value. The four components in question are: **level** - the value the time series would reach if it were a straight line; **trend** - linear behaviour over time, taking the form of a steady increase or decrease in value; **seasonality** - patterns in the data repeating over a certain period of time (e.g. higher traffic during afternoon hours recurring every day); and **noise** - random variation in the data that cannot be described by an empirical model. Combining these 4 components will form a time series.

Linear models involve fitting a linear function of a certain degree (most often of degree 1, 2 or 3) into a time series, and extrapolating values into the future using this function. An approach successful in predicting a simple time series with invariable characteristics, it may fail if the time series in question exhibits temporal irregularities, such as sudden changes in trend, or varying seasonality.

Autoregression models are based on a principle that values of a time series at previous time steps $(x_t, x_{t-1}, x_{t-2}, ...)$ can be used as an input to a regression equation, that is then used to predict the value at the next time step (x_{t+1}) [20]. Autoregression models are successful in case if the time series values exhibit autocorrelation - values at subsequent time steps are correlated with values at previous time steps. In order to determine whether there is an autocorrelation present in the time series, an *Autocorrelation Function (ACF)* is used to create a plot that shows correlation between future time series value and values at previous time steps (called *lagged* values). The autoregression model is often denoted as $AR(p)$ model, where p is the order of the model, i.e. number of lagged values used in the autoregression process (e.g. for $p = 3$, 3 previous values of time series are used to predict the next time step).

Another time series forecasting method is the **moving average** technique [159]. This model assumes that the current value of the time series x_t depends on the mean of the time series, the current error term and previous error terms. The moving average model is denoted as $MA(q)$, where q is the order of the model, analogically to the AR (autoregression) model.

The autoregression (AR) and moving average (MA) models are often used together, forming autoregressive moving average (ARMA) or autoregressive integrated moving average (ARIMA) models [20]. While the ARMA model combines the autoregression and moving average principles, the ARIMA model adds the *Integrated* term to the equation, by differencing the time series, and thus getting rid of the trend term present. The integration component is denoted as $I(d)$, where d is the order of differencing. If the time series to be predicted exhibits seasonality, the Seasonal variation of ARIMA model (SARIMA) is often used, adding the order of seasonality to the models autoregressive and moving average components [91].

Exponential smoothing models are centered around an assumption that the predicted value is based on previous values of the time series, except that the nearest (latest) values influence the next value more than the further (earlier) values. This relationship is modelled in the exponential smoothing method as a weighted average of all previous values, with the weights decreasing exponentially from the nearest to the oldest value of the time series [69]. The *Holt-Winters* exponential smoothing approach takes into account trend and seasonality factors present in the time series (traditional exponential smoothing fails if the data is trended and seasonal) [221].

The methods described above, i.e. linear models, autoregression, moving average and exponential smoothing, are more commonly considered as *traditional* approaches to time series forecasting. These have been applied over various time series forecasting problems in the past, and are still in use to this day. However, when referring to traditional time series prediction methods, it should be emphasised that they have certain limitations. First of all, most of these methods assume that there is a certain linear relationship in the time series, and they are not able to deal with more complex models. it should be also mentioned that real data often contain missing records that traditional methods do not accept. Many phenomena depend on more than one variable, so following this line, a prediction model should take into account many variables, while most traditional methods assume the prediction of a time series only for a one-dimensional time series dataset. Moreover, they can often be applied to only a single time series, and predicting the value of another time series is based on devising another model with different parameters. Thus, as can be seen, while traditional methods perform well for simple problems and have been used in many fields for many years, for more complex problems they may not produce satisfactory results. As a partial solution to this problem, the use of machine learning methods, in particular deep neural networks was proposed, capable of dealing with complex data sets by capturing representations that are invisible neither to the human observer nor to traditional methods and algorithms.

4.3.2 Machine Learning in time series forecasting

Being a technique for processing data and creating a model based on learning from examples, machine learning has become an obvious candidate to take over the role of traditional algorithms in time series forecasting. Machine learning algorithms take examples containing input data and output data and, through an iterative process called learning, create a model that, for given input data, can determine the correct value at the output, with a given accuracy. The issue of time series forecasting can be extrapolated to the field of machine learning, since (as mentioned in the previous chapter) it is also largely based on determining a future value (output) from past values (input). So, **with enough input-output examples, the machine learning algorithm could also learn the task of time series forecasting.**

Related to the above, an important issue in working with time series and machine learning is the proper preparation of data for learning and testing the ML algorithm. A time series represents a single entity, while machine learning requires multiple examples of data to effectively learn the relationship between input and output. This problem is solved by transforming the time series into a supervised learning problem. The time series is divided into samples containing input-output pairs, where the input is the n values of the series treated as past values, and the output is the m predicted values of the series. Such pairs are created using a so-called rolling window approach. The goal of the ML algorithm is to learn the relationships

between the individual input-output pairs in order to be able to correctly predict the future unknown values.

Another important issue is to define the nature of the time series forecasting problem in the context of the data at hand. Depending on whether we have one value at each time step or several values of different variables for each time step, a distinction is made between **univariate** and **multivariate** forecasting. In **univariate** forecasting only a single variable at each time step is known (e.g. energy consumption), and the value of this variable is forecasted by the ML algorithm. If there is more than one variable known, (e.g. energy consumption, day of the week, air temperature, etc.), **multivariate** forecasting can be applied to either predict the value of a single variable based on values of multiple variables in the past, or predict multiple variables based on their historical data.

Supervised machine learning algorithms are used in the task of time series forecasting. Among the algorithms used in time series forecasting, are: Random Forest algorithm [85], Gradient Boosting Machine (GBM) [64], Linear Regression models (e.g. Ridge Regression, Lasso Regression) [183] and Support Vector Machines [104]. Determination of the highest-performance model is instance-specific, and some models may perform better than other in a specific use case. Accuracy metrics for each of the models tested are used as an indicator for the best model to use.

4.3.3 Applying Deep Learning to time series forecasting

The ability to model non-linear relationships in the input data, models that are data-driven and do not require a lot of a priori assumptions about the problem, and the ability to generalize are often indicated as factor behind the use of complex algorithms using neural networks instead of simple machine learning models. Increase in computing power available facilitated the growth of the deep learning field, resulting in new architectures and more complex models. The state of the art neural network models achieve better results than traditional benchmarks across different datasets, e.g. text, images, video and audio. These successes have motivated research in applying deep neural networks in time series forecasting. The first works about application of artificial neural networks in forecasting were published after 1986, facilitated by the introduction of the backpropagation algorithm [237]. In more recent years, the Recurrent Neural Networks (RNNs), as well as Convolutional Neural Networks (CNNs) and Transformer models represent the most frequently applied deep learning architectures for time series forecasting. Majority of them are tailored specifically to work with time series data, e.g. the ability to process sequential data by the RNNs has been translated to use with time series data. However, some modern architectures were proposed that do not take into account any temporal properties and can forecast with as high accuracy as other architectures. Selected modern deep learning architectures developed in recent years will be described below[1]. The diversity of architectures stems from variety of time series forecasting problems in different domains, requiring an individual approach.

[1]Please bear in mind that the deep learning field is rapidly developing, and new discoveries are made over the span of a single year. Methods described in this thesis are considered state-of-the-art during writing (2022), and may be superseded by other approaches in the future.

Recurrent Neural Networks and DeepAR

Recurrent Neural Networks (RNNs) were created to process sequential data. Initially, these data were strings of characters and words, used in the problem of natural language processing (*NLP*). Given that a time series is also a time-ordered sequence, RNNs became an object of forecasting research.

At the heart of the RNN's operation is an internal memory, able to preserve the state of the network and use it as input information at subsequent stages of the sequence. In this way, the network is able to remember past data in the sequence and treat the sequence as an ordered entity, predicting subsequent values given the past data. The memory is recursively updated with new information as successive stages of the sequence are processed [180]. When processing long sequences, RNNs can suffer from a *vanishing/exploding gradient* problem. A variant of RNN, a **Long Short-Term Memory (LSTM)** network was proposed by Hochreiter and Schmidhuber, that uses layers of LSTM cells containing gating mechanisms to control the flow of information through the network, reducing the extreme gradients [86]. LSTM networks have been widely applied to the time series forecasting problem [35, 188, 194].

One of the novel networks using RNNs is **DeepAR**, developed in 2019 by Amazon. It is based on the LSTM architecture, using Monte Carlo simulations to make probabilistic predictions. An important feature of the model is the ability to create a global model, based on learning relationships from a set of multiple time series. This approach distinguishes DeepAR from many network architectures and traditional methods, which learn from a single time series and create local models capable of forecasting only a given series [189].

N-BEATS

A common approach in forecasting with deep learning has been to assume that in order for neural networks to be capable of forecasting, it is necessary to use architectures that take into account the time dimension and treat the time series as a sequence, an example of which is RNN. An example of an architecture that contradicts this assumption and does not use any temporal properties for forecasting is the **N-BEATS** architecture (short for Neural Basis Expansion Analysis for interpretable Time Series forecasting), developed by a team at Element AI in 2019. The architecture is the first 100% pure application of deep learning without time-specific components, which has outperformed previously used traditional and hybrid approaches.

The network consists of many hidden fully connected layers, creating a very deep structure. The residual connections contained in the network enable more effective learning and interpretability of results. The layers of the network are arranged in blocks, each responsible for a single task, e.g. first block models a given time series based on input and output sequences, second block models and corrects the errors of the first block, and so on [164].

Convolutional Neural Networks and Temporal Convolutions

Convolutional Neural Networks (CNNs) have been developed for working with images, yielding very good results in tasks such as image classification and

object detection. CNNs have also found application in working with time series. For this to be possible, it is necessary to use one-dimensional convolutional filters instead of the two-dimensional filters used in image processing. Such networks are capable of reading hidden representations in a time series, which they can use in forecasting. However, two features of CNNs should be noted: they are time invariant (they do not account for the time dimension and process the sequence as a whole) and they learn on the entire learning dataset. In the case of a time series, this can lead training data leaking into the forecast data.

An approach to using CNNs in forecasting, considering a time dimension in the data, was the **Temporal Convolutional Network (TCN)**. The convolutional layers in a TCN are based on causality, meaning that input values for an output at time t are only the values at time t and earlier. This ensures that there is no leakage from historical data to forecasted data. The TCN uses historical data sequences to predict sequences of the same length (the output dimension corresponds to the input dimension). For very long sequences, this requires a deep structure of convolutional layers with large filters [9].

The Transformer concept and Temporal Fusion Transformers

Another architecture proposed for time series forecasting is the **Transformer**, introduced by Google Brain in 2017. Transformer is built using stacks of encoder and decoder layers. Each encoder consists of a self-attention layer and a linear layer, while decoders consist of a self-attention layer, encoder-decoder attention and a linear layer. The self-attention mechanism allows the model to learn the relationships between elements of a sequence and relate individual elements to others (originally, this approach was intended for text processing, relating individual words to other words in a sentence). This affects the subsequent modelling of the output sequence by the decoder (using the encoder-decoder attention) [207].

The transformer processes sequences of length trained during learning. In order to be able to predict long sequences and learn temporal dependencies, a model using transformers - **Temporal Fusion Transformer (TFT)** was proposed by researchers from University of Oxford and Google AI. TFT uses recursive layers to model local sequences and a self-attention mechanism to process sequences as a whole. In addition, the architecture has gates to retain information that is not relevant to the prediction. The TFT is designed to process multidimensional sets, with the additional feature of interpretability of the learned model - the model indicates the individual elements of the sequence that have the greatest impact on the prediction [127].

4.3.4 Can Machine Learning outperform traditional methods?

Ever since machine learning and deep learning methods have been proposed as an alternative approach to time series forecasting, it has been a matter of discussion whether they can provide better results than traditional forecasting methods. A number of studies has been conducted in that matter, using results from various time series forecasting competitions held. The most widely discussed are the *M* competitions, conducted for almost 40 years [135]. Their aim is to improve the accuracy of time series forecasting by empirical evaluation of a number of forecasting approaches using real-life data. The latest, *M5* competition, was held in 2020 and its results were published in 2022 [135]. The next *M6* competition is currently

taking place (at the time of writing this section - end of 2022) and is scheduled to end at the beginning of 2023.

At the beginning, when first approaches of using machine learning algorithms and neural networks for time series forecasting were proposed, the general consensus was that overall, the traditional forecasting methods (like ARIMA or exponential smoothing) are more accurate. Despite its successes in other fields, such as image classification and speech recognition, machine learning was still inferior to statistical methods employed for forecasting since several years. This fact also manifested itself in the results of subsequent *M* competitions. Machine learning was better than traditional methods only in several specific use cases. However, the surge of interest in applying machine learning and deep learning to time series, caused by the potential benefits of using these methods rather than traditional ones, has caused a breakthrough in the field of time series forecasting. A large amount of research conducted in this field, coupled with technological advances (e.g. use of GPU - Graphics Processing Unit - for parallelization), has led to the development of more complex algorithms, that began surpassing the traditional methods.

First signals of the aforementioned phenomenon were visible in the results of the *M4* competition. The winner of this competition was a hybrid approach, linking traditional exponential smoothing method with a Recurrent Neural Network (RNN) model. Other hybrid approaches combining traditional methods with ML were also ranked high in the competition. However, methods using a pure-ML approach performed worse than traditional in this competition, which was contradictory to the results of other studies claiming superiority of ML algorithms over traditional methods for time series forecasting. Moreover, simple traditional approaches were shown to be as accurate as sophisticated ML algorithms [136].

The latest *M5* competition was the first competition where all of the highest-performing methods were based on machine learning algorithms. Contrary to the previous *M4* competition, pure-ML methods were this time better than traditional approaches. Both machine learning (LightGBM) and deep learning (N-BEATS, Neural Networks) were applied by the best-performing competitors [135]. Ongoing research on using machine learning and deep learning architectures for time series forecasting should support the conclusion that machine learning can outperform traditional forecasting methods. Among the factors leading to this situation are data availability, complex algorithms able to learn convoluted temporal patterns, sophisticated preprocessing approaches, and increasing computational power.

4.4 Recent applications of Machine Learning in mining subsidence and InSAR studies

Machine learning and deep learning have applications in various fields, as has already been mentioned. This is no different for SAR interferometry research, where there is active work on processing InSAR results using machine learning algorithms and neural networks. The vast and growing amount of remote sensing data acquired by satellite systems is indicated as the basis for research in this area. Such an amount of data is not possible to process manually by a human user, so work should be undertaken to develop automated algorithms that process the data, extract information and support decision-making based on the results obtained. Since research connecting machine learning and InSAR is a vast area and contains a number of different particular applications, this section will only tackle selected works, focusing particularly on application of machine learning and InSAR for (mostly) mining-induced displacement forecasting. Selected applications of deep learning in InSAR studies will also be mentioned.

4.4.1 Displacement forecasting

The first work about applying machine learning methods in studying the influence of mining was conducted in 1999, and included examining the occurrence of mining-induced tremors and creating a prediction model using Artificial Neural Networks (ANNs) [186]. In 2003 [4], a first approach at mining subsidence prediction was proposed, applying subsidence measurement data as input for a simple neural network. Since then, a number of researchers across the world studied the mining subsidence phenomenon using machine learning and deep learning algorithms. For example, in [122] work was conducted on predicting mining subsidence with a Support Vector Machine-based regression model trained on time series displacement data. A similar approach was proposed in [27] and [198], this time applying Support Vector Regression to subsidence data derived using the DInSAR technique. A neural network approach with Genetic Algorithm for parameter estimation was proposed in [123], applied for mining subsidence prediction in China. A number of research papers were also published tackling the issue of assessment of areas prone to subsidence and analysing potential risk factors. Ground subsidence susceptibility was studied with Artificial Neural Networks [102, 117, 167, 233], as well as with other machine learning approaches, e.g. Random Forest Regression [179].

Studies on landslide displacement prediction were carried out applying machine learning methods in time series forecasting approach, using LSTM neural networks [142, 143, 232] and other machine learning techniques. [134] provides a thorough review of applications of machine learning in landslide prediction task. Other cases of displacement prediction using machine learning involve dam displacements [238], urban development [120], airport runway displacement [133], and groundwater withdrawal [120].

Most recent works on ground displacement prediction include more modern methods of time series forecasting, such as Recurrent Neural Networks or Encoder-Decoder architectures, together with statistical approaches. [84] applied traditional ARIMA methods together with modern neural network (e.g. LSTM) models to predict slow (in the order of a few millimeters) deformation. Traditional methods proved to yield better forecasting results than neural network models, especially for highly seasonal data. [111] proposed using PSInSAR measurements of mining

subsidence together with a LSTM model to forecast the displacement. Another approach was presented by [119], where LSTM model was supported by Geographic Weighting, to consider both temporal nonlinearities in time series data and spatial variations of land subsidence in the studied area. PSInSAR results on displacements caused by water extraction were used as an input dataset. [178] used the SBInSAR measurement technique for subsidence estimation in the vicinity of a lake in Iran, to predict displacement using time series forecasting with 3 neural network models: Multilayer Perceptron (MLP), Convolutional Neural Network (CNN) and LSTM model. An ensemble model was also proposed, and proved to have the highest accuracy on the time series forecasting problem.

4.4.2 InSAR applications

Although InSAR methods are most often used to perform local analyses (using a single satellite frame), a notion of studying natural and anthropogenic phenomena on a global scale is also popular, taking advantage of global coverage with satellite SAR data. A substantial amount of data is produced every day for the whole globe, while further analysis and post-processing of these data may prove to be a tedious task for a human observator when it comes to working on a larger scale. **Continuous monitoring of vast areas around the globe requires automation of processing and decision making, a task that is feasible for machine learning and deep learning algorithms.** Their ability to process large amounts of data, as well as capability of finding complex non-linear associations in data, is indicated as the main rationale for research into the application of these methods to InSAR data.

A deep learning algorithm based on convolutional layers was proposed to detect deformation caused by mining and tunneling on a national scale (United Kingdom) [5]. A similar approach was used in [19] for detecting deformations caused by volcanic activity, as well as in [67] for simultaneous detection and classification of volcanic deformation in SAR interferograms. Another example of using deep learning to detect mining subsidence was proposed in [226], utilising a neural network in phase unwrapping as well. A number of works on InSAR phase unwrapping using deep learning were published [195, 243].

Deep neural networks were applied in detecting subtle ground deformations caused by seismic activity [21, 185]. Atmospheric phase filtering is also an active research topic among InSAR community, and a number of deep learning approaches were studied for this problem [33, 241]. Neural networks were proposed for interferometric phase filtering and coherence estimation [157], as well as finding similar temporal patterns in InSAR time series with unsupervised classification [6].

Some authors indicated that the InSAR data (interferogram images) available may still not be sufficient for properly training the deep neural network (sinde a CNN requires thousands of images, which are impossible to acquire for a single study area), thus they proposed to use synthetic generated InSAR datasets for training [5, 6, 67, 185].

Chapter summary

The chapter introduced theoretical information about machine learning, deep learning and their application in time series forecasting. The following sections de-

scribed the basic classification of machine learning algorithms, and presented how ML algorithms and neural networks extract information from data. Selected neural network architectures were presented, highlighting those suitable for processing time series sequences. The current state of the art in time series forecasting was then presented, along with applications of ML models and neural networks. Finally, selected studies applying machine learning to subsidence prediction and combining the use of machine learning with SAR interferometry were outlined.

In this chapter, the application of machine learning in time series forecasting is considered, incorporating the results of InSAR displacement measurements. Time series forecasting using machine learning algorithms is becoming an increasingly widely used approach due to the development of these methods and their growing advantage over traditional statistical methods. In the field of ground surface displacement forecasting, research has also been conducted, but a lack of application of machine learning algorithms with data from InSAR methods for mining displacement forecasting has been identified. The combination of these two approaches can provide a tool for remote monitoring of mining areas and making predictions about subsidence in the near future.

A method of applying machine learning models trained on time series ground displacement data will be studied in this thesis. The copper ore mine area in southwest Poland has been selected for the studies, since the influence of underground mining is evident in the area in form of subsidence troughs. The study area will be described in the next Chapter.

Chapter 5

Study area

The area selected for this study is the Legnica-Głogów Copper Belt (LGCB) area in south-west Poland. The LGCB area is a part of a geological structure called the Fore-Sudetic Monocline. The LGCB area is an industrial complex comprised of 5 counties in the Lower Silesia Voivodeship. The selection of LGCB for the studies conducted in this dissertation was prompted by the nature of the mining operations in this area. Underground copper ore mining in the area leads to subsidence of an extensive nature due to the significant depth of mining. The mining system used in the LGCB area leads to slow subsidence, meaning that the InSAR technique achieves high efficiency for this area (there are no problems associated with a high spatial gradient of displacement). Moreover, mining works conducted in this region lead to increased local seismic activity, a factor that further intensifies the subsidence phenomenon. This chapter will provide a description of the study area, with emphasis on underground mining operations and their influence on the ground surface.

5.1 Geological conditions

The copper ore deposits extracted in the LGCB area are located in the marginal zone of the structure known as the Fore-Sudetic Monocline. In the area where the copper ore deposit is located, the monocline is made of Permian and Triassic sedimentary rocks, inclined at an angle of several degrees (not more than 10 in most parts) towards the north-east. The Permian and Triassic formations are covered by Tertiary and Quaternary sediments. The documented deposits of the Fore-Sudetic Monocline are classified as sediment-hosted copper ore deposits. The deposit copper-bearing rocks belong to the white and white-grey sandstones of the Rotliegendes and Zechstein and the copper-bearing shales and carbonate rocks (mainly dolomites) of the Zechstein. The deposit lies at a depth of approximately 350 to 1,400 metres [172]. The geological structure of the area is presented in Figure 5.1. The study area is also located in the vicinity of several tectonic faults, which further complicate the conditions of copper ore extraction.

5.2 Copper ore mining in LGCB

The history of copper ore mining in the LGCB area began in 1957, when a team of geologists led by Professor Jan Wyżykowski published research confirming the discovery of copper ore deposits lying between Legnica and Glogow at considerable

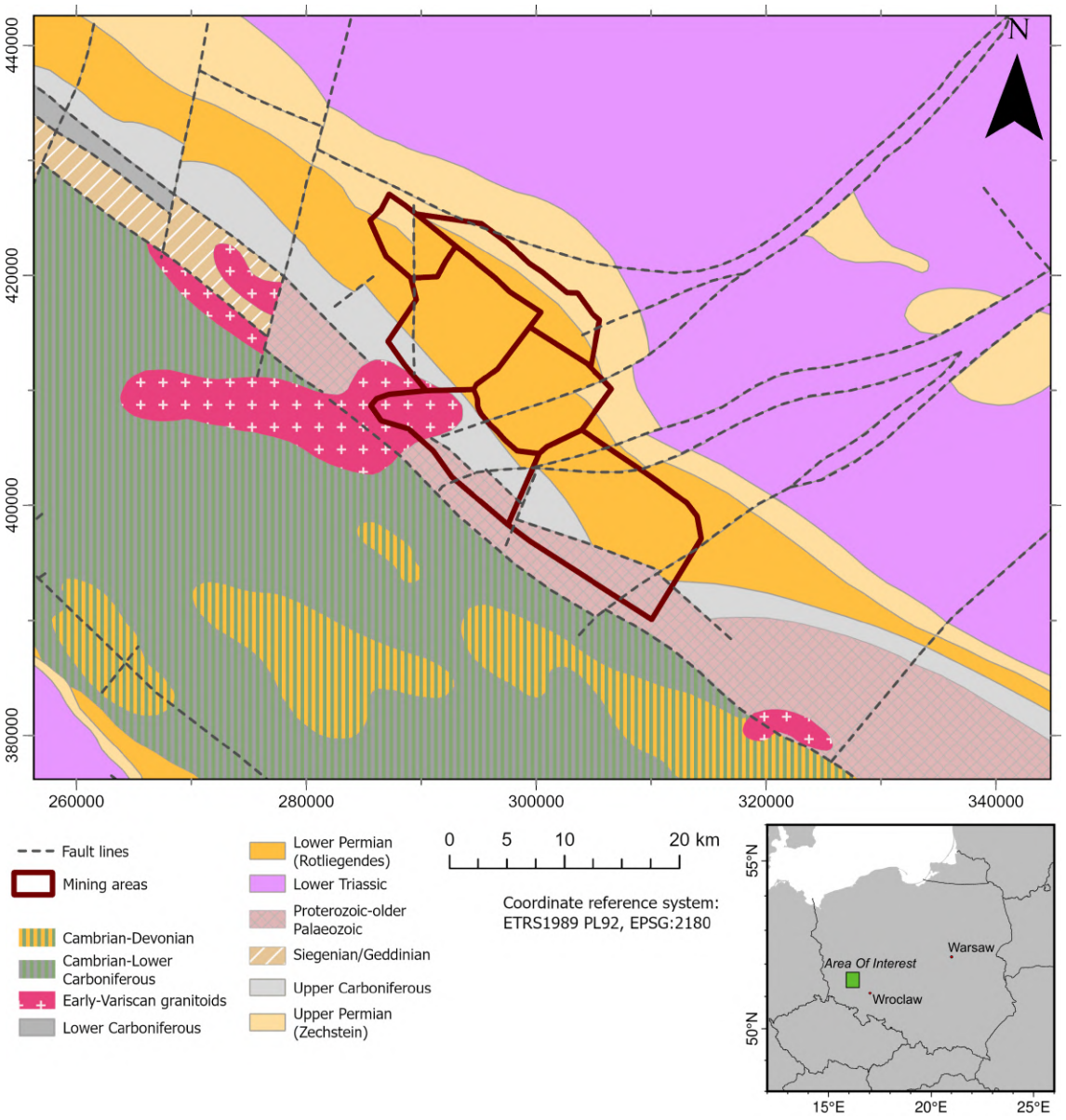

Figure 5.1: Geological conditions within the study area, with locations of tectonic faults highlighted. Source: Polish Geological Institute - National Research Institute

depths [227]. To date, there has been no large-scale copper mining in Poland, except for smaller mines located in Boleslawiec and Zlotoryja (southwestern Poland), Miedziana Gora and Miedzianka (south-central Poland). The discovery of copper-bearing shale deposits in the area of Legnica, Lubin and Głogów led to the establishment of a mining industry in the area in 1968, consisting of mines, processing plants and copper smelters, combined into a company called *Kombinat Górniczo-Hutniczy Miedzi (KGHM)*. Thanks to the extraction of copper ores in the LGCB area, Poland is the one of largest copper producers in Europe.

The LGCB site consists of seven mining areas (*Lubin-Małomice*, *Polkowice*, *Rudna*, *Sieroszowice*, *Radwanice Wschodnie*, *Głogów Głęboki-Przemysłowy*, *Gaworzyce*), covering a total area of approximately 491,737 square kilometres. Figure 5.2 depicts all mining areas of the LGCB, superimposed on an orthofoto background.
Copper ore reserves are estimated at 1552 million tonnes (as at 31.12.2021) [201], with current plans to continue mining until 2060, with the prospect of extending

this period if new mining fields are opened (exploration works are being carried out in further areas).

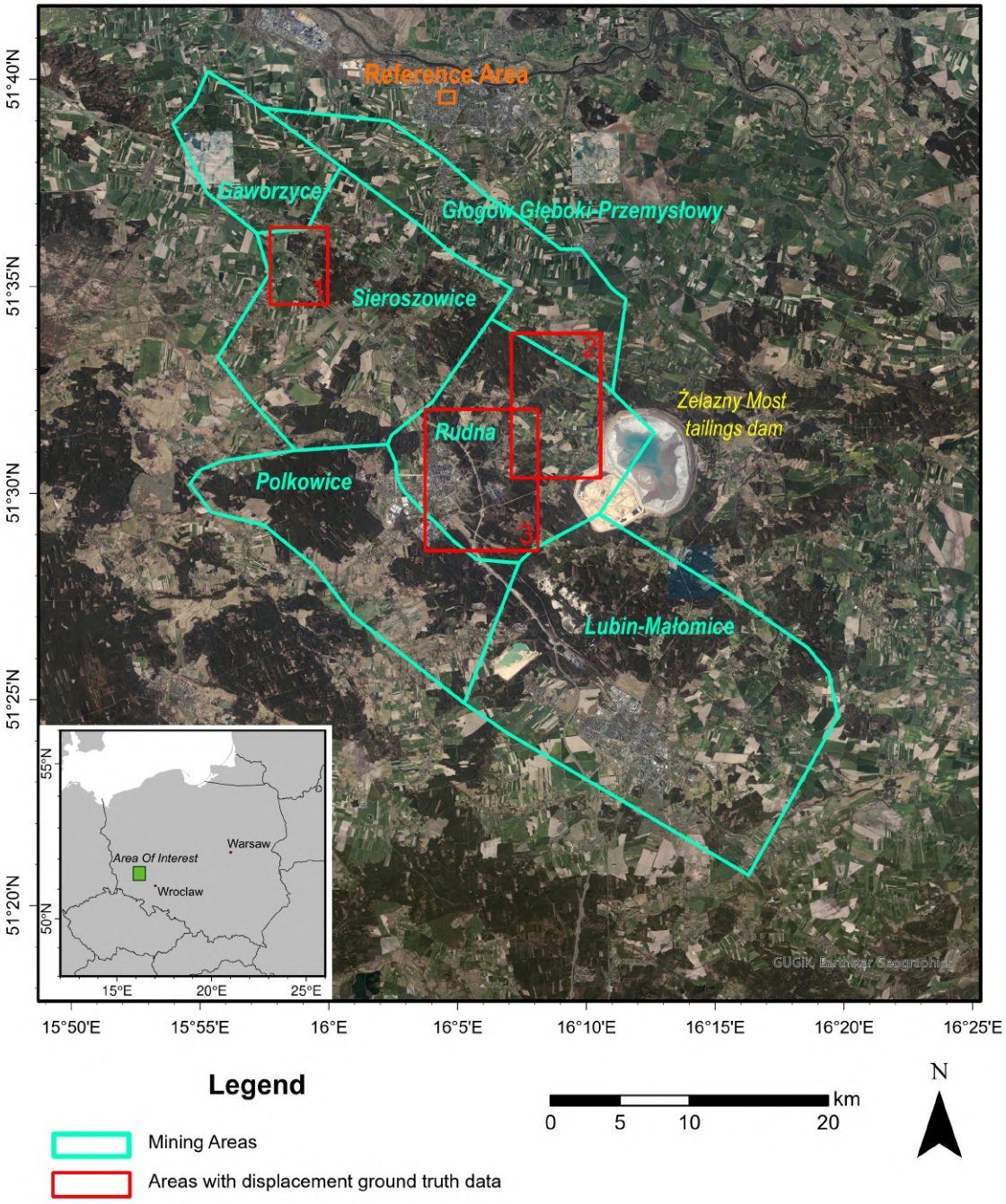

Figure 5.2: Locations of mining areas of the Legnica-Głogów Cooper Belt region, with selected subareas highlighted in red, for which leveling data were obtained. A reference area for InSAR measurements is highlighted in orange

Copper ore deposits in the LGCB region vary in thickness, ranging from 0.4 metres to 26 metres. Deposits with thicknesses between 2-4 metres predominate, but deposits with greater thicknesses also occur regularly, mainly in the Rudna mining area. The deposit is slightly sloping in a north-eastern direction, the slope, however, does not exceed a few to a dozen degrees. Copper ore deposits are mined with

chamber-pillar systems, with roof collapse for deposit thicknesses of up to about 5 meters, and with hydraulic backfilling for parts of deposits with thicknesses above 5 meters. The depth of the exploited deposit varies for mining areas within the LGCB, and ranges from 800 to 1,250 metres, and even 1,350 metres in the Głogów Głęboki-Przemysłowy area [172].

5.3 Selected aspects of the environmental impact of copper ore mining in the LGCB area

5.3.1 Storage of flotation tailings

The low content (around 1.5%) of copper in the mined ore necessitates the need to enrich it so that the concentrate can be further processed in the smelter furnace. The process of enriching copper ore leads to the generation of significant amounts of tailings. Their disposal represents a significant undertaking. Since the start of mining operations at the LGCB, tailings have been stored in tailings dams. Initially, the *Gilów tailings dam* was used (until 1980), and from 1977 until now the waste has been stored in the ***Żelazny Most tailings dam***. The location of the Żelazny Most tailings dam has been indicated on Figure 5.2. The Żelazny Most storage facility has been expanded in 2021, adding approximately 6 square kilometers to already present 14.5 km^2, totalling up to 20.5 square kilometers of storage basin. The mining authority is also working on the use of tailings waste for hydraulic backfilling of mine workings [172].
The stability of tailings dams is a key issue in ensuring the safety of the areas adjacent to them. In order to prevent a geotechnical failure and a leading disaster, the structure needs to be constantly monitored. Monitoring techniques include geodetic measurements (leveling and GPS), seismic measurements, piezometry and inclinometry [172]. Recently, satellite interferometry (InSAR) measurements have also been conducted on the area to derive vertical and horizontal displacement values of the dam [140].

5.3.2 Mining-induced seismicity

The LGCB area is characterised by a high risk of mining tremors. Among the geological factors responsible for this state are the ability to accumulate and rapidly discharge elastic energy through the thick carbonate rocks overlying the deposits, the depth of the deposit, and the presence of tectonic structures (faults) in the area of the deposit. The high intensity of mining operations, the high surface area of the exploited deposit, the lengths of the mining fronts and the mining system used are indicated as mining factors [172].
Due to mining tremors of up to 4.8-4.9 M_W occurring in the LGCB area, this region is considered to be the most seismically active in Poland. Three major areas of spatial concentration of seismic events can be distinguished in Poland: the Upper Silesia Coal Basin (where hard coal mining also leads to seismic hazards), the *Old Copper Basin* (the surroundings of copper ore mines near Bolesławiec and Złotoryja), and the LGCB region. The LGCB region clearly predominates in terms of number of seismic tremors. In order to study seismicity, seismic measurement stations have been deployed in the LGCB area, measuring quantities such as energy and the approximate location of the epicentre. The phenomenon of the effect of

mining tremors on the ground surface was also investigated, indicating ground subsidence acceleration after high-energy tremors (above $1*10^7$ J) [7, 137, 145]. The seismic events recorded in the study area between 2013 and 2021 using the IS-EPOS (Induced Seismicity - European Plate Observing System) monitoring system [118] are highlighted in Figure 5.3. As observed, the majority of seismic events detected in the study area were located in the Rudna mining area, as well as in neighbouring areas.

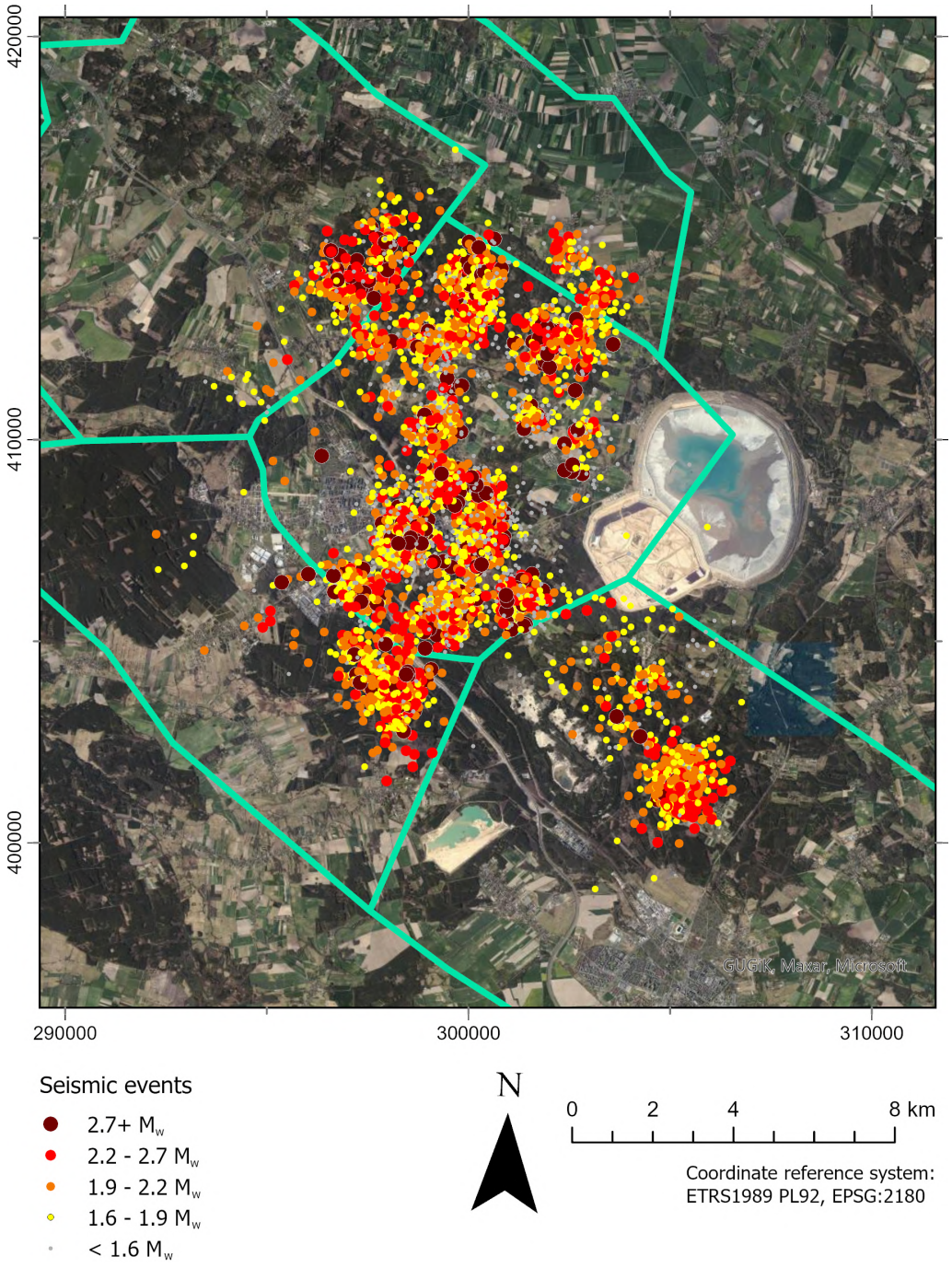

Figure 5.3: Seismic event locations in the study area, observed between 2013 and 2021 using the IS-EPOS monitoring stations [118]

5.3.3 Ground surface displacements

The estimated area affected by underground copper ore mining in the LGCB area is approximately 536.5 square kilometers. Mining at considerable depths leads to subsidence over extensive areas. The filling of post-mining voids by the rock mass leads to adverse impacts on the surface, which include **direct influences** - continuous deformation of the land surface (subsidence troughs), and **secondary influences** - including mining tremors, large-scale water drainage troughs, local floodings and droughts, hydrological changes and the resulting degradation of agricultural and forest areas, and threats to the stability of structures. Out of the direct influences, only continuous deformation should be considered in the LGCB area (discontinuous deformations do not occur) [172].
Surface displacement in the LGCB leads to mining damages, including building stability losses owing to ground subsidence, soil and vegetation changes due to hydrological changes, local flooding, and damage to buildings and technical infrastructure due to high-energy seismic tremors. In order to prevent damage and minimise material losses, mining is carried out with the situation on the surface taken into consideration - away from built-up areas and including protective pillars below critical areas (e.g. road infrastructure, tailings dams). Regular measurements of land surface displacement and deformation are carried out in the LGCB area using surveying methods. Displacement measurement networks include a GPS station network, a precision levelling network, geometric levelling networks and a network to monitor stability of tailings dams.
Subsidence troughs of varying sizes and shapes have been located across the LGCB area. Their locations coincide with the location of mined copper ore seams. Vertical displacements within the troughs, recorded by means of geodetic surveys, range from 1.75 metres to 3.25 metres. Subsidence recorded by geodetic methods includes direct subsidence caused by material extraction, and secondary subsidence induced by groundwater withdrawal. Surveys to date estimate the existence of a large-scale drainage basin, within which surface subsidence reaches 0.8 metres [172].
Predictions of ground surface displacements are being conducted in the area using the Budryk-Knothe theory, modified for the mining and geological conditions present at the LGCB area. In addition to traditional surveying methods, the InSAR satellite radar interferometry technique is used to measure displacements in the LGCB area. Measurements by this method provide a source of ground surface displacement information independent of geodetic measurements, with high temporal resolution and covering the entire LGCB area [7, 82, 94, 110, 137, 140, 145, 148, 149, 166, 222]. It should be noted that studies often overlook the fact that horizontal displacements occur in the area, leading to erroneous interpretations of the displacement values if Line-of-Sight measurements are considered. Also, a lack of ground truth verification of vertical displacement time series obtained by InSAR methods can be recognized.

Chapter Summary

An overview of the study area selected in this thesis has been provided in this chapter. Geological, mining, and tectonic conditions of the study area have been discussed. The study area is characterised by a high coverage of urbanised and agricultural areas, making it suitable for ground surface displacement measurements by InSAR methods. The methodology for determining the time series of vertical displacements in the study area will be provided in the next Chapter.

Chapter 6

Determination of surface displacements using InSAR

The subject of this dissertation research is land surface displacement monitoring and prediction in mining areas. Given the ability of InSAR methods to measure displacements over wide areas using imagery acquired remotely by satellites, the amount of data obtained by this measurement system far exceeds the amount that other methods, such as leveling or GPS, are capable of acquiring. Due to the fact that machine learning (and especially deep learning) methods can require vast amounts of data in order to successfully learn patterns present in input data, InSAR was selected as the source of information on ground surface displacements for further analysis with time series forecasting methods.

This chapter will focus on describing data and methods used for InSAR analyses throughout the dissertation. Workflows on acquiring time series displacement data using InSAR methods, starting with data acquisition, and ending with obtaining a final product, will be extensively described. SAR interferometry is a remote measurement technique, thus emphasis must be put on its limitations and drawbacks, that need to be taken into account when this method is put into production, e.g. by mining authorities to monitor subsidence induced by raw material extraction. Opportunities and limitations accompanying the application of InSAR to mining displacement monitoring will be described together with the methodology throughout this chapter, starting with Differential Interferometry (DInSAR), going further into time series analysis with Persistent Scatterer (PSInSAR) and Small Baseline (SBInSAR) methods, and finishing with projecting the Line-of-Sight (LOS) measurements to obtain vertical displacements.

6.1 Data sources

6.1.1 SAR imagery

Building a time series of displacements using InSAR techniques requires large amounts of SAR data. In order to successfully derive displacement time series using PS or SB approaches, a minimum of 25-30 SAR images are needed. Sentinel-1 SAR imagery was selected for the estimation of displacement time series in this dissertation, mainly because Sentinel-1 is a part of ESA Copernicus programme, which provides users with Earth Observation data free of charge, and also because Sentinel-1 satellites provide constant data stream with at least 12-day intervals since the Sentinel-1A was put into orbit in November 2014, with the exception of Sentinel-

1B temporary malfunction at the end of 2021[1].

Sentinel-1 SAR data available for download are provided in several formats, the most popular 3 being RAW (raw acquisition of SAR data, L0 product), GRD (Ground Range Detected, L1 product, applied commonly in Earth Observation, e.g. for flooded areas detection), and SLC (Single Look Complex, L1 product, raw data processed to the form of amplitude/phase complex files, ready for interferometric processing). The SLC format was chosen for conducting the InSAR analyses. Data acquired by the Sentinel-1 satellite were acquired using the Terrain Observation with Progressive Scans (TOPS) SAR Interferometric Wide (IW) swath mode. The Interferometric Wide swath mode allows the SAR device to simultaneously image a 250 kilometer-wide swath of Earth's surface. In TOPS SAR mode, the 250 km swath is divided into 3 sub-swaths in the range direction, and each sub-swath is divided into 9 bursts in the azimuth direction.

A single SLC format image, consisting of 3 sub-swaths, is stored in a *.zip format, approximately 4.7 gigabytes in size, ready to download. Data can be downloaded using a number of services, e.g. the Copernicus Open Access Hub (SciHub), or the Alaska Satellite Facility (ASF) Vertex Portal. The ASF portal was selected as the download source of Sentinel-1 data for the purpose of this thesis, since it provides an API that enables bulk download of satellite imagery data using Python programming language.

Table 6.1: Basic information on SAR data acquired for the study

Property	**Dataset 1**	**Dataset 2**
Sensor	Sentinel-1A/B	Sentinel-1A/B
File format	SLC	SLC
Flight direction	ascending	descending
Orbit number	73	22
Frames	162, 163, 164, 165, 166, 167	419, 420, 421, 422
Beam mode	IW	IW
Polarization	VV	VV
Start time	May 20, 2016	May 17, 2016
End time	Oct 26, 2020	Oct 23, 2020
No. of acquisitions (images)	277	255
No. of consecutive time periods (epochs)	257	255

Tab. 6.1 lists information on the acquired SAR datasets. Data were downloaded from both ascending and descending satellite orbits. Sentinel-1A/B data were acquired in IW mode, using vertical sent - vertical received (VV) polarisation for both orbit paths. Not all acquisitions covered the study area entirely, thus images from consecutive frames needed to be stitched together for further InSAR analysis (mainly in the case of ascending data). The downloaded data spanned the period between May 17, 2016 and October 26, 2020, amounting to 277 acquisitions from the ascending path, and 255 acquisitions from the descending path. After stitching image pairs acquired on the same day, a total of 257 and 255 time periods were

[1]On December 23rd, 2021, the Sentinel-1B satellite's power system unit malfunctioned, causing the satellite to halt image acquisition.

obtained for the ascending and descending orbit paths, respectively. Although both datasets covered the same amount of days, some epochs were missing in both flight directions, possibly due to satellite being offline while flying over the study area, hence the different number of time periods. A detailed list of all Sentinel-1 acquisitions is provided in Appendix A for the ascending orbit and Appendix B for the descending orbit.

6.1.2 Sentinel-1 orbital data

For accurate determination of surface displacement using SAR interferometry, precise orbit ephemerides of SAR satellites have to be considered. This ensures high accuracy of image coregistration, as well as minimizes errors due to differences in the satellite's position during consecutive image acquisitions (geometric phase error).

For Sentinel-1, orbit files are maintained and distributed by European Space Agency in form of *restituted* orbits available shortly after SAR image acquisition and *precise* orbits updated approximately 20 days after acquisition. For Sentinel-1 data used in this thesis, precise orbit files were downloaded for all SAR images to ensure higher accuracy of results.

6.1.3 Digital Elevation Model

The process of substracting the topographic phase from a SAR interferogram, creating a differential interferogram (displacement phase without the influence of topography), requires a Digital Elevation Model (DEM) to be used for simulating the topographic phase. A number of global, open-source DEMs are commonly used for topographic phase removal during InSAR processing, e.g. ASTER, SRTM, Copernicus DEM or WorldDEM.

The Shuttle Radar Topographic Mission (SRTM) 1-arc second DEM [55] was used as a Digital Elevation Model throughout processing of SAR data in this thesis.

6.2 Differential Interferometry

First method described within this chapter will be the foundation for further analyses using time series InSAR techniques - Differential Interferometry (DInSAR). It is used to create interferograms, which are further required by time series methods to correctly estimate the displacement time series. Depending on the time series processing method, SAR images can be matched into pairs (further described in a later section on time series processing), resulting in a stack of interferograms, then utilised by a time series InSAR algorithm. The process of creating a single differential interferogram consists of a number of steps, some of which are optional, depending on the final product needed for further analysis. The workflow of the differential interferometry process is presented in Figure 6.1.

Although InSAR methods are utilised in this thesis to derive a time series of displacements using a stack of SAR images, this section will be describing a process of forming a single interferogram, and thus only two SAR images are assumed to be of interest.

6.2.1 SLC co-registration

The downloaded SLC files for a pair of SAR images need to be co-registered in order to calculate an interferogram. In the case of Sentinel-1, sub-pixel accuracy of

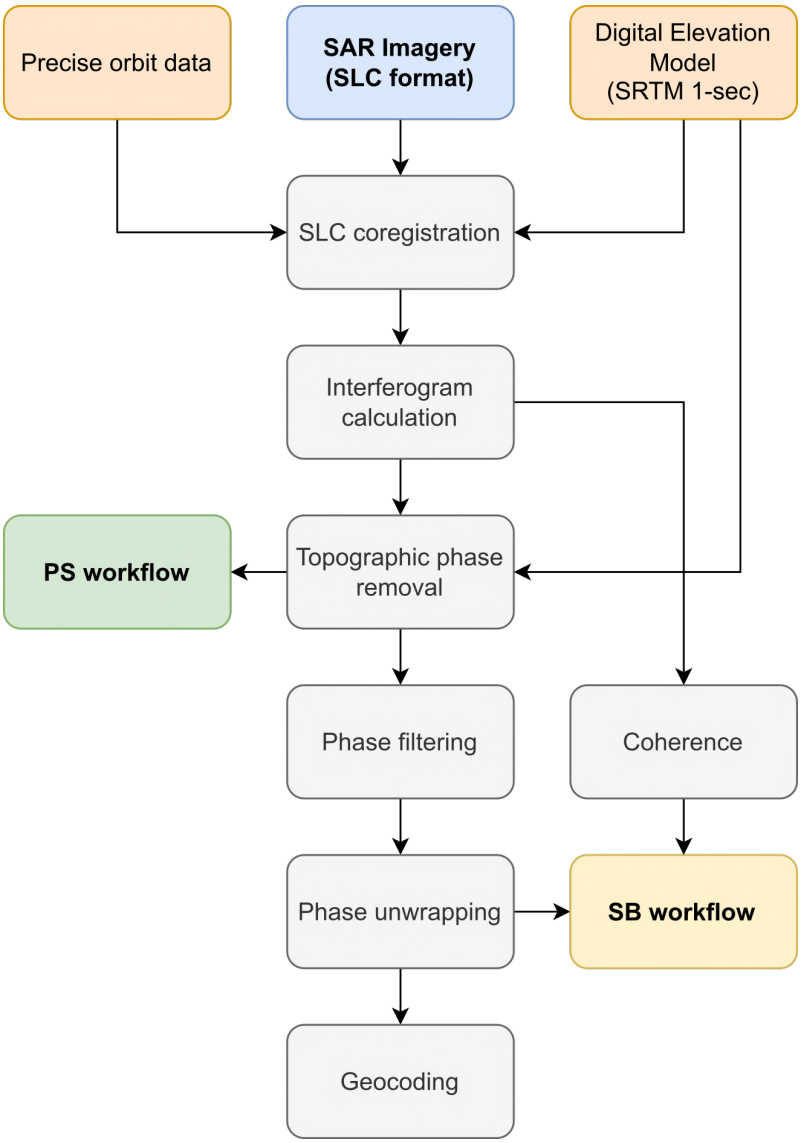

Figure 6.1: Schematic workflow of the interferometric processing

co-registration is required to avoid phase misalignments between consecutive bursts. *Traditional* image alignment technique (rough estimate of offsets between reference and secondary images based on orbits, then refined using 2-D cross-correlation of fragments of images) used for images acquired in e.g. ScanSAR mode, is insufficient in the case of Sentinel-1 and often results in phase shifts present on burst boundaries. For that matter, a geometric alignment algorithm applied in numerous modern InSAR processing software packages was applied for co-registering Sentinel-1 SAR data. Below is a brief description of the co-registration process of Sentinel-1 data.

In this approach, two SAR images are aligned geometrically based on precise orbital data, and the SLC bursts are deramped before interpolation using the Enhanced Spectral Diversity (ESD) approach. The deramping process of bursts aims at reducing the difference between the Doppler rate at the upper and lower edges of bursts, thus reducing potential phase mismatches at boundaries between bursts. Geometric alignment is performed by first constructing a low-resolution Digital Elevation Model covering the extent of SLC images. Then, using the DEM and precise

orbital data, a mapping of each pixel of longitude, latitude and height into range and azimuth coordinates of the SAR system is performed for both reference and secondary images. Using these look-up tables, differences in range and azimuth can be calculated as regular offset grids in range/azimuth coordinates. Using these grids, a mapping of the secondary image to the reference image is provided and the geometric alignment is completed.

The next part involves deramping of consecutive bursts in the secondary image. First, the reference SLC image is *deburst* to create a continuous image, using times of acquisition of consecutive bursts and aligning their boundaries. Then, a complex phase ramp is computed in accordance to [151], for each of the consecutive bursts. Each burst SLC is multiplied by the complex conjugate of the phase ramp, effectively de-ramping the SLC. The de-ramped burst SLC is then resampled to the reference SLC using range and azimuth shifts calculated during the geometric alignment. After resampling, the complex phase ramp is re-calculated and again multiplied by the resampled burst SLC of secondary image. This results in de-ramped bursts of the secondary SAR image, aligned to the reference image with high accuracy allowing phase estimation without mismatches between consecutive burst boundaries.

6.2.2 Differential interferogram calculation

The interferogram image (phase difference between reference and secondary acquisitions) is calculated as a complex conjugate of the reference and secondary phase images. The differential interferogram is created as a difference between the total phase calculated using 2 SAR acquisitions, and the phase component induced by terrain topography. In order to calculate this component, a Digital Elevation Model is utilised to create a *simulated* topographic phase image. The simulated phase is then subtracted from the actual interferogram, resulting in a **differential interferogram**.

Topographic phase contribution is calculated using an external DEM and precise orbit information. From these data, the radius of the satellite's orbit, the length of baseline (distance between satellites during consecutive acquisitions) and baseline's orientation can be computed. Topographic information (DEM) is also interpolated to the range and azimuth coordinate system of the satellite, and the values of look angle are computed for each pixel. All of these variables are then used to calculate the topographic phase, which is subtracted from the interferogram.

6.2.3 Coherence calculation

Coherence is viewed as a measure of interferogram quality. The absolute value of coherence is between 0 and 1, where 0 means no coherence and 1 means that there is a fully coherent (stable) pixel. The higher the coherence, the better the Signal-to-Noise Ratio (SNR) that defines the quality of interferometric phase. Generally, for coherent pixels the interferometric phase is less noisy, thus e.g. urban areas or areas with bare rocks will be feasible for displacement studies with interferometric methods. Coherence γ is estimated using the equation:

$$\gamma = \frac{|E(u_1 u_2^*)|}{\sqrt{E(|u_1|^2)E(|u_2|^2)}}, \tag{6.1}$$

where E is the mean value within an assumed spatial window of complex pixels, u_1 and u_2 are complex reference and secondary SAR images, respectively, and * is a

conjugation operator.

Figure 6.2 depicts interferometric coherence for two differential interferograms calculated using Sentinel-1 data over the study area. Coherence images in radar coordinates present the estimated coherence during (August) and after (November) summer, where the vegetation cover is the most dense. A positive change of coherence values can be noticed when the vegetation cover is more scarce.

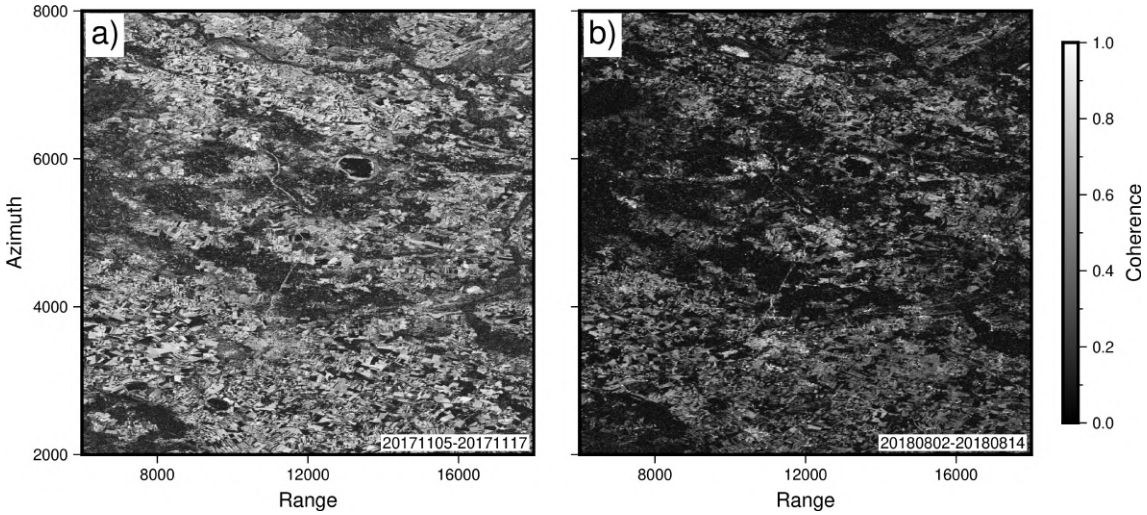

Figure 6.2: Coherence values obtained for interferograms calculated using SAR images: (a) November 5, 2017 - November 17, 2017; (b) August 2, 2018 - August 14, 2018. Images in local coordinates (range and azimuth) of the satellite

6.2.4 Phase unwrapping

Differential interferogram estimated in previous subsections contains *wrapped* interferometric phase - known only modulo-2π.

$$\Phi = \phi + n * 2\pi \tag{6.2}$$

For correct interpretation of interferometric phase in terms of estimating ground surface displacements, phase has to be *unwrapped*, i.e. the correct number of n full phase cycles need to be added to the phase measured using InSAR. In the case of continuous phase present in the interferogram, the unwrapping process is simplified to integrating the phase. However, most cases involve phase jumps induced by various phenomena, e.g. phase noise or large spatial gradient of deformation, and these are much more demanding when it comes to unwrapping. Phase unwrapping over discontinuities may yield *unwrapping errors*, resulting in incorrect estimation of ground displacement.

Differential interferograms created as part of measurements conducted in this thesis, were unwrapped using the SNAPHU algorithm [32]. This algorithm solves the phase ambiguity problem assuming that it is an optimisation problem, the objective of which is to find the most likely unwrapped phase solution given the observed wrapped phase. An approximate solution of this problem is achieved in SNAPHU with the use of network-flow approach, using shortest path and spanning trees algorithms to correctly estimate the unwrapped phase.

The problem of phase unwrapping is very significant in the case of applying InSAR for areas of underground mining. Two issues arise in this scenario. Firstly, high spatial gradient of deformation caused by rapid subsidence in mining area can cause

errors in phase unwrapping, therefore resulting in underestimating the actual displacement. Second, underground mining is often carried out below rural areas (e.g. agricultural or forested) to minimise damages to the infrastructure, which leads to loss of interferometric coherence and increase in noise which, in turn, again results in phase unwrapping errors. While overcoming the first factor is difficult and would need to involve applying a deformation model during phase unwrapping to correctly unwrap high gradient phase, the second factor (noise due to incoherence) can be partially avoided by means of multilooking and phase filtering.

6.2.5 Interferometric noise handling

A case when phase of an interferogram is smooth and not distorted is very rare. In majority of cases, a noise term is visible on the phase image in the form of 'granulation' or 'white noise'. As was explained before, a number of factors can influence the radar signal while imaging the Earth's surface, e.g. atmospheric disturbances, thermal noise, geometric decorrelation (due to different incidence angles of consecutive pixels), temporal decorrelation (changes of surface cover between acquisitions) or volume decorrelation (scattering of signal while traveling through volumetric objects, e.g. trees). All of those factors affect the radar signal in a different magnitude, totaling up to a noise term visible on the interferometric phase image. Noise can notably alter the result of interferometric processing, often making it completely impossible to interpret the interferometric phase if the noise is too dominant, or causing the interferometric phase to be unwrapped incorrectly due to phase jumps. During the processing of interferometric data, a number of ways of mitigating the noise term can be included to enhance the final results.

The first process, called **multi-looking**, is a way of noise reduction in SAR interferogram by averaging adjacent pixels. For the cost of losing geometric resolution, the phase accuracy is significantly increased through noise reduction, especially when it comes to spatially uncorrelated noise (e.g. temporal, geometric, volume decorrelation) [60]. A common practice is to use rectangular filters for averaging, so that the dimensions of a multi-looked pixels are approximately equal. For example, in the case of Sentinel-1, pixels of 5 m in range and 20 m in azimuth can be averaged using a filter of 5x1 (5 in range, 1 in azimuth), resulting in approximately 25x20 m multi-looked pixel.

Multilooking is often insufficient as an only way of reducing interferometric noise and improve the Signal-to-Noise Ratio, another way is to filter an interferogram using one (or more) of commonly used image filtering methods. Two of the most commonly applied filtering methods in InSAR processing software are Goldstein filter and Gaussian filter. Goldstein filter uses a Fast Fourier Transform (FFT) to enhance the SNR of the image, by varying the characteristic of the filter on the power spectrum of the interferometric fringes [74]. Gaussian filter is an anisotropic filter, which strength varies depending on local fringe rates and local noise levels [210]. Both Goldstein and Gaussian filtering are used throughout the processing of interferograms throughout the thesis.

Figure 6.3 includes an example interferogram before and after applying a Gaussian filter. Significant noise reduction is evident after filtering, improving the interpretability of interferometric fringes, and allowing for an improved process of phase unwrapping. While filtering overall is usually applied during the InSAR processing chain, attention needs to be paid to the strength of the filter, since a strong filter

can introduce artifacts to the image and cause loss of information.

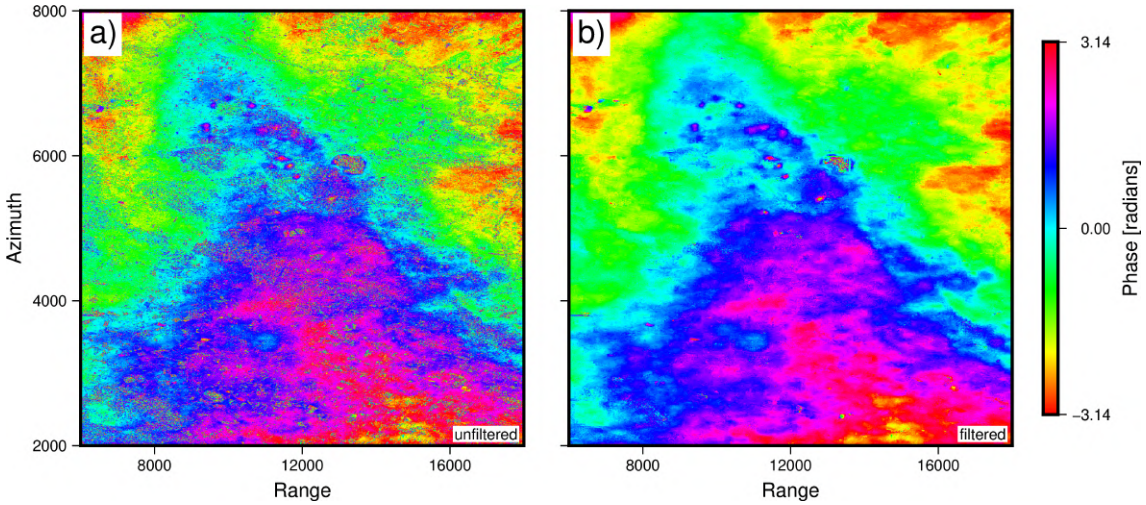

Figure 6.3: Sample interferogram (a) before and (b) after applying a Gaussian filter

6.2.6 Geocoding

The processes of image registration, interferogram formation, multilooking, filtering and unwrapping are all conducted on data in local reference frame of the radar acquisition, in range and azimuth coordinate system. In order for the processing results to have a spatial reference allowing further analyses, a **geocoding** process is performed. Geocoding is an operation of transforming the data from local range-azimuth coordinates to a geographic coordinate system with a reference ellipsoid. This can be achieved using a look-up table derived during the co-registration process. Pixels in range and azimuth coordinates are resampled to the geographical coordinates.

6.3 Time series analysis using the Persistent Scatterer and Small Baseline methods

The main source of information on deformations within the mining area studied in this thesis are InSAR methods that utilise a time series of interferograms, or Multi Temporal InSAR (MTInSAR) methods. The Persistent Scatterer (PS) method and Small Baseline (SB) method were both studied and used for displacement determination. Although both methods were designed with different applications in mind (the PS approach focuses on pixels with a single dominant scatterer, while the SB method is optimised for pixels with multiple distributed scatterers), both can be applied for studying displacements over mining areas. Results from both methods were achieved and compared with respect to applicability to mining deformation studied. This section provides a description of the theoretical and practical issues regarding these methods.

6.3.1 Persistent Scatterer InSAR workflow

Generally, the Persistent Scatterer (PS) approaches to InSAR processing focus on pixels within a SAR image that contain a singular, dominant scatterer. If a scatterer is dominant within a resolution cell, and therefore returns significantly more

energy than other scatterers, this resolution cell (pixel) is considered as a *persistent scatterer*. Decorrelation of such pixel, caused by factors described earlier (e.g. geometric and temporal decorrelation), is much lower, since the total decorrelation consists of contributions from all scatterers within a pixel (random variations of phase for all scatterers).

An overall workflow of the PS approach is presented in Figure 6.4. Subsequent sections will describe in more detail each step taken towards estimation of displacements within PS pixels of a time series of interferograms.

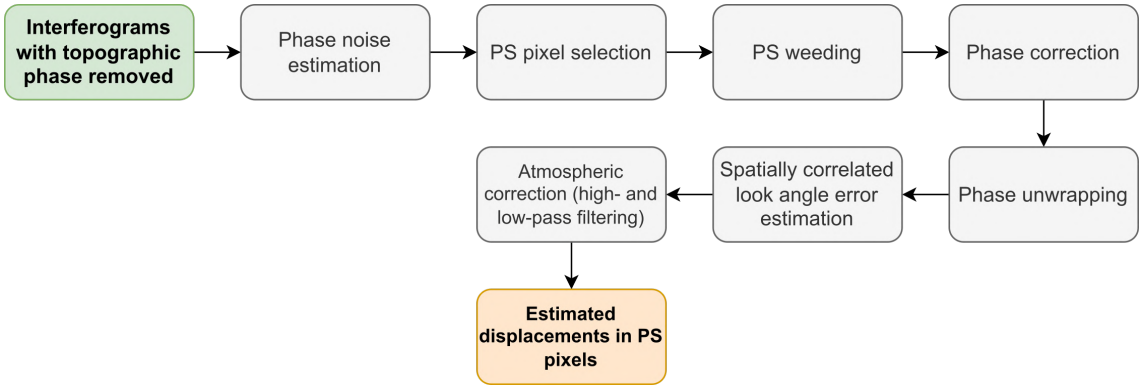

Figure 6.4: Workflow diagram of PS processing using the StaMPS approach

Interferogram formation

The PS algorithm uses a stack of interferograms, all created in relation to the *reference* image. The selection of the best reference image for a stack of SAR data is based on perpendicular and temporal baselines. A common practice is to select an image in the middle of the studied temporal period, and to minimise the average spatial baseline in time series of interferograms. This approach minimises both spatial and temporal baselines, reducing the decorrelation induced by geometric and temporal factors. Baseline plots for the PS method, for both ascending and descending Sentinel-1 data used in the study, are presented on Figure 6.5. Images in the middle, connected to all the other images, are the selected *reference* images.

Interferograms in the PS method are formed with accordance to the methodology described in the earlier section. It should be noted that no multi-looking or filtering were applied during the formation of interferograms, as these techniques average contributions of scatterers within a resolution cell, and thus reduce the influence of objects dominantly reflecting the signal. Interferograms are not unwrapped prior to PS pixel selection, as the unwrapping process is carried out in later stages of PS processing.

Selection of PS candidate pixels

The PS method selects pixels in SAR interferograms that have the lowest decorrelation and their phase information can be utilised to estimate displacement values over a studied area. There are various approaches to selection of PS pixels, but only the approach used for PS processing in this thesis will be described. Since at the start of the PS processing only raw interferograms are available, there are no initial candidates for PS pixels. These candidates are selected using the amplitude dispersion method (a relationship between the standard deviation of the difference

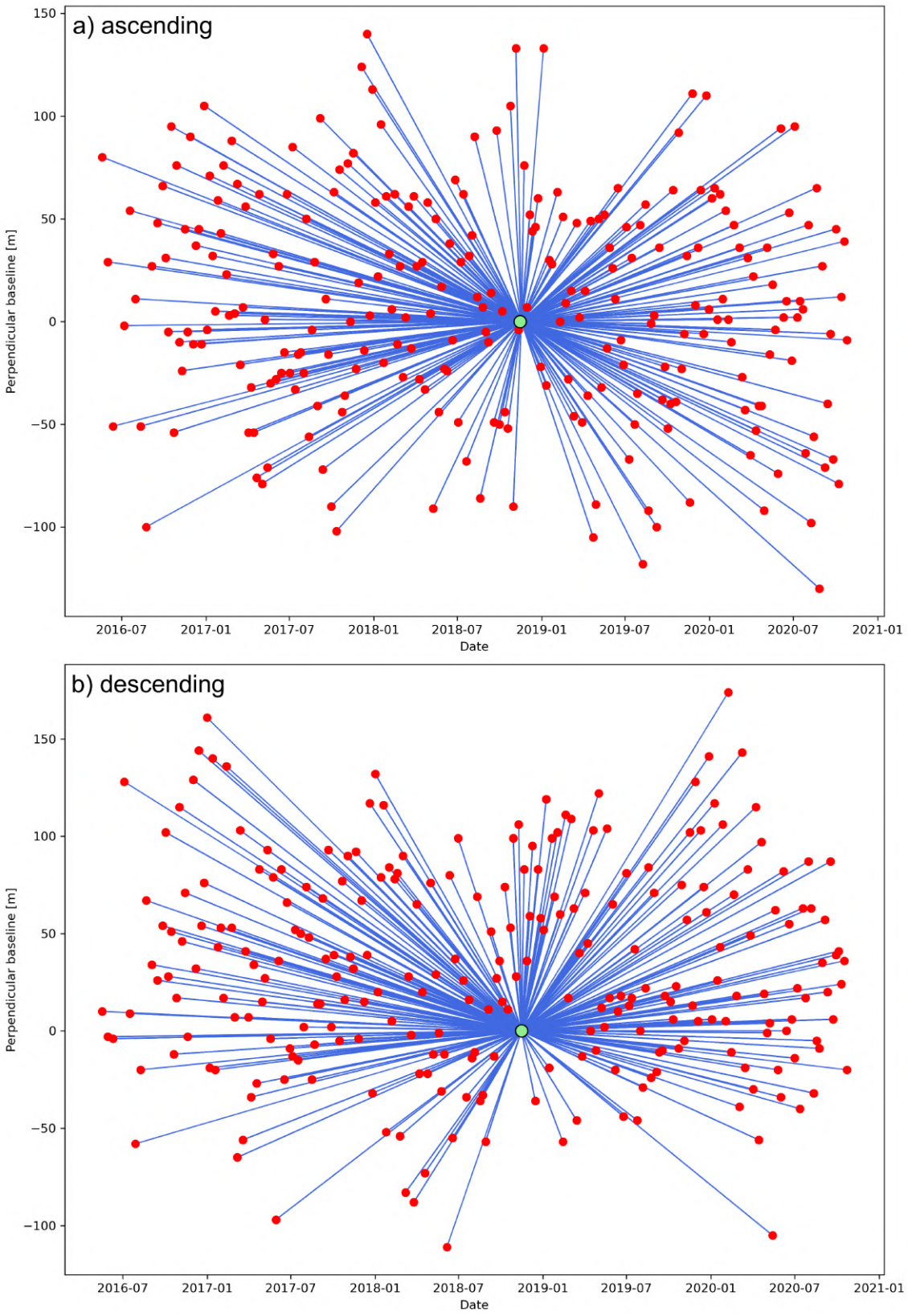

Figure 6.5: Baseline plots of interferograms created for the PSInSAR processing, using (a) ascending and (b) descending Sentinel-1 data. Green dots highlight reference images

in amplitude between reference and secondary acquisitions), applying a threshold of 0.4. Next, the set of initial PS candidate pixels is used to select only the pixels with low decorrelation characteristics, for which displacements can be accurately estimated. The approach used is based on a property of most of the phase terms (deformation, atmospheric delay, orbit error) - they are correlated spatially. This way, for each PS candidate, these spatially-correlated terms are found through spatial filtering. They are then subtracted from the total phase, and the remaining phase (assumed to be only the spatially-uncorrelated DEM error and phase noise) is modeled as a residual contribution to the phase due to error in the DEM. The difference between the modeled phase and the actual remaining phase is an estimate of noise for the pixel. Based on an assumed threshold, pixels that exhibit noise lower that the threshold, are selected as PS candidates for further processing [88].

Spatially-uncorrelated DEM error phase correction

The phase of the selected PS pixels is corrected for the spatially-uncorrelated DEM error (mostly due to error in the DEM used for topographic phase estimation, as well as from incorrect mapping of DEM to radar coordinates), estimated as a residual contribution in the previous step. The spatially-uncorrelated error due to the DEM is subtracted from the phase for all PS pixels.

Phase unwrapping

After the spatially-uncorrelated DEM error phase term has been estimated and subtracted, the remaining phase in the PS points is considered to be consisting of the displacement component, atmospheric component, orbit error component, spatially-correlated DEM error component and noise component. To properly estimate displacement values based on wrapped phase data for PS pixels, the approach is to first unwrap the phase, and then to subtract all spatially-correlated phase terms in order to obtain the displacement component (still subject to the noise component).

A 3-D (three-dimensional) unwrapping algorithm is applied to solve the integer number of full phase cycles in PS pixels, provided that the pixels are dense enough and the phase jumps between neighbouring pixels do not exceed π (to avoid unwrapping errors). Phase is unwrapped spatially (2-D), and then temporally (3-D) to find the correct solution to the phase unwrapping problem, while making no assumptions about the nature of the underlying displacement signal. Phase is filtered prior to unwrapping to reduce noise and aid the unwrapping process by reducing errors [88].

Removal of spatially-correlated phase terms

After the removal of spatially-uncorrelated phase term induced by the DEM error prior to phase unwrapping, the spatially-correlated part of unwrapped phase is now estimated and removed (mainly the spatially-correlated DEM error, but also spatially-correlated atmosphere and orbit errors). This estimation consists of high-pass filtering of the unwrapped phase in time and low-pass filtering in space. The estimated spatially-correlated error is the subtracted from the unwrapped phase. The remaining phase term is the sum of displacement phase and uncorrelated noise. In practice, the spatially-correlated error can influence the unwrapping procedure by introducing phase jumps and hinder the solution, thus the spatially-correlated

error can be subtracted from the phase prior to unwrapping and the unwrapping can be repeated.

It should be noted that the atmospheric phase term estimated through high- and low-pass filtering refers only to the part of atmospheric delay that is spatially-correlated, and does not take into account the phase delay caused by atmosphere that is not correlated spatially. This can further be estimated by using various techniques (e.g. weather models, GPS observations, spectrometer data, linear and power-law estimation) and subtracted from the unwrapped phase.

6.3.2 Small Baseline InSAR methodology

If a resolution cell in a stack of co-registered SAR images does not contain a single dominant scatterer, the decorrelation can be large enough to obstruct the deformation signal. In that case, the Persistent Scatterer methods will fail in detecting coherent, stable pixels. An alternative approach to processing time series InSAR data, the Small Baseline (SB) method [13] overcomes that limitation through a different technique of pairing together SAR images that form interferograms.

Creating a network of interferograms

Image pairs in the SB method are formed in a way that minimises the temporal and spatial baselines, creating a *network* of interferograms. A single SAR image can be paired with more than one another SAR image to form the interferogram, provided that the time interval between the two acquisitions, and their perpendicular baseline, are short enough (shorter by defined thresholds, e.g. 50 days and 150 meters). Minimisation of temporal and spatial baselines causes the decorrelation to reduce significantly, thus making the deformation signal detectable, despite lack of a dominant scatterer within a resolution cell.

Interferogram networks used in SB analysis for this thesis are presented in Figure 6.6. Each dot represents a single SAR image, the x-axis represents time at which images were acquired, and the y-axis represents the perpendicular baseline of each image with respect to the reference image (an image to which all other images in the stack were co-registered). Lines connecting the images depict the interferogram pairs fulfilling the baseline thresholds of 30 days for the temporal baseline and 100 meters for the perpendicular baseline. A full connection within the network is of importance for the inversion step, since gaps in the network cause the solution to fail if no prior assumptions about the deformation phenomena are made (this will be further described in the next steps).

Coherence estimation and phase unwrapping

The SB method requires essentially 2 datasets: coherence (used for selection of coherent pixels for further analysis of deformation) and unwrapped phase (used for inversion of displacement time series using the SB network). The interferometric coherence is estimated for each interferogram, using the approach described in Section 6.2.3.

For the study area surveyed with InSAR, the phase unwrapping is performed for the whole phase image without masking of low-coherence pixels. This approach is applied to maximise the amount of information obtained and to avoid abnormalities in the SB inversion procedure caused by gaps in the SB network caused by masking

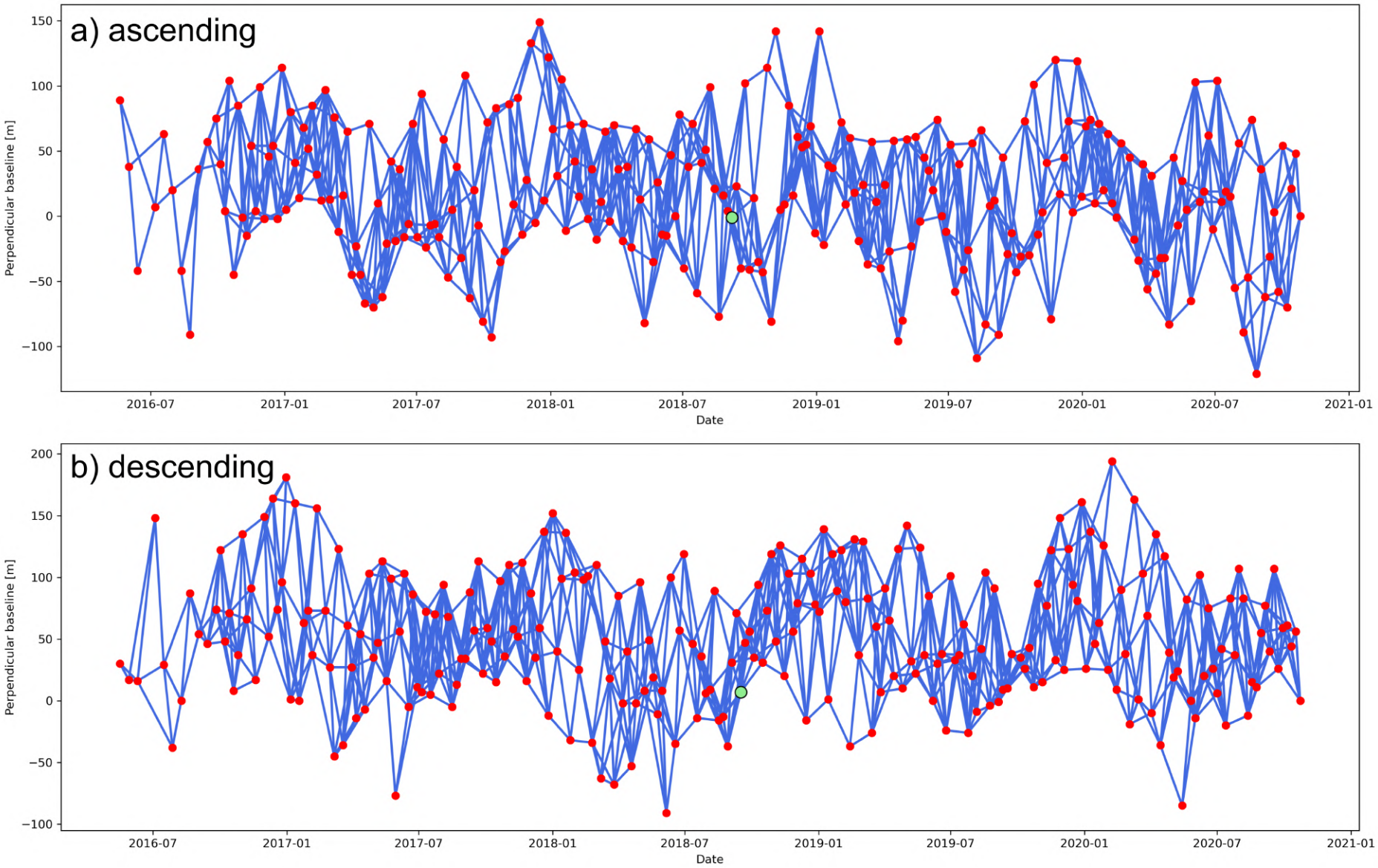

Figure 6.6: Baseline plots of interferograms created for the SBInSAR processing, using (a) ascending and (b) descending Sentinel-1 data. Green dots highlight reference images

of pixels on individual interferograms. Interferograms are unwrapped using the SNAPHU algorithm, as described in Section 6.2.4. Interferograms were quality-checked for phase unwrapping errors and missing data (e.g. a result of missing SLC burst information). For this reason, several interferograms were excluded from further processing, while ensuring the continuity of the SB network of interferograms.

Network inversion for displacement estimation

In order to estimate the displacement time series using a dataset of short spatio-temporal baseline interferograms, a Small Baseline inversion is performed on the network of interferograms. Using a stack of N SAR images, M unwrapped interferograms were created, forming a vector of $\mathrm{d} = [d_1, ..., d_M]^T$. The unknown vector of *N-1* incremental displacements (displacements between consecutive time epochs, e.g. *t-1* and *t*), $\mathrm{m} = [m_1, ..., m]^T$, can be derived by inverting and solving the equation:

$$\mathrm{d} = \mathrm{Gm}, \tag{6.3}$$

where G is a design matrix of size *M x (N-1)*, that describes the relationship between the incremental displacements and interferograms in the SB network [155]. Equation can be solved through e.g. least squares approach or using singular value decomposition (SVD), obtaining the inversion output and the incremental displacements. These can further be summed to obtain cumulative displacement and mean displacement velocity.

The state of the connections within the interferogram network is projected on the SB inversion in a way that if there are network gaps, introduced e.g. by pixel masking in select unwrapped interferograms or lack of unwrapped interferograms for a short period in the network, there is an insufficient amount of data to solve the equation (the G matrix is rank-deficient) using the least squares method. The SVD approach solves the equation, but introduces displacement values of 0 in the network gaps. A modification of SB approach, *NSBAS*, can deal with network gaps through assumption of a temporal model of displacement (e.g. linear). However, the solution can yield underestimation of displacements if rapid displacement occur during the temporal gaps in the network.

The SB inversion in this thesis was performed using a least squares approach, with a fully-connected network of interferograms to avoid misinterpreting non-linearities in time series of displacements.

Spatio-temporal filtering

Similar to the Persistent Scatterer approach, the displacement time series derived using the SB algorithm is also containing signals other than displacements: the DEM error, the atmospheric delay and decorrelation induced by different look angles and thermal noise, amongst others. The time series data can thus be further processed to reduce these errors, by means of spatio-temporal filtering, as was the case in the PS approach. A high-pass in time and low-pass in space filter can be applied to the data to estimate the noise components and separate them from the displacement time series.

6.4 Estimation of vertical displacement using Line-Of-Sight observations

The objective of this dissertation is to develop a method of mining displacement prediction using machine learning and InSAR measurements. The displacement of mining areas that is measured by other geodetic methods (e.g. leveling and/or GPS) is acquired in vertical and horizontal planes. However, InSAR measures the displacement in the Line-of-Sight of a satellite, that is a projection of 3D displacement information to a 1 dimension (LOS). InSAR measurement therefore includes both vertical and horizontal displacements occurring over an area of interest, as was described in detail in Section 3.2.3. If non-zero horizontal displacement is present in the Area of Interest (AOI), it will manifest in the LOS measurement [191]. Theoretical assumptions about subsidence phenomenon over underground mining areas, as well as empirical data gathered through various studies argue that horizontal displacements do occur and should be considered when examining the impact of underground mining works on the ground surface.

A review of approaches applied in literature to projecting LOS measurements to vertical and horizontal components was introduced in Chapter 3. An approach based on [191] was selected for resolving vertical displacements over the study area of this thesis, as it allows to derive vertical and horizontal displacement from two independent acquisition paths of SAR data, while minimising errors induced by projecting LOS data without the third acquisition path (needed to resolve a full 3-dimensional displacement field).

6.4.1 Method of decomposing 2 LOS signals for time series InSAR data

Based on Equation 3.14, the vertical and horizontal (in Azimuth Look Direction) components of displacement can be retrieved by solving the inverted equation, provided that LOS measurements from 2 acquisition paths are known, together with incidence angle values and heading angles for each orbit path. **Before projecting the LOS measurements to vertical and horizontal components, a series of assumptions are made about the approach**:

1. The component of displacement in the North-South direction (horizontal) is assumed to be 0. It is apparent that, taking a subsidence trough as an example, a N-S displacement will be present and its magnitude will be similar to the E-W (East-West) displacement. However, given the low sensitivity of a near-polar orbit SAR system to the N-S displacement (explained in detail in Section 3.2.3), this component is neglected to simplify the calculations.

2. Methodology of retrieving InSAR displacements in this thesis concerns measuring time series of values as inputs for machine learning algorithms. Therefore, vertical displacements will be derived as a time series using sequential data from MTInSAR algorithms.

3. To fulfill the above assumption, temporal resampling needs to be performed on time series data in order to compensate for a temporal shift in image acquisition between orbital paths in ascending and descending acquisitions. This shift equals to 3 days for the selected Sentinel-1 datasets over the study area.

4. Projection of LOS displacements will be carried out for resolution cells that are uniform for both ascending and descending datasets, therefore a spatial

resampling will be carried out prior to solving the inversion problem.

5. Since time series InSAR processing methods are used for obtaining displacements from ascending and descending satellite orbits, these measurements are relative to a point in space that is considered as stable. Therefore, both ascending and descending time series datasets should be referenced to the same reference point in the study area.

Equation 3.14 can be written as $b = Ax$, and solved by least-squares approximation:

$$x = (A^T A)^{-1} A^T b \tag{6.4}$$

Substituting the matrices from equation 3.14, we get

$$\begin{bmatrix} d_V \\ d_H \end{bmatrix} = \left(\begin{bmatrix} cos\theta_{asc} & cos\theta_{dsc} \\ \frac{sin\theta_{asc}}{cos\Delta\alpha} & sin\theta_{dsc} \end{bmatrix} \begin{bmatrix} cos\theta_{asc} & \frac{sin\theta_{asc}}{cos\Delta\alpha} \\ cos\theta_{dsc} & sin\theta_{dsc} \end{bmatrix} \right)^{-1} \begin{bmatrix} cos\theta_{asc} & cos\theta_{dsc} \\ \frac{sin\theta_{asc}}{cos\Delta\alpha} & sin\theta_{dsc} \end{bmatrix} \begin{bmatrix} d_{LOS}^{asc} \\ d_{LOS}^{dsc} \end{bmatrix}, \tag{6.5}$$

which, after performing matrix operations, yields:

$$\begin{bmatrix} d_V \\ d_H \end{bmatrix} = \frac{1}{det} \begin{bmatrix} a_{22} b_V - a_{12} b_H \\ -a_{12} b_V + a_{11} b_H \end{bmatrix}, \tag{6.6}$$

For the sake of readability, the above equation contains variables corresponding to products resulting from performing matrix operations, which are clarified below:

$$\begin{aligned} a_{11} &= cos^2\theta_{asc} + cos^2\theta_{dsc}, \\ a_{12} &= \frac{sin\theta_{asc} cos\theta_{asc}}{cos\Delta\alpha} + sin\theta_{dsc} cos\theta_{dsc}, \\ a_{22} &= \left(\frac{sin\theta_{asc}}{cos\Delta\alpha} \right)^2 + sin^2\theta_{dsc}, \\ b_V &= cos\theta_{asc} d_{LOS}^{asc} + cos\theta_{dsc} d_{LOS}^{dsc}, \\ b_H &= \frac{sin\theta_{asc}}{cos\Delta\alpha} d_{LOS}^{asc} + sin\theta_{dsc} d_{LOS}^{dsc}, \\ det &= a_{11} a_{22} - a_{12}^2 \end{aligned}$$

The LOS displacement values for ascending (d_{LOS}^{asc}) and descending (d_{LOS}^{dsc}) acquisition tracks come from InSAR time series estimation using Sentinel-1 data. Incidence angles (θ_{asc} and θ_{dsc}) were assumed to be variable across the SAR scene, to increase the decomposition accuracy, as in [65]. Incidence angle values are estimated using precise orbit data and a DEM (SRTM-1) of the study area, to account for slope effect on the angle value. The $\Delta\alpha$ value was calculated using heading angles of 349.8279° and 190.1187° for ascending and descending tracks, respectively (constant for the whole SAR scene).

6.4.2 Processing of LOS PS and SB InSAR results

LOS displacement decomposition was performed for both PS and SB processing results from ascending and descending geometries. Time series data from both tracks were resampled temporally to a common 6-day sampling, to compensate for a 3-day shift in track acquisition of Sentinel-1 satellite for the study area. The ascending path sampling was selected as temporal reference, and the descending time

series data were resampled to unify the temporal sampling. A common number of epochs was also assumed for each time series to avoid data gaps.

Spatial resampling was performed for both PS and SB datasets. A common resolution cell of 30 m by 30 m was established for all datasets to be resampled to. PS and SB data were both resampled to this spatial resolution for comparison purposes.

SB results are already in raster format (due to processing algorithm used, that resamples the data points to grid), therefore data for each consecutive epoch were simply resampled to a common 30 m grid. On the contrary, PS data are in vector format (points) and need to be converted to raster. Additionally, PS points are not detected over the whole study area and spatial gaps are introduced, making it impossible to obtain both ascending and descending data in some areas.

Point data from the PS method were interpolated to 30 m grid using the Inverse Distance Weighting (IDW) method. Because PS points can be detected in different locations on ascending and descending tracks due to different LOS geometries, resampled data may not overlap spatially. A buffer of 100 meters around PS points was assumed for interpolation to increase the amount of grid data cells containing data from both paths. Incidence angle grids estimated for both tracks were also resampled to the common grid prior to displacement decomposition.

After the preprocessing of PS and SB datasets, projection of LOS measurements from ascending and descending acquisitions was performed according to Equation 6.6.

Chapter Summary

This chapter provided the necessary explanations of the methodologies applied for the displacement estimation in the study area. A description of interferometric processing, from raw SAR imagery, to estimated vertical displacement time series, has been presented, including time series interferogram processing approaches of Persistent Scatterer (PS) and Small Baseline (SB) methods. The results of interferometric processing described in this chapter will be time series data on vertical ground surface displacements within the study area, presented later in Chapter 8. Since the time series displacement data is to be processed by machine learning algorithms for application in prediction, it needs to be processed accordingly. The methodology of pre-processing InSAR time series data and machine learning model development for time series forecasting of ground displacements will be provided in the next chapter.

Chapter 7

Subsidence prediction using time series forecasting

InSAR methods allow remote monitoring of ground surface displacements over wide areas. The short revisit time of the surveyed area (6 days for Sentinel-1A/B satellites until 2022) allows the acquisition of high volumes of surface displacement data. Such amount of data allows for detection and detailed description of the surface displacement phenomenon, complementing measurement methods such as GNSS or leveling. One of the theses of this dissertation is that the displacement dataset acquired by InSAR methods can be used to predict future short-term displacements using machine learning algorithms.

This chapter introduces the reader to the data processing methods and forecasting techniques used in the dissertation. A framework for the processing of displacement time series, obtained using the methods described in Chapter 6, will be presented, together with appropriate data preparation for use with machine learning algorithms in the context of time series forecasting. The chapter will include descriptions of the displacement forecasting approaches and methods used, including benchmark methods, machine learning methods and neural networks. Comparing the methods used to determine their effectiveness requires defining the accuracy metrics adopted, so the final section of the chapter will describe selected accuracy metrics used to evaluate the performance of the forecasting methods.

7.1 Data preprocessing

7.1.1 Sampling data points from displacement dataset

The time series of vertical displacements in the study area have different characteristics due to the subsidence caused by underground mining. An effective displacement forecasting model should take into account the magnitude of displacements and forecast both higher and lower displacement values at points within the subsidence troughs. Furthermore, the analysis of the effectiveness of the model in predicting displacements should be based on a sufficiently large sample of data to allow unambiguous comparison of the model with the benchmark model.

For the aforementioned reasons, in order to test the thesis presented in the dissertation on the feasibility of displacement forecasting using machine learning and InSAR data, calculations using time series forecasting were performed in Area No. 1 and Area No. 3, highlighted in Figure 5.2 (Chapter 5). Within the areas, measurement points (pixels) were selected, each with a time series of displacements

determined by time series InSAR methods. Area No. 1 contains a total of 14,763 pixels, of which 150 points were selected, located in the central part of the area, spaced at regular intervals of 150 metres. Area No. 3 contains 53,244 pixels, of which 528 points were selected for model development, in a manner similar to Area No. 1. The points selected for model development cover time series with different subsidence characteristics. The selected points do not cover entire areas so that it is possible to estimate the effectiveness of the models in predicting displacements for time series outside the set used to develop the models. Figure 7.1 shows the location of the points selected for the time series analysis.

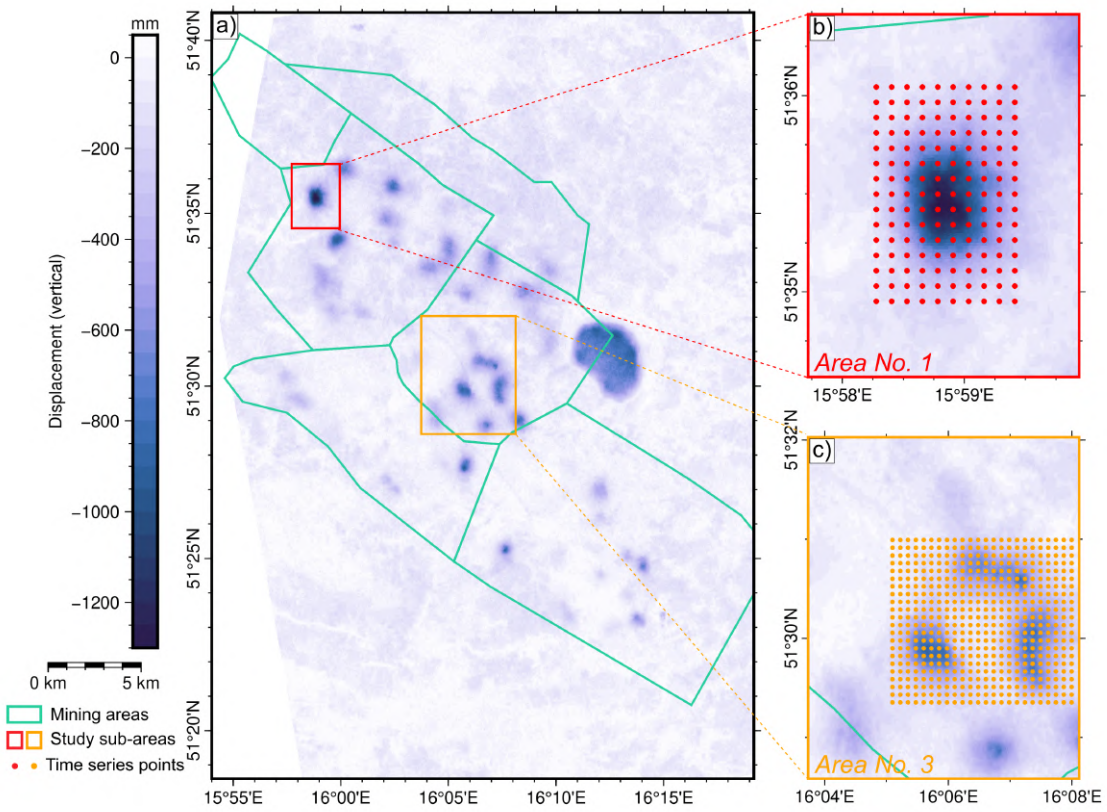

Figure 7.1: (a) Locations of areas selected for the analysis of displacement forecasting models, presented in (b) for Area No. 1, and in (c) for Area No. 3. Background shows cumulative vertical displacements (20 May 2016 - 26 October 2020)

7.1.2 Missing values

The vertical displacement dataset was obtained by combining two datasets from two SAR imaging acquisition paths. Due to missing imagery or the exclusion of some imagery from the InSAR time series analysis (due to high decorrelation), the final vertical displacement dataset has few missing values, for the acquisition dates of the missing or excluded imagery. Time series forecasting algorithms, in particular machine learning methods and neural networks, require data at uniform intervals and without missing values. For this reason, the set of vertical displacements was supplemented with missing dates to ensure temporal continuity with a temporal resolution of 6 days. Missing displacement values on these days were filled in through ordinary linear interpolation, based on the previous and next values in the time series, to minimize the risk of introducing unnecessary assumptions.

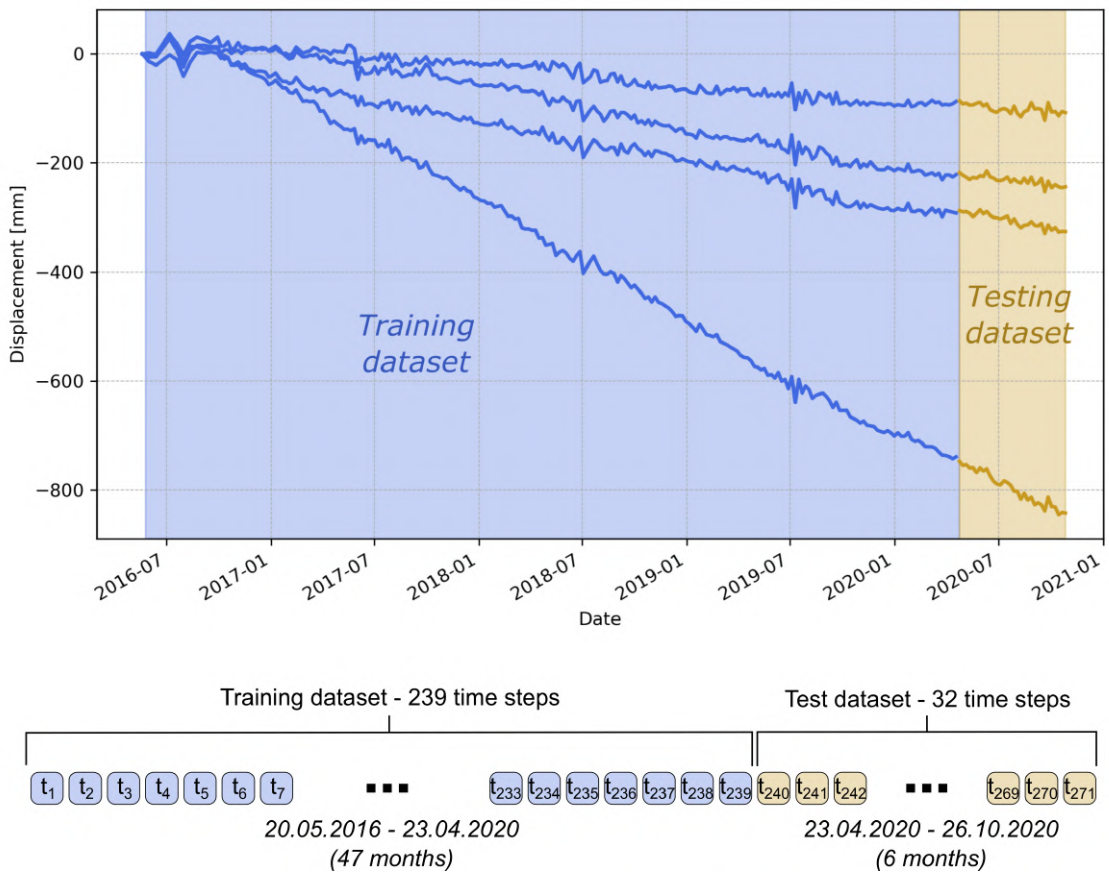

Figure 7.2: A schematic of splitting time series data into training and testing samples, shown for randomly selected 4 data points in Area No. 1 (top) and detailed division into separate datasets (bottom

7.1.3 Partitioning into training and test datasets

The datasets used in machine learning algorithms have to be divided into subsets - training data, on which the model learns dependencies in order to make predictions, and test data - with which the predictions of the model are compared to assess its performance. The model is learned on training data without access to test data, in order to prevent data leakage.

In the context of time series forecasting, the split between training and test data is carried out in the time domain - the model is trained on historical data, and based on the relationships learned from this data, forecasts the values of the phenomenon in subsequent time steps into the future. The forecast is then compared with the actual values to determine the model performance. In order to divide the time series data into training and test subsets, it is necessary to define the time horizon that the algorithm aims to forecast. In this dissertation, the following strategy is adopted: based on historical data of displacement values in the study area, displacement values are forecast for the next six months ahead. The forecast horizon is therefore 6 months, and according to this, the time series was divided into training and test sets, covering the initial **47 months** and the final **6 months**, respectively. A schematic of the division of the dataset into training and test data for the example time series is shown in Figure 7.2. The **training set** includes data acquired from **20 May 2016** to **23 April 2020** and contains **239** time steps, while the **test set** includes data acquired between **23 April 2020** and **26 October 2020** and contains

32 time steps.

7.2 Model training and subsidence forecasting

7.2.1 Framing time series forecasting as a supervised learning problem

Supervised machine learning methods will be used to predict vertical displacements in this research. These methods are based on learning dependencies from input-output data pairs. The time series must therefore be transformed into samples containing input and output data, each sample containing a certain number of time steps as input, and a certain number of steps as output. The number of input and output steps can vary depending on the data available and the model used.

The method of creating samples from the time series for supervised learning is shown in Figure 7.3. From the time series in the training set, consecutive samples containing x input steps and y output steps are extracted. The sampling window is moved from the beginning to the end of the training sequence. Each input-output time series pair is a single sample for the supervised learning algorithm.

Figure 7.3: Generation of training samples using a *rolling window* approach over a time series

The study adopted different values for the number of input steps, depending on the method used. The number of output steps was assumed to be the same for all models and was 32 steps, thus covering the entire forecast horizon. The parameters of the datasets created for training, including the number of input time steps, will be provided for each model in the next Section.

7.2.2 Forecasting strategies

In this study, various algorithms and time series forecasting models were used to predict vertical displacements. These models are based on different forecasting approaches. The forecasting strategies used will be described in this sub-section, categorised by the number of time series used to create the models (*local* and *global* forecasting models), and by the method of forecasting subsequent time steps over a given time horizon (*one-step* and *multi-step* forecasts).

Local and global models

Local and *global* time series forecasting models were tested in the forecasting of vertical displacements in the study area. **Local** models forecast only the time series at a given location, based on the historical values of this series. This means that a new local model is created for each time series, and possible relationships between time series at subsequent points are not considered.

Global models are trained on a set of multiple time series, learning the relationships found in series with different temporal patterns. These models can incorporate information from multiple time series to predict future values of one or more target time series. The global approach to time series forecasting allows to create a single model based on multiple input time series, able to predict future values of a given time series.

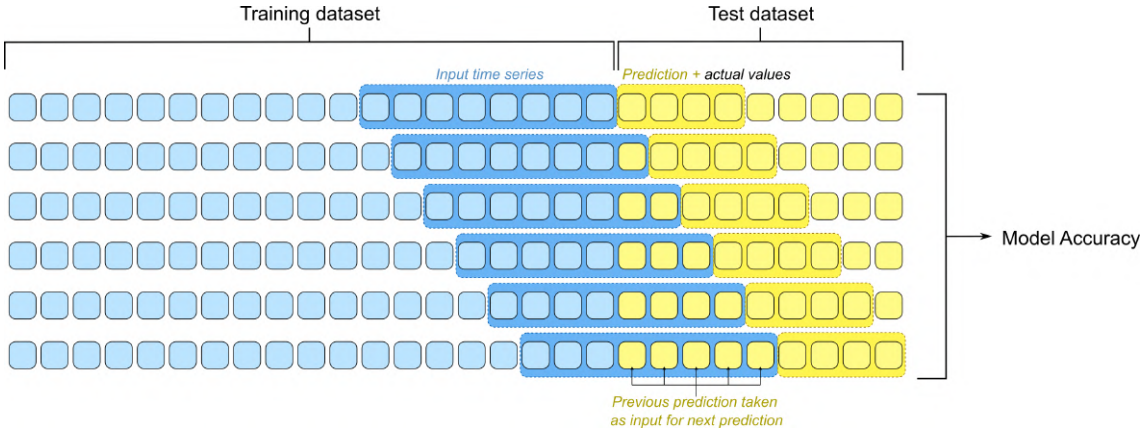

Figure 7.4: A diagram showing how recursive forecasting works in principle

One-step and multi-step models

The models and algorithms used in the thesis are based on different approaches to forecasting future values of a time series over a given prediction horizon.

The first approach is **one-step** forecasting, used by algorithms such as ARIMA or Exponential Smoothing. The model in this approach is trained to predict the value of the time series in the next step based on the values in the previous steps. When the prediction horizon covers more than a single step, the prediction is performed in an autoregressive manner, i.e. the predicted value is treated as part of the historical series, and the next step is predicted. The process is repeated until the end of the sequence covered by the prediction horizon is reached.

Another approach is **multi-step** time series forecasting, based on forecasting the value of a time series for multiple time steps at once. Multi-step forecasting allows for simultaneous forecasting of time series values over a long-term horizon. Multi-step time series forecasting can be realized using two strategies. First strategy involves predicting subsequent future time steps in a *recursive* manner, where predicted values for previous time steps are used as inputs to predict values of multiple next time steps, similar to the autoregressive approach in one-step forecasting explained earlier. The schematic of recursive multi-step forecasting is presented in Figure 7.4.

Direct, or *one-shot* forecasting involves predicting all the future time steps within forecast horizon at once. A pattern of direct multi-step forecasting is presented in Figure 7.5.

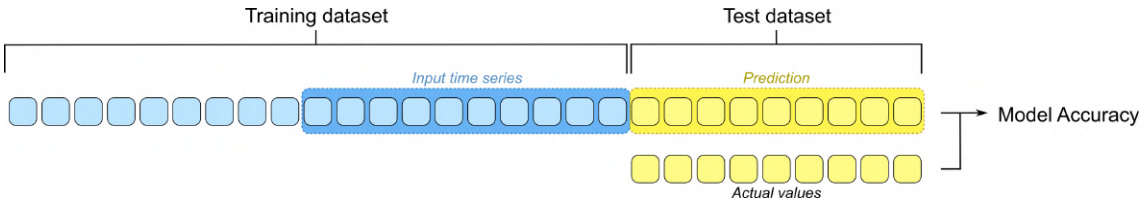

Figure 7.5: Direct forecasting, where the entire sequence (forecast horizon) is forecast in one iteration, based on the input sequence

Machine learning models and neural networks (except for the Recurrent Neural Network, which is designed as a recursive model) **adopted in this thesis are based on one-shot multi-step forecasting strategy**, where the model is trained to predict all time steps within the forecasting horizon in one forecast.

7.3 Time series forecasting models

This section introduces the statistical and machine learning methods used in the thesis to forecast the time series of vertical displacements. The models listed will be compared with the baseline model and with each other to determine the most effective approach. For each method, separate models were created for the datasets in Area No. 1 and Area No. 3.

7.3.1 Naive baseline model

In order to determine whether a given forecasting model is effective, it is necessary to compare it with a baseline model that is based on certain assumptions on the time series. In the case of time series forecasting, **naive forecasting** is generally used as the approach used as a baseline for comparison against tested models.

Several types of naive models can be used, the simplest being a naive model that predicts a future value based on the last known value. The values forecast in subsequent steps by such a model are therefore equal to the last known value. Another approach is the naive mean model, in which the predicted value is the average of past values. For time series with an observable trend, a frequently used naive model is the naive drift model, which forecasts future values by fitting a line between the first and last values in the training time series, and extending this line for subsequent forecast time steps. In this way, the naive approach takes into account the trend present in the data, as opposed to the last known value or naive mean approaches.

The baseline model used in this dissertation is the last naive model mentioned, the naive drift.

7.3.2 AutoARIMA model

One of the traditional forecasting approaches based on statistical methods is the ARIMA (Autoregressive Integrated Moving Average) model. In this thesis, the **AutoARIMA** algorithm was implemented as a method to forecast displacement values. This algorithm is an automated method using the ARIMA model, designed to automate the optimal selection of ARIMA model parameters (order of autoregression, integration and moving average components), based on the characteristics of the input time series.

Optimal parameters of the ARIMA model are found by iteratively testing different model parameters combinations. Each model is then evaluated using a selection criterion - the Akaike Information Criterion (AIC). The model with the lowest criterion value is selected as the model with the most optimal combination of parameters [91].

Since the ARIMA model uses a one-step strategy to predict future values of a time series, an autoregressive approach was used to predict the entire forecast horizon, using the predicted values as input for forecasting subsequent future values.

7.3.3 Exponential Smoothing model

Another traditional forecasting approach is the **Exponential Smoothing** algorithm. The Holt-Winters' Exponential Smoothing algorithm was adopted, based on fitting a model to the historical data using smoothing parameters - level (representing the average value of the time series), trend (rate at which the time series is increasing or decreasing) and seasonality (periodic fluctuations of time series). The model also has the ability to adapt to changes in the time series over time through a method of updating the smoothing parameters [91].

The Exponential Smoothing approach used in this study was used with a multi-step, direct forecasting strategy (forecasting entire forecast horizon at once).

7.3.4 Linear regression

The first machine learning method used in the dissertation to predict vertical displacements in the study area is the **linear regression** method. This method assumes that there is a linear relationship between the input variables and the output variable, in the case of a time series the relationship is between the input sequence and the output sequence. Furthermore, the assumption of linear regression is that this relationship will be invariant over time [153].

The model used assumes that there is a linear relationship between sequences in the time series. The lengths of the input and output sequences were assumed to be 32 time steps each. In this way, the linear regression model predicts the next 32 time steps based on the previous 32 time steps using the estimated linear relationship.

The linear regression model was tested in both local (separate model for each time series in the set) and global (one model trained on all time series in the dataset) approaches.

7.3.5 Lasso regression

Lasso regression is a machine learning method that adds a penalty term to the linear regression equation. The penalty term in the case of Lasso regression is L1 regularization. Using regularization allows Lasso regression to select a subset of relevant predictors from a set of potential predictors. This means that selected lagged (past) values in the time series included in the model are given various weights, contrary to linear regression when each time series value is assumed to have the same impact on the prediction [92].

Model using Lasso regression was created as a global model trained on a dataset of time series points, with training sequences of 50 time steps for input, and 32 time steps for output.

7.3.6 Ridge regression

Ridge regression is a variant of linear regression that also includes a penalty term in the objective function to manipulate the values of regression coefficients. Ridge regression uses L2 regularization as the penalty term to reduce the magnitudes of regression coefficients, leading to better generalization of the model (ability to predict on unseen data).

The Ridge model used in the dissertation is a global model, assumed to train of sequenced of 40 input time steps and 32 output time steps.

7.3.7 ElasticNet regression

The **ElasticNet regression** approach is a method that combines the L1 and L2 regularization terms of Lasso and Ridge regression, respectively. This hybrid method was designed to combine the advantages of both models, and the two penalties are controlled by a hyperparameter that can be tuned to balance the influence of coefficient sparsity (Lasso) and small coefficients (Ridge).

Similar to previous regression models, the Ridge model was trained as a global model, with 50 lagged (past) time steps as input and 32 time steps as output.

7.3.8 N-BEATS neural network

First of the neural network models used in this dissertation, the **N-BEATS** (Neural Basis Expansion Analysis for interpretable Time Series forecasting) model is a deep learning architecture developed for time series forecasting. The model is composed of stacks, containing blocks of fully connected neural networks, each comprising several layers of neurons. The input time series is decomposed by N-BEATS structures into a set of basis functions, each capturing different patterns in the time series (e.g. trends, seasonality, cycles). The output of a stack are data values forecasted based on the patterns in the input time series. If the model is built using multiple stacks, then outputs of multiple stacks are joined together to provide the final forecast. Each stack can identify a different property of the input time series, and contribute to the final forecast in a different way [164].

The N-BEATS architecture adopted in the thesis is a model composed of 40 stacks of fully connected neural networks. Each neural network has 4 layers with 256 neurons each. Model was trained for 200 epochs on the training time series dataset as a global model, with 50 time steps assumed as input sequence, and 32 time steps as output sequence for prediction (entire forecast horizon).

7.3.9 Recurrent Neural Network

Another model using neural networks is the **Recurrent Neural Network (RNN)** model, based on *Long Short-Term Memory (LSTM)* cells. In order to utilise the ability of the LSTM model to capture long-term dependencies in time series data, the training dataset was partitioned into samples containing 100 input steps and 32 output steps.

Model was created using 2 recurrent layers with 200 cells each. The prediction is provided by the model in an autoregressive approach, where the model outputs a value for a single prediction time step, and uses historical data and last prediction to forecast the next time steps until the length of the forecast horizon is reached. The RNN model was trained as a global model on the selected datasets for 200 epochs.

7.3.10 Block Recurrent Neural Network

BlockRNN is another Recurrent Neural Network model used for the study. The model is also based on LSTM cells, like the previous RNN architecture. However, the BlockRNN model can provide forecasted time series values in fixed-length blocks, which means that this model forecasts time series in a multi-step manner, contrary to the previous RNN model.

The BlockRNN model was created using 3 recurrent layers with 100 cells each, followed by a fully connected layer with 32 nodes, allowing the model to forecast the entire forecast horizon at once. This model was trained for 200 epochs, on a training dataset with 100 input time steps and 32 output time steps.

7.3.11 Ensemble of machine learning regression models

In view of the effectiveness of an **ensemble of regression models** reported in time series forecasting, this approach was also tested in the study. In the ensemble approach, multiple selected time series forecasting models are trained on a training set, and their predictions are combined to produce a final forecast.

The ensemble model was created by combining the regression approaches used previously, taking into account the linear regression model, the Lasso model, the Ridge model and the ElasticNet model. The final ensemble model was trained as a global model on a set of time series, with the training set divided into subsets containing 50 input steps and 32 output steps. The model predicts all 32 steps of the prediction horizon at once.

7.4 Metrics used for assessing model performance

An important part of working with time series forecasting models is to assess their performance in predicting unknown values for specific data. A number of accuracy metrics are used to assess the performance of forecasting models. The accuracy metrics applied in this thesis will be listed and described below.

7.4.1 Mean Absolute Error (MAE)

Mean Absolute Error (MAE) is an accuracy metric used for time series forecasting, that measures absolute average difference between the actual and predicted values in a forecasted time series.

In time series forecasting task, MAE is measured by calculating the absolute difference between predicted $\hat{y}_i$ and actual y_i values for each of n time steps in the forecasted sequence. Then the absolute differences are averaged over the entire time series. The equation below is used to calculate MAE:

$$MAE = \frac{1}{n}\sum_{i=1}^{n}(|y_i - \hat{y}_i|) \tag{7.1}$$

MAE is expressed in the same units as the original time series. A low value of MAE indicates a better performance of the forecasting model, meaning that the predictions of the model are closer to the actual values. It doesn't take into account the fact whether the model is underestimating or overestimating the actual values.

7.4.2 Root Mean Squared Error (RMSE)

Another metric used for evaluating the performance of a time series forecasting model is the **Root Mean Squared Error (RMSE)**. It measures the difference between the actual and predicted values of a time series.

The RMSE is calculated by averaging the squared differences between respective actual y_i and predicted $\hat{y}_i$ values of time series with n elements. Then, a square root of the average is calculated, according to equation:

$$RMSE = \sqrt{\frac{1}{n}\sum_{i=1}^{n}(y_i - \hat{y}_i)^2} \tag{7.2}$$

The value of RMSE is expressed in the same units as the time series. The lower the RMSE, the better the forecasting performance of a model. The fact that the differences between actual and predicted values are squared before averaging, causes the RMSE to give more emphasis to errors with high values.

7.4.3 Mean Absolute Percentage Error (MAPE)

The **Mean Absolute Percentage Error (MAPE)** is an accuracy metric for evaluating time series forecasting models that measures the percentage difference between models, unlike the previous MAE and RMSE metrics.

MAPE is calculated using a formula:

$$MAPE = \frac{1}{n}\sum_{i=1}^{n}|\frac{y_i - \hat{y}_i}{y_i}|, \tag{7.3}$$

where an absolute percentage difference between actual y_i and predicted $\hat{y}_i$ values is averaged over the entire length of a sequence (time series). Low values of MAPE indicate a good performance of a forecasting algorithm.

Chapter Summary

In this chapter, the methods used in the development and evaluation of time series predictive models were presented. The data selection and processing strategy presented was used to prepare a suitable dataset for testing various predictive models. Selected approaches to model development and time series forecasting were introduced, along with a description of the various machine learning and neural network methods used in the dissertation. Finally, the accuracy metrics used in the study for time series forecasting were outlined.

The next chapter will include the results obtained from the study, including the measured values of vertical displacements within the study area and the results obtained by the forecasting models for the displacement prediction task.

Chapter 8

Results and discussion

This chapter will provide an overview of the results obtained during the research conducted within this doctoral thesis. The chapter was divided into two sections, describing separate parts of the conducted study. The first part (Section 8.1) included an analysis of vertical ground surface displacements using InSAR methods. The second part (Section 8.2) was based on using the measurement results of InSAR vertical displacement analysis in training machine learning models for displacement prediction.

8.1 InSAR processing

As part of this thesis, an analysis of ground surface displacements caused by underground mining activities was carried out. The displacement analysis was based on the remote sensing method of satellite radar interferometry (InSAR). With reference to the objectives of the dissertation, one of which is displacement time series forecasting, displacement values were determined using Time Series InSAR processing techniques. SBAS and PS methods were used for this purpose, as described in Chapter 6.3. The results obtained with the SBAS method were selected for further analysis due to the better coverage of the analysed area with measurement data in comparison with the PS method.

To obtain the vertical displacement values, observations from two independent acquisition paths of SAR imagery were used, according to the methodology described in Chapter 6.4. Verification of the adopted methodology and the obtained results was carried out using field measurement data, which are measurement data from levelling lines, acquired during the analysed period by the company conducting mining works in the studied area. Moreover, the results of processing of SAR imagery were compared spatially with data on the conducted underground exploitation (areas of exploitation fields). The verification of displacement measurements with the InSAR method was therefore carried out in 3D - vertical displacements (1D) were verified with levelling measurements, while the spatial extent of displacements (2D) was verified with levelling measurements and mining data. This section will present the results of the measurements carried out together with their field verification.

8.1.1 InSAR processing - Persistent Scatterer (PS) method

PSInSAR displacement time series analysis was carried out for 2 independent SAR imaging acquisition paths (1 ascending and 1 descending) covering the study

area. The results of processing stacks of SAR images with the PSInSAR algorithm are sets of points on the surface of the analysed area, with each point having a determined time series of displacements in the analysed time period. The temporal resolution of the time series corresponds to the temporal resolution of the acquired SAR data - 6 days for both acquisition paths (ascending and descending).

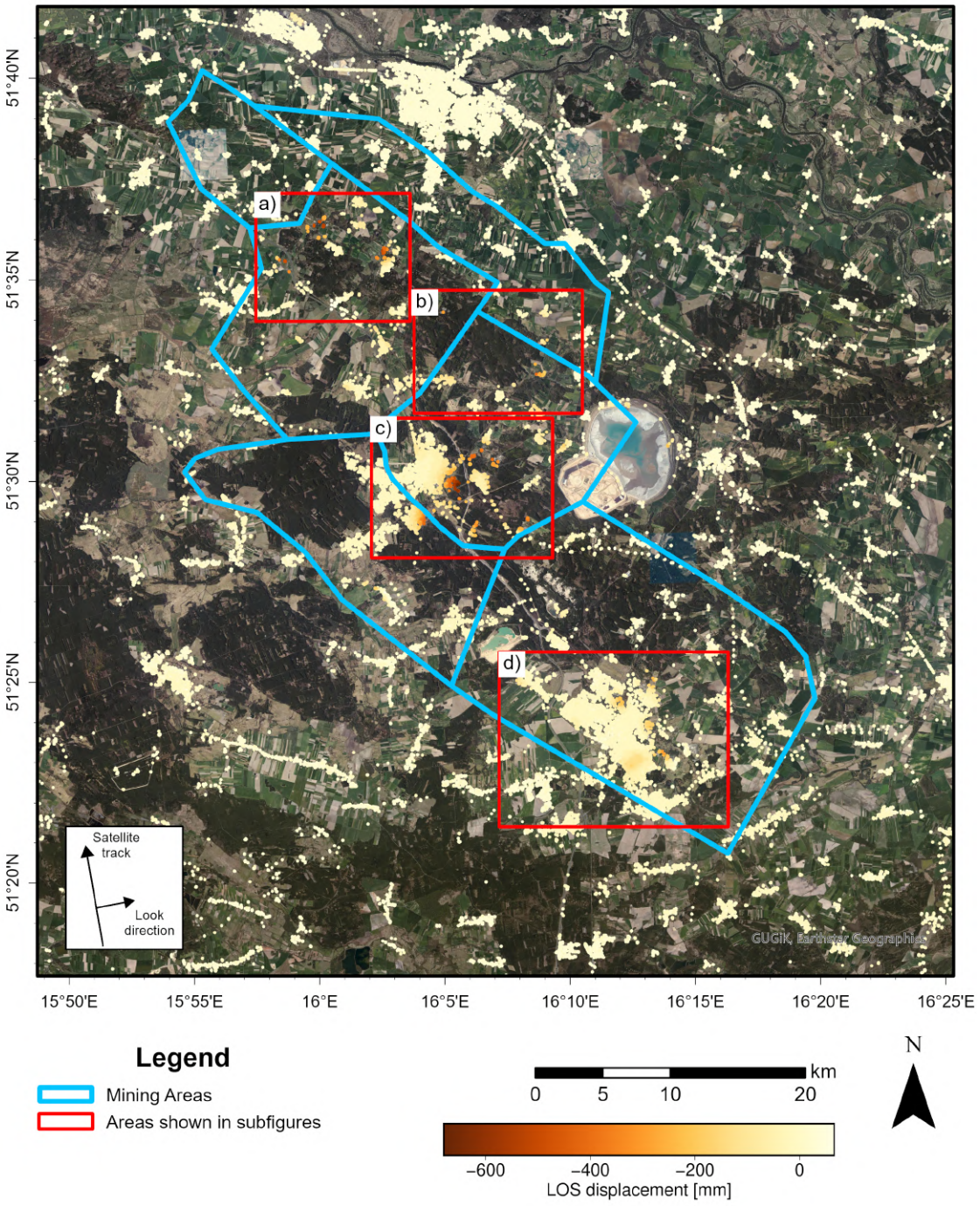

Figure 8.1: Result of Persistent Scatterer (PS) InSAR processing of ascending SAR data, with mining areas marked in blue

Figure 8.1 shows the result of the PS processing obtained for the ascending path of Sentinel-1 over the study area. The results of PS method for the descending path are presented in Figure 8.2. Maps of PS points for both ascending and descending

data indicate that measurement points have been successfully detected by the PSInSAR method. The spatial coverage of PS points varies across the study area, with the highest density of points in urban areas, mainly in the northern part of the study area (Głogów town), as well as within towns of Polkowice and Lubin (highlighted on Fig. 8.1 with *c)* and *d)*, respectively). Other areas of high PS density include smaller towns within the study area, as well as road structures.

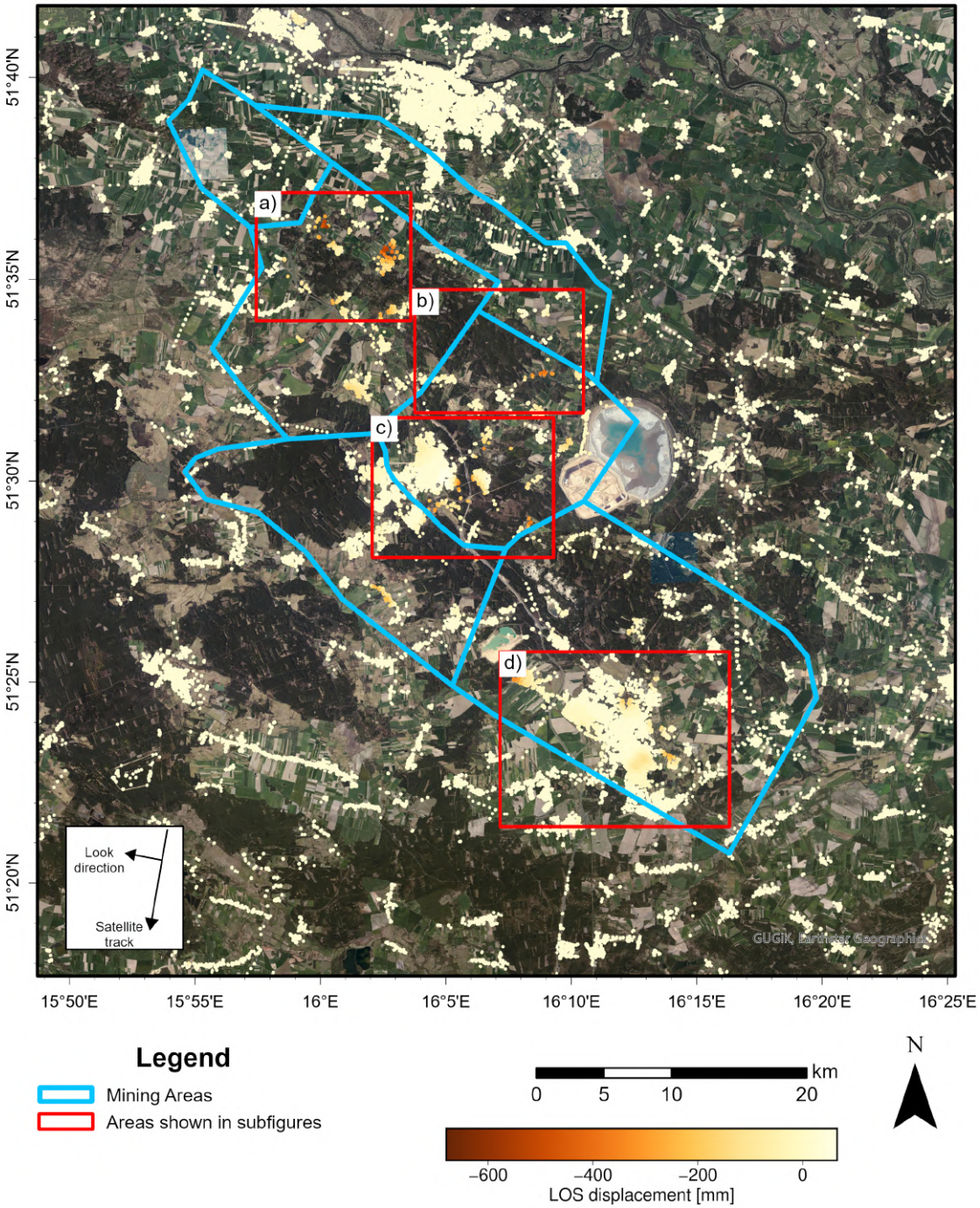

Figure 8.2: Result of Persistent Scatterer (PS) InSAR processing of descending SAR data over the study area (mining areas in blue)

While the majority of PS points detected over the study area do not demonstrate significant values of LOS displacement, several areas with high displacement

values can be observed. These areas are indicated on Figures 8.1 and 8.2 with red rectangles. A maximum value of LOS displacements observed in these areas reach around -650 millimetres.

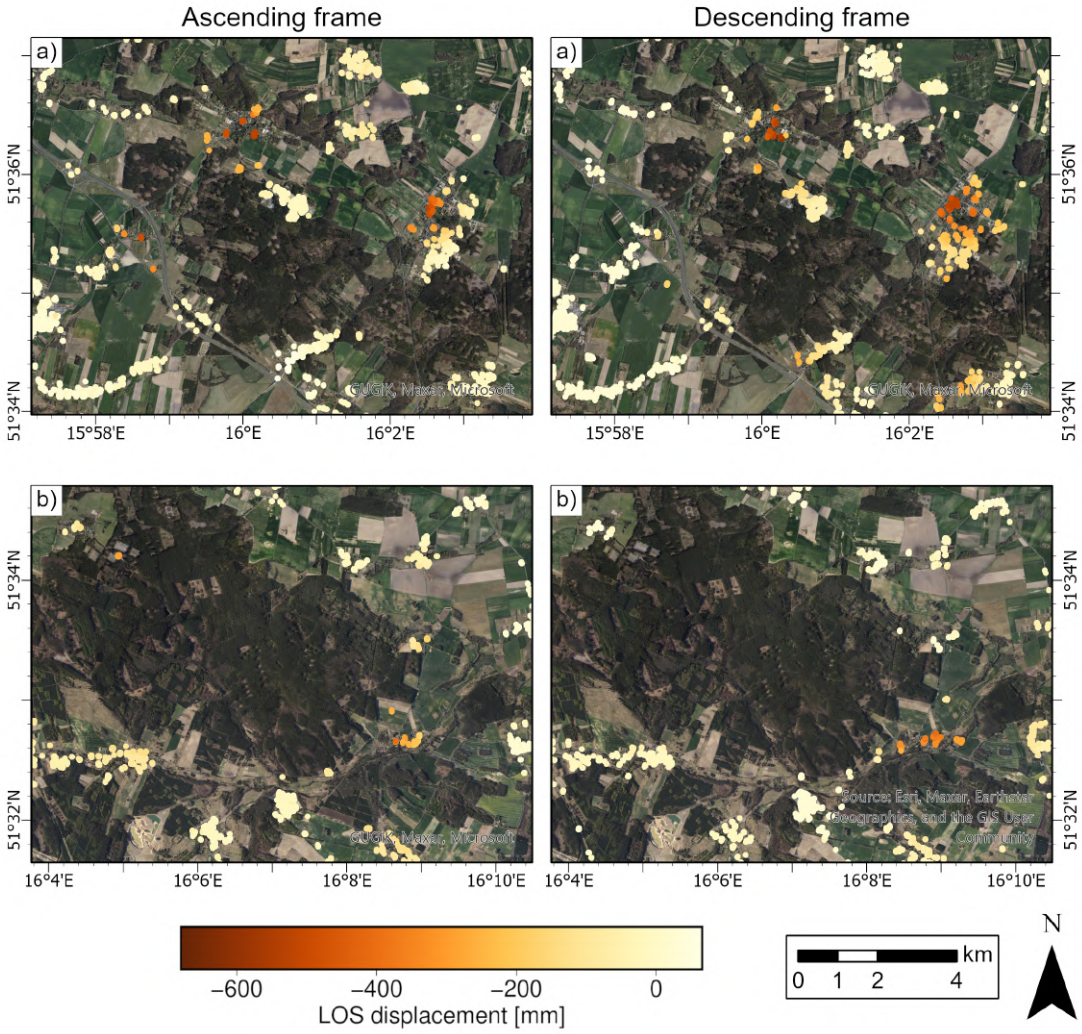

Figure 8.3: PS processing results of ascending (left) and descending (right) data for subareas highlighted in Fig. 8.1

Figures 8.3 and 8.4 provide a more detailed overview of the results in the selected sub-areas highlighted in Figures 8.1 and 8.2. Figure 8.3 details the distribution of PS points in sub-areas *a)* and *b)*, for the two SAR data acquisition paths. The maps of the PS points again show that the measurement points were mainly detected in the areas of buildings and infrastructure objects. However, there are no points detected in areas of forests and agricultural fields, due to the limitations of the PS method. This conclusion is true for all PS results presented. Due to the low density of PS points in the areas analysed, it is difficult to determine the exact patterns of land surface displacement. Zones of displacement are visible in 2 zones in area a) (in the central part), an additional 2 zones can be distinguished in the southern part of area a), but only for the result from the descending path. In area b), on the other hand, only a single significant displacement zone is apparent in the south-eastern part of the area.

A higher density of PS points was achieved for areas *c)* and *d)*, visible in Figure

8.4. The higher density is due to the higher density of buildings, as these areas include the towns of Polkowice (*c)*) and Lubin (*d)*). Numerous zones of deformation are visible in both areas, and in some cases it is even possible to determine the extent of displacement, mainly in area d. The highest values of displacement (-650 millimetres) were observed in the central part of area *c)*, for the ascending path. Displacement values in area *d)* are significantly lower, reaching up to -200 millimetres.

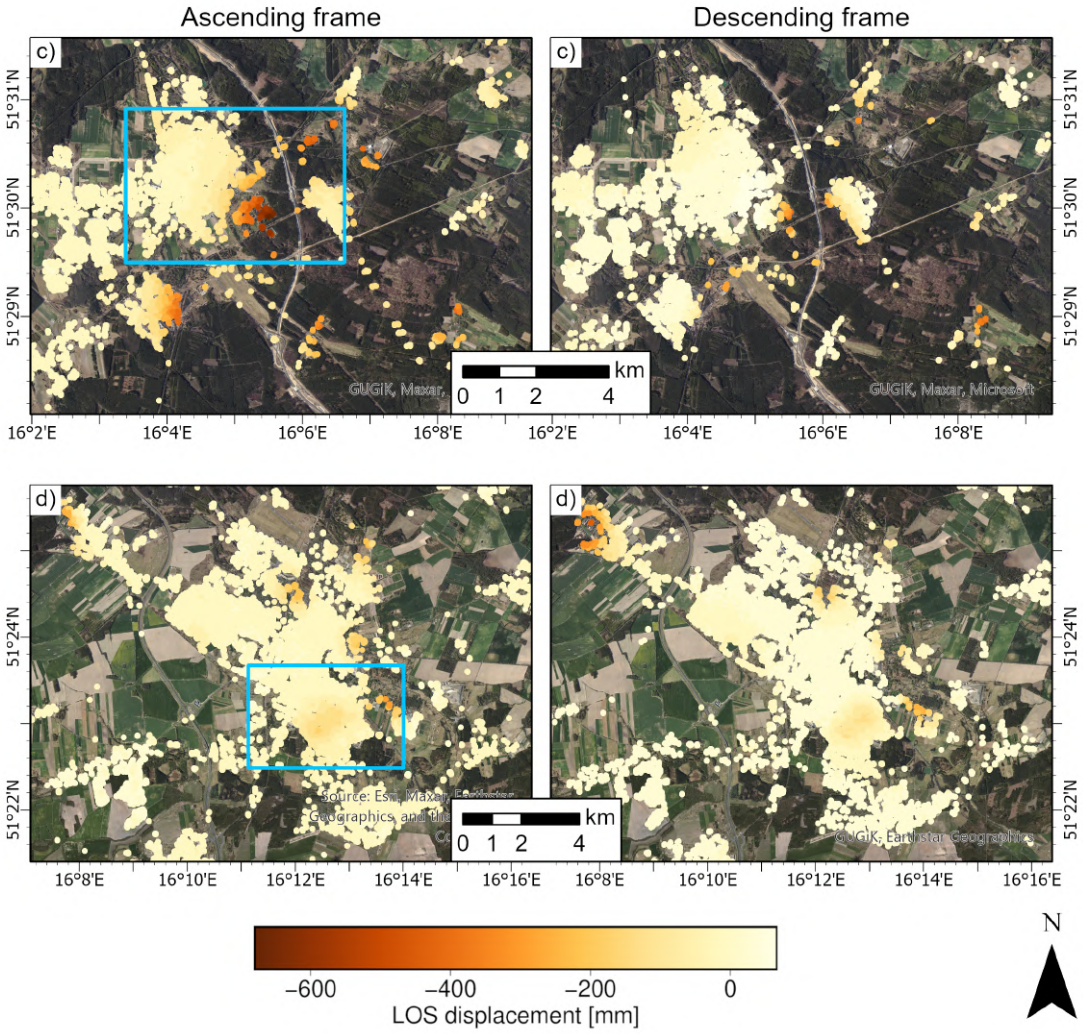

Figure 8.4: PS processing results of ascending (left) and descending (right) data for subareas highlighted in Fig. 8.1.

Figure 8.4 contains two areas highlighted in blue, for which separate maps of PS points have been created, shown in Figures 8.5 and 8.6. These two maps highlight the density of PS points, obtained over the study area, with examples covering urban and non-urban areas. PS point locations shown in Figures 8.5 and 8.6 have been obtained for the ascending SAR data. As one can see both in Figures 8.5 and 8.6, the majority of PS points detected in the area are located in built-up areas and on man-made structures, such as buildings, roads or electricity poles.

Figure 8.5 gives a detailed insight into the location of the PS points detected on the SAR imagery set, in the Polkowice town. While majority of the area does not show signs of land deformation, non-zero displacement values are present in part

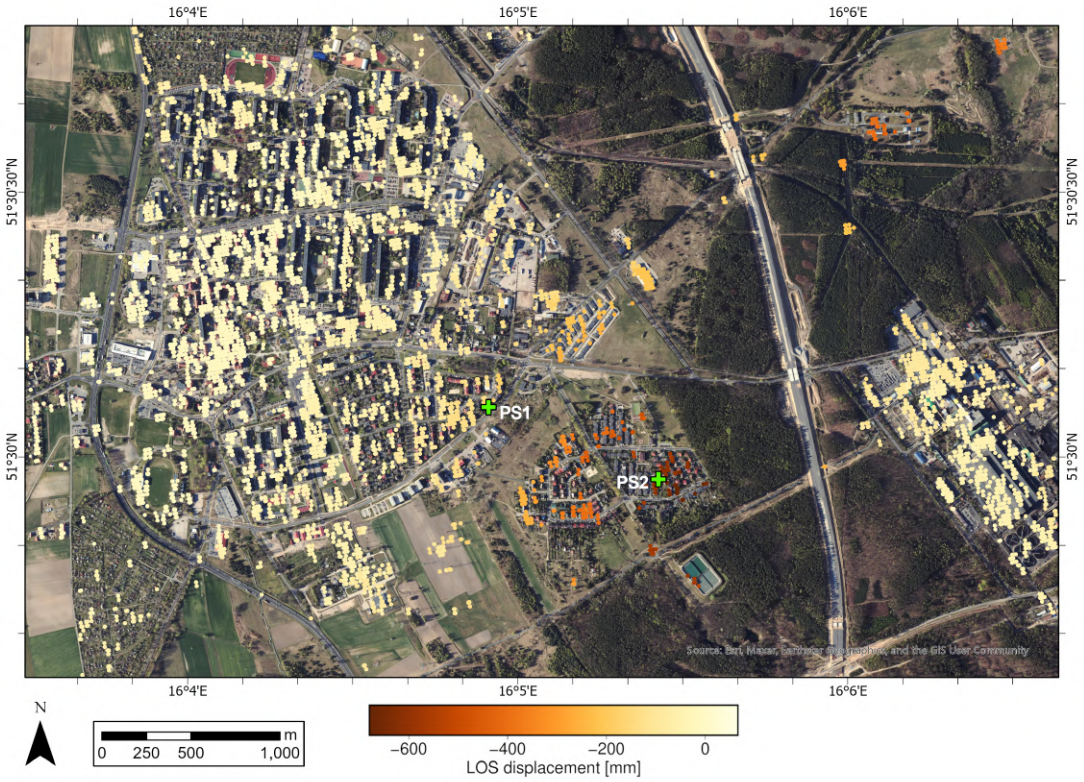

Figure 8.5: Map of PS points detected over the area highlighted in Fig. 8.4c (Polkowice town)

of the town (visible in the central part of the figure). Displacement values increase from west to east, with peaks in the easternmost parts of the city. Points further east were not detected due to the presence of forests. Based on the values at the individual points, a pattern of displacement is outlined, indicating the existence of a subsidence trough in this area.

Figure 8.6 shows a map of the PS points detected for a fragment of the town of Lubin. Although not as significant as in the previous figure, negative displacement values can also be observed in this area. The displacement values of the points are arranged in a circular shape, with the centre near the middle of the figure. This also indicates the presence of a subsidence basin in this area, in the build-up zone, where LOS displacements reach values of up to -200 mm.

A number of points have been highlighted on both Figures 8.5 and 8.6, for which time series plots of displacement values were prepared. These time series plots include displacement time series in selected points from both ascending and descending data. Figures containing these plots, together with time series plots of vertical displacements derived from ascending and descending data, will be shown in subsection 8.1.3.

8.1.2 InSAR processing - Small Baseline (SB) method

Similar to the PS analysis, the SB analysis was carried out for 2 independent acquisition paths covering the study area. It should be noted that the PS and SB method analyses were carried out on the same SAR datasets from corresponding acquisition paths, for subsequent comparison of results. The result of SB processing of SAR interferograms are time series values of displacements over the study area,

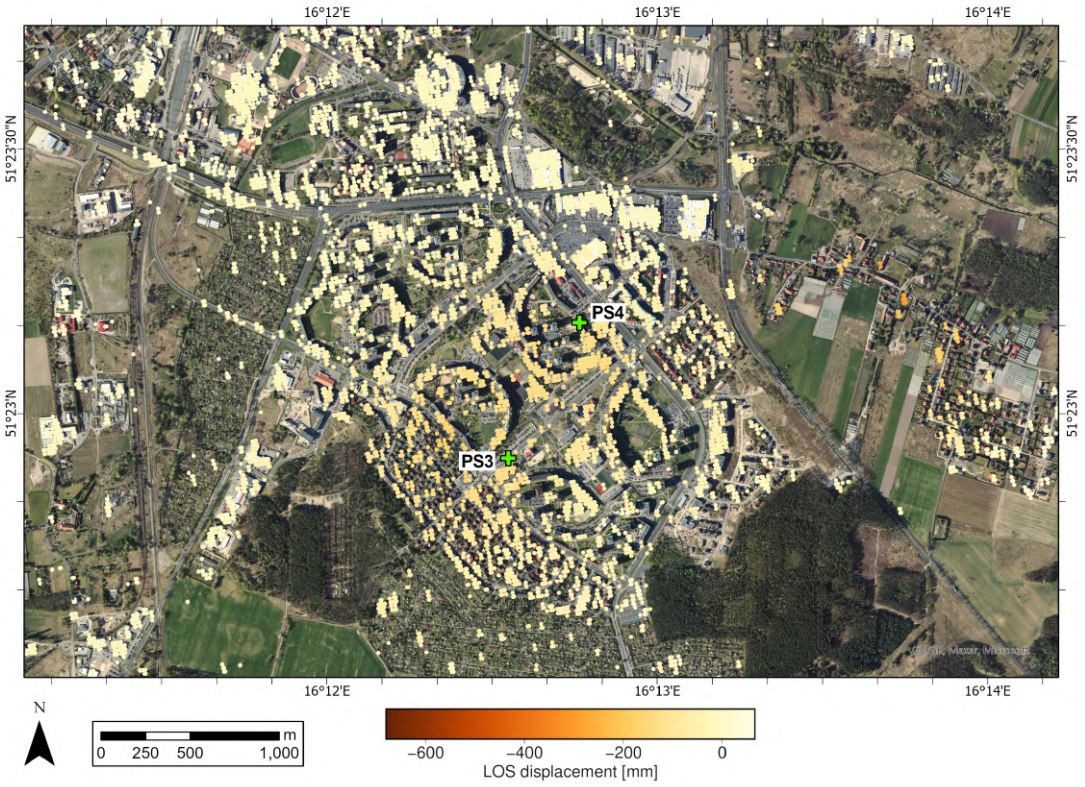

Figure 8.6: Map of PS points detected over the area highlighted in Fig. 8.4d (Lubin town)

resampled to a 30-meter resolution grid during processing. The temporal resolution of the displacement time series was 6 days, corresponding to the Sentinel-1A/B temporal resolution of acquisition.

Results of subsequent processing of ascending and descending SAR data using the SB method are presented in Figure 8.7. Areas highlighted with red rectangles are areas in which the data from leveling measurements and spatial extents of mining fields are provided. A validation of InSAR measurements of displacements will be carried out within these three areas, in subsection 8.1.3.

Presented in Figure 8.7, the results of SBInSAR processing of SAR imagery clearly show the spatial distribution of ground surface displacements in the study area. Individual zones of LOS displacement are visible on the results from both data acquisition paths. These zones assume mostly circular shapes, resembling the extent of subsidence basins. It is worth noting that the ground surface displacements visible in the results do not reflect the total extent of subsidence troughs present in the study area, but only the extent of LOS displacements in their area during the study period.

Zones of displacement were mainly observed in the Sieroszowice (north-western part of the study area) and Rudna (central part of the study area) mining areas. Single zones were also observed in the areas of: the southern part of the Głogów Głęboki-Przemysłowy mining area (northern part of the study area), the eastern part of the Polkowice area (south of the Rudna mining area) and the Lubin-Małomice area (south-eastern part of the study area). Significant displacement values were also measured in the *Żelazny Most* tailings dam area, located in the eastern part of the study area.

The maximum cumulative displacement values in the visible zones reach -1080

mm for the ascending path and -1220 mm for the descending path (displacement zone in the Polkowice area). The displacement values in the other displacement zones range from -400 mm to -900 mm. It should be emphasised that long-term displacements of the order of -100 mm (approximately -20mm/year) were observed over a major part of the study area.

Data shown in Figure 8.7 represents cumulative displacement values over the entire study period. It should be noted that the result of SB processing is a time series of displacements, obtained for each of the dates shown in the SB network. For each of the pixels, shown in the ascending and descending SB processing results, a time series of displacement can be derived. For visualisation purposes, example time series of displacements from the SB method will be shown in the later subsection 8.1.3, together with time series of vertical displacements calculated using data from two acquisition paths, and with displacement values measured using the leveling technique.

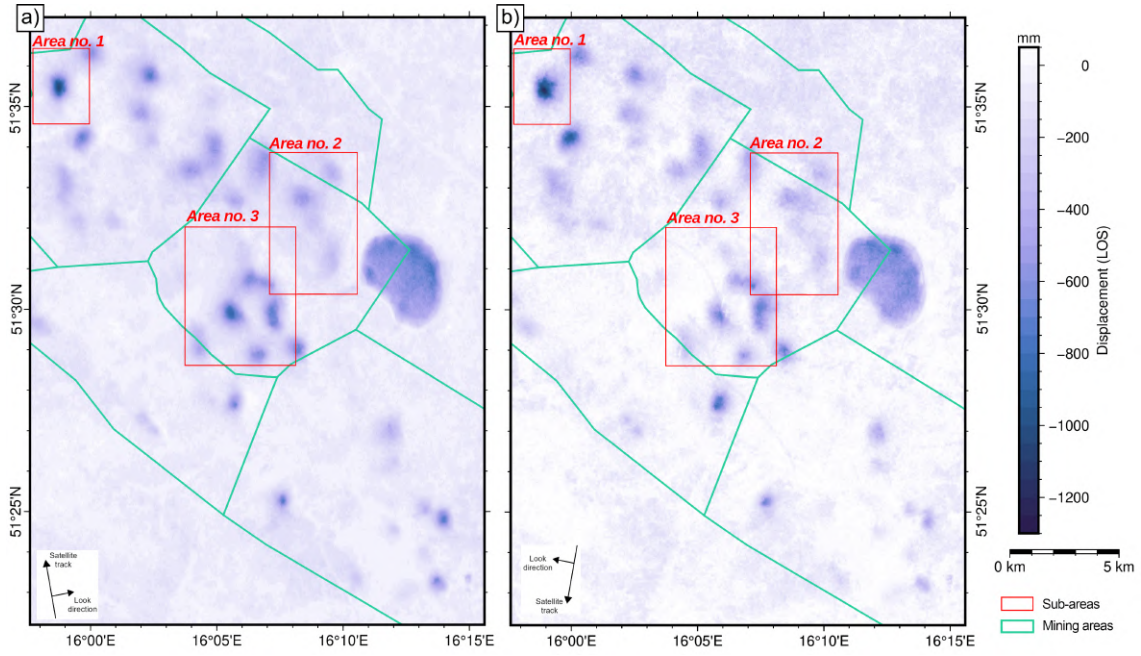

Figure 8.7: Results of Small Baseline (SB) InSAR processing of ascending (a) and descending (b) SAR data

The spatial distribution of the cumulative displacement values shows an offset of the subsidence areas relative to each other on the results from the two independent paths. This phenomenon is highlighted in Figure 8.13, which shows the contour lines of the areas of subsidence (values of -200 mm) for the two imaging acquisition paths. As mentioned in previous chapters regarding the horizontal displacements and their influence on the LOS measurements, this offset may be an evidence of horizontal movements present in the study area. As the ground surface in the area of a subsidence trough is prone to both vertical and horizontal displacements, the Line-of-Sight measurement using satellite SAR interferometry will be subject to displacements in both vertical and horizontal directions. The offset seen in the results of the SB method for the ascending and descending paths justifies the need for a vertical and horizontal displacement analysis using measurements in the Line-Of-Sight of the satellite. The results of the projection of LOS measurements to vertical and horizontal time series displacements will be presented in the next subsection.

8.1.3 Determination of vertical and horizontal displacements

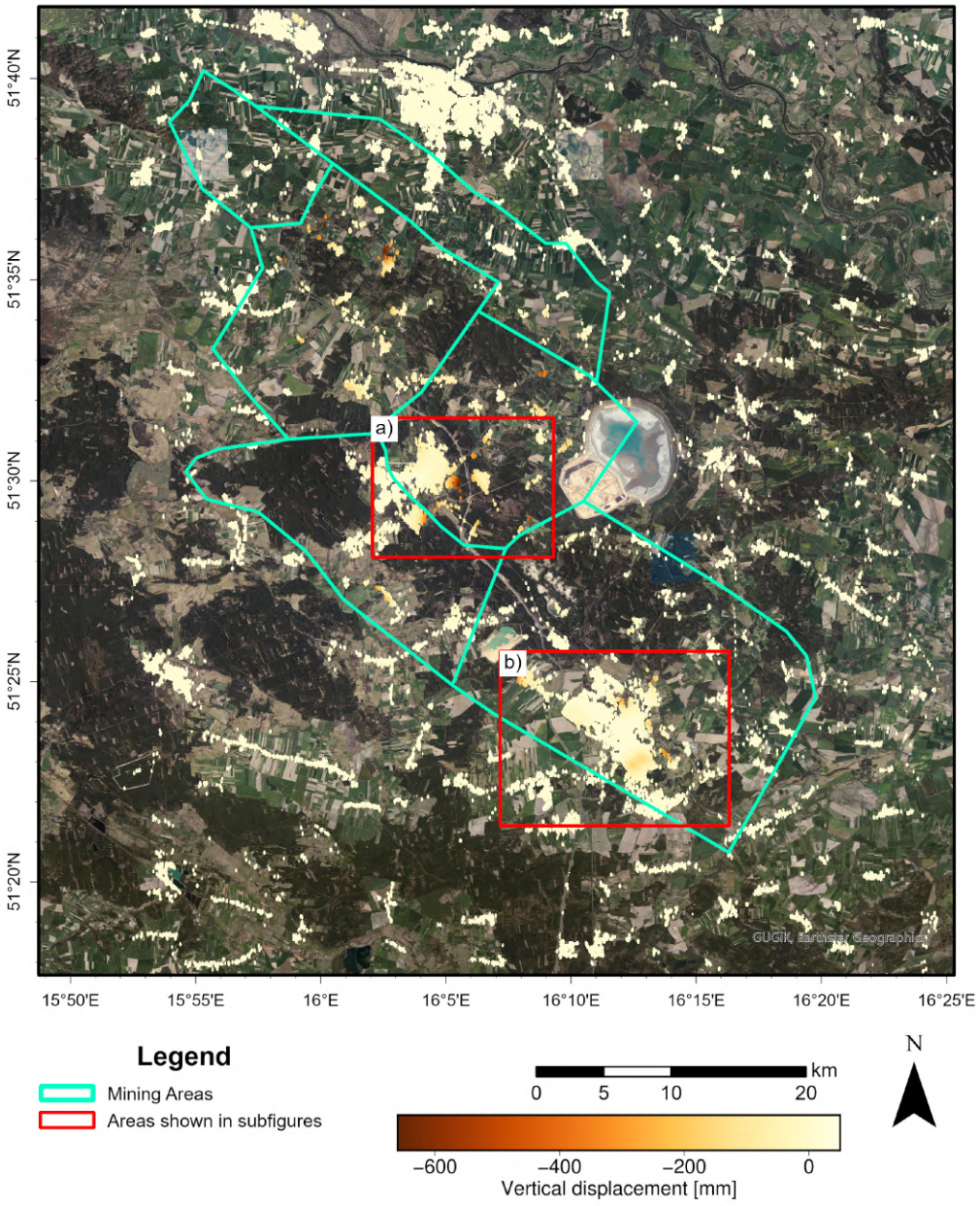

Figure 8.8: Vertical component of displacement after projecting PSInSAR results ascending and descending paths. Cumulative values of displacement for the study period (20 May 2016 - 26 October 2020)

Ground surface displacements measured by InSAR techniques in the satellite LOS were transformed to vertical and horizontal (in the East-West direction) displacements using the methodology described in Chapter 6.4. Decomposition of the LOS displacements was performed for the time series of displacements obtained by both the SB method and the PS method. The decomposition results are time series of land surface displacements in the vertical direction (subsidence or uplift) and in the horizontal east-west direction. Displacement maps were produced for both the SB and PS methods. In order to determine the time series of vertical and horizontal displacements, assumptions were made regarding the temporal resolution of

measurements, due to the offset between the acquisition dates of the ascending and descending path images (3 days). It was assumed that vertical displacement values would be determined for the dates of the images acquired from the ascending path. The dates for data from the descending path were therefore shifted 3 days forward in time with respect to the image acquisition dates. The vertical and horizontal displacement values presented are for the period from 20 May 2016 to 26 October 2020.

Displacement components obtained from PS method

Displacement components in the vertical and horizontal East-West (E-W) directions were successfully determined by decomposing the LOS displacements measured on the ascending and descending paths for the PSInSAR method. The results of the processing are the vertical and horizontal displacement maps of the study area, shown in Figures 8.8 and 8.9 respectively. As with the results from the individual data acquisition paths, the maps show the cumulative displacement values measured for the period under study. Due to the methodology adopted for decomposing the displacements from the PS measurements (resampling points to a regular square grid), the values of the displacement components were determined only at the locations where the displacements were measured for the two acquisition paths. Points with a displacement value measured only from the ascending path, or only from the descending path, were discarded.

Figure 8.8 presents cumulative values of vertical displacement in the study area, obtained using ascending and descending LOS displacement decomposition. The result obtained in terms of spatial distribution of displacements is similar to the results from single acquisition paths. Slight differences can be seen in the position of the displacement zones compared to the results from the ascending and descending paths, particularly in the east-west direction. Another difference is in the cumulative values of point displacements, and the time series of displacements for the ascending and descending paths, and vertical displacements. The differences in displacement values in the time series will be discussed later on.

Cumulative values of horizontal displacements (in the East-West direction) are shown in Figure 8.9. The result in the form of horizontal displacements is characterised by a different distribution of displacements than the results obtained for LOS measurements and vertical displacements, which were dominated by displacements with a negative sign (subsidence for the vertical component). The obtained values of horizontal displacements have a positive or negative sign. Horizontal displacements should be interpreted in such a way that displacements with a positive sign (red color) represent eastward displacements, while those with a negative sign (blue color) represent westward displacements. The highest values of displacement in the horizontal direction were observed in the subsidence zones discussed in subsection 8.1.1. The highest values of horizontal displacement in the west direction reached 245 mm (shown with a negative sign in the figure), while in the east direction 385 mm.

Two sub-areas were highlighted in Figures 8.8 and 8.9, covering towns of Polkowice and Lubin (*a)* and *b)*, respectively). The vertical and horizontal displacements in these sub-areas are shown in Figure 8.10. When comparing the vertical and horizontal displacement values displayed, it is important to note the spatial distribution of the displacements. The highest values of horizontal displacements are observed in the subsidence regions. This is consistent with the theoretical pattern of dis-

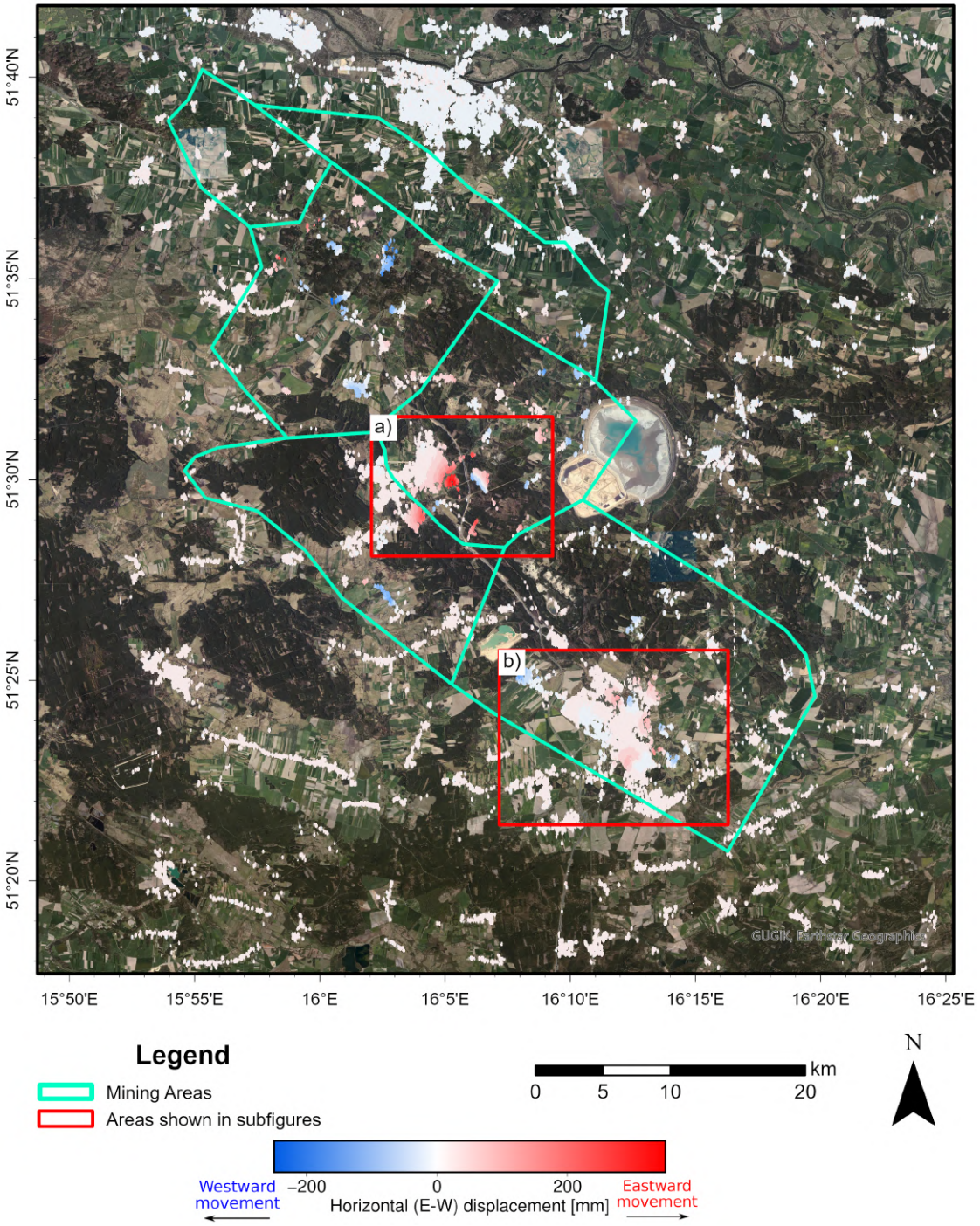

Figure 8.9: Horizontal component of displacement in the East-West direction obtained for the PSInSAR measurements. Cumulative values of displacement for the study period (20 May 2016 - 26 October 2020)

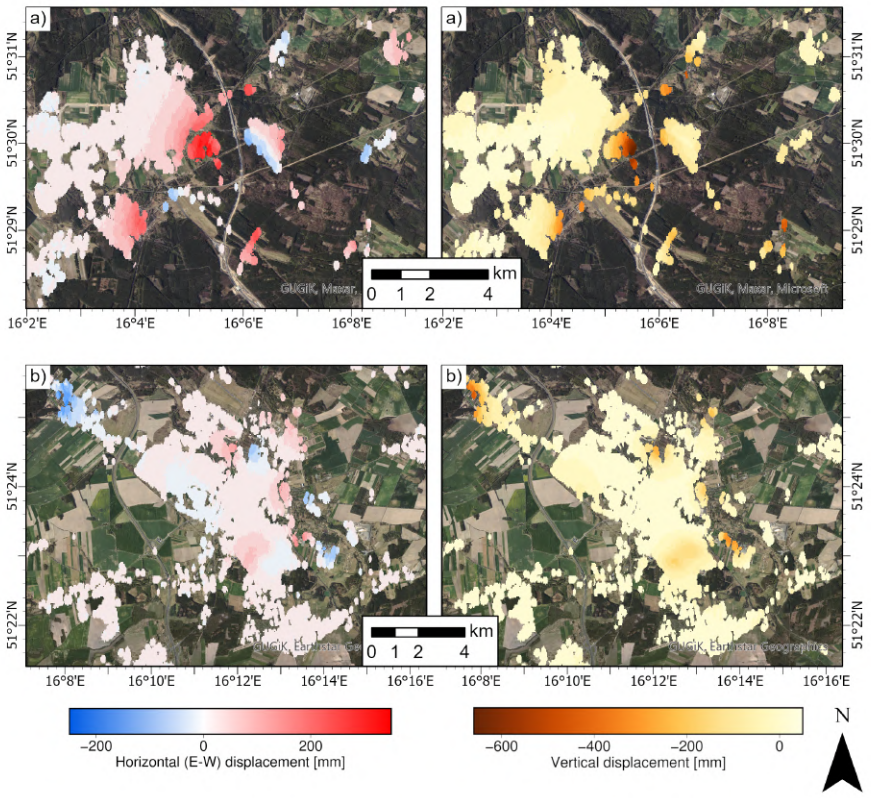

Figure 8.10: Horizontal and vertical displacements measured with the PS method after decomposition, for selected sub-areas *a)* and *b)*.

placements within the subsidence trough, where the highest vertical displacement (subsidence) is observed in the central part of the trough, while horizontal displacements are observed at the edges of the trough, with no horizontal displacement in the trough center. A good example of this phenomenon are the subsidence zones in the central part of sub-area *b)*, where the observed values of horizontal displacement are low in the area of the highest subsidence (center of the subsidence zone), while the values increase in areas away from the centre of the subsidence zone. For the subsidence zones listed, a regularity can be observed in which the left side of the zone is displaced to the east (towards the centre of the zone) and the right side accordingly is displaced to the west (also towards the centre of the zone). This indicates that the ground surface within the subsidence trough is subject to horizontal displacements towards the centre of the basin.

Figure 8.11 shows the time series of displacements at selected PS point locations, highlighted in Figures 8.5 and 8.6. Time series were produced for LOS displacements measured for ascending and descending paths, and for vertical displacements after decomposition of LOS displacements. From the time series plots, differences can be noticed between the displacements measured in 2 different geometries and after decomposition of the LOS displacements. The example of point PS1 shows how displacement values can be measured differently by two different lines of sight. While the LOS displacement measured by the ascending path reached about -150mm and indicates subsidence, the descending path measured a value of about +50 mm indicating uplift. The discrepancy in values may be due to the presence of horizontal displacement in the study area. Decomposition of the LOS signals results in a ver-

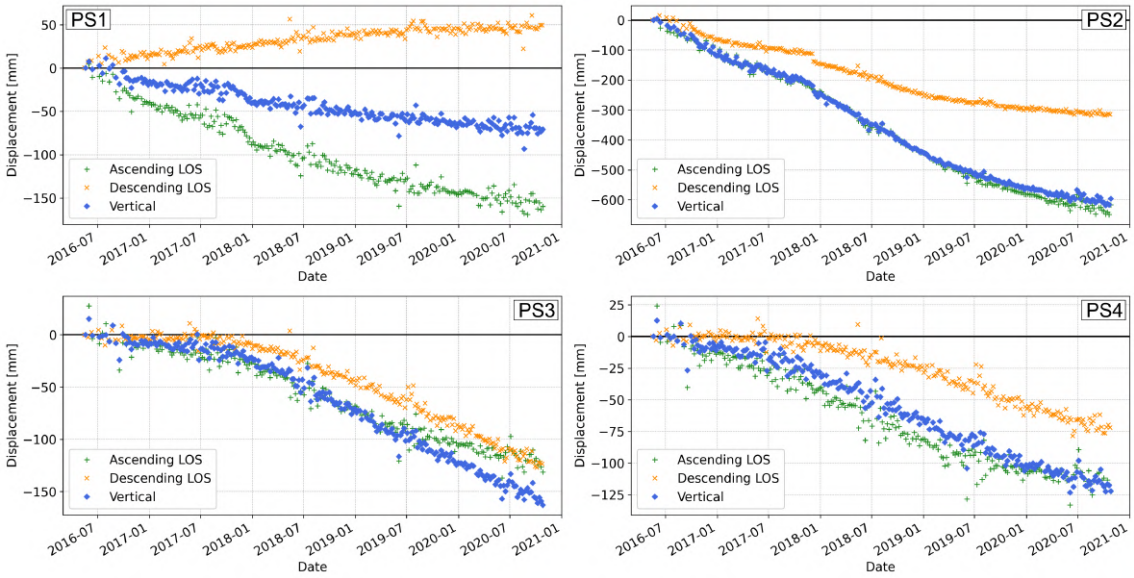

Figure 8.11: Time series of displacements measured using the PSInSAR method. Vertical displacement time series were obtained through decomposition of LOS displacements. Locations of points were highlighted in Figures 8.5 (PS1 and PS2) and 8.6 (PS3 and PS4)

tical displacement value of approximately -70 mm. The values obtained at PS2 indicate a possible underestimation of vertical displacement by one of the acquisition paths. In this case, the decomposition showed a vertical displacement more similar to that measured by the ascending path. A similar phenomenon, but of lower magnitude, was observed at point PS4. Point PS3, on the other hand, showed similar values of the total LOS displacement (with a slightly different time series), while the vertical displacement after decomposition has a higher value. It should be noted that the displacement values, obtained from the LOS measurements and after decomposition to vertical and horizontal components, should be verified using ground truth data. However, no *in situ* measurements were available for the locations studied in Figure 8.11. A better overlap of the displacement measurements with the field measurements was achieved for the SB method results, so a comparison of the time series of the different displacement values (LOS and vertical) with the *in situ* data will be carried out for the SB results in the next subsection.

Displacement components obtained from the SB method

Decomposition of the LOS signals from the ascending and descending paths of the SAR data acquisition was also carried out for the results of the SBInSAR method, following the methodology presented in Section 6.4. The results obtained in the form of vertical displacements and horizontal displacements in the east-west direction will be presented, with emphasis on the differences between LOS data and vertical displacements. Vertical displacements after decomposition of SB LOS displacements will be compared with vertical displacements after decomposition of PS measurements.

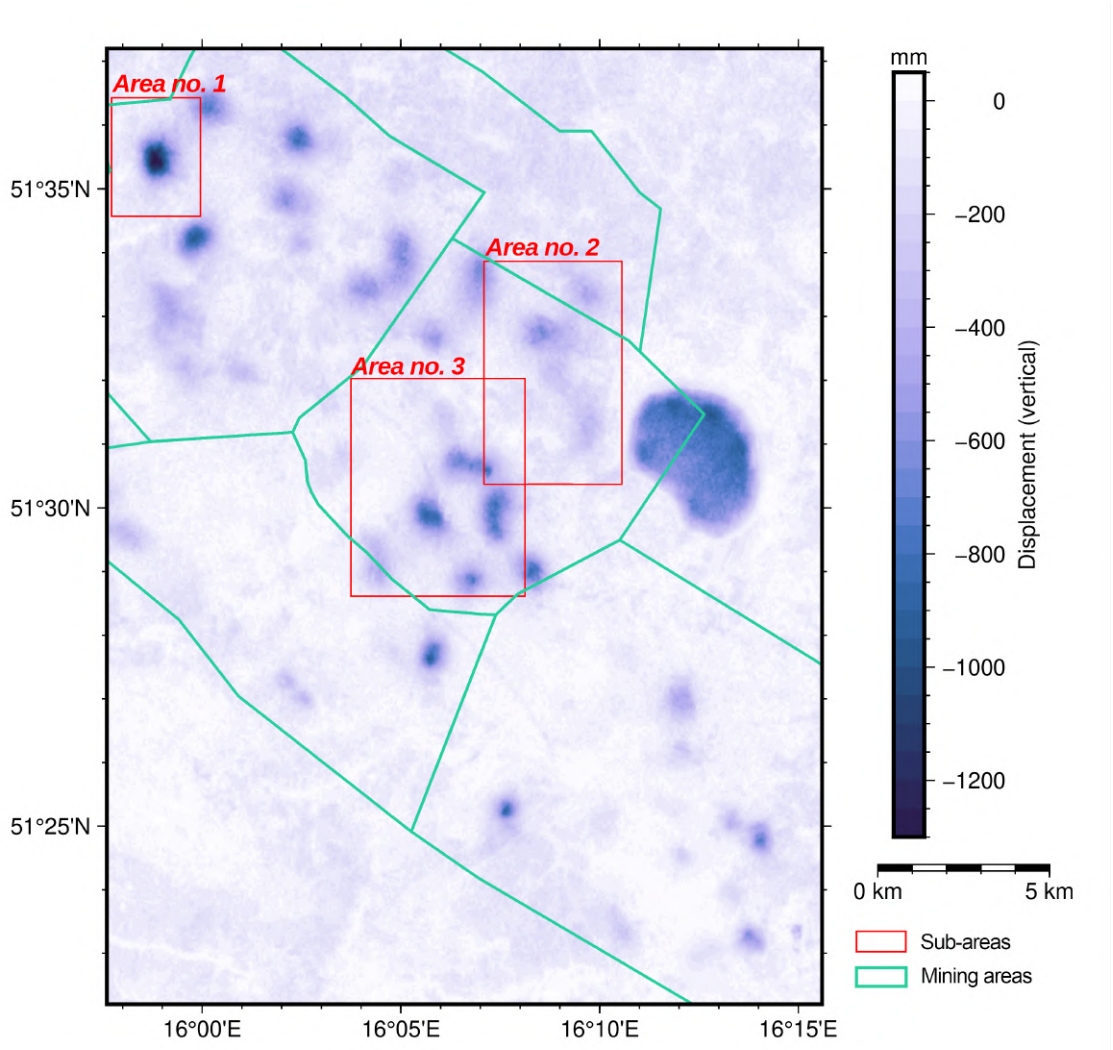

Figure 8.12: Vertical displacements measured by SBInSAR after decomposition. Areas with leveling data were highlighted

Figure 8.12 shows the result of the decomposition of the LOS displacements measured by the SB method, in terms of the vertical component of the displacement. Areas highlighted in Figure 8.12 are areas in which data with leveling measurements and mining fields are available. Zones of negative vertical displacements (subsidence) can be located in the study area. The location of these zones coincides with the location of the zones in Figure 8.7 showing the LOS displacements for the ascending and descending paths. The locations of zones on the results from the ascending and descending paths are shifted relative to each other, the result for vertical displace-

ments is also shifted relative to the ranges of zones on the LOS measurements. As was already mentioned, the offset between the displacement zones in two independent acquisition paths might be a result of horizontal displacements present in the area. Through the acquisition geometry of SAR data, the LOS deviates from the nadir by the look angle, thus - if there is a presence of horizontal displacements - shifting the results from the ascending and descending paths slightly. Therefore, it can be hypothesised that the actual vertical displacement field is located between the fields observed on the LOS measurements. This is confirmed by Figure 8.13, showing a map of vertical displacements in Area No. 1 highlighted in Figure 8.13, with -300 mm displacement contour lines superimposed.

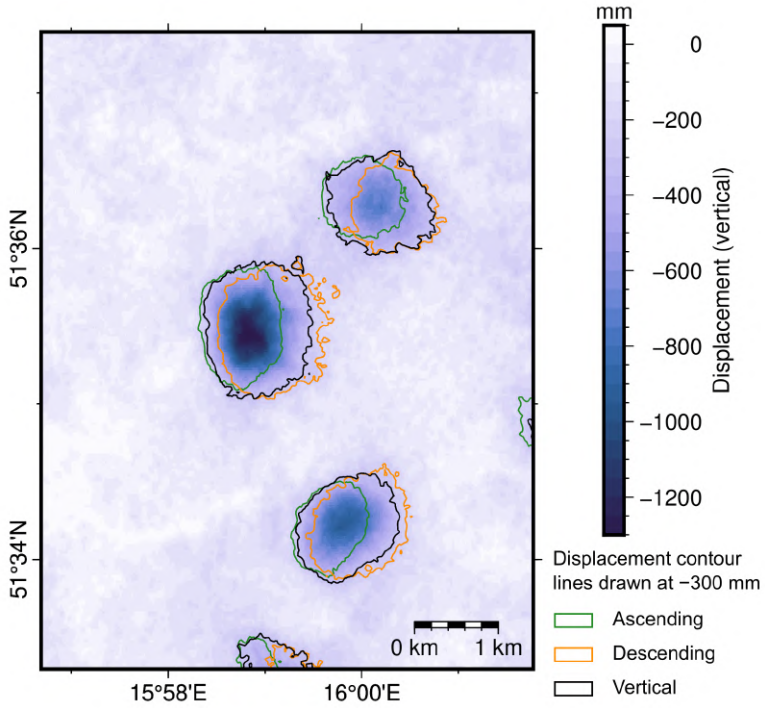

Figure 8.13: Vertical displacements measured with SBInSAR in Area No. 1 (highlighted in Figure 8.12), with contour lines drawn at -300mm for ascending, descending and vertical

From Figure 8.12 it is possible to read the cumulative values of vertical displacements measured by the SBInSAR method from 20 May 2016 to 26 October 2020. The ground surface in the study area is subject to subsidence, caused by mining activities in the area. The maximum measured subsidence in the study area is -1300mm, observed in the subsidence zone in Area 1 (Sieroszowice mining area). In the other subsidence zones, cumulative displacements ranging from -700 mm to -950 mm were observed. Majority of subsidence zones are recorded in the Sieroszowice and Rudna mining areas. This indicates that underground mining activities must have been carried out primarily in these two mining areas. The presence of subsidence outside the main zones with the highest displacement should also be emphasised. Outside these areas, slow subsidence is observed, adding up to values between -50 mm and -150 mm. Scattered zones of subsidence can also be observed in the Głogów Głęboki-Przemysłowy, Polkowice and Lubin-Małomice mining areas.

The horizontal component of displacements in the east-west (E-W) direction is shown in Figure 8.14. Horizontal displacements with a negative sign (in the west direction) and with a positive sign (in the east direction) occur in the study area.

Comparing the locations of the horizontal displacements with the locations of the vertical displacements in Figure 8.12, a relationship similar to that for the decomposition results of the PS measurements can be observed. Due to the coverage of the entire analysis area by the SB results, more zones of horizontal displacement are visible than on the PS method results. Again, the zones of greatest horizontal displacement are located in the areas with the highest subsidence. Horizontal displacement values observed in the area range between 500 mm to the west (marked as -500 mm in the figure) to 500 mm to the east (marked as +500 mm in the figure). As can be seen from the horizontal displacement map, large parts of the Sieroszow-

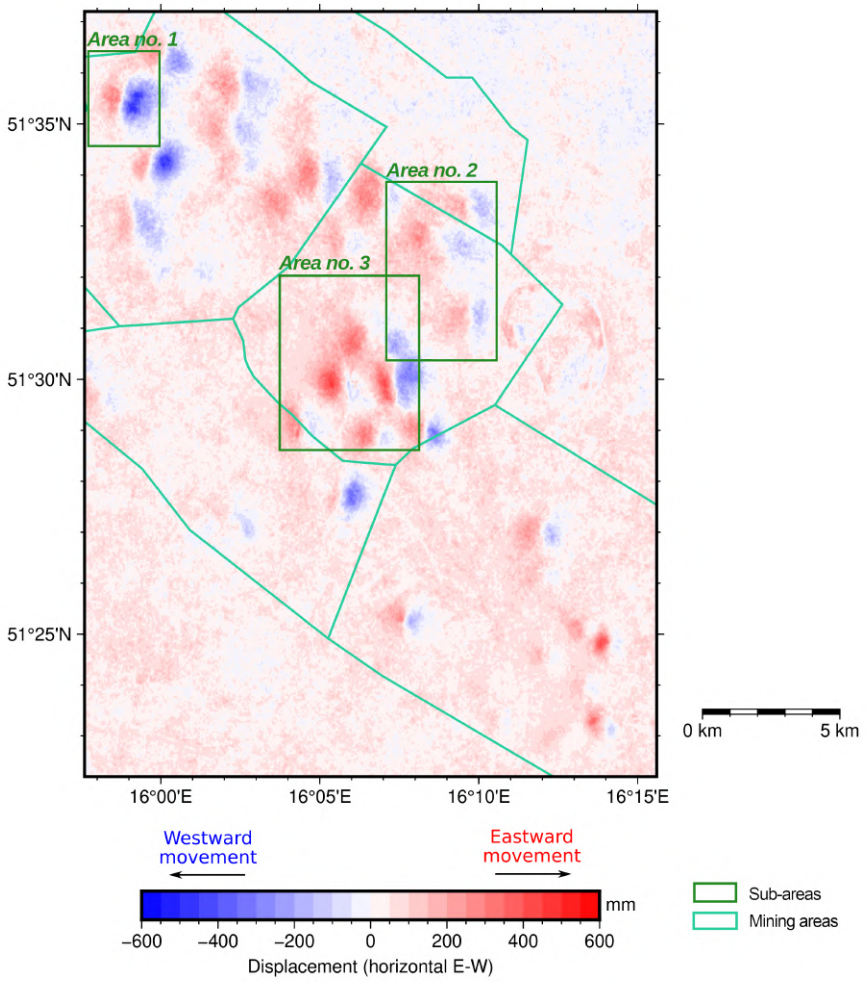

Figure 8.14: Horizontal displacements (in the East-West direction) measured by SBInSAR after decomposition. Areas with ground truth data are also highlighted

ice and Rudna mining areas are subject to significant horizontal displacement. This observation confirms the importance of taking horizontal displacements into account when projecting LOS InSAR observations to vertical displacements.

The temporal development of displacements is presented by cross-sections, on which the time series of displacements are marked (each line representing a single epoch in the time series analysis). The cross-sections are highlighted in the Figures 8.17 to 8.19 in the next subsection. The selected cross-sections presented in Figure 8.15 highlight the time series of displacements for the LOS measurements (ascending - green and descending - orange), as well as the time series of vertical

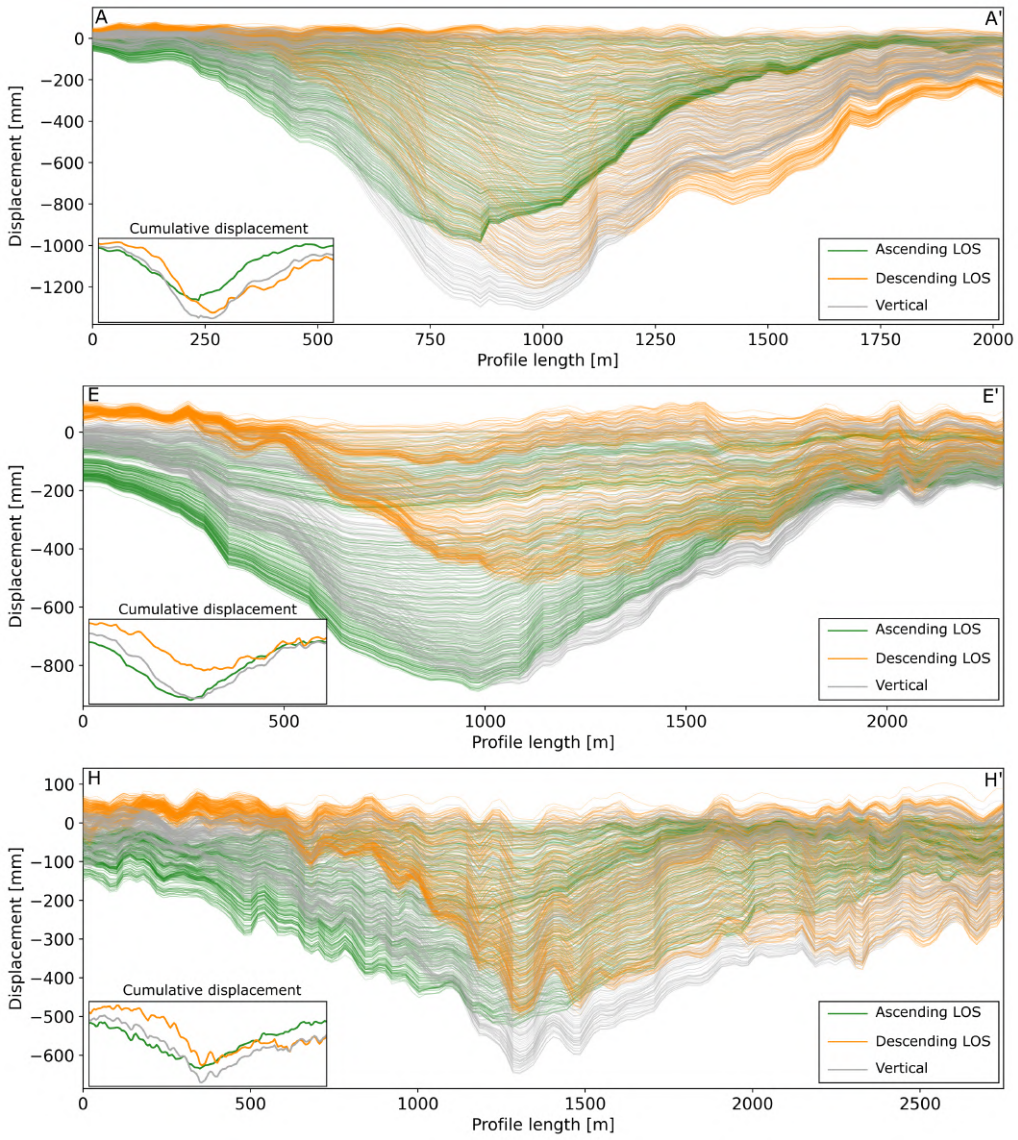

Figure 8.15: Time series profiles derived from ascending (green) and descending (orange) LOS SBInSAR measurements, compared with vertical (gray) time series of displacements. Locations of profiles are highlighted in Figures 8.17 (AA'), 8.19 (EE') and 8.18 (HH').

(gray) displacements determined by decomposing the LOS values into displacement components. The cumulative displacement values in cross-section are included in the bottom left corner of each cross-section.

Two dependencies can be observed in Figure 8.15. Firstly, with reference to the analysis of the position of the settlement areas relative to the LOS measurements and the vertical displacement values, the cross-sections again show that the course of the displacements observed by the two independent paths differs in the horizontal plane. The time series from the ascending and descending paths are shifted relative to each other in the satellite direction, due to the imaging geometry. The extents of the subsidence troughs may therefore be misinterpreted if measurements from a single acquisition path are used. Secondly, it is important to note the displacement values, especially the cumulative values over the study period. As can be seen in sections AA', EE' and HH', the vertical displacement values are frequently higher than the LOS values. This may indicate that the actual vertical displacement values may be underestimated by the LOS measurements (a factor caused by the skewed

imaging geometry). In order to confirm this assumption, verification of the InSAR measurements with field measurements is necessary.

Comparison of vertical displacements from PS and SB methods

The vertical displacement values determined for the PSInSAR and SBInSAR measurements were compared in terms of cumulative displacement values. The comparison was made for the PS points where the vertical displacements were determined. For each of these points, the displacement measured by the SB method at that location was assigned.

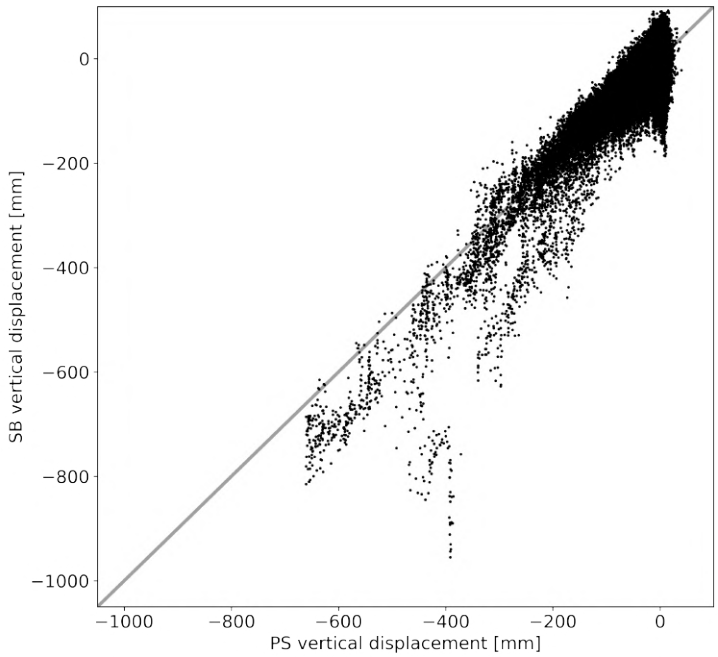

Figure 8.16: Comparison of cumulative vertical displacement values observed in locations of PS points from both PS (X-axis) and SB (Y-axis) InSAR methods

Figure 8.16 presents a scatter plot comparing the vertical cumulative displacements measured by the SB (Y-axis) and PS (X-axis) methods. A significant correlation between the values obtained by the PS and SB methods can be deduced from the plot, especially for the values of vertical displacement not exceeding -200 mm. However, it is important to note the relationship between high subsidence values. With values exceeding -300 mm for the SB method, the cumulative values obtained for the PS method are generally lower than for the SB method. In the most extreme case, a displacement of approximately -950 mm in the SB method was measured by the PS method as only -400 mm. This would indicate that the PS method underestimates high displacement values, or that the SB method overestimates them. The differences in cumulative vertical displacement values range from approximately 100 mm to 200 mm for the two methods. In the next section, these results will be compared with the displacements obtained at the leveling points by leveling measurements, in order to verify which method is more effective in determining vertical displacements in the study area.

8.1.4 Ground truth verification

The remote sensing measurements of ground surface displacements were verified using field leveling results and mining data. Data were obtained from the mining authority operating in the study area. The data included the results of the levelling measurements for the time period studied in the dissertation, as well as data on the monthly mining field operations conducted during the study period. Data were made available for 3 sub-areas selected within the study area. These sub-areas were highlighted in Figures 8.12 and 8.14. The leveling measurements were used to verify the vertical displacement values obtained after decomposing the LOS signals measured by the SB and PS methods. The LOS displacements from the SB method were also compared with the leveling results to verify the validity and justification of the displacement decomposition using data from two independent acquisition paths.

Overview of sub-areas with ground truth data

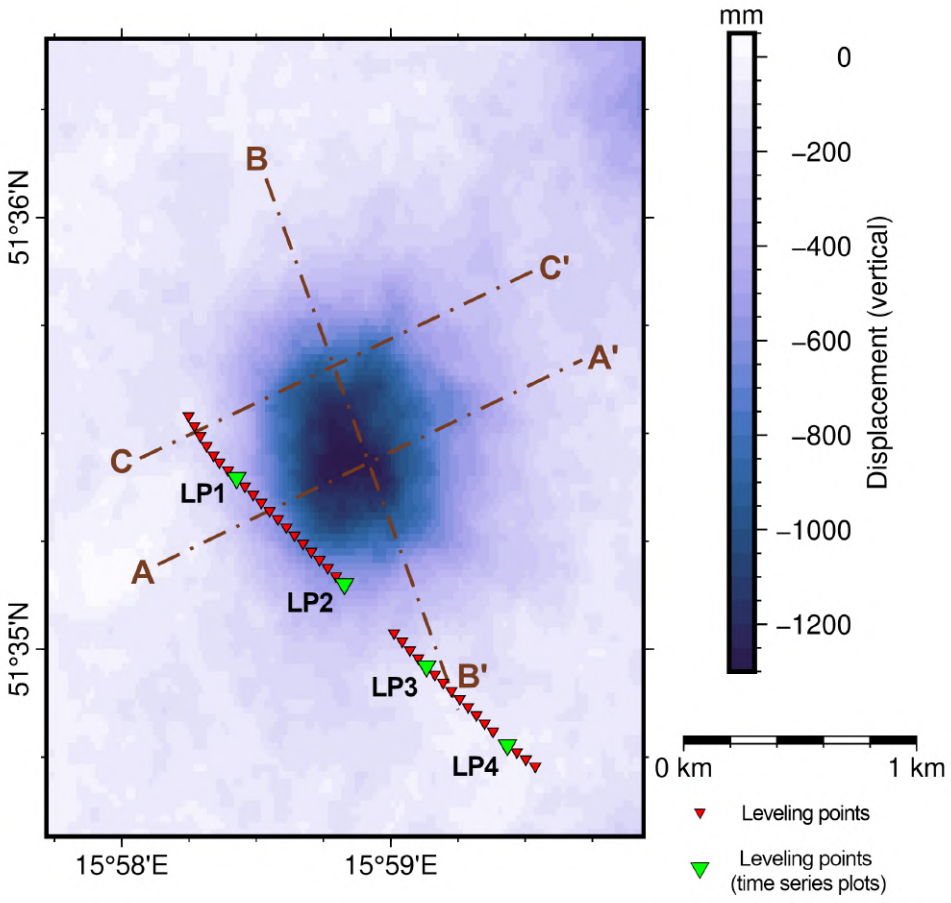

Figure 8.17: View of vertical displacements acquired using the SB method in Area No. 1, with leveling points and cross-section lines highlighted

Figure 8.17 presents Area No. 1, which includes a single subsidence zone in the north-western part of the study area, in the Sieroszowice mining area. The figure shows leveling points, for which the results of vertical displacement measurements were obtained. A total of 38 leveling points are located within this area. Time series

plots of displacements were prepared for the leveling points highlighted and labeled, which are shown later in this subsection. The figure also shows the lines for which cross-sections were prepared.

Area No. 2 is shown in Figure 8.18 and includes the north-eastern part of the Rudna mining area and to the north also a section of the Głogów Głęboki-Przemysłowy mining area. In contrast to Area No. 1, Area No. 2 contains a significant number of leveling lines covering a large part of the area, located also within zones where subsidence of the ground surface has been observed with InSAR methods. There are a total of 275 levelling points in the extent of Area No. 2. Two cross sections have also been marked in this area (GG' and HH').

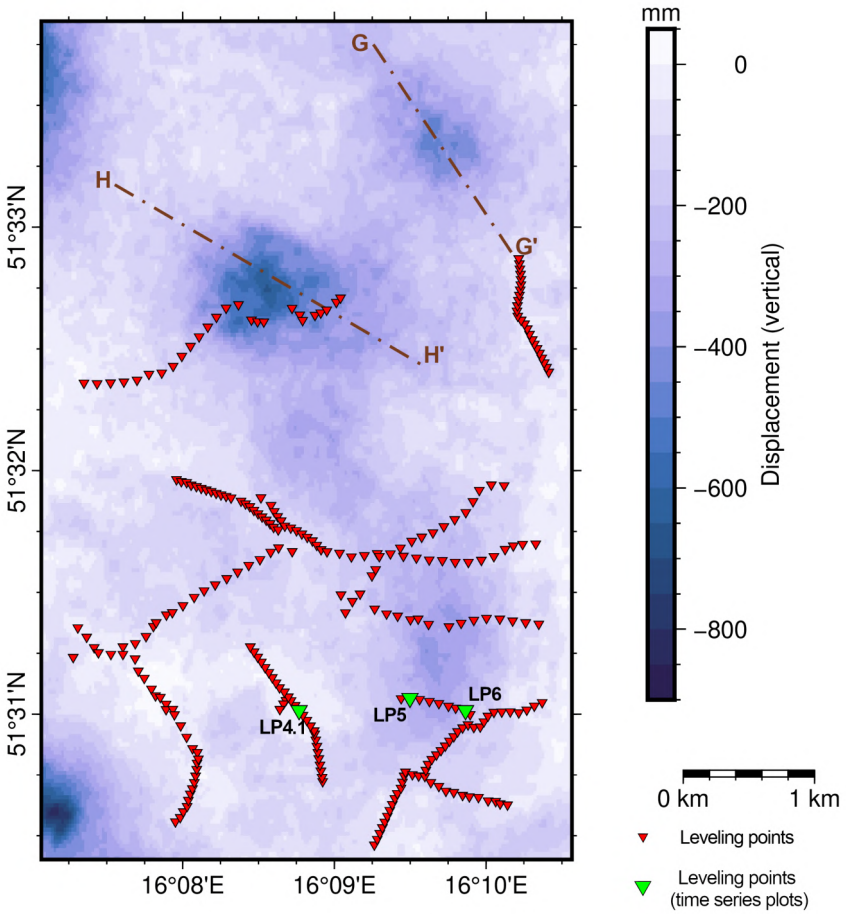

Figure 8.18: View of vertical displacements acquired using the SB method in Area No. 2, with levelling points and cross-section lines highlighted

Figure 8.19 shows the extent of Area No. 3, with visible vertical displacements measured using the SB method. Area No. 3 covers the central and south-western part of the Rudna mining area. Area No. 3 contains 438 leveling points, combined into leveling lines crossing the study area, in particular through areas where subsidence was detected using the SB method, but also through areas with very low or no subsidence. This should ensure the InSAR measurements to be accurately verified, both for sites with high subsidence values and sites with low vertical displacements.

Verification of displacements measured by the PS method

The previous subsection included a comparison of the cumulative vertical displacement values observed with the PS and SB methods, at the locations of PS measurement points. A pattern was observed showing that at points with high values of vertical displacements, the values measured by the PS method were generally lower than those obtained by the SB method. Therefore, a comparison of the cumulative displacement values with the displacements measured by levelling measurements will confirm which method achieved values closer to the true subsidence values in the studied area.

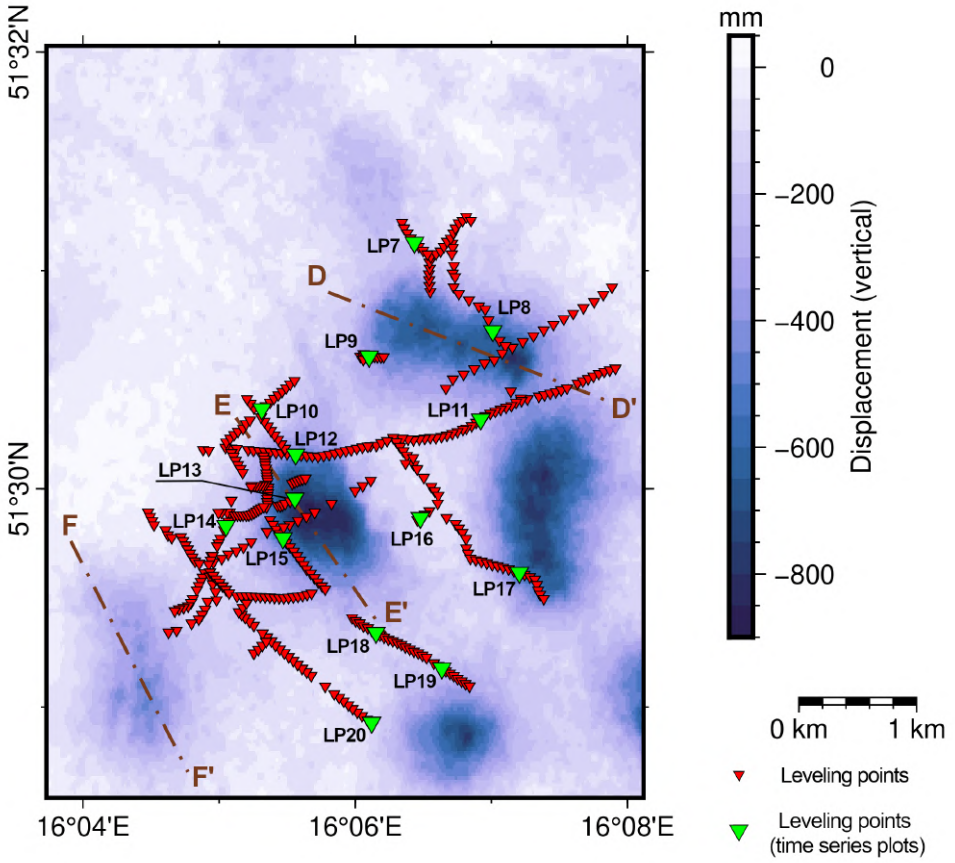

Figure 8.19: View of vertical displacements acquired using the SB method in Area No. 3, with levelling points and cross-section lines highlighted

Figure 8.20 shows scatter plots of the (cumulative) displacement values measured by the leveling method (X axis) and the PS and SB methods (Y axis). The values were observed at the locations of the leveling points for which PS and SB displacement values were available. A total of 254 leveling points (out of 751 total) were selected for analysis. The results of both InSAR time series methods show a high correlation with the leveling measurements, with an R^2 coefficient of 0.95 for the PS method and 0.94 for the SB method. The main difference apparent when comparing the two graphs is the slope of the fitted trend line relative to the ideal fit ($x = y$). The results of the PS method are more deviated from the ideal fit than the results of the SB method. It should be pointed out here that for high values of vertical displacements measured by leveling, the results of the PS method are always lower than the leveling measurement. This indicates a general underestimation of

the cumulative displacements by the PS method. As indicated in Figure 8.20b, the problem also occurs in SB measurements, but the differences in underestimation of displacement values are lower for this method. Displacement values obtained by the SB method compared to field measurements will be discussed in more detail later in this subsection.

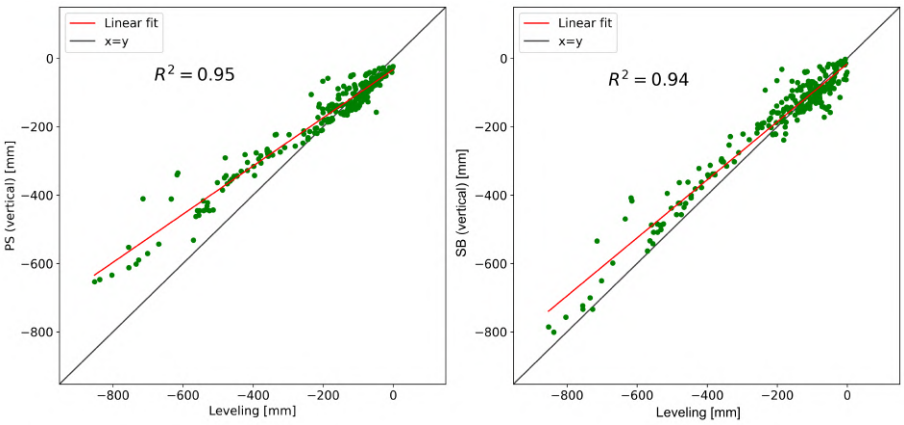

Figure 8.20: Comparison of vertical displacement values measured by the PS (a) and SB (b) methods with leveling measurements

At this stage of the study, it was decided to continue the study of vertical displacements in the study area using only the results of the SBInSAR method. The results of the PS method were excluded from further consideration for the following reasons:

- The study area is an area with diverse land cover, dominated by croplands, forests and, to a smaller extent, buildings. Therefore, the results of the SB method cover the study area better than the results of the PS method, which is due to the different methodology of processing SAR images by the two methods. With the increased coverage, the results of the SB method allow the impacts of underground mining activities on the ground surface to be observed in a more detailed manner.

- The smaller coverage of the study area by the PS points means that displacement measurements cannot be compared at all points for which field measurements were obtained. This was indicated during the analysis in Figure 8.20, where of all 751 leveling points, 254 had values of vertical displacement measured using PSInSAR.

- As indicated in this subsection, the results of the SB method agreed with the leveling measurements more than the results of the PS method. The dissertation analyses land surface displacements of varying magnitudes. Therefore, the validity of the displacements at both slowly subsiding points (e.g. on the periphery of the subsidence zones) and rapidly subsiding points (within the main subsidence zones) needs to be taken into account.

- The results of the PS method do not coincide spatially with the obtained mining field data. For the PS method, it is therefore not possible to spatially verify the measurement results with the mining extraction data.

Verification of SB time series with leveling data

The results of the vertical displacement measurements of the ground surface using the SB method were compared with the displacement values measured by the leveling method at the leveling points. During the verification of the SB method results, time series, cumulative values and annual average vertical displacement velocities were analysed.

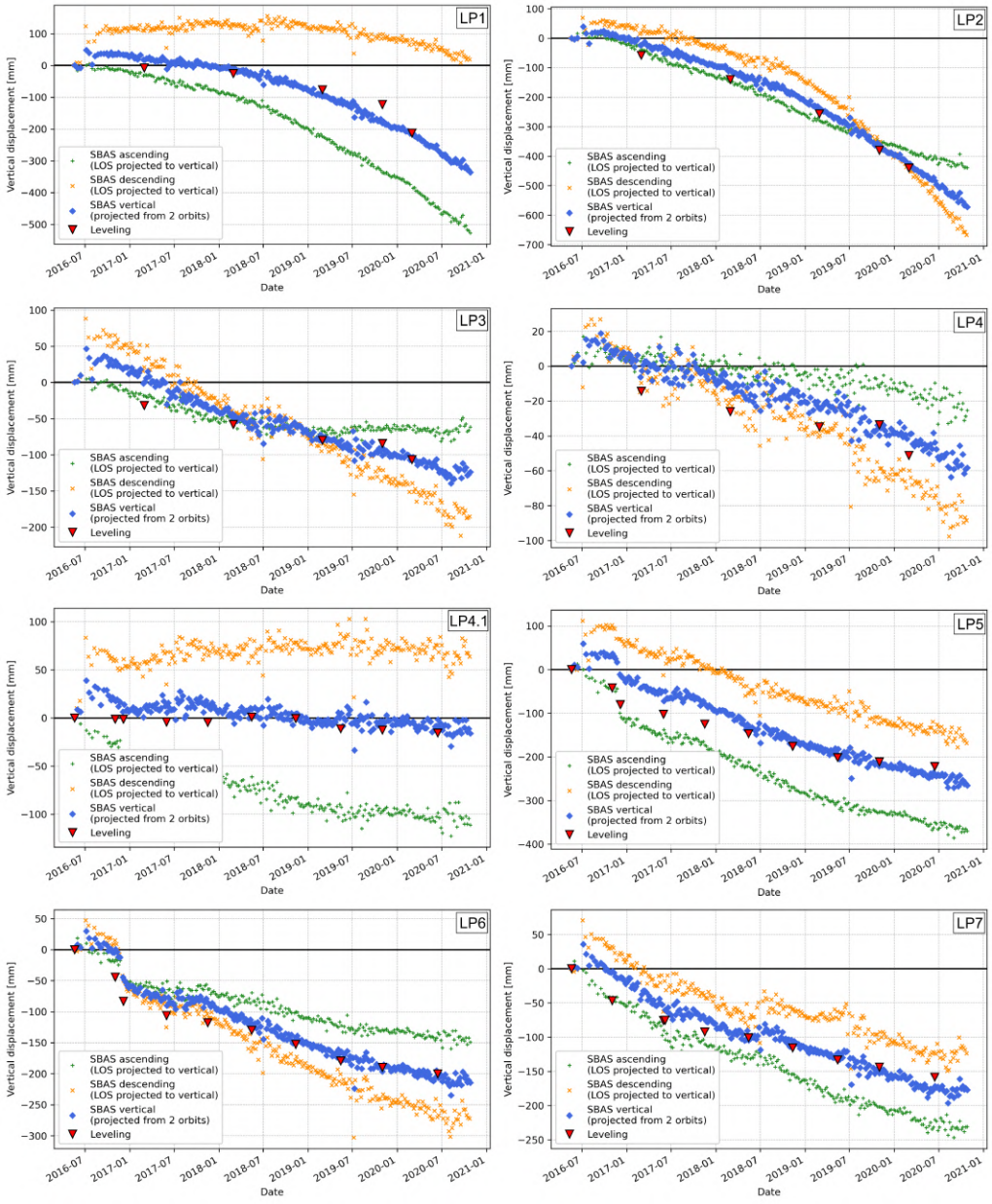

Figure 8.21: Time series plots created for selected leveling points, indicating displacements measured with SBInSAR and leveling

Figures 8.21, 8.22 and 8.23 show the time series of vertical displacements observed at selected leveling points, highlighted in Figures 8.17, 8.18 and 8.19. Time series of displacements were produced for each point:

- LOS displacements measured from single data acquisition path (ascending - green, descending - orange), converted to vertical displacements with horizontal

displacements neglected (according to the formula $d_V = \frac{d_{LOS}}{cos\theta}$, where d_V - vertical displacement, d_{LOS} - displacement in Line of Sight, θ - incidence angle);

- vertical displacements (blue) calculated by decomposition of the LOS values measured from the 2 paths, according to the methodology described in the dissertation;

- vertical displacements from the leveling measurements (red triangles).

The time series plots show displacement values at points of varying character of displacement. Points with slow subsidence (e.g. LP3, LP4, LP10, LP16), points with high displacement values (e.g. LP2, LP8, LP13), and points with low displacement values close to zero (LP4.1) are included.

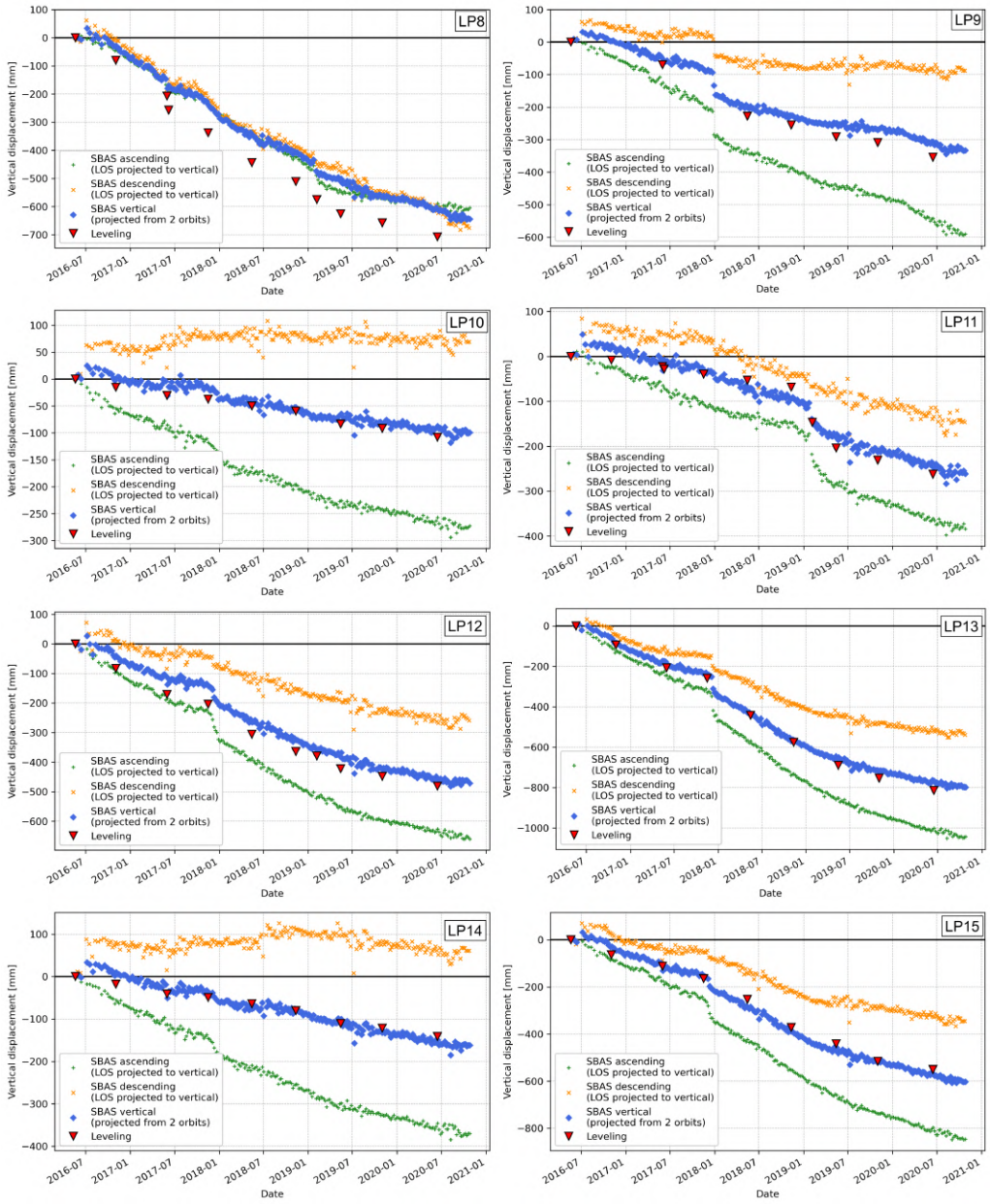

Figure 8.22: Time series plots created for selected leveling points, indicating displacements measured with SBInSAR and leveling

When examining the individual plots, it is particularly noticeable that there is a discrepancy in the measured vertical displacement values from singular paths, and those determined from the decomposition of LOS values from ascending and descending paths. An example is the time series at LP1, where subsidence was observed on the ascending path (up to over -500 mm), while the descending path observed initial uplift and then very gradual subsidence. Decomposition of the vertical displacements from the two paths yielded a subsidence result (to approximately -350 mm). A similar situation has been observed in points LP10 and LP14. Comparing the vertical displacement time series with the leveling result, the decomposition result is much more similar to the leveling measurement.

Discrepancies between the displacement values measured from the two Lines of Sight and those estimated after the decomposition of the LOS values are noticeable in a number of the presented time series plots. It is apparent how the LOS measurements deviate from the actual displacement values obtained by field measurements. Only the vertical displacement values after decomposition of the two LOS signals yield results close to the actual values, as is evident in all plots. A comparison of the displacement values at the leveling points before and after decomposition of LOS displacements will be elaborated on later in this section.

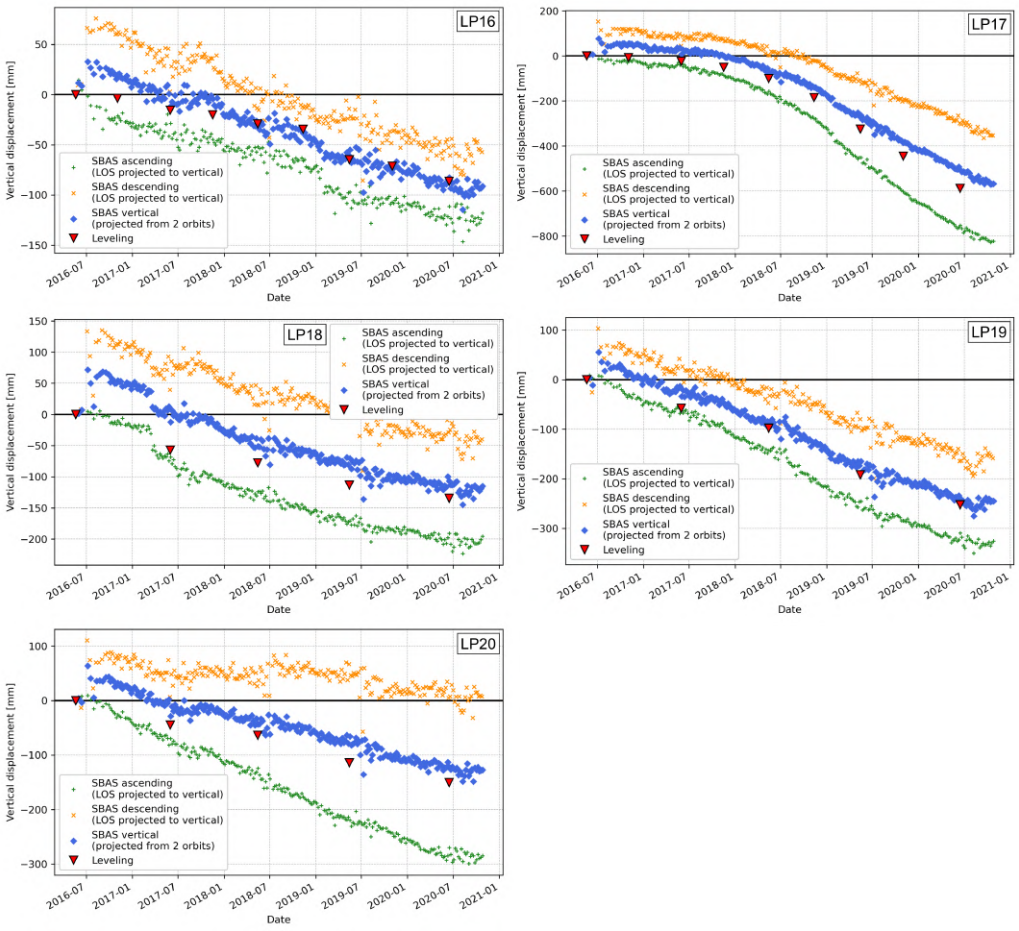

Figure 8.23: Time series plots created for selected leveling points, indicating displacements measured with SBInSAR and leveling

The deviations in the time series of displacements are due to the different geometry of data acquisition. When horizontal displacements are neglected and vertical displacements are determined from a single acquisition path (ascending or descend-

ing), the results of the InSAR measurements show a mismatch with the field measurements. Taking into account the existence of horizontal displacements in the study area leads to more accurate vertical displacement values.

Part of the graphs (LP5, LP6, LP8, LP18) show an underestimation of the displacement from the SBAS method compared to the displacement from the levelling in part or the entire time series. Point LP8 is an example of a point where rapid displacement was not detected by the InSAR method. The rapid displacement is visible on the values measured by the levelling method, and was measured between May and June 2017. The reason why the high displacement was not observed by the SBAS method may be due to low coherence in the study area during the summer, which caused errors during phase unwrapping. In the case of points LP5, LP6 and LP18, it can be seen that the underestimation of the displacement in the time series is caused by a sudden jump in the displacement values during the initial period of the analysed time.

Rapid displacements can also be observed at points LP5, LP6, LP9, LP11, LP12, LP13. It should be noted that for the displacements measured by levelling the temporal resolution (approximately 6 months) does not allow the exact time of the rapid displacement to be observed. The temporal resolution of the InSAR measurements (6 days for Sentinel-1A/B satellites) allows better observation of the variability in displacement values over time. An example of a situation where a sudden jump in displacement velocity is not observable in the levelling results is the time series at point LP9. In this case, the results of the SB method indicate that the rapid displacement occurred in December 2017. It should be mentioned here that a high-energy mining tremor occurred in the area near point LP9 during this period.

It is worth noting a phenomenon seen at points LP2 and LP3. The displacement values measured from the LOS diverge from the vertical displacement values, but the nature of the difference is variable over time. At the beginning of the analysed period, at both points the values measured from the ascending path were lower than the values observed from the descending path. In the middle of the analysed period (LP3) and in the last year (LP2), a change occurred, i.e. the displacement on the ascending path was higher than on the descending path. One reason for this could be a change in the value of the horizontal displacement at the selected points.

Point LP4.1 is an example of a situation where the displacement values measured along the LOS in a given point can be misinterpreted as actual uplift or subsidence. The LOS measurement from the ascending path shows subsidence in this case, while the ascending measurement shows uplift. However, after decomposition of the LOS signals, the actual vertical displacement is close to zero, as confirmed by the values from the leveling.

A comparison of the cumulative displacement values along the selected leveling lines is shown in Figures 8.24 and 8.25. Figure 8.24 shows the leveling line marked in Area 1 (Figure 8.17). The line consists of 21 leveling points. For each of them, cumulative vertical displacement values were determined using the LOS values (ascending and descending) projected to vertical displacements, the values after decomposition of LOS displacements and the values from the leveling survey. Figure 8.25 shows the leveling line marked in area 3 (Figure 8.19). The line is composed of 17 leveling points.

The cumulative displacement values on the leveling line displayed in Figure 8.24 indicate a situation, where the displacement values from one acquisition path are underestimated or overestimated relative to the actual values. The horizontal displacement values of the leveling points shown in the top part of Figure 8.24 indicate

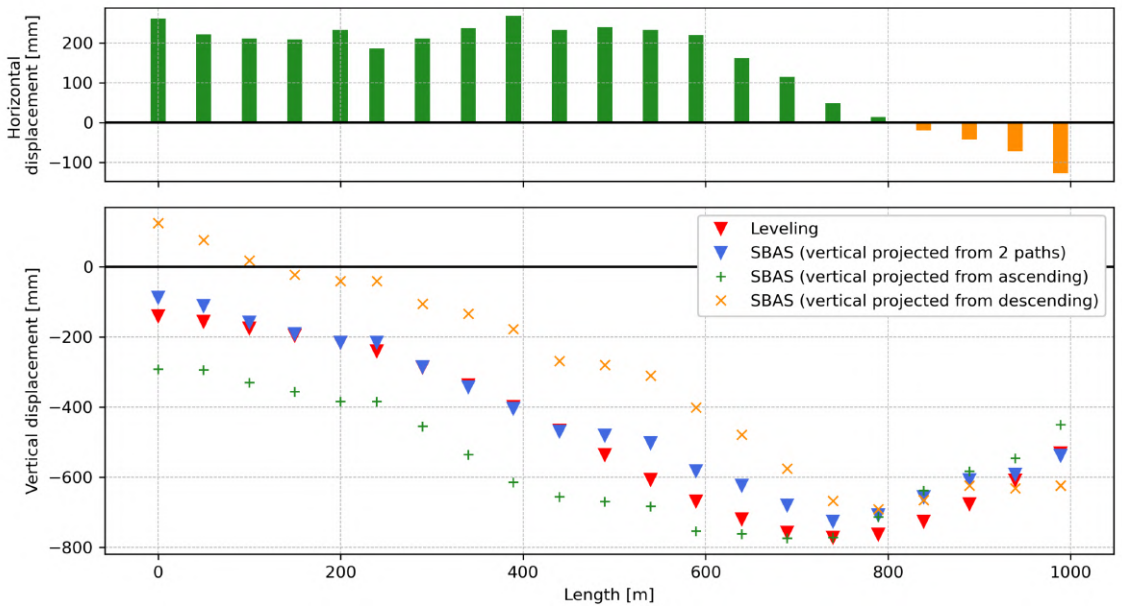

Figure 8.24: Bottom: cumulative vertical displacement values from SBInSAR and leveling. Top: cumulative horizontal displacement values derived after decomposition of LOS displacements, measured at leveling points (green - eastward displacement, orange - westward)

that the points are subject to horizontal displacement in addition to subsidence. A relationship appears in the horizontal displacement values and the differences in the vertical displacement values measured on the ascending and descending paths. The higher the horizontal displacement value, the greater the discrepancy between the values measured on the 2 paths. In addition, the character of the disparity, i.e. whether the subsidence on the ascending path is higher than on the descending path or vice versa, is dependent on the direction of the horizontal displacement. When a point is displaced eastwards (positive sign), subsidence on the ascending path is higher. If there is westward displacement (negative sign), higher subsidence is observed on the descending path.

The values measured on the separate paths differ significantly from the actual vertical displacement values. The RMSE is 128 mm and 188 mm for the ascending and descending paths, respectively. The situation is improved when horizontal displacements are taken into account and the displacement values from the two paths are decomposed. It can be seen in the graph that the values after decomposition are significantly closer to the actual displacement values. Considerable differences still exist at points with high displacement values. However, the RMSE value has been reduced to 51 mm.

Figure 8.25 shows a leveling line where only eastward horizontal displacements have been observed, as indicated in the top part of the figure. A similar relationship to the previous Figure 8.24 can be seen here. The displacement values measured on the individual paths again deviate from the actual values, and the difference between the values increases as the horizontal displacement increases. The vertical displacement values obtained after decomposition of the LOS values are considerably closer to the actual vertical displacement values. For cumulative displacement measurements from a single path, RMSE values of 191 mm were obtained for the ascending path and 236 mm for the descending path. After decomposition and determination of the vertical component of the displacement, the RMSE value decreased to 37 mm.

Observations made on time series of displacements at leveling points and on cu-

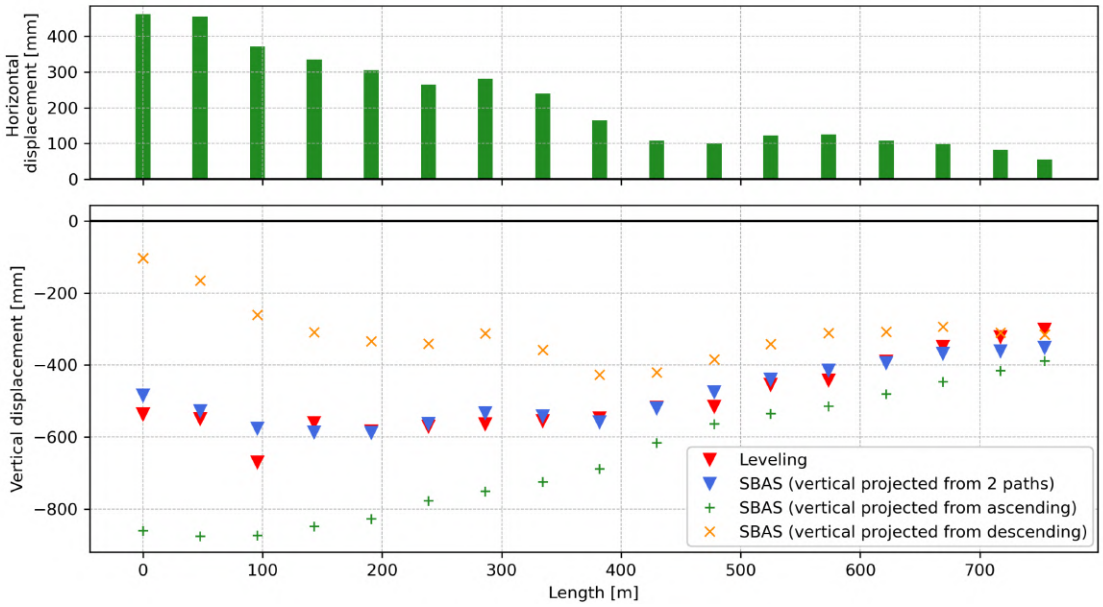

Figure 8.25: Cumulative vertical displacement values from SBInSAR compared with leveling (bottom) and horizontal displacements (top)

mulative displacement values confirm that, when determining vertical displacements from LOS measurements, the exclusion of horizontal displacements is only reasonable if such displacements are non-existent or very small. Otherwise, the measured vertical displacement values differ significantly from the actual values. Taking into account the existence of non-zero values of horizontal displacements (even only in the East-West direction) significantly improves the accuracy of vertical displacement measurements with SBInSAR.

Comparisons between the displacement values measured by SBInSAR and those measured by leveling were made at all leveling points for which measurements covered the period studied in the dissertation (20 May 2016 - 26 October 2020). A total of 751 leveling points were considered. Figure 8.26 contains the results of the analysis of cumulative displacement values (scatter plots on the left and histograms on the right). A comparative analysis of the results obtained from independent acquisition paths - ascending (a), descending (b) and vertical values after LOS displacement decomposition (c) - was performed.

The graphs in Figure 8.26 provide a number of insights into the accuracy of SB results compared to a leveling measurement. Firstly, one should note the relationship of the InSAR measured values to the leveling values (scatter plots on the left). Ideally, all points on the plot should be as close as possible to the straight line marked in black on the graphs. This would mean a perfect match between the measured InSAR and leveling values. The graphs for the ascending path (a), descending path (b) and for the values after LOS decomposition (c) show that there is no perfect match between these measurements and the leveling values. However, it is important to note the degree of scatter between the values in the graphs for ascending and descending values. For a number of measurement points, there is a significant difference in the measured vertical displacements. For the measurement from the ascending path, the values measured by the SB method are either overestimated or underestimated relative to the field measurements. For the descending path, a substantial number of points had their displacement values underestimated

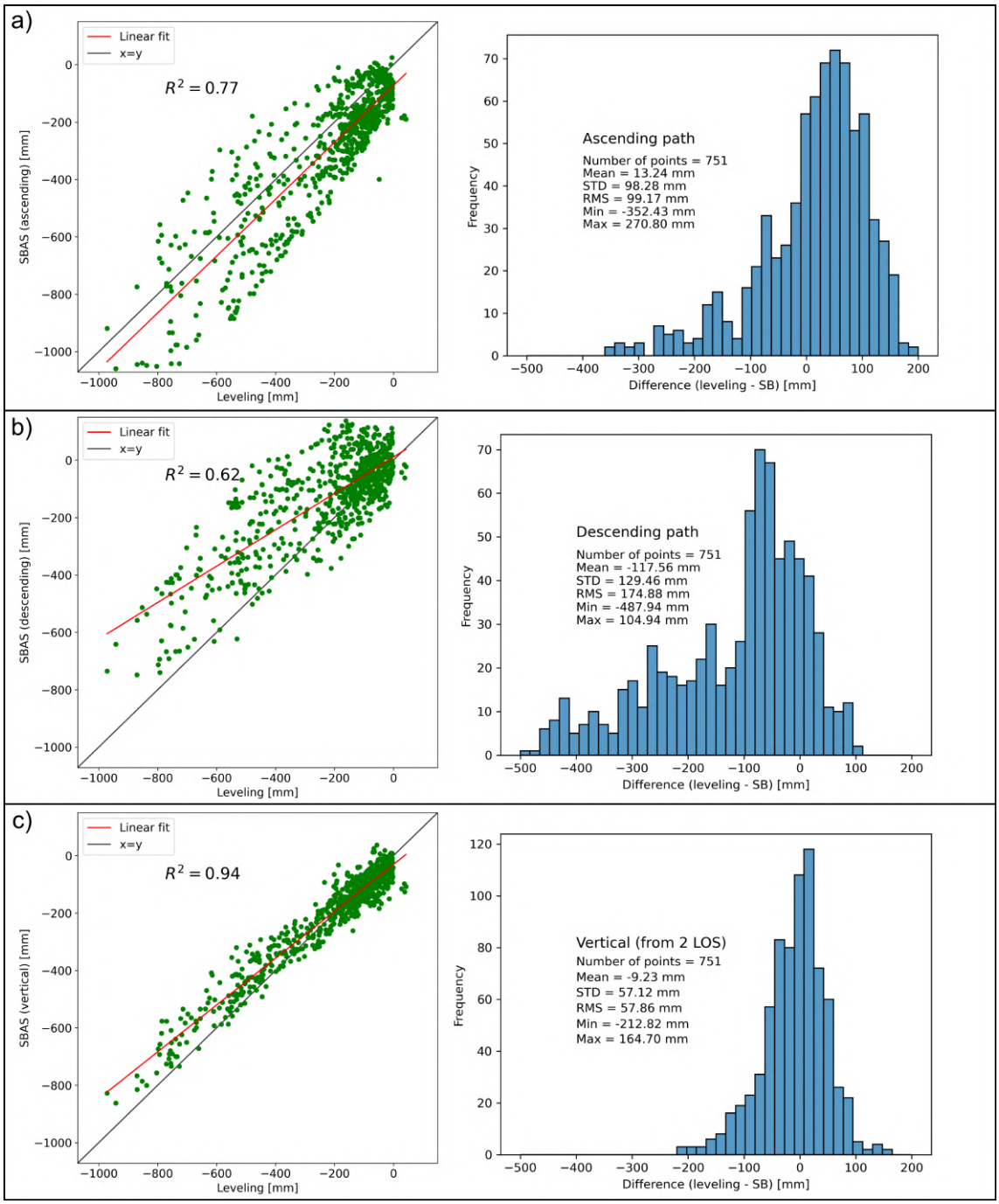

Figure 8.26: Comparison of values measured by SBInSAR with vertical displacement values measured by leveling in 751 points. Ascending (a), descending (b) and vertical (c) values were compared. Scatter plots (left) compare cumulative displacement values measured over the study period. Histograms (right side) show the distributions of differences in displacement values (in mm) between two methods

by the SB method. The difference can be seen for the displacement values after the LOS decomposition (scatter plot in part c). The dispersion of points was significantly reduced, indicating a better agreement between the SB measurement and the leveling. The R^2 values for the single-path measurements were 0.77 and 0.62 for the ascending and descending paths, respectively. For the measurements after LOS decomposition, the R^2 is 0.94, indicating an improved agreement between SB values and actual values.

The improvement in the accuracy of vertical displacement measurements, after taking into account the horizontal displacements and the decomposition of the LOS values, is also evident in the distributions of differences between the values measured by InSAR and leveling. Histograms showing the distributions of differences are shown in the right-hand side of Figure 8.26. When there is high agreement between displacement measurements by InSAR and leveling methods, the differences between the cumulative values are expected to be as low as possible with the mean close to zero. In addition, attention should be paid to the value of the standard deviation, which informs about the accuracy of the obtained results. A high standard deviation will indicate a significant discrepancy between the values measured by the two methods.

The distribution of differences in vertical displacement values for the ascending path is indicated in the histogram in part (a). The mean is +13 mm, indicating a slight overestimation of the vertical displacement values by the SB method. The differences between the measured values are often different from zero and have high values, as indicated by the high standard deviation value of 98 mm. The histogram in part (b) shows the distribution of differences for the descending path. In this case, the mean equals -117 mm, indicating a significant underestimation of the displacement values by the SB method in the descending path. In addition to this, the high value of the standard deviation (129 mm) again indicates a considerable discrepancy in the measurements of the two methods. On the distribution for the descending path, it can be seen that the differences between the two measurements can reach close to 500 mm (0.5 m).

The distribution of difference values for the LOS decomposition method is shown in part (c) of Figure 8.26. A significant improvement in terms of accuracy can be observed. The average difference value is -9 mm, indicating a slight underestimation of the actual displacement value. Compared to the previous results from single acquisition paths, there is a significant improvement in the standard deviation value (57 mm), indicating a reduction in the differences between the two measurement methods.

Spatial verification of SB measurement results

In addition to the quantitative analysis of the displacement values measured by the SBInSAR method, a verification of the obtained values was carried out in terms of the conformity of the spatial distribution of the displacements with the distribution of the mining fields. The analysis was carried out for 3 areas for which data on mining fields were made available.

Figure 8.27 contains the displacement values measured by the SBInSAR method superimposed on the polygons representing the positions of the mining fields in Area No. 1. In this area, the displacement measurement recorded a single dominant zone of subsidence. When the displacement map is compared with the mining fields map, the spatial distribution of displacements coincides with the location of the mining

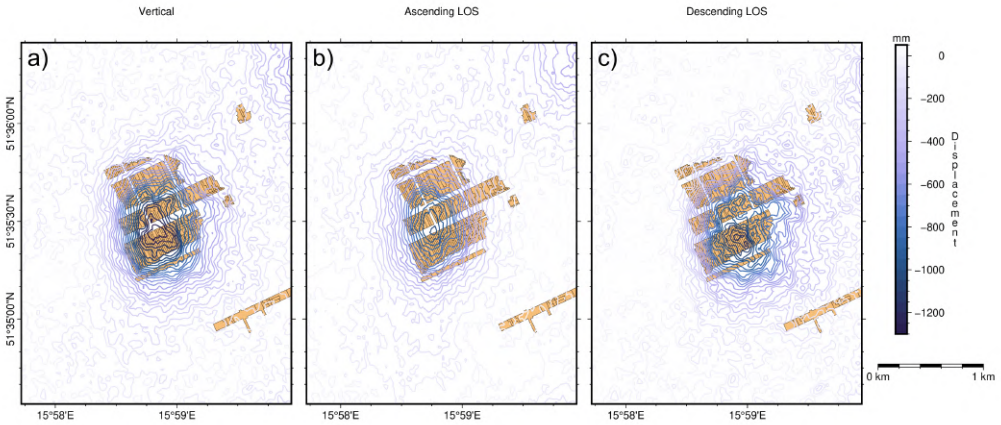

Figure 8.27: Displacements measured by SBInSAR for Area No. 1, (a) vertical, (b) ascending LOS and (c) descending LOS), compared with mining field locations marked using orange polygons

fields. It can therefore be concluded that mining activities are the main source of ground surface displacement in this area. Despite the fact that the measurements from the individual LOS paths (b and c) and after decomposition of the LOS values (a) all coincide with the course of the mining fields, a subtle difference in the location of the subsidence zone in relation to the exploited field is noticeable. The subsidence zone on the ascending path (b) is slightly offset to the west, while on the descending path (c) it is offset to the east. The alignment of the subsidence zone for the vertical displacement values after decomposition (a) follows the alignment of the depleted field most closely.

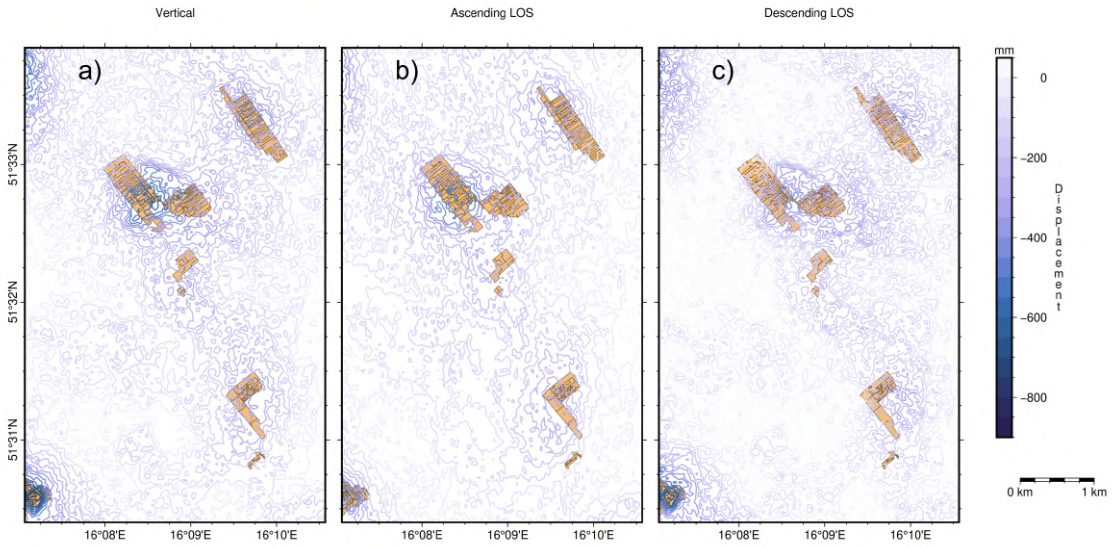

Figure 8.28: Displacements measured by SBInSAR for Area No. 2, (a) vertical, (b) ascending LOS and (c) descending LOS), compared with mining field locations marked using orange polygons

Figure 8.28 shows a spatial comparison of the locations of the displacement zones with the locations of the mining fields in Area 2. Several displacement zones were recorded in this area. As can be seen from the figure, each displacement zone on the surface corresponds to an exploitation field underground, and the highest displacement values are recorded specifically in the exploitation field areas. A slight offset of the displacement zones relative to the extraction fields is also evident in the maps

of displacement values from ascending and descending paths.

The spatial relationship between the displacements measured by the InSAR method and the areas where mining was carried out can also be seen in Area No. 3, which is shown in Figure 8.29. The displacement zones correspond again to the mining areas. For two of the displacement zones, in the eastern and southern part of the area, there was no mining data available from the mining authority. In Area No. 3, the relationship between the surface area of the mining areas and the observed subsidence should be highlighted. Higher values of subsidence are recorded for mining fields with a large area (central part of the area) than for fields with a small area (northern and south-western part of the area). It would therefore be expected that the subsidence zones in the eastern and southern parts of Area No. 3 were also subject to large-scale mining operations.

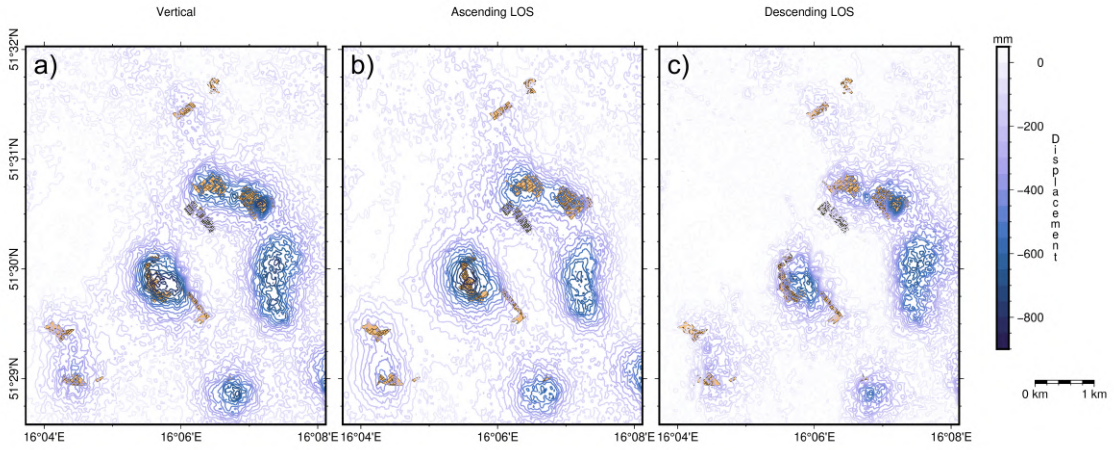

Figure 8.29: Displacements measured by SBInSAR for Area No. 3, (a) vertical, (b) ascending LOS and (c) descending LOS), compared with mining field locations marked using orange polygons

The locations of the mining fields in the study area were also compared with the time course of vertical displacements obtained using the SBInSAR method. For the mining fields, the month and year in which mining was carried out is known. The mining fields were grouped by year of exploitation. Similarly, for the vertical displacement data, cumulative displacement values were calculated for each year during the studied period. The annual vertical displacement values and the locations of the mining activities carried out were summarised on selected cross sections. The results of this compilation are shown in Figures 8.30, 8.31 and 8.32. The locations of cross-sections were also highlighted in Figures 8.17, 8.18 and 8.19.

Figure 8.30 compares the time course of vertical displacements with the locations of the mining fields in the range of 300 meters for cross section *AA'*. Exploitation in this area was gradually carried out in a south-west direction. Along the cross-section, mining proceeded from right to left. Analysing the cumulative annual displacement values along the cross-section, it can also be seen that, year after year, the zones of greatest subsidence move in the same direction. At the same time, it should be noted that high values of annual cumulative displacements are located at the cross-section in places where exploitation was carried out in a given year. The progression of subsidence with the progression of mining is therefore evident, indicating a direct relationship between the occurrence of displacements in the studied area and underground mining.

Figure 8.31 shows a summary of the annual displacements with exploitation data

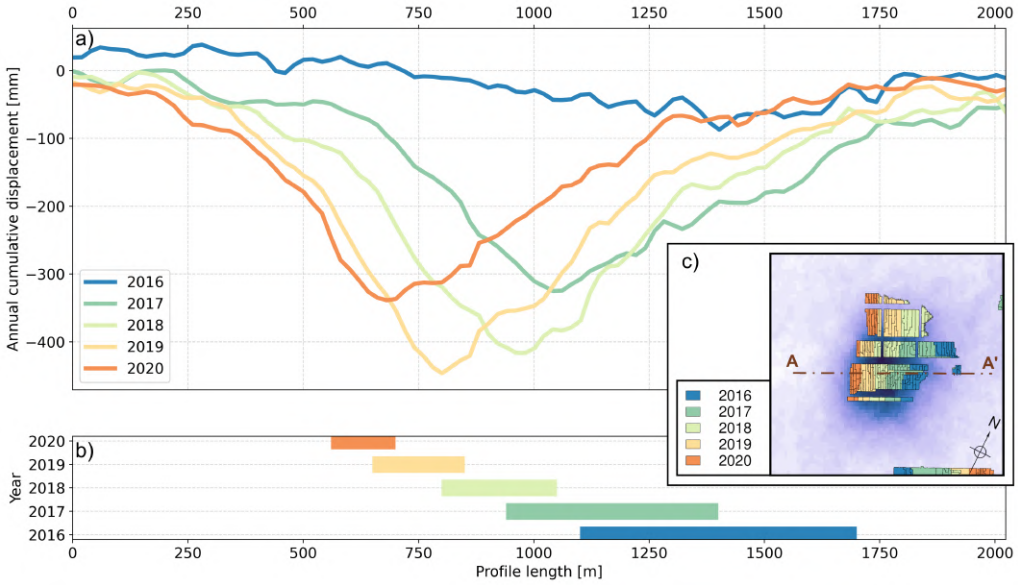

Figure 8.30: Annual values of cumulative vertical displacement (a), compared with the time progression of mining exploitation (b) on cross section AA' through the subsidence zone (c)

along cross-section *DD'*. Although there is no apparent temporal progression of displacements in a given direction, the influence of mining on increased subsidence values is still evident. It is important to note here that the values of subsidence are influenced by the size of the exploited fields in a given year, as can be seen for the 2019 data, where the highest annual subsidence was observed in vicinity of the larger mining field. In addition to this, there is no information on the thickness of the selected seam in a given mining field, which could also have had a significant impact on the recorded vertical displacement values.

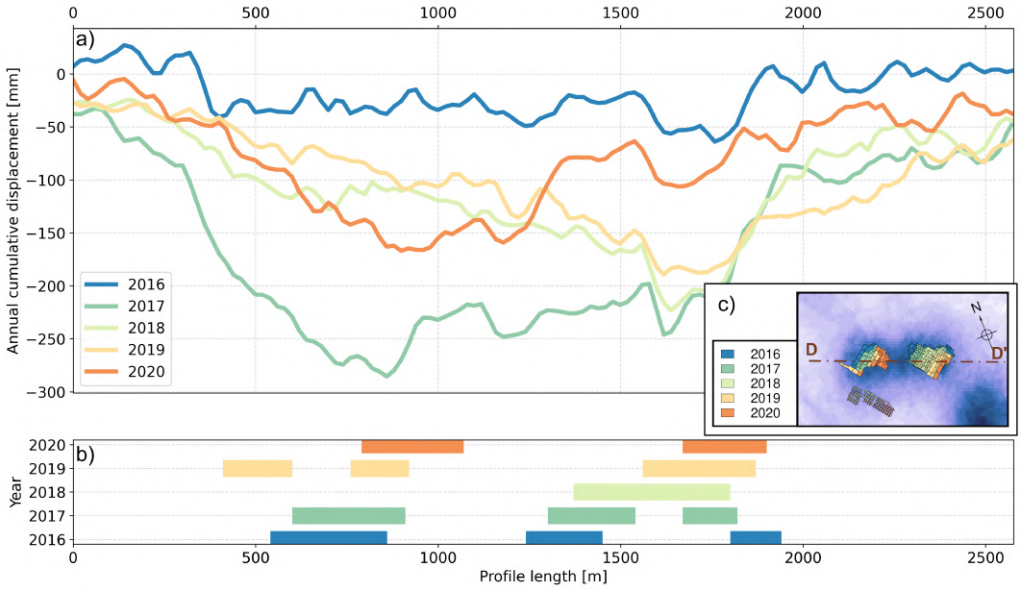

Figure 8.31: Annual values of cumulative vertical displacement (a), compared with the time progression of mining exploitation (b) on cross section DD' through the subsidence zone (c)

Similar relationships can be seen in Figure 8.32, which shows a comparison of annual vertical displacement values with mining along the *HH'* section. The rela-

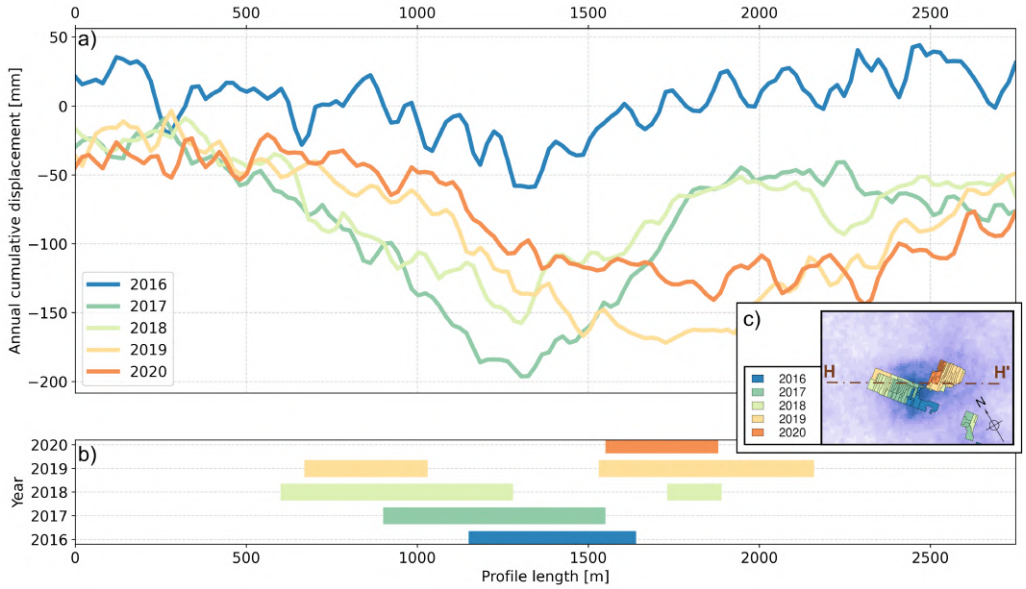

Figure 8.32: Annual values of cumulative vertical displacement (a), compared with the time progression of mining exploitation (b) on cross section HH' through the subsidence zone (c)

tionship between the highest annual displacement and the locations of the mining fields was recorded for 2016, 2017, partly for 2018, 2019 (the mining fields in the right part of the cross-section have a much larger area, and the highest subsidence was recorded there in that year) and 2020.

8.2 Subsidence forecasting

The second part of the dissertation was an analysis of the feasibility of using machine learning algorithms to predict ground surface displacement in a mining area. The analysis was based on a time series forecasting approach, using the results of ground surface displacement measurements obtained using the SBInSAR method. Vertical displacement values in the form of time series were used as input data for learning a set of machine learning-based algorithms.

The displacement time series were prepared to work with machine learning algorithms, taking into account the filling in of missing values or the division into training and test datasets. The models presented in Section 7.3 were trained on sets of time series in 2 test areas, one of which has a single subsidence zone within it, while the other has several subsidence zones with different displacement characteristics. Models based on machine learning and neural networks have been compared with traditional time series forecasting methods. The accuracy metrics described in Section 7.4 were used to assess the performance of the models. The potential applicability of the models for forecasting large sets of time series to generate vertical displacement forecast maps was also explored. The results of these studies will be presented in this section.

8.2.1 Performance of models applied to displacement forecasting

The time series forecasting models used within the dissertation were tested on test sets not used during model development. The displacement values forecast by the individual models under the assumption of forecasting 6 months (32 time series samples) ahead, were compared with the actual displacement values measured by the SBInSAR method. Accuracy metrics of Mean Absolute Error (MAE), Root Mean Squared Error (RMSE) and Mean Average Percentage Error (MAPE) were used in assessing the performance of selected forecasting approaches.

Table 8.1 contains accuracy metrics calculated for the tested models in Area No. 1, based on calculating means of values achieved in each of 150 selected time series points used for training models. The first model, the Naive model, is the baseline for each model applied. Models with values of metrics that are better than the baseline model are considered to be effective models. The MAE, RMSE and MAPE values for the Naive model are 17.51 mm, 20.16 mm and 6.81%, respectively. According to Table 8.1, all of the models applied reached metrics values lower than the baseline model, indicating that all of the models are effective in forecasting time series of displacements.

The AutoARIMA and Exponential Smoothing (ES) methods obtained satisfactory results, based on the accuracy metrics. However, it should be stressed that these two are local models, which means that a separate model is created for each time series point, and that forecasting displacement values outside the tested 150 points would require new separate models to be created. Another local approach, based on the Linear Regression model, achieved accuracy metrics values slightly below the Naive model, although far worse than the AutoARIMA and ES approaches. This indicates that applying machine learning model in a local approach may fail, most likely due to lack of training data, since each model is trained only on a separate time series.

By adopting a global approach, for the same model trained on all time series, much better results can be achieved in terms of forecasts. The global machine

Table 8.1: Accuracy metrics for time series forecasting models applied in the study (mean values for 150 testing time series in Area No. 1)

Model	**MAE [mm]**	**RMSE [mm]**	**MAPE [%]**
Naive	17.51	20.16	6.81
AutoARIMA	10.82	13.07	4.79
Exponential Smoothing	9.95	11.93	4.42
Linear regression (local)	17.09	19.89	6.43
Linear regression (global)	9.47	11.56	3.93
Lasso regression	10.94	13.07	4.17
Ridge regression	9.46	11.56	3.93
ElasticNet regression	11.52	13.64	4.31
N-BEATS	11.44	13.63	4.23
RNN	10.44	12.63	4.02
BlockRNN	13.97	16.06	4.56
Regression Ensemble	**8.98**	**10.93**	**3.84**

learning model based on linear regression achieved accuracy metrics of: MAE - 9.47 mm, RMSE - 11.56 mm and MAPE - 3.93%. The performance of a global linear regression approach surpassed the AutoARIMA and ES approaches. A similar performance was achieved by the Ridge regression model, and the Lasso and ElasticNet regression models performed slightly worse than linear regression. In terms of neural network approaches, each of the 3 applied methods performed better than the Naive model, with the RNN model outperforming the AutoARIMA approach. Hovewer, it should be noted that the neural network-based models generally performed slightly worse than simple machine learning regression approaches.

The Ensemble model based on a set of machine learning regression models proved to be the most effective model in terms of performance, while achieving the lowest values for each of the accuracy metrics investigated. The Regression Ensemble approach obtained the **MAE** value of **8.98 mm**, indicating a 48.7% improvement over the Naive model, the **RMSE** value of **10.93 mm**, indicating a 45.8% improvement, and **MAPE** of **3.84%**, showing a 43.6% improvement over the Naive model.

Table 8.2 presents the values of accuracy metrics obtained for Area No. 3, calculated as mean of values obtained in all 528 time series points used for model development. The Naive model, used as a baseline to evaluate the performance of time series forecasting models, obtained MAE, RMSE and MAPE values of 11.41 mm, 13.71 mm, and 9.11%, respectively. Contrary to the results obtained in Area No. 1, presented in Table 8.1, not all of the approaches surpassed the Naive baseline approach. The AutoARIMA approach and the local linear regression model failed to outperform the Naive model in terms of MAE and RMSE values of accuracy metrics. Moreover, the global linear regression model, as well as Ridge regression and N-BEATS neural network, obtained the values of MAPE higher than the Naive baseline model.

As in Area No. 1, majority of methods based on a global approach performed better than local models. This indicates that a single model trained on multiple time series is able to outperform multiple local models trained exclusively on singular time series datasets. **A model of this kind can also potentially be used to produce predictions at new points previously not seen by the model at the training stage**. This will be further investigated in the next subsection.

For Area No. 3, it should be noted that models using neural networks achieved

Table 8.2: Accuracy metrics for time series forecasting models applied in the study (mean values for 528 testing time series in Area No. 3)

Model	**MAE [mm]**	**RMSE [mm]**	**MAPE [%]**
Naive	11.41	13.71	9.11
AutoARIMA	11.45	13.99	7.70
Exponential Smoothing	10.69	13.10	**7.57**
Linear regression (local)	15.42	18.39	8.75
Linear regression (global)	10.90	13.30	10.85
Lasso regression	**9.63**	11.84	8.02
Ridge regression	10.10	12.36	10.10
ElasticNet regression	9.78	11.92	8.63
N-BEATS	10.11	12.20	9.48
RNN	10.43	12.75	8.63
BlockRNN	9.71	**11.77**	**7.63**
Regression Ensemble	9.78	**11.78**	9.04

performance similar to machine learning regression models. Since this study area contains several zones of subsidence, contrary to Area No. 1 spanning a single subsidence trough, a more complex character of time series sequences might be better represented using a complex neural network model. The BlockRNN architecture can be considered to have performed the best out of the tested approaches, with the lowest value of RMSE reaching 11.77 mm and the lowest MAPE of 7.63%. In terms of the MAE value, the only model performing better was the Lasso regression model with MAE of 9.63 mm, 0.08 mm lower than the BlockRNN model.

It should also be stressed that the Ensemble of regression models performed satisfactorily, reaching values of accuracy metrics close to the lowest ones in the tested set of forecasting models. The RMSE value of 11.78 mm was almost identical to the value obtained by the BlockRNN model. The MAE of 9.78 mm was also close to that obtained using the BlockRNN architecture. Only the MAPE value was slightly higher (9.04%), indicating a possibility that the model may be ineffective in forecasting time series with low values of displacements (outside the trough areas), since MAPE obtains very high values if the actual values of time series are closer to zero.

The prepared models were used to forecast the time series within Area No. 1 and Area No. 3 (in addition to the time series used to train the models). In this way, displacement forecasts were developed for all measurement points (pixels) located within the study areas. Figure 8.33 shows the displacement predictions at selected points in Area No. 1. Points of varying subsidence character, located in the centre of the subsidence trough, on the periphery of the trough and outside the trough, were selected to develop the predictions. Forecasts were developed at selected points using selected predictive models: AutoARIMA, Linear regression, Lasso regression, N-BEATS model, RNN model and Ensemble model.

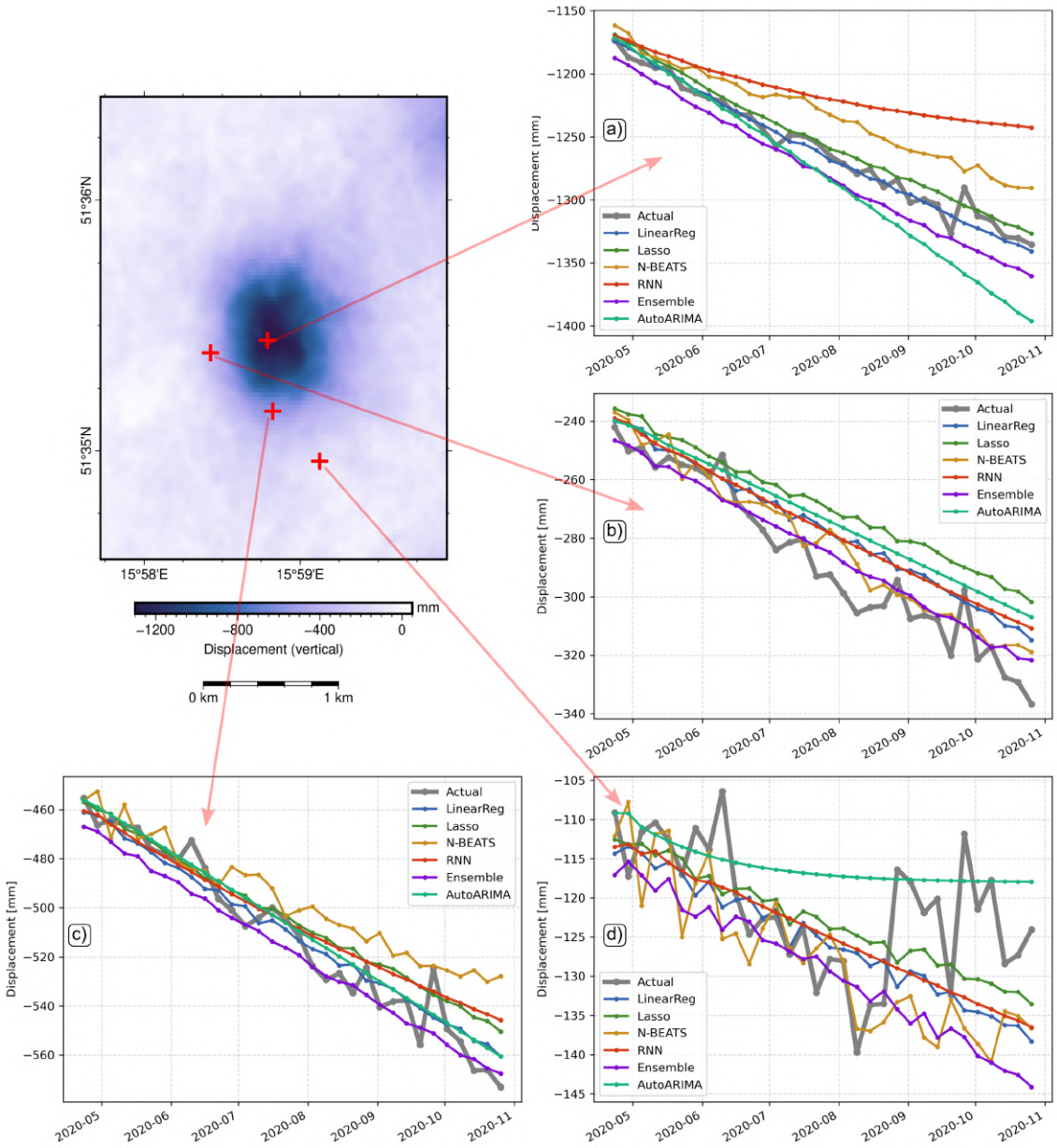

Figure 8.33: Examples of ground surface displacement predictions developed by selected models for Area No. 1

It can be seen in Figure 8.33 that the selected time series forecasting models are effective in predicting displacement values in the study area. Several observations can be drawn from the analysis of the time series forecasts. Firstly, at the point with high subsidence values in the centre of the subsidence trough (Figure 8.33a), the uncertainty of the autoregressive models increases as the time series progresses. Secondly, the regression models (Linear, Lasso) achieve the greatest agreement with the actual values. The Ensemble model, on the other hand, slightly overestimates the displacement value, while the N-BEATS model underestimates the values.

For points located on the trough edges (Figure 8.33b and 8.33c), the models achieve correct predictions. For these points, the trend is the dominant component of the time series and the models have correctly estimated its magnitude. It is also important to note how the different models approach the prediction of variability in the data. Regression, and autoregressive models give little indication of the variability in the data, while the N-BEATS model adjusts the nature of the variability in

the forecast dataset to the variability in the input dataset. Figure 8.33d also shows the fit of the models to the variability in the data. The time series at this point is characterised by low displacement values, slightly overestimated by the models.

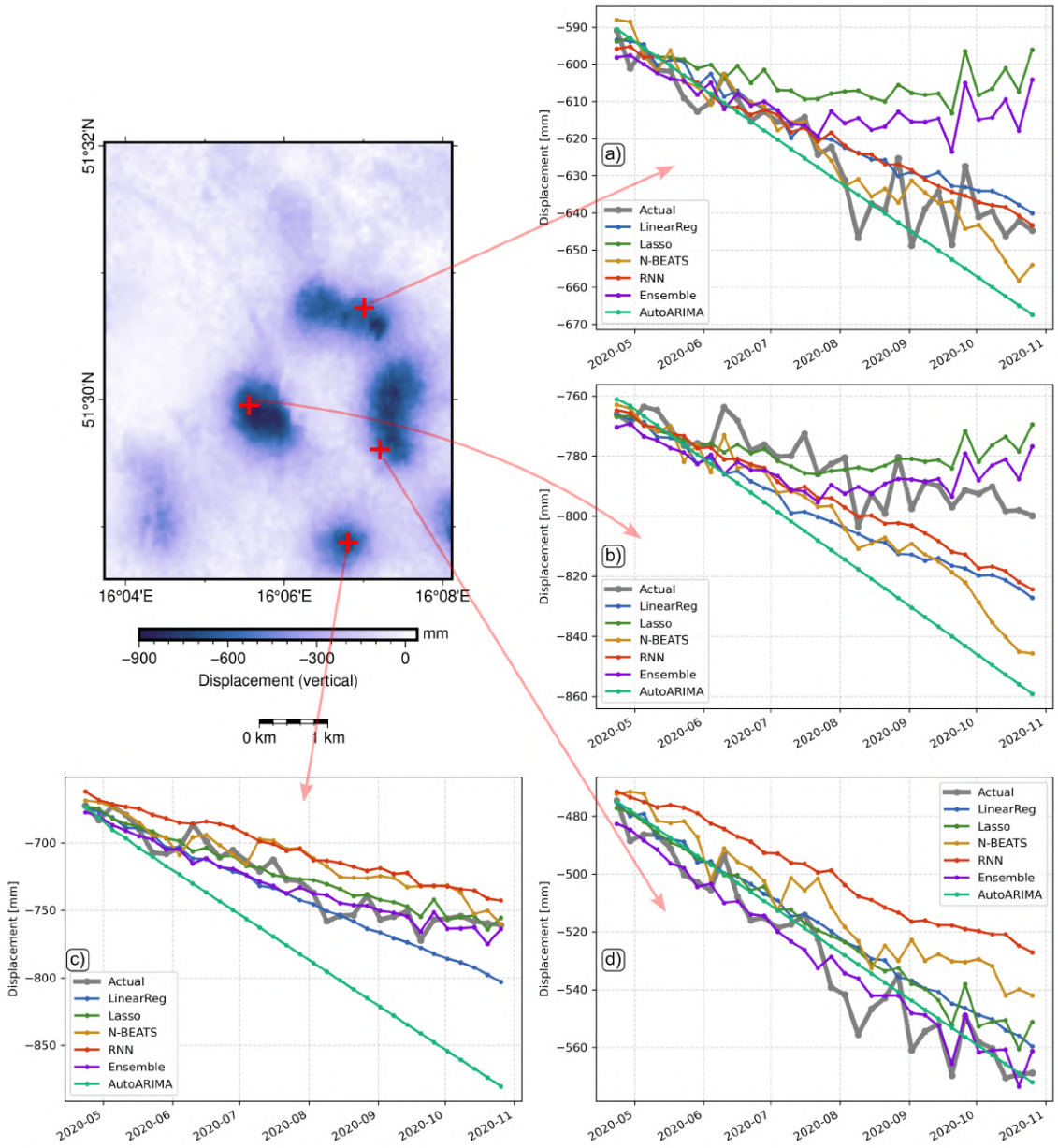

Figure 8.34: Predictions of ground surface displacement at selected locations in Area No. 3, prepared using selected time series forecasting models

Examples of displacement predictions at selected points in Area No. 3 are presented in Figure 8.34. Points located in separate subsidence zones have been selected. It can again be observed that the models predict the trend correctly in the majority of cases, with instances of overestimation (Figure 8.34b) and underestimation (Figure 8.34a). However, the more highly differentiated nature of the time series in this area has resulted in increased uncertainty in model predictions.

Due to the high depth of exploitation and the extraction system used (chamber-pillar), the displacements occurring in the study area are continuous, and even changes in underground exploitation do not cause a sudden increase in the value

of the displacements, the increase being a spread-out process over time. Abrupt changes in the time series, such as suddenly accelerated subsidence (due to a subsurface shock) or oscillations resulting from noise in the data (imperfection of the measurement method), will be very tough or impossible for the models to predict. It should be stressed that the models presented in this study were developed based solely on vertical displacement data. In this sense, the models are univariate models. Expanding the models to include additional variables, such as information on ongoing and planned mining operations, geological, hydrological data and other factors influencing the subsidence behaviour, has the potential to make the models more accurate in specific cases.

8.2.2 Generalization potential of global models

The previous subsection analysed the performance of the models in predicting displacement values for the test sequences at the points where the models were trained. Sample forecasts over a time horizon of 6 months (23 April 2020 - 26 October 2020) were also observed. This subsection will elaborate on the use of the global model to forecast displacements in the area beyond the training area. Firstly, the result of the global forecast for the entire Area No. 1 and Area No. 3 will be presented.

Area predictions were made for Areas No. 1 and 3, forecasting the time series values at each point (pixel) included in that area. In this way, maps of forecast displacement values for the forecast horizon were produced. These values were analysed in terms of cumulative displacements (subsidence predicted 6 months ahead) and their correspondence to the actual values. Forecasts were developed for the Naive model and for the Ensemble Regression model for comparison.

Figure 8.35 shows the displacement prediction for the entire Area No. 1 using the Naive model, compared with the actual values measured using the SBInSAR method. The Naive model is a local model, so a separate model was fitted for each point. The map of displacements observed by the InSAR method over a period of 6 months (Figure 8.35a) shows that the largest subsidence during this period occurs in the western part of the subsidence trough, in line with the course of underground mining. This phenomenon was observed in the previous section when comparing the results of the InSAR measurements with the mining data. Vertical displacements during this period are up to approximately -200 mm.

A naive linear model produces a forecast based on the assumption that time series is linear. The forecast map shown in Figure 8.35b therefore shows a shape similar to that of the trough measured throughout the model training period (until 23 April 2020). Comparing the displacement pattern with the actual values yields the difference map in Figure 8.35c. From the differences between the naive prediction and the actual values, it can be seen that the naive subsidence prediction model does not take into account changes in the pattern of subsidence in Area No. 1, as can be seen in the underestimation of the predicted values (blue) in the western part of the trough, and in the overestimation (red) in the eastern part. The difference values reach -130 mm.

Figure 8.36 shows the prediction for this area by a global model based on the Ensemble Regression machine learning model. With this model, the predicted vertical displacements (Figure 8.36b) more closely resemble the spatial distribution of the actual values. The agreement is indicated by the difference map between the predicted and actual values of the cumulative displacements on Figure 8.36c. It should be noted that the spatial pattern of the subsidence trough during this period was

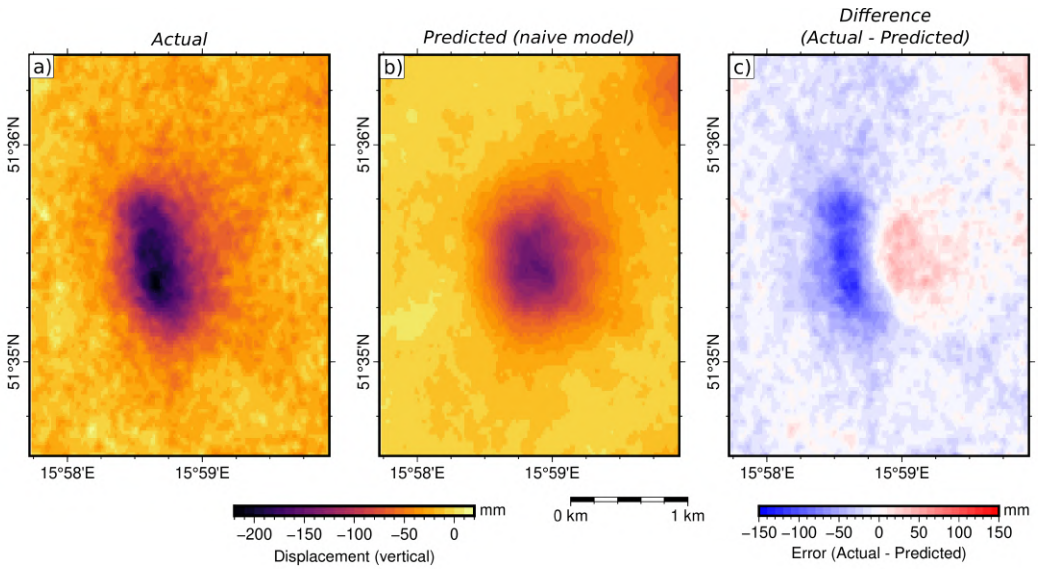

Figure 8.35: (a) Vertical displacement values measured in Area No. 1 during forecast horizon (23 April 2020 - 26 October 2020) with InSAR; (b) Naive model prediction; (c) Difference between actual and predicted values

correctly represented by the machine learning model. This means that the model, by taking into account the nature of the individual time series, can predict changes in displacement in the case of spatial progression of exploitation. This property may also be important for the correct determination of the predicted deformation indicators.

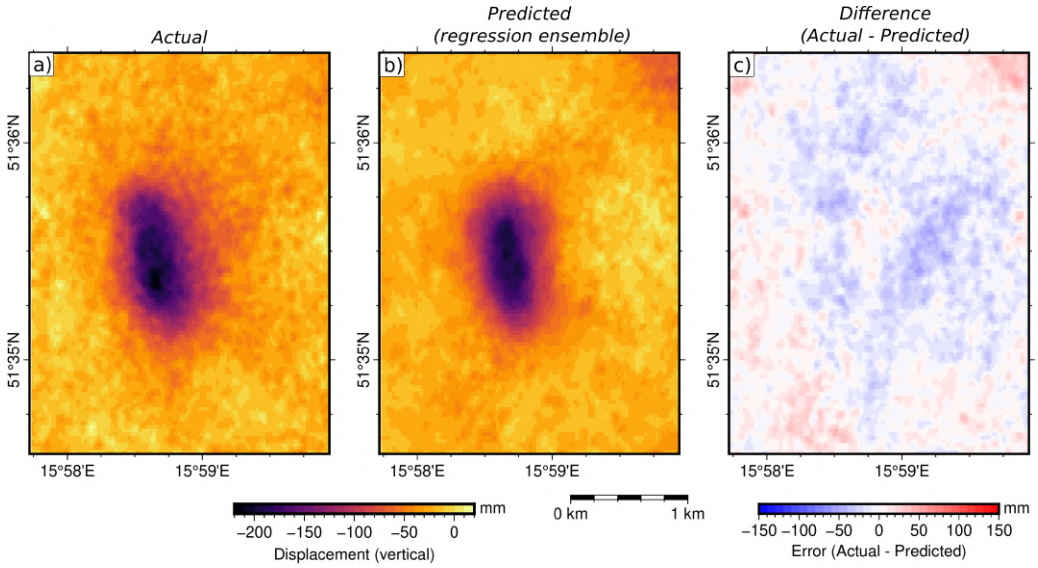

Figure 8.36: (a) Vertical displacement values measured in Area No. 1 during forecast horizon (23 April 2020 - 26 October 2020); (b) Ensemble Regression model prediction; (c) Difference between actual and predicted values

In the context of using a model learned from a set of time series as a global model, it is worth noting the prediction of the Ensemble model in the north-eastern corner of Area No. 1. There is another subsidence trough in this location; however, there are no significant displacements in this trough during the prediction period.

Despite this, the model predicts subsidence at this location. The implication is that the model is incorrectly interpreting the time series at this location because their pattern was not taken into account when training the model (the training points were not located in this area).

The results presented in Figures 8.35 and 8.36 confirm the assessment of model performance presented in Table 8.1. The machine learning model in general has a higher forecast accuracy than the naive approach. What is more, the model is able to predict the displacement values for thousands of new time series points, despite being trained only on 150 points.

The results of the naive and global model prediction analysis for Area No. 3 are shown in Figures 8.37 and 8.38. In terms of InSAR observed displacements, this area is considerably more complex, and includes several subsidence zones. This affects the accuracy of the predicted displacements.

Figure 8.37 shows the prediction for Area No. 3 using the naive approach. The spatial distribution of displacements corresponds to the distribution of displacements during the model training period. The actual measured displacements occur in the same subsidence zones, but are characterised by different magnitudes. This indicates the variable nature of the time series of displacements, related to the progression of underground mining in the area. The differences can be observed in Figure 8.37c, highlighting areas of overestimated and underestimated subsidence values.

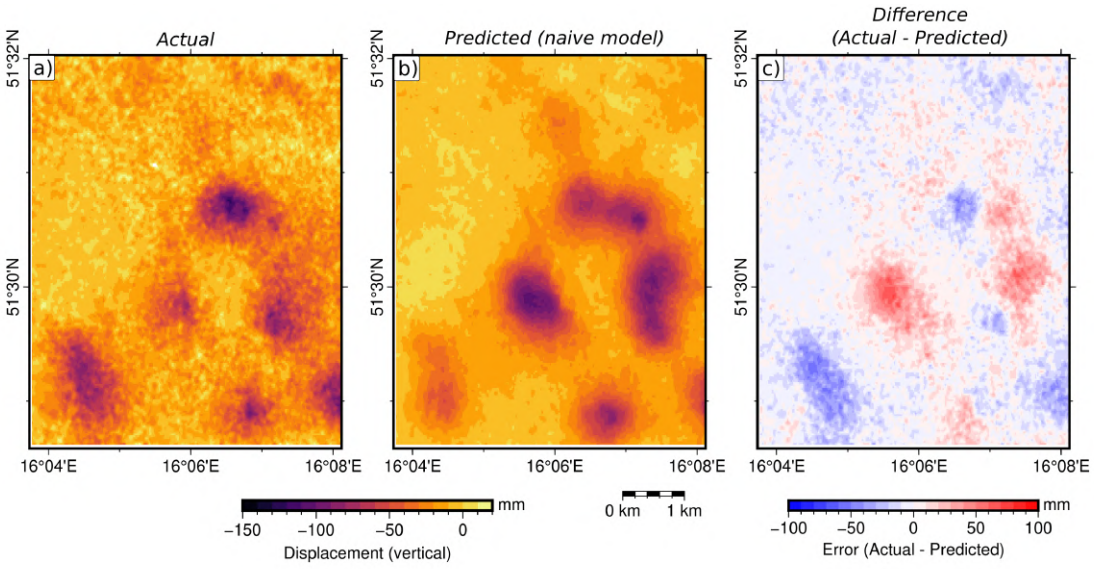

Figure 8.37: (a) Vertical displacement values measured in Area No. 3 during forecast horizon (23 April 2020 - 26 October 2020); (b) Naive model prediction; (c) Difference between actual and predicted values

The subsidence predictions made using the Ensemble Regression model (trained using points selected in Area No. 3) are shown in Figure 8.38. The cumulative displacement values predicted by the global machine learning model correctly reflect the locations of the most significant subsidence. Despite the reduction in the degree of overestimation of the predicted displacements, the difference map still shows significant errors in the prediction, particularly in terms of underestimation of subsidence values (blue colour). The most significant example of underestimation is near the central part of the area. An example of a time series from this area is shown earlier in Figure 8.33a. The reason for this behaviour may be a misinterpretation of the time series in this area by the model. Compared to Area No. 1 presented

earlier, the accuracy of the 6-month displacement forecast decreases in Area No. 3. It should be noted here that Area No. 3 has a more complex subsidence pattern, with many different time series patterns. Preparing separate models for each of the troughs (as in Area No. 1) could produce better results.

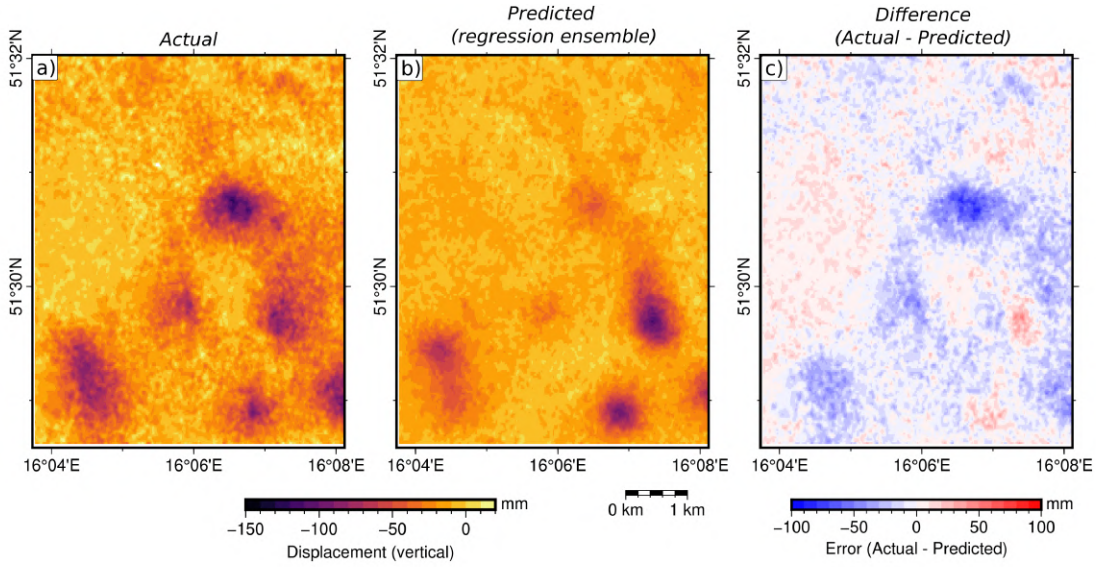

Figure 8.38: (a) Vertical displacement values measured in Area No. 3 during forecast horizon (23 April 2020 - 26 October 2020); (b) Ensemble Regression model prediction; (c) Difference between actual and predicted values

In addition to the capacity of the models to predict cumulative displacements for the entire Areas No. 1 and 3, the consistency of the global predictions with the actual data was also examined in terms of the entire progress of the time series. For this purpose, the RMSE values for the area forecasts were calculated, comparing the forecast values with the actual values in all 32 steps of each time series. The RMSE maps were developed, where high values of RMSE indicate low agreement between the time series of predicted and actual displacement values.

Figure 8.39 shows the maps of RMSE values for Area No. 1, generated for the naive prediction and Ensemble machine learning model. Comparing the map of RMSE values with the map of actual displacements measured over the forecast horizon period, the high RMSE values indicate that the naive model fails in terms of correctly predicting displacements and has low forecast accuracy. The mean RMSE value for the Naive model obtained was 15.2 mm with a standard deviation of 10.3 mm, while the mean RMSE for the Ensemble model was 11.4 mm with a standard deviation of 5.2 mm. The RMSE values obtained for the Ensemble model show an improvement with respect to the Naive model, and also show that the model correctly predicts the course of displacements over a given horizon of 6 months. The forecast accuracy as measured by the RMSE error is similar for the whole area, with no local clusters of increases in error values (except in the north-east corner).

The RMSE values calculated for the Area No. 3 predictions using the Naive model and the Ensemble model are shown in Figure 8.40. The RMSE maps show areas where the accuracy of the models in predicting displacement decreases. The machine learning model has significantly low accuracy in the subsidence trough in the central part of the area. Despite this, an improvement over the naive model can be observed. The mean and standard deviation of the RMSE values for the naive model were 13.9 mm and 6.5 mm, respectively, while the Ensemble model had a

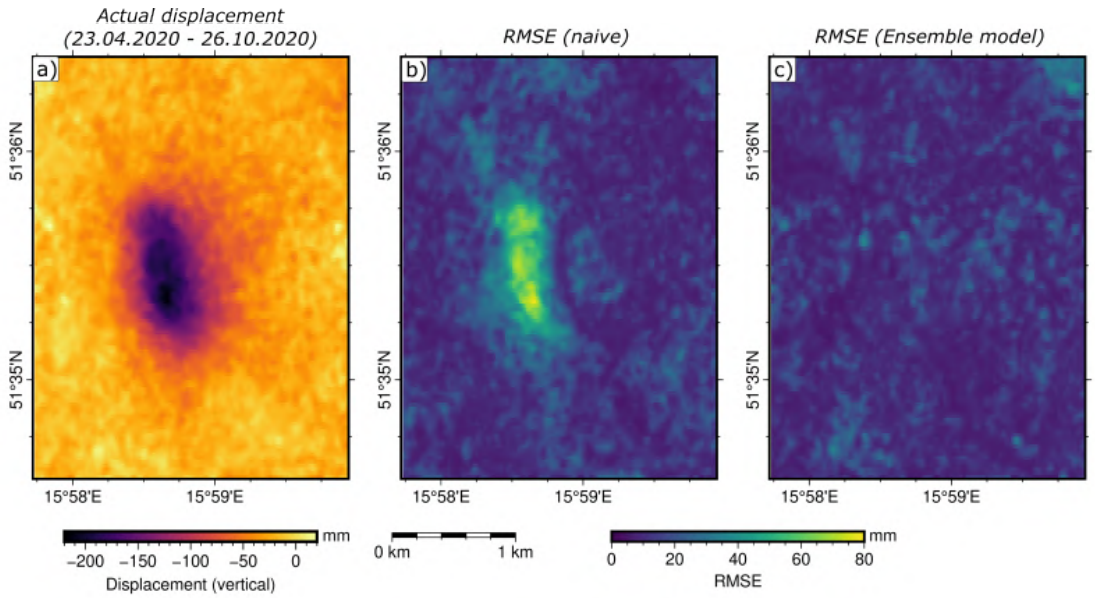

Figure 8.39: (a) Cumulative displacement measured in Area No. 1 using InSAR; (b) RMSE values obtained for the Naive forecasts; (c) RMSE values obtained by the Ensemble Regression model

mean of 11.0 mm and a standard deviation of 5.2 mm, respectively.

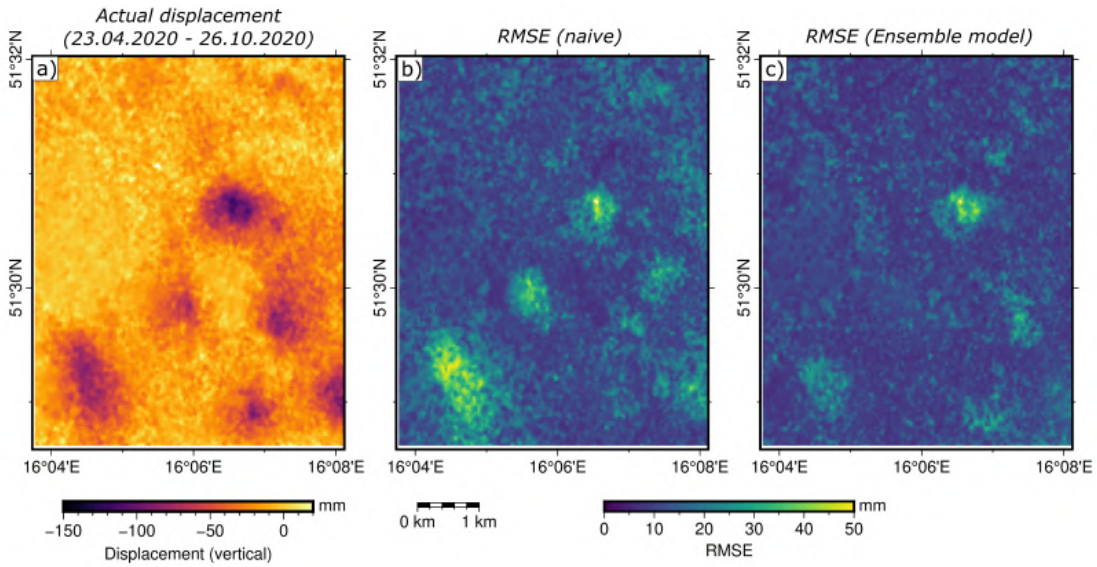

Figure 8.40: (a) Cumulative displacement measured in Area No. 3 using InSAR; (b) RMSE values obtained for the Naive forecasts; (c) RMSE values obtained by the Ensemble Regression model

Chapter Summary

This chapter concludes the research conducted within the dissertation by presenting and discussing the results obtained. The two main parts of the chapter were built around the description of the results obtained in the two thematic blocks carried out in the thesis. The first part of the chapter was based on the presentation of the results of the measurement of vertical displacements by the InSAR method, and the verification of the remote sensing method results with the displacement

values obtained with field leveling measurements. The second part of this chapter was based on the issue of vertical surface displacement prediction based on machine learning algorithms.

Section 8.1 presented the InSAR-derived ground surface displacement results for the study area of Legnica-Głogów Copper Belt area (LGCB). The results of displacement measurements with the PS (Persistent Scatterer) and SB (Small Baseline) methods, based on SAR Sentinel-1 data from two acquisition paths - ascending and descending - were presented. The data from the two paths were used to decompose the LOS displacement values into vertical displacements considering horizontal displacements in the East-West direction. Vertical displacement values from the PS and SB methods were analysed for comparison. The results of the SB method were selected for further analysis, which was justified by the greater coverage of the study area and better agreement with the displacement values derived from the leveling results obtained. The results of the SB method were comprehensively verified with the obtained results of leveling measurements and data on locations of exploitation fields in selected subareas. **Analysis of the area using the SB method showed the presence of vertical displacement fields, moreover, the displacement values measured by remote methods had a high correlation with the results of the ground measurements.**

Section 8.2 contained the results obtained for the ground surface displacement prediction methods developed as part of the thesis. Selected time series forecasting methods, based on traditional methods, machine learning models and neural networks, were applied to forecast time series of displacements based on vertical displacement values derived from InSAR. The section presented the performance of the models compared to the baseline model using selected accuracy metrics. Based on the accuracy metrics calculated at the test points, the Ensemble Regression model was selected as the most effective model. **The Ensemble model was then used in predicting displacement at the selected test areas, successfully predicting the time course of displacement over a six-month period.**

The results presented in the chapter demonstrate the feasibility of using InSAR measurements of ground surface displacement in mining areas as input data for creating machine learning algorithms for displacement prediction. The decomposition of the displacement values from the two LOS paths, taking into account horizontal displacements, allows the time series of vertical displacements to be determined. This enables subsidence in mining areas to be detected much more accurately than when using a single LOS measurement. Furthermore, displacement data in the form of time series can be used as input for machine learning algorithms. Given the character of the progression of displacements over time in the study area, it is possible to create a *data-driven* model that predicts displacement values over a given period of time in the future.

Chapter 9

Summary

Overview

This doctoral thesis addresses the issue of measuring and forecasting ground surface displacements in areas affected by underground mining activities. The research hypothesis, formulated on the basis of a literature review, highlighted the lack of work on the application of artificial intelligence methods and Interferometric SAR displacement measurements in the prediction of displacements in mining areas. Although numerous studies were conducted on the use of machine learning algorithms in displacement prediction, few works have been carried out on the combined use of multi-temporal InSAR observations with high temporal resolution and state-of-the-art machine learning based time series forecasting methods. The research carried out as part of the thesis aimed to answer the research question posed, and to combine the knowledge of remote sensing and artificial intelligence. The result of this research is a proposed data-driven displacement forecasting method as an alternative to other displacement forecasting methods.

Conclusions and takeaways

Based on the results presented in the previous chapter, detailed conclusions can be drawn about the research carried out:

- The InSAR method, particularly the techniques associated with processing time series of SAR imagery to produce displacement time series (e.g. PSInSAR, SBInSAR), provide a source of data on the changes occurring at the surface due to underground exploitation of natural resources.
- While Line-Of-Sight (LOS) measurements from a single orbital path of SAR data acquisition can provide a general understanding of the displacements occurring on the ground surface, the presence of horizontal displacements can lead to misinterpretation of the results due to the imaging geometry. Therefore applying measurements from at least 2 independent acquisition paths of SAR data is crucial for properly resolving the vertical displacement field and its temporal progression.
- The importance of verifying the results of InSAR measurements with the results of field measurements was emphasised. As the application of InSAR methods in displacement measurements progresses and accuracy increases, the need for ground truth verification should be decreasing. While the results of

InSAR and leveling were compared, the potential of InSAR to measure ground displacements with high temporal resolution was highlighted, giving a deeper insight into the process of surface deformation caused by mining exploitation.

- A time series forecasting approach applied to ground displacement data is a valid method for displacement prediction, given a proper preparation of time series data. A number of algorithms can be applied for time series prediction, including traditional autoregressive methods, as well as machine learning algorithms. While both approaches give satisfactory results in terms of forecasting future course of displacement over a time series, a potential of machine learning methods lies in applying them using a global approach. This way, a single model can be trained using multiple time series measured in locations across a studied area, and then be used to forecast displacements in this area or even in other areas with similar time series patterns. Among the models designed in this approach, an Ensemble model that uses several regression models was the most successful. Among the global models, recurrent neural networks showed high performance for complex training data. Furthermore, research conducted in this thesis showed that regression models can still outperform neural networks in the task of time series forecasting.

- Machine learning allows the creation of a data-driven predictive model based on InSAR displacement measurements to predict the displacement values over time. This approach allows the creation of a method that is an alternative to other mining displacement forecasting methods being used. At the same time, it should be emphasised that this method is based on the absence of the need for field measurements, with high temporal resolution and good coverage of the surveyed area with measurement points. The creation of such methods is justified in light of the increasing amount of data acquired by satellite sensors and the development of methods for their processing.

Limitations

When defining the research objectives, the scope of work necessary to fulfil them was defined. The research defined by the scope of the work has been carried out in full, but it is important to note the limitations of the proposed solutions, arising from the defined scope. Firstly, the scope covering the determination of vertical displacements by the InSAR method did not include consideration of the influence of the atmosphere on the measured displacement values. There was also no study of the effect of fading signal (phase bias) on SB displacement measurements. Taking these factors into account could have had a positive impact on the accuracy of the displacements determined using time series InSAR. Secondly, when determining the time series of displacements using the SB method, no coherence-based selection of measurement points was carried out. In this case, the accuracy of displacement measurements at points with high temporal decorrelation may be lower, which will translate into the accuracy of the predicted displacement. Another limitation relates to the use of machine learning models for displacement prediction. These models are often referred to as *black box* models, whose internal operating principle is difficult or impossible to interpret. Increasing the explanatory power of the models would undoubtedly be important in terms of interpreting the impact of displacement values and other variables on the predictions. Machine learning models can also be of high complexity, posing a barrier of entry and causing them to be difficult to

integrate into existing workflows. Nevertheless, further studies in the field of applying ML models for displacement forecasting should enable the practical application of such approaches. Lastly, during the development of methodology for applying InSAR measurements with machine learning models, only the displacement values were considered as input data for the algorithms to be based on. Other data, such as mining data (e.g. seam thickness, temporal progress of exploitation), geological data (e.g. geological structure of rock mass layers) or other types of data that could be used as covariates, were not considered. The integration of additional data would lead to more complex models, with the possibility of examining the influence of individual factors on the occurrence of displacements. In doing so, it should be emphasised that taking into account each additional variable would involve appropriate pre-processing of the input data, as the data is usually not ready for machine learning algorithms.

Research contributions

During the research conducted in this dissertation, a number of machine learning models were developed and used to predict mining displacements in selected areas. The models were based on the measurement results of vertical displacements using the InSAR method, taking into account the occurrence of horizontal displacements in the area and the decomposition of LOS values. **In the light of the results obtained and presented in the thesis, it can be concluded that the research hypothesis stated at the beginning of the dissertation:**

Models based on machine learning algorithms and measurement data from the InSAR method can be applied to effectively predict vertical ground surface displacement in areas affected by underground mining,

has been proven.

Further recommendations

It should be noted that the solution to the research problem presented in the thesis can be further developed. Suggestions for the further development of the subject matter addressed in the dissertation include:

- **Work to improve the accuracy of vertical displacement measurements in mining areas.** Despite the high agreement of SBInSAR measurements after decomposition with leveling measurements, there is still room for improvement. Possible issues to be addressed include the effect of interferogram phase unwrapping on the estimated displacement time series, the effect of atmospheric (tropospheric and ionospheric) delays on the accuracy of displacement determination, or the detectability of rapid displacements due to induced seismicity, in light of signal decorrelation.
- **Expanding the dataset with further displacement measurements, and adding additional variables that act as covariates in the model.** The inclusion of data on factors that affect displacements, or are the effects of displacements that occur, can affect the predictions provided by the model. In this approach, it would also be possible to relate variables (e.g. mining, geological, hydrological data) to surface deformation by exploring the relationships

between them as interpreted by the machine learning model and assessing the feature importance of each variable.

- **Application of other machine learning models and neural networks.** The dissertation proposes the use of selected models used for time series forecasting. As research in AI progresses, more models will emerge that achieve high performance in time series forecasting. Possible directions for development in this area would be the use of models capable of taking into account the relevance of specific features and variables in forecasting, or development of models that take into account spatial dependencies in the data.

Bibliography

[1] N. C. B. (UK), Ed., *Subsidence Engineers' Handbook*, 2d rev. ed. London: The Board, 1975, 111 pp.

[2] S. Abdikan, M. Arıkan, F. Sanli, and Z. Cakir, "Monitoring of coal mining subsidence in peri-urban area of Zonguldak city (NW Turkey) with persistent scatterer interferometry using ALOS-PALSAR," *Environmental Earth Sciences*, vol. 71, no. 9, pp. 4081–4089, 2014.

[3] P. S. Agram, "Persistent scatterer interferometry in natural terrain," Ph.D. dissertation, Stanford University, Ann Arbor, United States, 2010, 164 pp. (visited on 12/01/2021).

[4] T. Ambrožič and G. Turk, "Prediction of subsidence due to underground mining by artificial neural networks," *Computers & Geosciences*, vol. 29, no. 5, pp. 627–637, 2003.

[5] N. Anantrasirichai, J. Biggs, K. Kelevitz, Z. Sadeghi, T. Wright, J. Thompson, A. M. Achim, and D. Bull, "Detecting Ground Deformation in the Built Environment Using Sparse Satellite InSAR Data With a Convolutional Neural Network," *IEEE Transactions on Geoscience and Remote Sensing*, vol. 59, no. 4, pp. 2940–2950, 2021.

[6] H. Ansari, M. Russwurm, S. M. Ali, S. Montazeri, A. Parizzi, and X. X. Zhu, "InSAR Displacement Time Series Mining: A Machine Learning Approach," in *International Geoscience and Remote Sensing Symposium (IGARSS)*, Brussels, Belgium, 2021, pp. 1–4.

[7] B. Antonielli, A. Sciortino, S. Scancella, F. Bozzano, and P. Mazzanti, "Tracking Deformation Processes at the Legnica Glogow Copper District (Poland) by Satellite InSAR—I: Room and Pillar Mine District," *Land*, vol. 10, no. 6, p. 653, 6 2021.

[8] W.-K. Baek and H.-S. Jung, "Precise Three-Dimensional Deformation Retrieval in Large and Complex Deformation Areas via Integration of Offset-Based Unwrapping and Improved Multiple-Aperture SAR Interferometry: Application to the 2016 Kumamoto Earthquake," *Engineering*, vol. 6, no. 8, pp. 927–935, 2020.

[9] S. Bai, J. Z. Kolter, and V. Koltun, *An Empirical Evaluation of Generic Convolutional and Recurrent Networks for Sequence Modeling*, 2018. arXiv: `1803.01271`.

[10] R. Bals, "Beitrag zur Frage der Vorausberechnung bergbaulicher Senkungen," *Mitt. aus dem Markscheidewesen*, vol. 32, 1931.

[11] W. Batkiewicz, *Odchylenia Standardowe Poeksploatacyjnych Deformacji Górotworu (Standard deviations of post-mining rock mass deformations)*. Państwowe Wydawn. Naukowe; Oddział w Krakowie, 1971.

[12] N. B. D. Bechor and H. A. Zebker, "Measuring two-dimensional movements using a single InSAR pair," *Geophysical Research Letters*, vol. 33, no. 16, 2006.

[13] P. Berardino, G. Fornaro, R. Lanari, and E. Sansosti, "A new algorithm for surface deformation monitoring based on small baseline differential SAR interferograms," *IEEE Transactions on Geoscience and Remote Sensing*, vol. 40, no. 11, pp. 2375–2383, 2002.

[14] J. Biggs, F. Dogru, A. Dagliyar, F. Albino, S. Yip, S. Brown, N. Anantrasirichai, and G. Atıcı, "Baseline monitoring of volcanic regions with little recent activity: Application of Sentinel-1 InSAR to Turkish volcanoes," *Journal of Applied Volcanology*, vol. 10, no. 1, p. 2, 2021.

[15] J. Blachowski, A. Chrzanowski, and A. Szostak-Chrzanowski, "Application of GIS methods in assessing effects of mining activity on surface infrastructure," *Archives of Mining Sciences*, vol. Vol. 59, no. 2 2014.

[16] J. Blachowski, E. Jiránková, M. Lazecký, P. Kadlečík, and W. Milczarek, "Application of satellite radar interferometry (PSInSAR) in analysis of secondary surface deformations in mining areas. Case studies from Czech Republic and Poland," *Acta Geodynamica et Geomaterialia*, vol. 15, no. 2, pp. 173–185, 2018.

[17] J. Blachowski, S. Cacon, and W. Milczarek, "Analysis of post-mining ground deformations caused by underground coal extraction in complicated geological conditions," *Acta geodynamica et geomaterialia*, vol. 6, no. 3, pp. 351–, 2009.

[18] P. Blanco-Sánchez, J. J. Mallorquí, S. Duque, and D. Monells, "The Coherent Pixels Technique (CPT): An Advanced DInSAR Technique for Nonlinear Deformation Monitoring," *Pure and applied geophysics*, vol. 165, no. 6, pp. 1167–1193, 2008.

[19] N. I. Bountos, I. Papoutsis, D. Michail, and N. Anantrasirichai, "Self-Supervised Contrastive Learning for Volcanic Unrest Detection," *IEEE Geoscience and Remote Sensing Letters*, vol. 19, pp. 1–5, 2022.

[20] G. E. P. Box and G. M. Jenkins, "Some Recent Advances in Forecasting and Control," *Journal of the Royal Statistical Society Series C*, vol. 17, no. 2, pp. 91–109, 1968.

[21] C. M. J. Brengman and W. D. Barnhart, "Identification of Surface Deformation in InSAR Using Machine Learning," *Geochemistry, Geophysics, Geosystems*, vol. 22, no. 3, e2020GC009204, 2021.

[22] C. Carnec, D. Massonnet, and C. King, "Two examples of the use of SAR interferometry on displacement fields of small spatial extent," *Geophysical Research Letters*, vol. 23, no. 24, pp. 3579–3582, 1996.

[23] M. Caro Cuenca, A. J. Hooper, and R. F. Hanssen, "Surface deformation induced by water influx in the abandoned coal mines in Limburg, The Netherlands observed by satellite radar interferometry," *Journal of Applied Geophysics*, vol. 88, pp. 1–11, 2013.

[24] Z. Chang, W. Yu, W. Wang, J. Zhang, X. Liu, and J. Zhu, "An approach for accurately retrieving the vertical deformation component from two-track InSAR measurements," *International Journal of Remote Sensing*, vol. 38, no. 6, pp. 1702–1719, 2017.

[25] R. S. Chatterjee, S. Thapa, K. B. Singh, G. Varunakumar, and E. V. R. Raju, "Detecting, mapping and monitoring of land subsidence in Jharia Coalfield, Jharkhand, India by spaceborne differential interferometric SAR, GPS and precision levelling techniques," *Journal of Earth System Science*, vol. 124, no. 6, pp. 1359–1376, 2015.

[26] B. Chen, K. Deng, and H. Fan, "Combining D-InSAR and SVR for monitoring and prediction of mining subsidence," *Zhongguo Kuangye Daxue Xuebao/Journal of China University of Mining and Technology*, vol. 43, no. 5, pp. 880–886, 2014.

[27] B. Q. Chen and K. Z. Deng, "Integration of D-InSAR technology and PSO-SVR algorithm for time series monitoring and dynamic prediction of coal mining subsidence," *Survey Review*, vol. 46, no. 339, pp. 392–400, 2014.

[28] B. Chen, K. Deng, H. Fan, and M. Hao, "Large-scale deformation monitoring in mining area by D-InSAR and 3D laser scanning technology integration," *International Journal of Mining Science and Technology*, vol. 23, no. 4, pp. 555–561, 2013.

[29] B. Chen, K. Deng, H. Fan, and Y. Yu, "Combining SAR interferometric phase and intensity information for monitoring of large gradient deformation in coal mining area," *European Journal of Remote Sensing*, vol. 48, no. 1, pp. 701–717, 2015.

[30] B. Chen, Z. Li, C. Yu, D. Fairbairn, J. Kang, J. Hu, and L. Liang, "Three-dimensional time-varying large surface displacements in coal exploiting areas revealed through integration of SAR pixel offset measurements and mining subsidence model," *Remote Sensing of Environment*, vol. 240, p. 111 663, 2020.

[31] C. Chen and H. Zebker, "Phase unwrapping for large SAR interferograms: Statistical segmentation and generalized network models," *IEEE Transactions on Geoscience and Remote Sensing*, vol. 40, no. 8, pp. 1709–1719, 2002.

[32] C. W. Chen and H. A. Zebker, "Two-dimensional phase unwrapping with use of statistical models for cost functions in nonlinear optimization," *JOSA A*, vol. 18, no. 2, pp. 338–351, 2001.

[33] Y. Chen, L. Bruzzone, L. Jiang, and Q. Sun, "ARU-Net: Reduction of Atmospheric Phase Screen in SAR Interferometry Using Attention-Based Deep Residual U-Net," *IEEE Transactions on Geoscience and Remote Sensing*, vol. 59, no. 7, pp. 5780–5793, 2021.

[34] Z. Chen, "Deformation monitoring of highway goaf based on three-dimensional laser scanning," in *2021 IEEE International Conference on Emergency Science and Information Technology (ICESIT)*, 2021, pp. 556–560.

[35] V. K. R. Chimmula and L. Zhang, "Time series forecasting of COVID-19 transmission in Canada using LSTM networks," *Chaos, Solitons & Fractals*, vol. 135, p. 109 864, 2020.

[36] A. Chrzanowski, C. Yong-qi, R. W. Leeman, J. Leal, and Maraven, "Integration of the global positioning system with geodetic leveling surveys in ground subsidence studies," *CISM journal*, vol. 43, no. 4, pp. 377–386, 1989.

[37] J. Chung, C. Gulcehre, K. Cho, and Y. Bengio, "Empirical evaluation of gated recurrent neural networks on sequence modeling," 2014.

[38] F. Cigna and D. Tapete, "Satellite InSAR survey of structurally-controlled land subsidence due to groundwater exploitation in the Aguascalientes Valley, Mexico," *Remote Sensing of Environment*, vol. 254, p. 112 254, 2021.

[39] M. Costantini, "A novel phase unwrapping method based on network programming," *IEEE Transactions on Geoscience and Remote Sensing*, vol. 36, no. 3, pp. 813–821, 1998.

[40] M. Crosetto, L. Solari, M. Mróz, J. Balasis-Levinsen, N. Casagli, M. Frei, A. Oyen, D. A. Moldestad, L. Bateson, L. Guerrieri, V. Comerci, and H. S. Andersen, "The Evolution of Wide-Area DInSAR: From Regional and National Services to the European Ground Motion Service," *Remote Sensing*, vol. 12, no. 12, p. 2043, 12 2020.

[41] P. Ćwiąkała, W. Gruszczyński, T. Stoch, E. Puniach, D. Mrocheń, W. Matwij, K. Matwij, M. Nędzka, P. Sopata, and A. Wójcik, "UAV Applications for Determination of Land Deformations Caused by Underground Mining," *Remote Sensing*, vol. 12, no. 11, p. 1733, 11 2020.

[42] K. Dai, Z. Li, R. Tomás, G. Liu, B. Yu, X. Wang, H. Cheng, J. Chen, and J. Stockamp, "Monitoring activity at the Daguangbao mega-landslide (China) using Sentinel-1 TOPS time series interferometry," *Remote Sensing of Environment*, vol. 186, pp. 501–513, 2016.

[43] F. De Zan and A. Monti Guarnieri, "TOPSAR: Terrain Observation by Progressive Scans," *IEEE Transactions on Geoscience and Remote Sensing*, vol. 44, no. 9, pp. 2352–2360, 2006.

[44] T. Deguchi, M. Kato, H. Akcin, and H. S. Kutoglu, "Monitoring of mining induced land subsidence using L- and C-band SAR interferometry," in *2007 IEEE International Geoscience and Remote Sensing Symposium*, 2007, pp. 2122–2125.

[45] J. F. Dehls, Y. Larsen, P. Marinkovic, T. R. Lauknes, D. Stødle, and D. A. Moldestad, "INSAR.No: A National Insar Deformation Mapping/Monitoring Service In Norway – From Concept To Operations," in *IGARSS 2019 - 2019 IEEE International Geoscience and Remote Sensing Symposium*, 2019, pp. 5461–5464.

[46] X. Diao, K. Wu, D. Hu, L. Li, and D. Zhou, "Combining differential SAR interferometry and the probability integral method for three-dimensional deformation monitoring of mining areas," *International Journal of Remote Sensing*, vol. 37, no. 21, pp. 5196–5212, 2016.

[47] M.-P. Doin, F. Lodge, S. Guillaso, R. Jolivet, C. Lasserre, G. Ducret, R. Grandin, E. Pathier, and V. Pinel, "Presentation Of The Small Baseline NSBAS Processing Chain On A Case Example: The ETNA Deformation Monitoring From 2003 to 2010 Using ENVISAT Data," vol. 697, p. 98, 2012.

[48] S. Dong, S. Samsonov, H. Yin, S. Yao, and C. Xu, "Spatio-temporal analysis of ground subsidence due to underground coal mining in Huainan coalfield, China," *Environmental Earth Sciences*, vol. 73, no. 9, pp. 5523–5534, 2015.

[49] B. Drzęźla, "Przybliżona ocena niektórych parametrów kinematyki niecki osiadania przy zmianach prędkości wybierania i postojach ścian (Approximate evaluation of some parameters of subsidence trough kinematics with changes in extraction velocities and wall rests)," *Przegląd Górniczy*, no. 9, pp. 10–16, 1995.

[50] A. Ehrhardt and A. Sauer, "Precalculation of subsidence, tilt and curvature over extractions in flat formations," *Bergbauwissenschaften*, vol. 8, pp. 415–428, 1961.

[51] J. Engelbrecht and M. R. Inggs, "Detection and monitoring of surface subsidence associated with mining activities in the Witbank Coalfields, South Africa, using differential radar interferometry," in *2011 IEEE International Geoscience and Remote Sensing Symposium*, 2011, pp. 1596–1599.

[52] H. Fan, X. Gao, J. Yang, K. Deng, and Y. Yu, "Monitoring mining subsidence using a combination of phase-stacking and offset-tracking methods," *Remote Sensing*, vol. 7, no. 7, pp. 9166–9183, 2015.

[53] H. Fan, K. Deng, C. Ju, C. Zhu, and J. Xue, "Land subsidence monitoring by D-InSAR technique," *Mining Science and Technology (China)*, vol. 21, no. 6, pp. 869–872, 2011.

[54] H. Fan, L. Wang, B. Wen, and S. Du, "A New Model for three-dimensional Deformation Extraction with Single-track InSAR Based on Mining Subsidence Characteristics," *International Journal of Applied Earth Observation and Geoinformation*, vol. 94, p. 102 223, 2021.

[55] T. G. Farr, P. A. Rosen, E. Caro, R. Crippen, R. Duren, S. Hensley, M. Kobrick, M. Paller, E. Rodriguez, L. Roth, D. Seal, S. Shaffer, J. Shimada, J. Umland, M. Werner, M. Oskin, D. Burbank, and D. Alsdorf, "The Shuttle Radar Topography Mission," *Reviews of Geophysics*, vol. 45, no. 2, 2007.

[56] G. Feng, Z. Li, X. Shan, L. Zhang, G. Zhang, and J. Zhu, "Geodetic model of the 2015 April 25 Mw 7.8 Gorkha Nepal Earthquake and Mw 7.3 aftershock estimated from InSAR and GPS data," *Geophysical Journal International*, vol. 203, no. 2, pp. 896–900, 2015.

[57] A. Ferretti, C. Prati, and F. Rocca, "Nonlinear subsidence rate estimation using permanent scatterers in differential SAR interferometry," *IEEE Transactions on Geoscience and Remote Sensing*, vol. 38, no. 5, pp. 2202–2212, 2000.

[58] A. Ferretti, *Satellite InSAR Data - Reservoir Monitoring from Space*. European Association of Geoscientists & Engineers EAGE, 2014.

[59] A. Ferretti, A. Fumagalli, F. Novali, C. Prati, F. Rocca, and A. Rucci, "A New Algorithm for Processing Interferometric Data-Stacks: SqueeSAR," *IEEE Transactions on Geoscience and Remote Sensing*, vol. 49, no. 9, pp. 3460–3470, 2011.

[60] A. Ferretti, A. Monti-Guarnieri, C. Prati, F. Rocca, and D. Massonet, "InSAR Principles - Guidelines for SAR Interferometry Processing and Interpretation," *ESA Training Manual*, vol. 19, 2007.

[61] A. Ferretti, C. Prati, and F. Rocca, "Permanent Scatterers in SAR Interferometry," *IEEE TRANSACTIONS ON GEOSCIENCE AND REMOTE SENSING*, vol. 39, no. 1, p. 13, 2001.

[62] Y. Fialko, M. Simons, and D. Agnew, "The complete (3-D) surface displacement field in the epicentral area of the 1999 MW7.1 Hector Mine Earthquake, California, from space geodetic observations," *Geophysical Research Letters*, vol. 28, no. 16, pp. 3063–3066, 2001.

[63] H. Filcek, J. Walaszczyk, and A. Tajduś, *Metody Komputerowe w Geomechanice Górniczej (Computer methods in mining geomechanics)*. Śląskie Wydaw. Techniczne, 1994.

[64] J. H. Friedman, "Greedy function approximation: A gradient boosting machine," *Annals of statistics*, pp. 1189–1232, 2001.

[65] T. Fuhrmann and M. C. Garthwaite, "Resolving Three-Dimensional Surface Motion with InSAR: Constraints from Multi-Geometry Data Fusion," *Remote Sensing*, vol. 11, no. 3, p. 241, 2019.

[66] S. L. Furst, S. Doucet, P. Vernant, C. Champollion, and J.-L. Carme, "Monitoring surface deformation of deep salt mining in Vauvert (France), combining InSAR and leveling data for multi-source inversion," *Solid Earth*, vol. 12, no. 1, pp. 15–34, 2021.

[67] M. Gaddes, A. Hooper, and F. Albino, "Simultaneous classification and location of volcanic deformation in SAR interferograms using deep learning and the VolcNet database," 2021, [Online]. Available: `https://eartharxiv.org/repository/view/1969/` (visited on 07/14/2021).

[68] M. Gao, H. Gong, B. Chen, C. Zhou, W. Chen, Y. Liang, M. Shi, and Y. Si, "InSAR time-series investigation of long-term ground displacement at Beijing Capital International Airport, China," *Tectonophysics*, vol. 691, pp. 271–281, 2016.

[69] E. S. Gardner Jr., "Exponential smoothing: The state of the art," *Journal of Forecasting*, vol. 4, no. 1, pp. 1–28, 1985.

[70] D. Gee, L. Bateson, A. Sowter, S. Grebby, A. Novellino, F. Cigna, S. Marsh, C. Banton, and L. Wyatt, "Ground Motion in Areas of Abandoned Mining: Application of the Intermittent SBAS (ISBAS) to the Northumberland and Durham Coalfield, UK," *Geosciences*, vol. 7, no. 3, p. 85, 3 2017.

[71] G. M. R. George E. P. Jenkins, *Time Series Analysis: Forecasting and Control*. Hoboken: Wiley, 2015.

[72] D. C. Ghiglia, *Two-Dimensional Phase Unwrapping: Theory, Algorithms and Software*. New York: John Wiley & Sons, 1998, 493 pp.

[73] G. Giardina, P. Milillo, M. J. DeJong, D. Perissin, and G. Milillo, "Evaluation of InSAR monitoring data for post-tunnelling settlement damage assessment," *Structural Control and Health Monitoring*, vol. 26, no. 2, e2285, 2019.

[74] R. M. Goldstein and C. L. Werner, "Radar interferogram filtering for geophysical applications," *Geophysical Research Letters*, vol. 25, no. 21, pp. 4035–4038, 1998. (visited on 08/04/2022).

[75] R. M. Goldstein, H. A. Zebker, and C. L. Werner, "Satellite radar interferometry: Two-dimensional phase unwrapping," *Radio Science*, vol. 23, no. 4, pp. 713–720, 1988.

[76] I. Goodfellow, Y. Bengio, and A. Courville, *Deep Learning*. The MIT Press, 2016.

[77] N. Gourmelen, S. W. Kim, A. Shepherd, J. W. Park, A. V. Sundal, H. Björnsson, and F. Pálsson, "Ice velocity determined using conventional and multiple-aperture InSAR," *Earth and Planetary Science Letters*, vol. 307, no. 1, pp. 156–160, 2011.

[78] S. Gudmundsson, F. Sigmundsson, and J. M. Carstensen, "Three-dimensional surface motion maps estimated from combined interferometric synthetic aperture radar and GPS data," *Journal of Geophysical Research: Solid Earth*, vol. 107, no. B10, 2002.

[79] F. Guglielmino, G. Nunnari, G. Puglisi, and A. Spata, "Simultaneous and Integrated Strain Tensor Estimation From Geodetic and Satellite Deformation Measurements to Obtain Three-Dimensional Displacement Maps," *IEEE Transactions on Geoscience and Remote Sensing*, vol. 49, no. 6, pp. 1815–1826, 2011.

[80] M. H. Haghighi and M. Motagh, "Sentinel-1 InSAR over Germany: Large-Scale Interferometry, Atmospheric Effects, and Ground Deformation Mapping," *ZfV - Zeitschrift für Geodäsie, Geoinformation und Landmanagement*, zfv 4/2017 2017.

[81] R. F. Hanssen, *Radar Interferometry. Data Interpretation and Error Analysis*, ser. Remote Sensing and Digital Image Processing. Dordrecht: Kluwer Academic Publishers, 2001, vol. 2.

[82] R. Hejmanowski, A. A. Malinowska, W. T. Witkowski, and A. Guzy, "An Analysis Applying InSAR of Subsidence Caused by Nearby Mining-Induced Earthquakes," *Geosciences*, vol. 9, no. 12, p. 490, 12 2019.

[83] R. Hejmanowski and W. T. Witkowski, "Suitability assessment of artificial neural network to approximate surface subsidence due to rock mass drainage," *Journal of Sustainable Mining*, vol. 14, no. 2, pp. 101–107, 2015.

[84] P. Hill, J. Biggs, V. Ponce-López, and D. Bull, "Time-Series Prediction Approaches to Forecasting Deformation in Sentinel-1 InSAR Data," *Journal of Geophysical Research: Solid Earth*, vol. 126, no. 3, e2020JB020176, 2021.

[85] T. K. Ho, "Random decision forests," in *Proceedings of 3rd International Conference on Document Analysis and Recognition*, vol. 1, IEEE, 1995, pp. 278–282.

[86] S. Hochreiter and J. Schmidhuber, "Long short-term memory," *Neural computation*, vol. 9, no. 8, pp. 1735–1780, 1997.

[87] A. Hooper, D. Bekaert, K. Spaans, and M. Arıkan, "Recent advances in SAR interferometry time series analysis for measuring crustal deformation," *Tectonophysics*, vol. 514–517, pp. 1–13, 2012.

[88] A. Hooper, H. Zebker, P. Segall, and B. Kampes, "A new method for measuring deformation on volcanoes and other natural terrains using InSAR persistent scatterers," *Geophysical Research Letters*, vol. 31, no. 23, 2004.

[89] J. Hu, Z. W. Li, X. L. Ding, J. J. Zhu, L. Zhang, and Q. Sun, "Resolving three-dimensional surface displacements from InSAR measurements: A review," *Earth-Science Reviews*, vol. 133, pp. 1–17, 2014, ISSN: 0012-8252.

[90] J. Huang, K. Deng, H. Fan, and S. Yan, "An improved pixel-tracking method for monitoring mining subsidence," *Remote Sensing Letters*, vol. 7, no. 8, pp. 731–740, 2016.

[91] R. J. Hyndman and G. Athanasopoulos, *Forecasting: Principles and Practice*. OTexts, 2018.

[92] R. J. Hyndman and Y. Khandakar, "Automatic time series forecasting: The forecast package for R," *Journal of statistical software*, vol. 27, pp. 1–22, 2008.

[93] (). "HyP3," [Online]. Available: `https://hyp3-docs.asf.alaska.edu/` (visited on 11/02/2022).

[94] M. Ilieva, Ł. Rudziński, K. Pawłuszek-Filipiak, G. Lizurek, I. Kudłacik, D. Tondaś, and D. Olszewska, "Combined study of a significant mine collapse based on seismological and geodetic data—29 January 2019, Rudna Mine, Poland," *Remote Sensing*, vol. 12, no. 10, p. 1570, 2020.

[95] E. Intrieri, F. Raspini, A. Fumagalli, P. Lu, S. Del Conte, P. Farina, J. Allievi, A. Ferretti, and N. Casagli, "The Maoxian landslide as seen from space: Detecting precursors of failure with Sentinel-1 data," *Landslides*, vol. 15, no. 1, pp. 123–133, 2018, ISSN: 1612-5118.

[96] M.-J. Jo, H.-S. Jung, and S.-H. Chae, "Advances in three-dimensional deformation mapping from satellite radar observations: Application to the 2003 Bam earthquake," *Geomatics, Natural Hazards and Risk*, vol. 9, no. 1, pp. 678–690, 2018.

[97] I. Joughin, R. Kwok, and M. Fahnestock, "Interferometric estimation of three-dimensional ice-flow using ascending and descending passes," *IEEE Transactions on Geoscience and Remote Sensing*, vol. 36, no. 1, pp. 25–37, 1998.

[98] H. S. Jung, Z. Lu, J. S. Won, M. P. Poland, and A. Miklius, "Mapping Three-Dimensional Surface Deformation by Combining Multiple-Aperture Interferometry and Conventional Interferometry: Application to the June 2007 Eruption of Kilauea Volcano, Hawaii," *IEEE geoscience and remote sensing letters*, vol. 8, no. 1, pp. 34–38, 2011.

[99] B. M. Kampes, *Radar interferometry: Persistent Scatterer Technique*, 1. Aufl., ser. Remote sensing and digital image processing. Dordrecht: Springer-Verlag, 2006, vol. 12.

[100] K. Karamvasis and V. Karathanassi, "Performance Analysis of Open Source Time Series InSAR Methods for Deformation Monitoring over a Broader Mining Region," *Remote Sensing*, vol. 12, no. 9, p. 1380, 2020.

[101] H. Keinhorst, "Betrachtungen zur Bergschädenfrage," p. 149, 1934.

[102] K.-D. Kim, S. Lee, and H.-J. Oh, "Prediction of ground subsidence in Samcheok City, Korea using artificial neural networks and GIS," *Environmental Geology*, vol. 58, no. 1, pp. 61–70, 2009.

[103] J. Kim, J. A. Coe, Z. Lu, N. N. Avdievitch, and C. P. Hults, "Spaceborne InSAR mapping of landslides and subsidence in rapidly deglaciating terrain, Glacier Bay National Park and Preserve and vicinity, Alaska and British Columbia," *Remote Sensing of Environment*, vol. 281, p. 113 231, 2022, ISSN: 0034-4257.

[104] K.-j. Kim, "Financial time series forecasting using support vector machines," *Neurocomputing*, vol. 55, no. 1-2, pp. 307–319, 2003.

[105] S. Kiranyaz, T. Ince, O. Abdeljaber, O. Avci, and M. Gabbouj, "1-D Convolutional Neural Networks for Signal Processing Applications," in *ICASSP 2019 - 2019 IEEE International Conference on Acoustics, Speech and Signal Processing (ICASSP)*, 2019, pp. 8360–8364.

[106] S. M. Knothe, *Prognozowanie Wpływów Eksploatacji Górniczej (Forecasting the Impacts of Mining Operations)*. Wydaw. Śląsk, 1984.

[107] T. Kochmański, "Całkowa teoria ruchów górotworu nad eksploatacją złoża pokładowego na podstawie pomiarów geodezyjnych (Integral theory of rock mass movements over bedrock exploitation based on geodetic measurements)," *Geodezja i Kartografia*, vol. 4, no. 2, 1955.

[108] A. Kowalski, *Deformacje Powierzchni Na Terenach Górniczych Kopalń Węgla Kamiennego (Surface deformations in the mining areas of hard coal mines)*. Główny Instytut Górnictwa, 2020.

[109] H. Kratzsch, *Mining Subsidence Engineering*. Berlin, Heidelberg: Springer Berlin Heidelberg, 1983.

[110] A. Krawczyk and Z. Perski, "Application of satellite radar interferometry on the areas of underground exploitation of copper ore in LGOM–Poland," in *First International Congress of the International Society for Mine Surveying*, vol. 2, 2000, pp. 209–218.

[111] S. Kumar, D. Kumar, P. K. Donta, and T. Amgoth, "Land subsidence prediction using recurrent neural networks," *Stochastic Environmental Research and Risk Assessment*, vol. 36, no. 2, pp. 373–388, 2022.

[112] J. Kwiatek, "Zastosowanie modelu ciała Kelvina do opisu nieustalonej niecki osiadania (Application of the Kelvin body model to the description of an undetermined subsidence basin)," in *Materiały Konferencji Naukowo-Technicznej: Przemysł Wydobywczy Na Przełomie XX i XXI Stulecia. Kraków, AGH*, 2000.

[113] M. Lazecký, E. Jiránková, and P. Kadlečík, "Multitemporal monitoring of Karvina subsidence troughs using sentinel-1 and TERRASAR-X interferometry," *Acta Geodynamica et Geomaterialia*, vol. 14, no. 1, pp. 53–59, 2017.

[114] M. Lazecký, E. Hatton, P. J. González, I. Hlaváčová, E. Jiránková, F. Dvořák, Z. Šustr, and J. Martinovič, "Displacements Monitoring over Czechia by IT4S1 System for Automatised Interferometric Measurements Using Sentinel-1 Data," *Remote Sensing*, vol. 12, no. 18, p. 2960, 18 2020.

[115] M. Lazecký, K. Spaans, P. J. González, Y. Maghsoudi, Y. Morishita, F. Albino, J. Elliott, N. Greenall, E. Hatton, A. Hooper, D. Juncu, A. McDougall, R. J. Walters, C. S. Watson, J. R. Weiss, and T. J. Wright, "LiCSAR: An Automatic InSAR Tool for Measuring and Monitoring Tectonic and Volcanic Activity," *Remote Sensing*, vol. 12, no. 15, p. 2430, 15 2020.

[116] Y. LeCun, B. Boser, J. Denker, D. Henderson, R. Howard, W. Hubbard, and L. Jackel, "Handwritten digit recognition with a back-propagation network," *Advances in neural information processing systems*, vol. 2, 1989.

[117] S. Lee, I. Park, and J.-K. Choi, "Spatial Prediction of Ground Subsidence Susceptibility Using an Artificial Neural Network," *Environmental Management*, vol. 49, no. 2, pp. 347–358, 2012.

[118] K. Leptokaropoulos, S. Cielesta, M. Staszek, D. Olszewska, G. Lizurek, J. Kocot, S. Lasocki, B. Orlecka-Sikora, M. Sterzel, and T. Szepieniec, "IS-EPOS: A platform for anthropogenic seismicity research," *Acta Geophysica*, vol. 67, no. 1, pp. 299–310, 2019.

[119] H. Li, L. Zhu, Z. Dai, H. Gong, T. Guo, G. Guo, J. Wang, and P. Teatini, "Spatiotemporal modeling of land subsidence using a geographically weighted deep learning method based on PS-InSAR," *Science of The Total Environment*, vol. 799, p. 149 244, 2021.

[120] H. Li, L. Zhu, H. Gong, H. Sun, and J. Yu, "Land subsidence modelling using a long short-term memory algorithm based on time-series datasets," in *Proceedings of the International Association of Hydrological Sciences*, vol. 382, Copernicus GmbH, 2020, pp. 505–510.

[121] J. Li and L. Wang, "Mining subsidence monitoring model based on BPM-EKTF and TLS and its application in building mining damage assessment," *Environmental Earth Sciences*, vol. 80, no. 11, p. 396, 2021.

[122] P. Li, Z. Tan, L. Yan, and K. Deng, "Time series prediction of mining subsidence based on a SVM," *Mining Science and Technology (China)*, vol. 21, no. 4, pp. 557–562, 2011.

[123] Y.-f. LI, X.-q. ZUO, Y.-y. MA, P. XIONG, and F. YANY, "Surface subsidence monitoring and prediction based on PS-InSAR technology and genetic neural network algorithm," *Progress in Geophysics*, vol. 35, no. 3, pp. 845–851, 2020.

[124] Z. Li, Z. Yang, J. Zhu, J. Hu, Y. Wang, P. Li, and G. Chen, "Retrieving three-dimensional displacement fields of mining areas from a single InSAR pair," *Journal of Geodesy*, vol. 89, no. 1, pp. 17–32, 2015.

[125] Z. Li, E. J. Fielding, and P. Cross, "Integration of InSAR Time-Series Analysis and Water-Vapor Correction for Mapping Postseismic Motion After the 2003 Bam (Iran) Earthquake," *IEEE Transactions on Geoscience and Remote Sensing*, vol. 47, no. 9, pp. 3220–3230, 2009.

[126] X. Lian, X. Liu, L. Ge, H. Hu, Z. Du, and Y. Wu, "Time-series unmanned aerial vehicle photogrammetry monitoring method without ground control points to measure mining subsidence," *Journal of Applied Remote Sensing*, vol. 15, no. 2, p. 024 505, 2021.

[127] B. Lim, S. Ö. Arık, N. Loeff, and T. Pfister, "Temporal fusion transformers for interpretable multi-horizon time series forecasting," *International Journal of Forecasting*, vol. 37, no. 4, pp. 1748–1764, 2021.

[128] J. Litwiniszyn, "Przemieszczenia górotworu w świetle teorii prawdopodobieństwa (Rock mass dislocations in light of probability theory)," *Archiwum Górnictwa i Hutnictwa*, vol. 2, no. 1, 1954.

[129] J. Litwiniszyn, "Teorie wpływu eksploatacji na powierzchnię wczoraj, dziś i jutro (Theories of the impact of exploitation on the surface yesterday, today and tomorrow)," in *Szkoła Eksploatacji Podziemnej, Mat. Konf*, 1993.

[130] B. Liu and G. Liao, *Basic law of ground surface movement due to coal mining*, 1965.

[131] F. Liu, J. R. Elliott, T. J. Craig, A. Hooper, and T. J. Wright, "Improving the Resolving Power of InSAR for Earthquakes Using Time Series: A Case Study in Iran," *Geophysical Research Letters*, vol. 48, no. 14, e2021GL093043, 2021.

[132] Z. Lu and D. Dzurisin, "InSAR imaging of Aleutian volcanoes," in *InSAR Imaging of Aleutian Volcanoes*, Springer, 2014, pp. 87–345.

[133] P. Ma, F. Zhang, and H. Lin, "Prediction of InSAR time-series deformation using deep convolutional neural networks," *Remote Sensing Letters*, vol. 11, no. 2, pp. 137–145, 2020.

[134] Z. Ma, G. Mei, and F. Piccialli, "Machine learning for landslides prevention: A survey," *Neural Computing and Applications*, vol. 33, no. 17, pp. 10 881–10 907, 2021.

[135] S. Makridakis, E. Spiliotis, and V. Assimakopoulos, "M5 accuracy competition: Results, findings, and conclusions," *International Journal of Forecasting*, 2022.

[136] S. Makridakis, E. Spiliotis, and V. Assimakopoulos, "The M4 Competition: 100,000 time series and 61 forecasting methods," *International Journal of Forecasting*, M4 Competition, vol. 36, no. 1, pp. 54–74, 2020.

[137] A. A. Malinowska, W. T. Witkowski, A. Guzy, and R. Hejmanowski, "Mapping ground movements caused by mining-induced earthquakes applying satellite radar interferometry," *Engineering Geology*, vol. 246, pp. 402–411, 2018.

[138] D. Massonnet, P. Briole, and A. Arnaud, "Deflation of Mount Etna monitored by spaceborne radar interferometry," *Nature*, vol. 375, no. 6532, pp. 567–570, 6532 1995.

[139] D. Massonnet, M. Rossi, C. Carmona, F. Adragna, G. Peltzer, K. Feigl, and T. Rabaute, "The displacement field of the Landers earthquake mapped by radar interferometry," *Nature*, vol. 364, no. 6433, pp. 138–142, 1993.

[140] P. Mazzanti, B. Antonielli, A. Sciortino, S. Scancella, and F. Bozzano, "Tracking Deformation Processes at the Legnica Glogow Copper District (Poland) by Satellite InSAR—II: Żelazny Most Tailings Dam," *Land*, vol. 10, no. 6, p. 654, 6 2021.

[141] W. S. McCulloch and W. Pitts, "A logical calculus of the ideas immanent in nervous activity," *The bulletin of mathematical biophysics*, vol. 5, no. 4, pp. 115–133, 1943.

[142] Q. Meng, H. Wang, M. He, J. Gu, J. Qi, and L. Yang, "Displacement prediction of water-induced landslides using a recurrent deep learning model," *European Journal of Environmental and Civil Engineering*, vol. 0, no. 0, pp. 1–15, 2020.

[143] F. Miao, X. Xie, Y. Wu, and F. Zhao, "Data Mining and Deep Learning for Predicting the Displacement of "Step-like" Landslides," *Sensors*, vol. 22, no. 2, p. 481, 2 2022.

[144] R. Michel, J.-P. Avouac, and J. Taboury, "Measuring ground displacements from SAR amplitude images: Application to the Landers Earthquake," *Geophysical Research Letters*, vol. 26, no. 7, pp. 875–878, 1999.

[145] W. Milczarek, "Application of a small baseline subset time series method with atmospheric correction in monitoring results of mining activity on ground surface and in detecting induced seismic events," *Remote Sensing*, vol. 11, no. 9, 2019.

[146] W. Milczarek, J. Blachowski, and P. Grzempowski, "Application of PSInSAR for assessment of surface deformations in post-mining area - case study of the former Walbrzych hard coal basin (SW Poland)," *Acta Geodynamica et Geomaterialia*, vol. 14, no. 1, pp. 41–52, 2017.

[147] W. Milczarek, "Application of PSInSAR for assessment of surface deformations in post_mining area _ case study of the former Walbrzych Hard Coal Basin (SW Poland)," *Acta Geodynamica et Geomaterialia*, pp. 41–52, 2016.

[148] W. Milczarek, A. Kopeć, and D. Głąbicki, "Estimation of tropospheric and ionospheric delay in DInSAR calculations: Case study of areas showing (natural and induced) seismic activity," *Remote Sensing*, vol. 11, no. 6, p. 621, 2019.

[149] W. Milczarek, A. Kopeć, D. Głąbicki, and N. Bugajska, "Induced Seismic Events - Distribution of Ground Surface Displacements Based on InSAR Methods and Mogi and Yang Models," *Remote Sensing*, vol. 13, no. 8, p. 1451, 8 2021.

[150] P. Milillo, D. Perissin, J. T. Salzer, P. Lundgren, G. Lacava, G. Milillo, and C. Serio, "Monitoring dam structural health from space: Insights from novel InSAR techniques and multi-parametric modeling applied to the Pertusillo dam Basilicata, Italy," *International journal of applied earth observation and geoinformation*, vol. 52, pp. 221–229, 2016.

[151] N. Miranda, "Definition of the TOPS SLC deramping function for products generated by the S-1 IPF," European Space Agency, Technical Note, 2017, p. 15.

[152] Y. Mohajerani, S. Jeong, B. Scheuchl, I. Velicogna, E. Rignot, and P. Milillo, "Automatic delineation of glacier grounding lines in differential interferometric synthetic-aperture radar data using deep learning," *Scientific Reports*, vol. 11, no. 1, p. 4992, 1 2021.

[153] D. C. Montgomery, C. L. Jennings, and M. Kulahci, *Introduction to Time Series Analysis and Forecasting*. John Wiley & Sons, 2015.

[154] Y. Morishita, "Nationwide urban ground deformation monitoring in Japan using Sentinel-1 LiCSAR products and LiCSBAS," *Progress in Earth and Planetary Science*, vol. 8, no. 1, p. 6, 2021.

[155] Y. Morishita, M. Lazecky, T. J. Wright, J. R. Weiss, J. R. Elliott, and A. Hooper, "LiCSBAS: An Open-Source InSAR Time Series Analysis Package Integrated with the LiCSAR Automated Sentinel-1 InSAR Processor," *Remote Sensing*, vol. 12, no. 3, p. 424, 3 2020.

[156] J. Mouginot, E. Rignot, and B. Scheuchl, "Continent-Wide, Interferometric SAR Phase, Mapping of Antarctic Ice Velocity," *Geophysical Research Letters*, vol. 46, no. 16, pp. 9710–9718, 2019.

[157] S. Mukherjee, A. Zimmer, X. Sun, P. Ghuman, and I. Cheng, "An Unsupervised Generative Neural Approach for InSAR Phase Filtering and Coherence Estimation," *IEEE Geoscience and Remote Sensing Letters*, vol. 18, no. 11, pp. 1971–1975, 2021.

[158] A. C. Müller, *Introduction to Machine Learning with Python: A Guide for Data Scientists*. 1st ed.., in collab. with S. Guido. Sebastopol: O'Reilly Media, Incorporated, 2016.

[159] C. R. Nelson, "The first-order moving average process : Identification, estimation and prediction," *Journal of Econometrics*, vol. 2, no. 2, pp. 121–141, 1974.

[160] D. Newman, Z. Agioutantis, and M. Karmis, "SDPS for windows: An integrated approach to ground deformation prediction," in *Proceedings of the 20th International Conference on Ground Control in Mining*, 2001, pp. 157–162.

[161] A.-M. Ng, L. Ge, Y. Yan, X. Li, H.-C. Chang, K. Zhang, and C. Rizos, "Mapping accumulated mine subsidence using small stack of SAR differential interferograms in the Southern coalfield of New South Wales, Australia," *Engineering Geology*, vol. 115, no. 1-2, pp. 1–15, 2010.

[162] A. Ng, L. Ge, K. Zhang, and X. Li, "Estimating horizontal and vertical movements due to underground mining using ALOS PALSAR," *Engineering Geology*, vol. 143–144, pp. 18–27, 2012.

[163] R. Niemiec and T. Niemiec, "Błądzenie losowe i jego zastosowanie do modelowania deformacji górotworu powodowanych eksploatacją górniczą (Random error and its application to the modelling of rock deformation caused by mining operations)," *Prace Naukowe GIG. Górnictwo i Środowisko/Główny Instytut Górnictwa*, no. 6, pp. 351–364, 2008.

[164] B. N. Oreshkin, D. Carpov, N. Chapados, and Y. Bengio, "N-BEATS: Neural basis expansion analysis for interpretable time series forecasting," 2019.

[165] B. Osmanoğlu, F. Sunar, S. Wdowinski, and E. Cabral-Cano, "Time series analysis of InSAR data: Methods and trends," *ISPRS Journal of Photogrammetry and Remote Sensing*, Theme Issue 'State-of-the-art in Photogrammetry, Remote Sensing and Spatial Information Science', vol. 115, pp. 90–102, 2016.

[166] K. Owczarz and J. Blachowski, "Application of DInSAR and Spatial Statistics Methods in Analysis of Surface Displacements Caused by Induced Tremors," *Applied Sciences*, vol. 10, no. 21, p. 7660, 2020.

[167] I. Park, J. Choi, M. Jin Lee, and S. Lee, "Application of an adaptive neuro-fuzzy inference system to ground subsidence hazard mapping," *Computers & Geosciences*, vol. 48, pp. 228–238, 2012.

[168] R. Pascanu, T. Mikolov, and Y. Bengio, "On the difficulty of training recurrent neural networks," in *International Conference on Machine Learning*, PMLR, 2013, pp. 1310–1318.

[169] K. Pawluszek-Filipiak and A. Borkowski, "Integration of DInSAR and SBAS Techniques to Determine Mining-Related Deformations Using Sentinel-1 Data: The Case Study of Rydułtowy Mine in Poland," *Remote Sensing*, vol. 12, no. 2, p. 242, 2020.

[170] S. Peng, *Surface Subsidence Engineering: Theory and Practice*. Csiro Publishing, 2020, 221 pp.

[171] Z. Perski, "The interpretation of ERS-1 and ERS-2 INSAR data for the mining subsidence monitoring in upper silesian coal Basin, Poland," presented at the International Archives of the Photogrammetry, Remote Sensing and Spatial Information Sciences - ISPRS Archives, vol. 33, 2000, pp. 1137–1141.

[172] A. Piestrzyński, *Monografia KGHM Polska Miedź S.A. (Monograph of KGHM Polska Miedź SA)*, Wyd. 2. Lubin: KGHM CUPRUM Sp. z o.o. CBR, 2008, 1080 pp.

[173] M. P. Poland, T. Lopez, R. Wright, and M. J. Pavolonis, "Forecasting, Detecting, and Tracking Volcanic Eruptions from Space," *Remote Sensing in Earth Systems Sciences*, vol. 3, no. 1, pp. 55–94, 2020.

[174] M. P. Poland and H. A. Zebker, "Volcano geodesy using InSAR in 2020: The past and next decades," *Bulletin of Volcanology*, vol. 84, no. 3, pp. 1–8, 2022.

[175] M. Polcari, M. Palano, J. Fernández, S. V. Samsonov, S. Stramondo, and S. Zerbini, "3D displacement field retrieved by integrating Sentinel-1 InSAR and GPS data: The 2014 South Napa earthquake," *European Journal of Remote Sensing*, vol. 49, no. 1, pp. 1–13, 2016.

[176] M. E. Pritchard and M. Simons, "An InSAR-based survey of volcanic deformation in the central Andes," *Geochemistry, Geophysics, Geosystems*, vol. 5, no. 2, 2004.

[177] M. Przyłucka, G. Herrera, M. Graniczny, D. Colombo, and M. Béjar-Pizarro, "Combination of Conventional and Advanced DInSAR to Monitor Very Fast Mining Subsidence with TerraSAR-X Data: Bytom City (Poland)," *Remote Sensing*, vol. 7, no. 5, pp. 5300–5328, 2015.

[178] A. Radman, M. Akhoondzadeh, and B. Hosseiny, "Integrating InSAR and deep-learning for modeling and predicting subsidence over the adjacent area of Lake Urmia, Iran," *GIScience & Remote Sensing*, pp. 1–21, 2021.

[179] O. Rahmati, F. Falah, S. A. Naghibi, T. Biggs, M. Soltani, R. C. Deo, A. Cerdà, F. Mohammadi, and D. Tien Bui, "Land subsidence modelling using tree-based machine learning algorithms," *Science of The Total Environment*, vol. 672, pp. 239–252, 2019.

[180] S. Raschka, Y. H. Liu, V. Mirjalili, and D. Dzhulgakov, *Machine Learning with PyTorch and Scikit-Learn: Develop Machine Learning and Deep Learning Models with Python*. Packt Publishing Ltd, 2022.

[181] D. Raucoules, C. Carnec, S. Le Mouelic, C. King, and C. Maisons, "Comparison between InSAR and leveling," in *IGARSS 2003. 2003 IEEE International Geoscience and Remote Sensing Symposium. Proceedings (IEEE Cat. No.03CH37477)*, vol. 4, 2003, 2939–2941 vol.4.

[182] D. J. Reddish and B. N. Whittaker, *Subsidence: Occurrence, Prediction and Control*. Amsterdam, Netherlands ; New York : New York, NY, U.S.A: Elsevier Science, 1989, 528 pp.

[183] G. Ristanoski, W. Liu, and J. Bailey, "Time series forecasting using distribution enhanced linear regression," in *Pacific-Asia Conference on Knowledge Discovery and Data Mining*, Springer, 2013, pp. 484–495.

[184] A. Rosi, V. Tofani, L. Tanteri, C. Tacconi Stefanelli, A. Agostini, F. Catani, and N. Casagli, "The new landslide inventory of Tuscany (Italy) updated with PS-InSAR: Geomorphological features and landslide distribution," *Landslides*, vol. 15, no. 1, pp. 5–19, 2018.

[185] B. Rouet-Leduc, R. Jolivet, M. Dalaison, P. A. Johnson, and C. Hulbert, "Autonomous extraction of millimeter-scale deformation in InSAR time series using deep learning," *Nature Communications*, vol. 12, no. 1, p. 6480, 1 2021.

[186] V. Rudajev and R. Číž, "Estimation of Mining Tremor Occurrence by Using Neural Networks," *pure and applied geophysics*, vol. 154, no. 1, pp. 57–72, 1999.

[187] D. E. Rumelhart, G. E. Hinton, and R. J. Williams, "Learning representations by back-propagating errors," *nature*, vol. 323, no. 6088, pp. 533–536, 1986.

[188] A. Sagheer and M. Kotb, "Time series forecasting of petroleum production using deep LSTM recurrent networks," *Neurocomputing*, vol. 323, pp. 203–213, 2019.

[189] D. Salinas, V. Flunkert, and J. Gasthaus, *DeepAR: Probabilistic Forecasting with Autoregressive Recurrent Networks*, 2019. arXiv: `1704.04110 [cs, stat]`.

[190] A. Sałustowicz, "Profil Niecki Osiadania Jako Ugięcie Warstwy Na Sprężystym Podłożu (Settlement Basin Profile as Deflection of a Layer on a Flexible Substrate)," *Archiwum Górnictwa i Hutnictwa*, vol. 1, no. 1, 1953.

[191] S. Samieie-Esfahany, R. F. Hanssen, K. van Thienen-Visser, and A. Muntendam-Bos, "On the effect of horizontal deformation on insar subsidence estimates," 2009.

[192] S. Samsonov and K. Tiampo, "Analytical optimization of a DInSAR and GPS dataset for derivation of three-dimensional surface motion," *IEEE Geoscience and Remote Sensing Letters*, vol. 3, no. 1, pp. 107–111, 2006.

[193] S. Samsonov, N. d'Oreye, and B. Smets, "Ground deformation associated with post-mining activity at the French–German border revealed by novel InSAR time series method," *International Journal of Applied Earth Observation and Geoinformation*, vol. 23, pp. 142–154, 2013.

[194] S. Siami-Namini, N. Tavakoli, and A. S. Namin, "A comparison of ARIMA and LSTM in forecasting time series," in *2018 17th IEEE International Conference on Machine Learning and Applications (ICMLA)*, IEEE, 2018, pp. 1394–1401.

[195] F. Sica, G. Gobbi, P. Rizzoli, and L. Bruzzone, "-Net: Deep Residual Learning for InSAR Parameters Estimation," *IEEE Transactions on Geoscience and Remote Sensing*, vol. 59, no. 5, pp. 3917–3941, 2021.

[196] P. Sikora, "Zastosowanie metody automatów komórkowych do opisu deformacji górotworu spowodowanych podziemną eksploatacją górniczą (Application of the cellular automata method to the description of rock deformation caused by underground mine exploitation)," *Gliwice, Publishing House of Silesian University of Technology*, Monography, 2019.

[197] M. Simons, Y. Fialko, and L. Rivera, "Coseismic Deformation from the 1999 M_w 7.1 Hector Mine, California, Earthquake as Inferred from InSAR and GPS Observations," *Bulletin of the Seismological Society of America*, vol. 92, pp. 1390–1402, 2002.

[198] L. Sui, F. Ma, and N. Chen, "Mining Subsidence Prediction by Combining Support Vector Machine Regression and Interferometric Synthetic Aperture Radar Data," *ISPRS International Journal of Geo-Information*, vol. 9, no. 6, p. 390, 2020.

[199] Q. Sun, L. Zhang, X. L. Ding, J. Hu, Z. W. Li, and J. J. Zhu, "Slope deformation prior to Zhouqu, China landslide from InSAR time series analysis," *Remote Sensing of Environment*, vol. 156, pp. 45–57, 2015.

[200] A. Szostak-Chrzanowski, "An iterative modelling of ground subsidence using non-linear elastic finite element analysis," in *5th International Symposium on Deformation Measurements*, 1988.

[201] M. Szuflicki, A. Malon, and M. Tymiński, "Bilans zasobów złóż kopalin w Polsce (Balance of mineral resources in Poland)," *Państwowy Instytut Geologiczy - Państwowy Instytut Badawczy*, p. 509, 2022.

[202] T. Tao, J. Liu, X. Qu, and F. Gao, "Real-time monitoring rapid ground subsidence using GNSS and Vondrak filter," *Acta Geophysica*, vol. 67, no. 1, pp. 133–140, 2019.

[203] R. Tomás, R. Romero, J. Mulas, J. Marturià, J. Mallorquí, J. Lopez-Sanchez, G. Herrera, F. Gutiérrez, P. González, J. Fernández, S. Duque, A. Concha-Dimas, G. Cocksley, C. Castañeda, D. Carrasco, and P. Blanco, "Radar interferometry techniques for the study of ground subsidence phenomena: A review of practical issues through cases in Spain," *Environmental Earth Sciences*, vol. 71, no. 1, pp. 163–181, 2014.

[204] R. Torres, P. Snoeij, D. Geudtner, D. Bibby, M. Davidson, E. Attema, P. Potin, B. Rommen, N. Floury, M. Brown, I. N. Traver, P. Deghaye, B. Duesmann, B. Rosich, N. Miranda, C. Bruno, M. L'Abbate, R. Croci, A. Pietropaolo, M. Huchler, and F. Rostan, "GMES Sentinel-1 mission," *Remote Sensing of Environment*, The Sentinel Missions - New Opportunities for Science, vol. 120, pp. 9–24, 2012.

[205] D. Tran, L. Bourdev, R. Fergus, L. Torresani, and M. Paluri, "Learning spatiotemporal features with 3d convolutional networks," in *Proceedings of the IEEE International Conference on Computer Vision*, 2015, pp. 4489–4497.

[206] S. R. Vahid Mirjalili, *Python Machine Learning: Machine Learning and Deep Learning with Python, Scikit-Learn, and TensorFlow 2*. Packt Publishing, 2019.

[207] A. Vaswani, N. Shazeer, N. Parmar, J. Uszkoreit, L. Jones, A. N. Gomez, L. Kaiser, and I. Polosukhin, "Attention is all you need," *Advances in neural information processing systems*, vol. 30, 2017.

[208] A. Vervoort, "Surface movement above an underground coal longwall mine after closure," *Natural Hazards and Earth System Sciences*, vol. 16, no. 9, pp. 2107–2121, 2016.

[209] J. Wang, X. Peng, and C. hui Xu, "Coal mining GPS subsidence monitoring technology and its application," *Mining Science and Technology (China)*, vol. 21, no. 4, pp. 463–467, 2011.

[210] P. Wang, B.-C. Zhang, and Y.-F. Wang, "An Anisotropic Gaussian Filter for Noise Filtering of InSAR Interferogram," in *2006 CIE International Conference on Radar*, 2006, pp. 1–4.

[211] Y. Wang, Z. Yang, Z. Li, J. Zhu, and L. Wu, "Fusing adjacent-track InSAR datasets to densify the temporal resolution of time-series 3-D displacement estimation over mining areas with a prior deformation model and a generalized weighting least-squares method," *Journal of Geodesy*, vol. 94, no. 5, p. 47, 2020.

[212] Z. Wang, R. Zhang, X. Wang, and G. Liu, "Retrieving three-dimensional co-seismic deformation of the 2017 Mw7.3 Iraq earthquake by multi-sensor SAR images," *Remote Sensing*, vol. 10, no. 6, 2018.

[213] E. Warchala, A. Szostak-Chrzanowski, and P. Stefanek, "Wykorzystanie MES do prognozowania przemieszczeń terenu wywołanych eksploatacją górniczą (The use of MES for the prediction of ground displacement caused by mining operations)," *Zeszyty Naukowe Instytutu Gospodarki Surowcami Mineralnymi i Energią PAN*, 2017.

[214] U. Wegmuller, C. Werner, T. Strozzi, and A. Wiesmann, "Monitoring mining induced surface deformation," in *IGARSS 2004. 2004 IEEE International Geoscience and Remote Sensing Symposium*, vol. 3, 2004, pp. 1933–1935.

[215] J. R. Weiss, R. J. Walters, Y. Morishita, T. J. Wright, M. Lazecky, H. Wang, E. Hussain, A. J. Hooper, J. R. Elliott, and C. Rollins, "High-resolution surface velocities and strain for Anatolia from Sentinel-1 InSAR and GNSS data," *Geophysical Research Letters*, vol. 47, no. 17, e2020GL087376, 2020.

[216] J. M. Wempen and M. K. McCarter, "Comparison of L-band and X-band differential interferometric synthetic aperture radar for mine subsidence monitoring in central Utah," *International Journal of Mining Science and Technology*, SI: Special Issue on Ground Control in Mining in 2016, vol. 27, no. 1, pp. 159–163, 2017.

[217] P. J. Werbos, "Backpropagation through time: What it does and how to do it," *Proceedings of the IEEE*, vol. 78, no. 10, pp. 1550–1560, 1990.

[218] C. Werner, U. Wegmuller, T. Strozzi, and A. Wiesmann, "Interferometric point target analysis for deformation mapping," in *IGARSS 2003. 2003 IEEE International Geoscience and Remote Sensing Symposium. Proceedings (IEEE Cat. No.03CH37477)*, vol. 7, IEEE, 2003, 4362–4364 vol.7.

[219] B. Widrow and M. E. Hoff, "Adaptive switching circuits," Stanford Univ Ca Stanford Electronics Labs, 1960.

[220] C. A. Wiley, "Pulsed doppler radar methods and apparatus," U.S. Patent 3196436A, 1965.

[221] P. R. Winters, "Forecasting Sales by Exponentially Weighted Moving Averages," *Management Science*, vol. 6, no. 3, pp. 324–342, 1960.

[222] W. T. Witkowski, D. Mrocheń, P. Sopata, and T. Stoch, "Integration of the Leveling Observations and Psinsar Results for Monitoring Deformations Caused by Underground Mining," in *2021 IEEE International Geoscience and Remote Sensing Symposium IGARSS*, 2021, pp. 6614–6617.

[223] P. Wright and R. Stow, "Detecting mining subsidence from space," *International Journal of Remote Sensing*, vol. 20, no. 6, pp. 1183–1188, 1999.

[224] T. J. Wright, Z. Lu, and C. Wicks, "Source model for the Mw 6.7, 23 October 2002, Nenana Mountain Earthquake (Alaska) from InSAR," *Geophysical Research Letters*, vol. 30, no. 18, 2003.

[225] T. J. Wright, B. E. Parsons, and Z. Lu, "Toward mapping surface deformation in three dimensions using InSAR," *Geophysical Research Letters*, vol. 31, no. 1, 2004.

[226] Z. Wu, T. Wang, Y. Wang, R. Wang, and D. Ge, "Deep Learning for the Detection and Phase Unwrapping of Mining-Induced Deformation in Large-Scale Interferograms," *IEEE Transactions on Geoscience and Remote Sensing*, vol. 60, pp. 1–18, 2022.

[227] J. Wyżykowski and W. Jórczak, "Dolnocechsztyńskie łupki miedzionośne (Lower Cechstein copper-bearing shales)," *Przegląd Geologiczny*, vol. 5, no. 5, p. 238, 5 1957.

[228] H. Xu, F. Chen, and W. Zhou, "A comparative case study of MTInSAR approaches for deformation monitoring of the cultural landscape of the Shanhaiguan section of the Great Wall," *Heritage Science*, vol. 9, no. 1, p. 71, 2021.

[229] X. Xu, D. T. Sandwell, and B. Smith-Konter, "Coseismic displacements and surface fractures from Sentinel-1 InSAR: 2019 Ridgecrest earthquakes," *Seismological Research Letters*, vol. 91, no. 4, pp. 1979–1985, 2020.

[230] N. Yagüe-Martínez, P. Prats-Iraola, F. Rodríguez González, R. Brcic, R. Shau, D. Geudtner, M. Eineder, and R. Bamler, "Interferometric Processing of Sentinel-1 TOPS Data," *IEEE Transactions on Geoscience and Remote Sensing*, vol. 54, no. 4, pp. 2220–2234, 2016.

[231] Y. Yan, M.-P. Doin, P. Lopez-Quiroz, F. Tupin, B. Fruneau, V. Pinel, and E. Trouve, "Mexico City Subsidence Measured by InSAR Time Series: Joint Analysis Using PS and SBAS Approaches," *IEEE Journal of Selected Topics in Applied Earth Observations and Remote Sensing*, vol. 5, no. 4, pp. 1312–1326, 2012.

[232] B. Yang, K. Yin, S. Lacasse, and Z. Liu, "Time series analysis and long short-term memory neural network to predict landslide displacement," *Landslides*, vol. 16, no. 4, pp. 677–694, 2019.

[233] W. Yang and X. Xia, "Prediction of mining subsidence under thin bedrocks and thick unconsolidated layers based on field measurement and artificial neural networks," *Computers & Geosciences*, vol. 52, pp. 199–203, 2013.

[234] Z. Yang, Z. Li, J. Zhu, A. Preusse, H. Yi, J. Hu, G. Feng, and M. Papst, "Retrieving 3-D Large Displacements of Mining Areas from a Single Amplitude Pair of SAR Using Offset Tracking," *Remote Sensing*, vol. 9, no. 4, p. 338, 2017.

[235] Z. Yang, Z. Li, J. Zhu, Y. Wang, and L. Wu, "Use of SAR/InSAR in Mining Deformation Monitoring, Parameter Inversion, and Forward Predictions: A Review," *IEEE Geoscience and Remote Sensing Magazine*, vol. 8, no. 1, pp. 71–90, 2020.

[236] C. Yu, Z. Li, N. T. Penna, and P. Crippa, "Generic Atmospheric Correction Model for Interferometric Synthetic Aperture Radar Observations," *Journal of Geophysical Research: Solid Earth*, vol. 123, no. 10, pp. 9202–9222, 2018.

[237] G. Zhang, B. Eddy Patuwo, and M. Y. Hu, "Forecasting with artificial neural networks:: The state of the art," *International Journal of Forecasting*, vol. 14, no. 1, pp. 35–62, 1998.

[238] J. Zhang, X. Cao, J. Xie, and P. Kou, "An Improved Long Short-Term Memory Model for Dam Displacement Prediction," *Mathematical Problems in Engineering*, vol. 2019, e6792189, 2019.

[239] S. Zhang, B. Chen, H. Gong, K. Lei, M. Shi, and C. Zhou, "Three-Dimensional Surface Displacement of the Eastern Beijing Plain, China, Using Ascending and Descending Sentinel-1A/B Images and Leveling Data," *Remote Sensing*, vol. 13, no. 14, p. 2809, 14 2021.

[240] K. Zhao and S.-n. Chen, "Study on artificial neural network method for ground subsidence prediction of metal mine," *Procedia Earth and Planetary Science*, vol. 2, pp. 177–182, 2011.

[241] Z. Zhao, Z. Wu, Y. Zheng, and P. Ma, "Recurrent neural networks for atmospheric noise removal from InSAR time series with missing values," *ISPRS Journal of Photogrammetry and Remote Sensing*, vol. 180, pp. 227–237, 2021.

[242] D. Zhou, K. Wu, R. Chen, and L. Li, "GPS/terrestrial 3D laser scanner combined monitoring technology for coal mining subsidence: A case study of a coal mining area in Hebei, China," *Natural Hazards*, vol. 70, no. 2, pp. 1197–1208, 2014.

[243] L. Zhou, H. Yu, Y. Lan, and m. xing, "Artificial Intelligence In Interferometric Synthetic Aperture Radar Phase Unwrapping: A Review," *IEEE Geoscience and Remote Sensing Magazine*, vol. 9, no. 2, pp. 10–28, 2021.

Appendix A

Ascending SAR acquisitions

Table A.1: List of SAR image acquisitions from the ascending path no. 73, used in the time series InSAR analyses

SAR Image
S1A_IW_SLC__1SDV_20160520T164313_20160520T164340_011345_01137E_19C7
S1A_IW_SLC__1SDV_20160601T164314_20160601T164341_011520_011934_76C2
S1A_IW_SLC__1SDV_20160613T164314_20160613T164341_011695_011EAD_9B98
S1A_IW_SLC__1SDV_20160707T164316_20160707T164343_012045_0129DA_E25B
S1A_IW_SLC__1SDV_20160719T164316_20160719T164343_012220_012F8B_352C
S1A_IW_SLC__1SDV_20160731T164317_20160731T164344_012395_01354B_97EC
S1A_IW_SLC__1SDV_20160812T164318_20160812T164345_012570_013B19_109F
S1A_IW_SLC__1SDV_20160824T164318_20160824T164345_012745_0140FA_C50E
S1A_IW_SLC__1SDV_20160905T164319_20160905T164346_012920_0146CB_AF42
S1A_IW_SLC__1SDV_20160917T164318_20160917T164346_013095_014C73_0E22
S1A_IW_SLC__1SDV_20160929T164320_20160929T164347_013270_015226_E9CD
S1B_IW_SLC__1SDV_20161005T164256_20161005T164324_002374_004029_A199
S1A_IW_SLC__1SDV_20161011T164320_20161011T164347_013445_0157AD_83A1
S1B_IW_SLC__1SDV_20161017T164256_20161017T164324_002549_0044D7_F00F
S1A_IW_SLC__1SDV_20161023T164319_20161023T164347_013620_015D28_ABA2
S1B_IW_SLC__1SDV_20161029T164256_20161029T164324_002724_0049C6_69B1
S1A_IW_SLC__1SDV_20161104T164319_20161104T164346_013795_01629F_AB8C
S1B_IW_SLC__1SDV_20161110T164256_20161110T164324_002899_004EA8_1585
S1A_IW_SLC__1SDV_20161116T164319_20161116T164346_013970_01680F_145A
S1B_IW_SLC__1SDV_20161122T164255_20161122T164323_003074_00539F_5E34
S1A_IW_SLC__1SDV_20161128T164319_20161128T164346_014145_016D6F_F88D
S1B_IW_SLC__1SDV_20161204T164255_20161204T164323_003249_005891_D8C7
S1A_IW_SLC__1SDV_20161210T164319_20161210T164346_014320_0172FE_EAEB
S1B_IW_SLC__1SDV_20161216T164255_20161216T164323_003424_005D95_4152
S1A_IW_SLC__1SDV_20161222T164318_20161222T164345_014495_017872_496C
S1B_IW_SLC__1SDV_20161228T164254_20161228T164322_003599_006297_B424
S1A_IW_SLC__1SDV_20170103T164317_20170103T164344_014670_017DCE_601E
S1B_IW_SLC__1SDV_20170109T164253_20170109T164321_003774_0067CA_F2F7
S1A_IW_SLC__1SDV_20170115T164316_20170115T164343_014845_01832D_2B17
S1B_IW_SLC__1SDV_20170121T164253_20170121T164320_003949_006CF5_4E62
S1A_IW_SLC__1SDV_20170127T164316_20170127T164343_015020_018891_A0D8
S1B_IW_SLC__1SDV_20170202T164252_20170202T164320_004124_007228_A9B3

Continued on next page

Table A.1 – continued from previous page

SAR Image
S1A_IW_SLC__1SDV_20170208T164316_20170208T164343_015195_018E04_55D1
S1B_IW_SLC__1SDV_20170214T164252_20170214T164320_004299_00775F_00F1
S1A_IW_SLC__1SDV_20170220T164316_20170220T164343_015370_019375_27E1
S1B_IW_SLC__1SDV_20170226T164252_20170226T164320_004474_007C97_940E
S1A_IW_SLC__1SDV_20170304T164315_20170304T164343_015545_0198BE_C2C6
S1B_IW_SLC__1SDV_20170310T164252_20170310T164320_004649_0081B3_7C98
S1A_IW_SLC__1SDV_20170316T164316_20170316T164343_015720_019DF9_A4C7
S1B_IW_SLC__1SDV_20170322T164252_20170322T164320_004824_0086D1_9A3D
S1A_IW_SLC__1SDV_20170328T164316_20170328T164343_015895_01A337_36E1
S1B_IW_SLC__1SDV_20170403T164253_20170403T164321_004999_008BE0_B6B9
S1A_IW_SLC__1SDV_20170409T164316_20170409T164344_016070_01A875_4CDD
S1B_IW_SLC__1SDV_20170415T164253_20170415T164321_005174_0090DF_411A
S1A_IW_SLC__1SDV_20170421T164317_20170421T164344_016245_01ADD0_516C
S1B_IW_SLC__1SDV_20170427T164254_20170427T164322_005349_009601_BDD3
S1A_IW_SLC__1SDV_20170503T164318_20170503T164345_016420_01B31E_28AB
S1B_IW_SLC__1SDV_20170509T164254_20170509T164322_005524_009AD9_9420
S1A_IW_SLC__1SDV_20170515T164318_20170515T164345_016595_01B871_DBCF
S1B_IW_SLC__1SDV_20170521T164255_20170521T164323_005699_009FBE_DF05
S1A_IW_SLC__1SDV_20170527T164327_20170527T164354_016770_01BDD3_268F
S1B_IW_SLC__1SDV_20170602T164245_20170602T164312_005874_00A4CB_2ED4
S1A_IW_SLC__1SDV_20170608T164328_20170608T164355_016945_01C341_B314
S1B_IW_SLC__1SDV_20170614T164246_20170614T164313_006049_00A9F1_D1D2
S1A_IW_SLC__1SDV_20170620T164329_20170620T164356_017120_01C8A7_E95E
S1B_IW_SLC__1SDV_20170626T164247_20170626T164314_006224_00AF07_6E75
S1A_IW_SLC__1SDV_20170702T164329_20170702T164356_017295_01CDEE_7524
S1B_IW_SLC__1SDV_20170708T164248_20170708T164315_006399_00B3FB_A4AB
S1A_IW_SLC__1SDV_20170714T164330_20170714T164357_017470_01D337_6ABC
S1B_IW_SLC__1SDV_20170720T164248_20170720T164315_006574_00B8FA_A436
S1A_IW_SLC__1SDV_20170726T164331_20170726T164358_017645_01D895_C5F0
S1B_IW_SLC__1SDV_20170801T164249_20170801T164316_006749_00BE01_F1D0
S1A_IW_SLC__1SDV_20170807T164331_20170807T164358_017820_01DDE9_CA05
S1B_IW_SLC__1SDV_20170813T164250_20170813T164317_006924_00C31A_D7B9
S1A_IW_SLC__1SDV_20170819T164332_20170819T164359_017995_01E336_AAEB
S1B_IW_SLC__1SDV_20170825T164250_20170825T164317_007099_00C82A_AB67
S1A_IW_SLC__1SDV_20170831T164332_20170831T164400_018170_01E879_B34B
S1B_IW_SLC__1SDV_20170906T164251_20170906T164318_007274_00CD41_ACF9
S1A_IW_SLC__1SDV_20170912T164333_20170912T164400_018345_01EDF6_E3D0
S1B_IW_SLC__1SDV_20170918T164251_20170918T164318_007449_00D263_3C3F
S1A_IW_SLC__1SDV_20170924T164333_20170924T164400_018520_01F351_DCFA
S1B_IW_SLC__1SDV_20170930T164251_20170930T164319_007624_00D76A_E154
S1A_IW_SLC__1SDV_20171006T164334_20171006T164401_018695_01F8A6_794D
S1B_IW_SLC__1SDV_20171012T164252_20171012T164319_007799_00DC66_4D13
S1A_IW_SLC__1SDV_20171018T164334_20171018T164401_018870_01FE02_FEB9
S1B_IW_SLC__1SDV_20171024T164252_20171024T164319_007974_00E168_1CF0
S1A_IW_SLC__1SDV_20171030T164334_20171030T164401_019045_020354_7ADE
S1B_IW_SLC__1SDV_20171105T164252_20171105T164319_008149_00E66E_71EA
S1A_IW_SLC__1SDV_20171111T164333_20171111T164400_019220_0208B8_9E3D

Continued on next page

Table A.1 – continued from previous page

SAR Image
S1B_IW_SLC__1SDV_20171117T164251_20171117T164318_008324_00EBB3_A9F3
S1A_IW_SLC__1SDV_20171123T164333_20171123T164400_019395_020E3F_903B
S1B_IW_SLC__1SDV_20171129T164251_20171129T164318_008499_00F11E_4DB7
S1A_IW_SLC__1SDV_20171205T164333_20171205T164400_019570_0213BD_A995
S1B_IW_SLC__1SDV_20171211T164251_20171211T164318_008674_00F6AC_172B
S1A_IW_SLC__1SDV_20171217T164332_20171217T164359_019745_02192D_249B
S1B_IW_SLC__1SDV_20171223T164250_20171223T164317_008849_00FC3E_CE30
S1A_IW_SLC__1SDV_20171229T164332_20171229T164359_019920_021E98_F099
S1B_IW_SLC__1SDV_20180104T164250_20180104T164317_009024_0101ED_9550
S1A_IW_SLC__1SDV_20180110T164331_20180110T164358_020095_02241F_BE6C
S1B_IW_SLC__1SDV_20180116T164249_20180116T164316_009199_01079F_394B
S1A_IW_SLC__1SDV_20180122T164331_20180122T164358_020270_0229AD_738D
S1B_IW_SLC__1SDV_20180128T164249_20180128T164316_009374_010D58_6EF3
S1A_IW_SLC__1SDV_20180203T164331_20180203T164358_020445_022F44_8801
S1B_IW_SLC__1SDV_20180209T164249_20180209T164316_009549_01131B_58AB
S1A_IW_SLC__1SDV_20180215T164330_20180215T164358_020620_0234D8_37DA
S1B_IW_SLC__1SDV_20180221T164248_20180221T164315_009724_0118D9_69AD
S1A_IW_SLC__1SDV_20180227T164330_20180227T164358_020795_023A72_2BDB
S1B_IW_SLC__1SDV_20180305T164248_20180305T164316_009899_011EB1_F31D
S1A_IW_SLC__1SDV_20180311T164330_20180311T164358_020970_023FF0_525A
S1B_IW_SLC__1SDV_20180317T164249_20180317T164316_010074_012473_E63D
S1A_IW_SLC__1SDV_20180323T164331_20180323T164358_021145_02457F_3FAE
S1B_IW_SLC__1SDV_20180329T164249_20180329T164316_010249_012A1D_5E85
S1A_IW_SLC__1SDV_20180404T164331_20180404T164358_021320_024B05_7863
S1B_IW_SLC__1SDV_20180410T164249_20180410T164316_010424_012FD0_32D0
S1A_IW_SLC__1SDV_20180416T164331_20180416T164358_021495_025079_0F76
S1B_IW_SLC__1SDV_20180422T164250_20180422T164317_010599_013564_EEDA
S1A_IW_SLC__1SDV_20180428T164332_20180428T164359_021670_0255F2_4B6B
S1B_IW_SLC__1SDV_20180504T164250_20180504T164317_010774_013B07_66D4
S1A_IW_SLC__1SDV_20180510T164333_20180510T164400_021845_025B81_B31C
S1B_IW_SLC__1SDV_20180516T164251_20180516T164318_010949_0140AD_E72F
S1A_IW_SLC__1SDV_20180522T164333_20180522T164400_022020_026114_67A2
S1B_IW_SLC__1SDV_20180528T164252_20180528T164319_011124_014662_D73F
S1A_IW_SLC__1SDV_20180603T164334_20180603T164401_022195_02669D_8993
S1B_IW_SLC__1SDV_20180609T164252_20180609T164319_011299_014BE8_702F
S1A_IW_SLC__1SDV_20180615T164335_20180615T164402_022370_026C0C_B3C0
S1B_IW_SLC__1SDV_20180621T164253_20180621T164320_011474_01514E_C3E3
S1A_IW_SLC__1SDV_20180627T164335_20180627T164402_022545_027130_9378
S1B_IW_SLC__1SDV_20180703T164254_20180703T164321_011649_0156C4_4A70
S1A_IW_SLC__1SDV_20180709T164336_20180709T164403_022720_02764B_FB13
S1B_IW_SLC__1SDV_20180715T164254_20180715T164322_011824_015C28_E6C7
S1A_IW_SLC__1SDV_20180721T164337_20180721T164404_022895_027BB3_CAAB
S1B_IW_SLC__1SDV_20180727T164255_20180727T164322_011999_016171_E20B
S1A_IW_SLC__1SDV_20180802T164337_20180802T164404_023070_028131_CEA6
S1B_IW_SLC__1SDV_20180808T164256_20180808T164323_012174_0166C9_D7B4
S1A_IW_SLC__1SDV_20180814T164338_20180814T164405_023245_0286D4_154C
S1B_IW_SLC__1SDV_20180820T164257_20180820T164324_012349_016C3E_1FA2

Continued on next page

Table A.1 – continued from previous page

SAR Image
S1A_IW_SLC__1SDV_20180826T164339_20180826T164406_023420_028C71_B67F
S1B_IW_SLC__1SDV_20180901T164257_20180901T164324_012524_0171A4_C9C8
S1A_IW_SLC__1SDV_20180907T164340_20180907T164407_023595_029208_209A
S1B_IW_SLC__1SDV_20180913T164258_20180913T164325_012699_0176FB_1183
S1A_IW_SLC__1SDV_20180919T164340_20180919T164407_023770_0297A9_5AC0
S1B_IW_SLC__1SDV_20180925T164258_20180925T164325_012874_017C61_EA69
S1A_IW_SLC__1SDV_20181001T164340_20181001T164407_023945_029D5D_870D
S1B_IW_SLC__1SDV_20181007T164258_20181007T164326_013049_0181B7_7FDE
S1A_IW_SLC__1SDV_20181013T164340_20181013T164407_024120_02A316_DAEB
S1B_IW_SLC__1SDV_20181019T164259_20181019T164326_013224_01871C_F425
S1A_IW_SLC__1SDV_20181025T164340_20181025T164407_024295_02A8BD_8734
S1B_IW_SLC__1SDV_20181031T164258_20181031T164326_013399_018C9C_F241
S1A_IW_SLC__1SDV_20181106T164340_20181106T164407_024470_02AEC7_051C
S1B_IW_SLC__1SDV_20181112T164258_20181112T164325_013574_01920C_4505
S1A_IW_SLC__1SDV_20181118T164340_20181118T164407_024645_02B536_951E
S1B_IW_SLC__1SDV_20181124T164258_20181124T164325_013749_019799_82BE
S1A_IW_SLC__1SDV_20181130T164339_20181130T164407_024820_02BB78_DD3D
S1B_IW_SLC__1SDV_20181206T164258_20181206T164325_013924_019D40_C054
S1A_IW_SLC__1SDV_20181212T164339_20181212T164406_024995_02C183_6E19
S1B_IW_SLC__1SDV_20181218T164257_20181218T164324_014099_01A2FA_3D14
S1A_IW_SLC__1SDV_20181224T164339_20181224T164406_025170_02C7D6_CF67
S1B_IW_SLC__1SDV_20181230T164257_20181230T164324_014274_01A8D0_7389
S1A_IW_SLC__1SDV_20190105T164338_20190105T164405_025345_02CE24_9E22
S1B_IW_SLC__1SDV_20190111T164256_20190111T164323_014449_01AE76_34CB
S1A_IW_SLC__1SDV_20190117T164338_20190117T164405_025520_02D474_0CBA
S1B_IW_SLC__1SDV_20190123T164256_20190123T164323_014624_01B411_C026
S1B_IW_SLC__1SDV_20190204T164256_20190204T164323_014799_01B9C5_555E
S1A_IW_SLC__1SDV_20190210T164337_20190210T164404_025870_02E129_AEE3
S1B_IW_SLC__1SDV_20190216T164255_20190216T164322_014974_01BF7E_C82A
S1A_IW_SLC__1SDV_20190222T164337_20190222T164404_026045_02E75C_2B5D
S1B_IW_SLC__1SDV_20190228T164255_20190228T164322_015149_01C53B_59B9
S1A_IW_SLC__1SDV_20190306T164337_20190306T164404_026220_02ED9E_353B
S1B_IW_SLC__1SDV_20190312T164255_20190312T164322_015324_01CAFC_3120
S1A_IW_SLC__1SDV_20190318T164337_20190318T164404_026395_02F417_E3A5
S1B_IW_SLC__1SDV_20190324T164255_20190324T164322_015499_01D0A6_2817
S1A_IW_SLC__1SDV_20190330T164337_20190330T164404_026570_02FA85_DA03
S1B_IW_SLC__1SDV_20190405T164256_20190405T164323_015674_01D671_9FFD
S1A_IW_SLC__1SDV_20190411T164337_20190411T164405_026745_0300EE_A03B
S1B_IW_SLC__1SDV_20190417T164256_20190417T164323_015849_01DC40_2279
S1A_IW_SLC__1SDV_20190423T164338_20190423T164405_026920_030742_ED90
S1B_IW_SLC__1SDV_20190429T164257_20190429T164324_016024_01E213_D281
S1A_IW_SLC__1SDV_20190505T164338_20190505T164406_027095_030DA8_0798
S1B_IW_SLC__1SDV_20190511T164257_20190511T164324_016199_01E7C1_D63C
S1A_IW_SLC__1SDV_20190517T164339_20190517T164406_027270_03132C_EA71
S1B_IW_SLC__1SDV_20190523T164258_20190523T164325_016374_01ED31_5676
S1A_IW_SLC__1SDV_20190529T164340_20190529T164407_027445_0318A4_87AA
S1B_IW_SLC__1SDV_20190604T164258_20190604T164325_016549_01F27A_8489

Continued on next page

Table A.1 – continued from previous page

SAR Image
S1A_IW_SLC__1SDV_20190610T164340_20190610T164407_027620_031E00_418E
S1B_IW_SLC__1SDV_20190616T164259_20190616T164326_016724_01F7A9_B935
S1A_IW_SLC__1SDV_20190622T164341_20190622T164408_027795_03233C_7D1B
S1B_IW_SLC__1SDV_20190628T164300_20190628T164327_016899_01FCD3_55B0
S1A_IW_SLC__1SDV_20190704T164342_20190704T164409_027970_032884_4E1B
S1B_IW_SLC__1SDV_20190710T164304_20190710T164331_017074_020201_E2AB
S1A_IW_SLC__1SDV_20190716T164343_20190716T164410_028145_032DD3_8CF1
S1B_IW_SLC__1SDV_20190722T164301_20190722T164328_017249_020717_6C53
S1A_IW_SLC__1SDV_20190728T164343_20190728T164410_028320_03332A_9A86
S1B_IW_SLC__1SDV_20190803T164302_20190803T164329_017424_020C57_885B
S1A_IW_SLC__1SDV_20190809T164344_20190809T164411_028495_033896_7F75
S1B_IW_SLC__1SDV_20190815T164303_20190815T164330_017599_0211BB_8131
S1A_IW_SLC__1SDV_20190821T164345_20190821T164412_028670_033EB0_9BE3
S1B_IW_SLC__1SDV_20190827T164303_20190827T164330_017774_021736_F56C
S1A_IW_SLC__1SDV_20190902T164345_20190902T164412_028845_0344C5_14FF
S1B_IW_SLC__1SDV_20190908T164304_20190908T164331_017949_021CA3_A150
S1A_IW_SLC__1SDV_20190914T164346_20190914T164413_029020_034ADB_50F7
S1B_IW_SLC__1SDV_20190920T164304_20190920T164331_018124_022210_1A2E
S1A_IW_SLC__1SDV_20190926T164346_20190926T164414_029195_0350CB_8BAA
S1B_IW_SLC__1SDV_20191002T164305_20191002T164332_018299_022782_43E7
S1A_IW_SLC__1SDV_20191008T164346_20191008T164414_029370_0356D7_7181
S1B_IW_SLC__1SDV_20191014T164305_20191014T164332_018474_022CF0_7013
S1A_IW_SLC__1SDV_20191020T164346_20191020T164414_029545_035CE3_78D6
S1B_IW_SLC__1SDV_20191026T164305_20191026T164332_018649_02324D_B40B
S1A_IW_SLC__1SDV_20191101T164347_20191101T164414_029720_0362F8_4AA7
S1B_IW_SLC__1SDV_20191107T164305_20191107T164332_018824_0237EF_571B
S1A_IW_SLC__1SDV_20191113T164347_20191113T164414_029895_03691D_EF29
S1B_IW_SLC__1SDV_20191119T164305_20191119T164332_018999_023D9A_FDE2
S1A_IW_SLC__1SDV_20191125T164346_20191125T164413_030070_036F2E_1032
S1B_IW_SLC__1SDV_20191201T164304_20191201T164331_019174_024328_7714
S1A_IW_SLC__1SDV_20191207T164346_20191207T164413_030245_03752F_C0D1
S1B_IW_SLC__1SDV_20191213T164304_20191213T164331_019349_0248BA_0976
S1A_IW_SLC__1SDV_20191219T164345_20191219T164412_030420_037B3D_B40C
S1B_IW_SLC__1SDV_20191225T164303_20191225T164330_019524_024E4D_453B
S1A_IW_SLC__1SDV_20191231T164345_20191231T164412_030595_038148_E543
S1B_IW_SLC__1SDV_20200106T164303_20200106T164330_019699_0253DC_32FE
S1A_IW_SLC__1SDV_20200112T164344_20200112T164411_030770_03875B_34F9
S1B_IW_SLC__1SDV_20200118T164302_20200118T164329_019874_02596E_7F8F
S1A_IW_SLC__1SDV_20200124T164344_20200124T164411_030945_038D7F_BBF3
S1B_IW_SLC__1SDV_20200130T164302_20200130T164329_020049_025F07_6125
S1A_IW_SLC__1SDV_20200205T164344_20200205T164411_031120_03939E_7435
S1B_IW_SLC__1SDV_20200211T164302_20200211T164329_020224_0264BB_2742
S1A_IW_SLC__1SDV_20200217T164343_20200217T164410_031295_0399AD_A4B0
S1B_IW_SLC__1SDV_20200223T164301_20200223T164328_020399_026A5A_039B
S1B_IW_SLC__1SDV_20200306T164301_20200306T164328_020574_026FE7_6398
S1A_IW_SLC__1SDV_20200312T164343_20200312T164410_031645_03A5C2_AF16
S1B_IW_SLC__1SDV_20200318T164301_20200318T164329_020749_02757A_171F

Continued on next page

Table A.1 – continued from previous page

SAR Image
S1A_IW_SLC__1SDV_20200324T164343_20200324T164410_031820_03ABF4_A43F
S1B_IW_SLC__1SDV_20200330T164302_20200330T164329_020924_027AFC_05C0
S1A_IW_SLC__1SDV_20200405T164344_20200405T164411_031995_03B215_B3ED
S1B_IW_SLC__1SDV_20200411T164302_20200411T164329_021099_02808C_D07E
S1A_IW_SLC__1SDV_20200417T164344_20200417T164411_032170_03B844_65BA
S1B_IW_SLC__1SDV_20200423T164302_20200423T164330_021274_028610_FB07
S1A_IW_SLC__1SDV_20200429T164345_20200429T164412_032345_03BE66_D853
S1B_IW_SLC__1SDV_20200505T164303_20200505T164330_021449_028B9E_3134
S1A_IW_SLC__1SDV_20200511T164345_20200511T164412_032520_03C42F_7577
S1B_IW_SLC__1SDV_20200517T164304_20200517T164331_021624_0290D9_B505
S1A_IW_SLC__1SDV_20200523T164346_20200523T164413_032695_03C97C_57B1
S1B_IW_SLC__1SDV_20200529T164305_20200529T164332_021799_02960B_A592
S1A_IW_SLC__1SDV_20200604T164347_20200604T164414_032870_03CEAB_F23D
S1B_IW_SLC__1SDV_20200610T164305_20200610T164332_021974_029B48_A25A
S1A_IW_SLC__1SDV_20200616T164347_20200616T164415_033045_03D3ED_62B5
S1B_IW_SLC__1SDV_20200622T164306_20200622T164333_022149_02A09E_F7E8
S1A_IW_SLC__1SDV_20200628T164348_20200628T164415_033220_03D93D_1A28
S1B_IW_SLC__1SDV_20200704T164306_20200704T164334_022324_02A5F5_2B6A
S1A_IW_SLC__1SDV_20200710T164349_20200710T164416_033395_03DE8B_BEF1
S1B_IW_SLC__1SDV_20200716T164307_20200716T164334_022499_02AB41_4060
S1A_IW_SLC__1SDV_20200722T164350_20200722T164417_033570_03E3EB_F454
S1B_IW_SLC__1SDV_20200728T164308_20200728T164335_022674_02B099_8D1F
S1A_IW_SLC__1SDV_20200803T164350_20200803T164417_033745_03E942_4452
S1B_IW_SLC__1SDV_20200809T164309_20200809T164336_022849_02B5FB_FAD8
S1A_IW_SLC__1SDV_20200815T164351_20200815T164418_033920_03EF4B_958B
S1B_IW_SLC__1SDV_20200821T164309_20200821T164336_023024_02BB71_B4CD
S1A_IW_SLC__1SDV_20200827T164352_20200827T164419_034095_03F574_1E76
S1B_IW_SLC__1SDV_20200902T164310_20200902T164337_023199_02C0E5_A470
S1A_IW_SLC__1SDV_20200908T164352_20200908T164419_034270_03FB9D_2D41
S1B_IW_SLC__1SDV_20200914T164311_20200914T164338_023374_02C662_9277
S1A_IW_SLC__1SDV_20200920T164353_20200920T164420_034445_0401DB_4E05
S1B_IW_SLC__1SDV_20200926T164311_20200926T164338_023549_02CBDE_F158
S1A_IW_SLC__1SDV_20201002T164353_20201002T164420_034620_0407FD_3DB6
S1B_IW_SLC__1SDV_20201008T164311_20201008T164338_023724_02D155_E2EE
S1A_IW_SLC__1SDV_20201014T164353_20201014T164420_034795_040E18_DA29
S1B_IW_SLC__1SDV_20201020T164311_20201020T164338_023899_02D6C4_953A
S1A_IW_SLC__1SDV_20201026T164353_20201026T164420_034970_04141A_8A75

Appendix B

Descending SAR acquisitions

Table B.1: List of SAR image acquisitions from the descending path no. 22, used in the time series InSAR analyses

SAR Image
S1A_IW_SLC__1SDV_20160517T050849_20160517T050916_011294_0111CF_76FA
S1A_IW_SLC__1SDV_20160529T050842_20160529T050909_011469_011790_251A
S1A_IW_SLC__1SDV_20160610T050842_20160610T050909_011644_011D09_3212
S1A_IW_SLC__1SDV_20160704T050844_20160704T050911_011994_012824_2EE9
S1A_IW_SLC__1SDV_20160716T050844_20160716T050911_012169_012DE3_9A83
S1A_IW_SLC__1SDV_20160728T050845_20160728T050912_012344_013391_5AFB
S1A_IW_SLC__1SDV_20160809T050846_20160809T050913_012519_01396F_72DD
S1A_IW_SLC__1SDV_20160821T050847_20160821T050913_012694_013F33_180F
S1A_IW_SLC__1SDV_20160902T050847_20160902T050914_012869_014526_7B51
S1A_IW_SLC__1SDV_20160914T050847_20160914T050914_013044_014AB8_8DD3
S1A_IW_SLC__1SDV_20160926T050848_20160926T050915_013219_01508D_ABDB
S1B_IW_SLC__1SDV_20161002T050813_20161002T050840_002323_003ED9_FD63
S1A_IW_SLC__1SDV_20161008T050848_20161008T050915_013394_015602_0D59
S1B_IW_SLC__1SDV_20161014T050813_20161014T050840_002498_004371_5BDE
S1A_IW_SLC__1SDV_20161020T050848_20161020T050915_013569_015B9D_E233
S1B_IW_SLC__1SDV_20161026T050813_20161026T050840_002673_004854_4987
S1A_IW_SLC__1SDV_20161101T050848_20161101T050915_013744_0160F4_504F
S1B_IW_SLC__1SDV_20161107T050802_20161107T050832_002848_004D2E_7EC4
S1A_IW_SLC__1SDV_20161113T050848_20161113T050915_013919_016684_DD03
S1B_IW_SLC__1SDV_20161119T050802_20161119T050832_003023_005239_697D
S1B_IW_SLC__1SDV_20161201T050801_20161201T050831_003198_005711_2737
S1A_IW_SLC__1SDV_20161207T050847_20161207T050914_014269_017152_805A
S1B_IW_SLC__1SDV_20161213T050801_20161213T050831_003373_005C25_7299
S1A_IW_SLC__1SDV_20161219T050847_20161219T050914_014444_0176D0_EF54
S1B_IW_SLC__1SDV_20161225T050816_20161225T050843_003548_006116_8B03
S1A_IW_SLC__1SDV_20161231T050846_20161231T050913_014619_017C44_0847
S1B_IW_SLC__1SDV_20170106T050814_20170106T050841_003723_006655_F5EA
S1A_IW_SLC__1SDV_20170112T050845_20170112T050912_014794_018183_6E6C
S1B_IW_SLC__1SDV_20170118T050814_20170118T050840_003898_006B6B_E527
S1A_IW_SLC__1SDV_20170124T050844_20170124T050911_014969_0186FD_27FF
S1B_IW_SLC__1SDV_20170130T050813_20170130T050840_004073_0070AA_423A
S1A_IW_SLC__1SDV_20170205T050844_20170205T050911_015144_018C4F_1680
Continued on next page

Table B.1 – continued from previous page

SAR Image
S1B_IW_SLC__1SDV_20170211T050813_20170211T050840_004248_0075D9_8FD9
S1B_IW_SLC__1SDV_20170223T050813_20170223T050840_004423_007B20_4DC2
S1A_IW_SLC__1SDV_20170301T050844_20170301T050911_015494_019728_8C58
S1B_IW_SLC__1SDV_20170307T050813_20170307T050840_004598_00803B_E91A
S1A_IW_SLC__1SDV_20170313T050844_20170313T050911_015669_019C78_1DF1
S1B_IW_SLC__1SDV_20170319T050813_20170319T050840_004773_008561_F512
S1A_IW_SLC__1SDV_20170325T050844_20170325T050911_015844_01A1A9_F27F
S1B_IW_SLC__1SDV_20170331T050813_20170331T050840_004948_008A69_A126
S1A_IW_SLC__1SDV_20170406T050845_20170406T050912_016019_01A6DC_8E48
S1B_IW_SLC__1SDV_20170412T050814_20170412T050841_005123_008F6C_D50B
S1A_IW_SLC__1SDV_20170418T050845_20170418T050912_016194_01AC3A_952F
S1B_IW_SLC__1SDV_20170424T050815_20170424T050842_005298_00947F_FD90
S1A_IW_SLC__1SDV_20170430T050846_20170430T050913_016369_01B18B_D494
S1B_IW_SLC__1SDV_20170506T050812_20170506T050839_005473_009978_067D
S1A_IW_SLC__1SDV_20170512T050846_20170512T050913_016544_01B6D2_FB6B
S1B_IW_SLC__1SDV_20170518T050812_20170518T050839_005648_009E42_3F8D
S1A_IW_SLC__1SDV_20170524T050851_20170524T050919_016719_01BC39_D7B2
S1B_IW_SLC__1SDV_20170530T050815_20170530T050842_005823_00A351_ACF7
S1A_IW_SLC__1SDV_20170605T050852_20170605T050920_016894_01C1AC_C08E
S1B_IW_SLC__1SDV_20170611T050816_20170611T050843_005998_00A86B_27BB
S1A_IW_SLC__1SDV_20170617T050853_20170617T050920_017069_01C711_946E
S1B_IW_SLC__1SDV_20170623T050817_20170623T050844_006173_00AD83_F38C
S1A_IW_SLC__1SDV_20170629T050854_20170629T050921_017244_01CC55_A21D
S1B_IW_SLC__1SDV_20170705T050817_20170705T050845_006348_00B282_FDE2
S1A_IW_SLC__1SDV_20170711T050854_20170711T050922_017419_01D1A6_0DF4
S1B_IW_SLC__1SDV_20170717T050818_20170717T050845_006523_00B783_6651
S1A_IW_SLC__1SDV_20170723T050855_20170723T050922_017594_01D6EE_BA71
S1B_IW_SLC__1SDV_20170729T050819_20170729T050846_006698_00BC7D_9076
S1A_IW_SLC__1SDV_20170804T050856_20170804T050923_017769_01DC50_761F
S1B_IW_SLC__1SDV_20170810T050820_20170810T050847_006873_00C190_7DCE
S1A_IW_SLC__1SDV_20170816T050856_20170816T050924_017944_01E19D_0340
S1B_IW_SLC__1SDV_20170822T050820_20170822T050847_007048_00C6A3_96B0
S1A_IW_SLC__1SDV_20170828T050857_20170828T050924_018119_01E6E9_4D7E
S1B_IW_SLC__1SDV_20170903T050821_20170903T050848_007223_00CBB8_BC5B
S1A_IW_SLC__1SDV_20170909T050857_20170909T050925_018294_01EC47_DF90
S1B_IW_SLC__1SDV_20170915T050821_20170915T050848_007398_00D0DC_5E68
S1A_IW_SLC__1SDV_20170921T050858_20170921T050925_018469_01F1A9_D549
S1B_IW_SLC__1SDV_20170927T050822_20170927T050849_007573_00D5E4_D8E5
S1A_IW_SLC__1SDV_20171003T050858_20171003T050925_018644_01F704_5006
S1B_IW_SLC__1SDV_20171009T050822_20171009T050849_007748_00DAEB_0D91
S1A_IW_SLC__1SDV_20171015T050858_20171015T050925_018819_01FC5A_365F
S1B_IW_SLC__1SDV_20171021T050822_20171021T050849_007923_00DFE2_AE9C
S1A_IW_SLC__1SDV_20171027T050858_20171027T050926_018994_0201AC_04E9
S1B_IW_SLC__1SDV_20171102T050822_20171102T050849_008098_00E4EA_9131
S1A_IW_SLC__1SDV_20171108T050858_20171108T050925_019169_020711_7BD5
S1B_IW_SLC__1SDV_20171114T050822_20171114T050849_008273_00EA21_8CA5
S1A_IW_SLC__1SDV_20171120T050858_20171120T050925_019344_020C93_B6C2

Continued on next page

Table B.1 – continued from previous page

SAR Image
S1B_IW_SLC__1SDV_20171126T050822_20171126T050849_008448_00EF78_238A
S1A_IW_SLC__1SDV_20171202T050858_20171202T050925_019519_021209_A76E
S1B_IW_SLC__1SDV_20171208T050822_20171208T050849_008623_00F501_431E
S1A_IW_SLC__1SDV_20171214T050857_20171214T050924_019694_021783_ECC9
S1B_IW_SLC__1SDV_20171220T050821_20171220T050848_008798_00FA9A_9E8B
S1A_IW_SLC__1SDV_20171226T050857_20171226T050924_019869_021CED_02C0
S1B_IW_SLC__1SDV_20180101T050821_20180101T050848_008973_010039_7E5A
S1A_IW_SLC__1SDV_20180107T050856_20180107T050923_020044_02226F_27B4
S1B_IW_SLC__1SDV_20180113T050821_20180113T050848_009148_0105F4_E7B4
S1A_IW_SLC__1SDV_20180119T050856_20180119T050923_020219_0227FF_E394
S1B_IW_SLC__1SDV_20180125T050820_20180125T050847_009323_010BAB_C44F
S1A_IW_SLC__1SDV_20180131T050855_20180131T050922_020394_022D8F_3FD7
S1B_IW_SLC__1SDV_20180206T050820_20180206T050847_009498_011168_D7D0
S1A_IW_SLC__1SDV_20180212T050855_20180212T050922_020569_02332B_CB7D
S1B_IW_SLC__1SDV_20180218T050820_20180218T050847_009673_011724_695D
S1A_IW_SLC__1SDV_20180224T050855_20180224T050922_020744_0238C1_D1CD
S1B_IW_SLC__1SDV_20180302T050820_20180302T050847_009848_011CF4_6C6A
S1A_IW_SLC__1SDV_20180308T050855_20180308T050922_020919_023E42_A2E8
S1B_IW_SLC__1SDV_20180314T050820_20180314T050847_010023_0122CA_E4AA
S1A_IW_SLC__1SDV_20180320T050855_20180320T050922_021094_0243D0_00DA
S1B_IW_SLC__1SDV_20180326T050820_20180326T050847_010198_012878_ABA4
S1A_IW_SLC__1SDV_20180401T050856_20180401T050923_021269_024958_0A97
S1B_IW_SLC__1SDV_20180407T050820_20180407T050847_010373_012E2C_7248
S1A_IW_SLC__1SDV_20180413T050856_20180413T050923_021444_024ECD_447B
S1B_IW_SLC__1SDV_20180419T050821_20180419T050847_010548_0133BF_8006
S1A_IW_SLC__1SDV_20180425T050856_20180425T050924_021619_025440_F107
S1B_IW_SLC__1SDV_20180501T050821_20180501T050848_010723_01395E_520E
S1A_IW_SLC__1SDV_20180507T050857_20180507T050924_021794_0259CC_7880
S1B_IW_SLC__1SDV_20180513T050822_20180513T050849_010898_013F08_EC25
S1A_IW_SLC__1SDV_20180519T050858_20180519T050925_021969_025F61_E598
S1B_IW_SLC__1SDV_20180525T050822_20180525T050849_011073_0144B8_15F4
S1A_IW_SLC__1SDV_20180531T050858_20180531T050925_022144_026502_2508
S1B_IW_SLC__1SDV_20180606T050822_20180606T050849_011248_014A48_05EB
S1A_IW_SLC__1SDV_20180612T050859_20180612T050926_022319_026A74_745E
S1B_IW_SLC__1SDV_20180618T050823_20180618T050850_011423_014FAD_5980
S1A_IW_SLC__1SDV_20180624T050900_20180624T050927_022494_026FB0_3B1B
S1B_IW_SLC__1SDV_20180630T050819_20180630T050846_011598_015522_2377
S1B_IW_SLC__1SDV_20180712T050819_20180712T050846_011773_015A8C_9A2E
S1A_IW_SLC__1SDV_20180718T050901_20180718T050928_022844_027A23_6CD3
S1B_IW_SLC__1SDV_20180724T050820_20180724T050847_011948_015FE0_0A70
S1A_IW_SLC__1SDV_20180730T050902_20180730T050929_023019_027FA9_1D5E
S1B_IW_SLC__1SDV_20180805T050820_20180805T050848_012123_016529_20C0
S1A_IW_SLC__1SDV_20180811T050903_20180811T050930_023194_02852C_656A
S1B_IW_SLC__1SDV_20180817T050821_20180817T050848_012298_016A93_3E03
S1A_IW_SLC__1SDV_20180823T050903_20180823T050930_023369_028AD4_7211
S1B_IW_SLC__1SDV_20180829T050822_20180829T050849_012473_017006_3D4E
S1A_IW_SLC__1SDV_20180904T050904_20180904T050931_023544_029063_0704

Continued on next page

Table B.1 – continued from previous page

SAR Image
S1B_IW_SLC__1SDV_20180910T050822_20180910T050849_012648_01756A_0B25
S1A_IW_SLC__1SDV_20180916T050904_20180916T050931_023719_029600_C0CB
S1B_IW_SLC__1SDV_20180922T050823_20180922T050850_012823_017AC5_B533
S1A_IW_SLC__1SDV_20180928T050905_20180928T050932_023894_029BAF_265A
S1B_IW_SLC__1SDV_20181004T050823_20181004T050850_012998_01801F_31D8
S1A_IW_SLC__1SDV_20181010T050905_20181010T050932_024069_02A16E_43A2
S1B_IW_SLC__1SDV_20181016T050823_20181016T050850_013173_018577_91EA
S1A_IW_SLC__1SDV_20181022T050905_20181022T050932_024244_02A71F_4C35
S1B_IW_SLC__1SDV_20181028T050823_20181028T050850_013348_018AE8_4707
S1A_IW_SLC__1SDV_20181103T050905_20181103T050932_024419_02ACEF_C573
S1B_IW_SLC__1SDV_20181109T050823_20181109T050850_013523_01905F_CE20
S1A_IW_SLC__1SDV_20181115T050905_20181115T050932_024594_02B35C_6CCC
S1B_IW_SLC__1SDV_20181121T050829_20181121T050856_013698_0195EB_13C7
S1A_IW_SLC__1SDV_20181127T050904_20181127T050931_024769_02B9D2_58E4
S1B_IW_SLC__1SDV_20181203T050829_20181203T050856_013873_019B88_680A
S1A_IW_SLC__1SDV_20181209T050904_20181209T050931_024944_02BFA8_DB42
S1B_IW_SLC__1SDV_20181215T050828_20181215T050855_014048_01A13E_F4A7
S1A_IW_SLC__1SDV_20181221T050903_20181221T050931_025119_02C5FD_778B
S1B_IW_SLC__1SDV_20181227T050828_20181227T050855_014223_01A70C_5BC9
S1A_IW_SLC__1SDV_20190102T050903_20190102T050930_025294_02CC4C_60EB
S1B_IW_SLC__1SDV_20190108T050828_20190108T050854_014398_01ACC3_9315
S1A_IW_SLC__1SDV_20190114T050903_20190114T050930_025469_02D296_7007
S1B_IW_SLC__1SDV_20190120T050827_20190120T050854_014573_01B263_3EDA
S1A_IW_SLC__1SDV_20190126T050902_20190126T050929_025644_02D905_B9FA
S1B_IW_SLC__1SDV_20190201T050827_20190201T050854_014748_01B801_5400
S1A_IW_SLC__1SDV_20190207T050902_20190207T050929_025819_02DF46_2621
S1B_IW_SLC__1SDV_20190213T050826_20190213T050853_014923_01BDBE_026E
S1A_IW_SLC__1SDV_20190219T050902_20190219T050929_025994_02E585_C3D1
S1B_IW_SLC__1SDV_20190225T050826_20190225T050853_015098_01C37E_7AEE
S1A_IW_SLC__1SDV_20190303T050902_20190303T050929_026169_02EBC7_C483
S1B_IW_SLC__1SDV_20190309T050826_20190309T050853_015273_01C944_F77E
S1A_IW_SLC__1SDV_20190315T050902_20190315T050929_026344_02F234_3BE5
S1B_IW_SLC__1SDV_20190321T050826_20190321T050853_015448_01CEEF_2F3A
S1A_IW_SLC__1SDV_20190327T050902_20190327T050929_026519_02F89E_A961
S1B_IW_SLC__1SDV_20190402T050827_20190402T050854_015623_01D4AF_565C
S1A_IW_SLC__1SDV_20190408T050902_20190408T050929_026694_02FF13_D69D
S1B_IW_SLC__1SDV_20190414T050827_20190414T050854_015798_01DA80_3BBC
S1A_IW_SLC__1SDV_20190420T050903_20190420T050930_026869_030565_AC20
S1B_IW_SLC__1SDV_20190426T050828_20190426T050855_015973_01E047_E863
S1A_IW_SLC__1SDV_20190502T050903_20190502T050930_027044_030BC6_9A7B
S1B_IW_SLC__1SDV_20190508T050828_20190508T050855_016148_01E61C_4F1C
S1A_IW_SLC__1SDV_20190514T050904_20190514T050931_027219_031196_1727
S1B_IW_SLC__1SDV_20190520T050822_20190520T050849_016323_01EB81_F92F
S1A_IW_SLC__1SDV_20190526T050904_20190526T050931_027394_03170F_795C
S1B_IW_SLC__1SDV_20190601T050823_20190601T050850_016498_01F0D5_CDF3
S1A_IW_SLC__1SDV_20190607T050905_20190607T050932_027569_031C74_1E82
S1B_IW_SLC__1SDV_20190613T050823_20190613T050851_016673_01F60C_586A

Continued on next page

Table B.1 – continued from previous page

SAR Image
S1A_IW_SLC__1SDV_20190619T050905_20190619T050933_027744_0321B6_9E6D
S1B_IW_SLC__1SDV_20190625T050824_20190625T050851_016848_01FB39_9568
S1A_IW_SLC__1SDV_20190701T050906_20190701T050933_027919_0326F1_0388
S1B_IW_SLC__1SDV_20190707T050825_20190707T050852_017023_020066_452B
S1A_IW_SLC__1SDV_20190713T050907_20190713T050934_028094_032C3F_EE2C
S1B_IW_SLC__1SDV_20190719T050826_20190719T050853_017198_020580_9DCC
S1A_IW_SLC__1SDV_20190725T050908_20190725T050935_028269_033187_19CB
S1B_IW_SLC__1SDV_20190731T050826_20190731T050853_017373_020AAB_CA2E
S1A_IW_SLC__1SDV_20190806T050909_20190806T050936_028444_0336E4_01A6
S1B_IW_SLC__1SDV_20190812T050827_20190812T050854_017548_021008_410D
S1A_IW_SLC__1SDV_20190818T050909_20190818T050936_028619_033CD9_53EC
S1B_IW_SLC__1SDV_20190824T050828_20190824T050855_017723_021581_9197
S1A_IW_SLC__1SDV_20190830T050910_20190830T050937_028794_0342FC_C396
S1B_IW_SLC__1SDV_20190905T050828_20190905T050856_017898_021AEB_21E9
S1A_IW_SLC__1SDV_20190911T050910_20190911T050937_028969_034910_A6BF
S1B_IW_SLC__1SDV_20190917T050829_20190917T050856_018073_022060_6611
S1A_IW_SLC__1SDV_20190923T050911_20190923T050938_029144_034F0A_CBBA
S1A_IW_SLC__1SDV_20191005T050911_20191005T050938_029319_035512_4C64
S1B_IW_SLC__1SDV_20191011T050829_20191011T050856_018423_022B41_4AD8
S1A_IW_SLC__1SDV_20191017T050911_20191017T050938_029494_035B18_25BD
S1B_IW_SLC__1SDV_20191023T050830_20191023T050857_018598_02309D_E085
S1A_IW_SLC__1SDV_20191029T050911_20191029T050938_029669_03612F_3020
S1B_IW_SLC__1SDV_20191104T050821_20191104T050849_018773_023627_036A
S1A_IW_SLC__1SDV_20191110T050911_20191110T050938_029844_036752_AE35
S1B_IW_SLC__1SDV_20191116T050821_20191116T050849_018948_023BDB_4A3F
S1A_IW_SLC__1SDV_20191122T050911_20191122T050938_030019_036D5F_5B02
S1B_IW_SLC__1SDV_20191128T050821_20191128T050849_019123_024171_7639
S1A_IW_SLC__1SDV_20191204T050910_20191204T050938_030194_037370_6E12
S1B_IW_SLC__1SDV_20191210T050820_20191210T050848_019298_0246FE_FA7B
S1A_IW_SLC__1SDV_20191216T050910_20191216T050937_030369_03797C_EDCA
S1B_IW_SLC__1SDV_20191222T050820_20191222T050848_019473_024C8F_BE96
S1A_IW_SLC__1SDV_20191228T050910_20191228T050937_030544_037F80_2479
S1B_IW_SLC__1SDV_20200103T050819_20200103T050847_019648_02521F_E67B
S1A_IW_SLC__1SDV_20200109T050909_20200109T050936_030719_03858D_844D
S1B_IW_SLC__1SDV_20200115T050819_20200115T050847_019823_0257B2_62B3
S1A_IW_SLC__1SDV_20200121T050909_20200121T050936_030894_038BB7_B798
S1B_IW_SLC__1SDV_20200127T050818_20200127T050846_019998_025D4C_9109
S1A_IW_SLC__1SDV_20200202T050908_20200202T050935_031069_0391D1_89C3
S1B_IW_SLC__1SDV_20200208T050818_20200208T050846_020173_0262FD_7EE7
S1A_IW_SLC__1SDV_20200214T050908_20200214T050935_031244_0397E3_E01A
S1B_IW_SLC__1SDV_20200220T050818_20200220T050846_020348_026899_D786
S1A_IW_SLC__1SDV_20200226T050908_20200226T050935_031419_039DEA_7C17
S1B_IW_SLC__1SDV_20200303T050818_20200303T050846_020523_026E38_4289
S1A_IW_SLC__1SDV_20200309T050908_20200309T050935_031594_03A3FD_5FCF
S1B_IW_SLC__1SDV_20200315T050818_20200315T050846_020698_0273C4_04EE
S1A_IW_SLC__1SDV_20200321T050908_20200321T050935_031769_03AA1D_B2B6
S1B_IW_SLC__1SDV_20200327T050818_20200327T050846_020873_027946_41DB

Continued on next page

Table B.1 – continued from previous page

SAR Image
S1A_IW_SLC__1SDV_20200402T050908_20200402T050935_031944_03B046_79BB
S1B_IW_SLC__1SDV_20200408T050818_20200408T050846_021048_027ED5_5C18
S1A_IW_SLC__1SDV_20200414T050909_20200414T050936_032119_03B672_43CD
S1B_IW_SLC__1SDV_20200420T050819_20200420T050847_021223_028459_EBBF
S1A_IW_SLC__1SDV_20200426T050909_20200426T050936_032294_03BC92_450D
S1B_IW_SLC__1SDV_20200502T050819_20200502T050847_021398_0289E3_9163
S1A_IW_SLC__1SDV_20200508T050910_20200508T050937_032469_03C298_DE2B
S1B_IW_SLC__1SDV_20200514T050828_20200514T050855_021573_028F48_D45B
S1A_IW_SLC__1SDV_20200520T050910_20200520T050937_032644_03C7E8_6211
S1B_IW_SLC__1SDV_20200526T050829_20200526T050856_021748_02946A_FB6B
S1A_IW_SLC__1SDV_20200601T050911_20200601T050938_032819_03CD2E_A088
S1B_IW_SLC__1SDV_20200607T050830_20200607T050857_021923_0299AC_1BFA
S1A_IW_SLC__1SDV_20200613T050912_20200613T050939_032994_03D25F_81D3
S1B_IW_SLC__1SDV_20200619T050830_20200619T050857_022098_029EF7_2810
S1A_IW_SLC__1SDV_20200625T050913_20200625T050940_033169_03D7AD_AD65
S1B_IW_SLC__1SDV_20200701T050831_20200701T050858_022273_02A458_D3A1
S1A_IW_SLC__1SDV_20200707T050913_20200707T050940_033344_03DD01_8379
S1B_IW_SLC__1SDV_20200713T050832_20200713T050859_022448_02A9AA_EC46
S1A_IW_SLC__1SDV_20200719T050914_20200719T050941_033519_03E25A_669F
S1B_IW_SLC__1SDV_20200725T050832_20200725T050900_022623_02AEF7_937D
S1A_IW_SLC__1SDV_20200731T050915_20200731T050942_033694_03E7BB_C086
S1B_IW_SLC__1SDV_20200806T050833_20200806T050900_022798_02B446_FF95
S1A_IW_SLC__1SDV_20200812T050915_20200812T050943_033869_03ED89_A69B
S1B_IW_SLC__1SDV_20200818T050834_20200818T050901_022973_02B9B4_9B80
S1A_IW_SLC__1SDV_20200824T050916_20200824T050943_034044_03F3B3_3243
S1B_IW_SLC__1SDV_20200830T050835_20200830T050902_023148_02BF35_0EC7
S1A_IW_SLC__1SDV_20200905T050917_20200905T050944_034219_03F9DB_75AD
S1B_IW_SLC__1SDV_20200911T050835_20200911T050902_023323_02C4AE_B6AC
S1A_IW_SLC__1SDV_20200917T050917_20200917T050944_034394_03FFFA_FB76
S1B_IW_SLC__1SDV_20200923T050835_20200923T050903_023498_02CA25_1AD4
S1A_IW_SLC__1SDV_20200929T050917_20200929T050945_034569_040632_F3AE
S1B_IW_SLC__1SDV_20201005T050836_20201005T050903_023673_02CFAB_6F56
S1A_IW_SLC__1SDV_20201011T050918_20201011T050945_034744_040C52_F6FA
S1B_IW_SLC__1SDV_20201017T050836_20201017T050903_023848_02D511_AFF2
S1A_IW_SLC__1SDV_20201023T050918_20201023T050945_034919_041264_9C2A